Stefan Weber, Dipl.-Ing. BSc

Emerging Photovoltaic Technologies – From Lead-Free Tin and Antimony Halide Perovskites to New Non-Fullerene Acceptors for Solar Cells

DOCTORAL THESIS

to achieve the university degree of
Doktor der technischen Wissenschaften

submitted to
Graz University of Technology

Supervisor
Univ.-Prof. Dipl.-Ing. Dr.techn. Gregor Trimmel

Institute for Chemistry and Technology of Materials

Graz, August 2020

AFFIDAVIT

I declare that I have authored this thesis independently, that I have not used other than the declared sources/resources, and that I have explicitly indicated all material which has been quoted either literally or by content from the sources used. The text document uploaded to TUGRAZonline is identical to the present doctoral thesis.

Date, Signature

Life is too short to compromise. (Phoebe)

Abstract

Throughout the last decades various new solar cell technologies have emerged with potential to improve energy output and/or reduce fabrication costs compared to existing technologies. Among them, perovskite solar cells and organic solar cells are the most dominant technologies in terms of power conversion efficiency and variability.

Perovskite solar cells have astonished the scientific community reaching already power conversion efficiencies in the range of silicon solar cells. However, the most efficient perovskite solar cells contain toxic lead, which makes the future of this technology uncertain. Thus, lead-free perovskites are currently heavily investigated as alternatives.

The first part of the thesis focusses on the investigation of antimony and tin perovskite solar cells. One approach to optimize the properties of lead-free perovskites is halide substitution. As shown within this thesis, the substitution of iodide with bromide reduces the unit cell and in turn increases the optical band gap as shown by Vegard's law.

Antimony perovskites were synthesized by using a rubidium antimony halide perovskite composition. The crystal system remained monoclinic and did not change upon substitution of iodide with bromide. Solar cells with a rubidium antimony bromide perovskite absorber provided only low current densities and open circuit voltages thus displayed only low device performances. Increasing the iodide content enhanced the current density and open circuit voltage to reach a power conversion efficiency of 1.37%.

Triple cation tin perovskites, composed of a methylammonium, formamidinium and phenethylammonium tin halide perovskite, were also investigated in the same matter. The iodide content was hereby substituted by bromide in the range of $x = 0 - 0.33$ and solar cells were fabricated using a normal device set-up. Results showed that already a small amount of bromine in the perovskite ($x = 0.25$) can increase the open circuit voltage and short circuit current to get a maximum device efficiency of 4.63%, in comparison to its iodide-based perovskite solar cells with a maximum device efficiency of 2.97%.

In the second part of this thesis, new non-fullerene acceptors for organic solar cells were investigated. Organic solar cells stand out due to their low weight and high flexibility in applications and processability, and new materials, so called non-fullerene acceptors started a new era of high efficient organic photovoltaics.

Herein, acceptor-donor-acceptor materials with perylene monoimides as acceptor unit and different fluorene derivatives as donor unit were linked by Suzuki coupling. The fluorene derivatives, namely, fluorene, silafluorene, carbazole and indenofluorene, exhibited similar optoelectronic properties such as HOMO/LUMO levels, band gaps or electron mobilities. Solar cells were fabricated with different donor/acceptor ratios and annealing conditions. Therein, the use of an indenofluorene-based acceptor reached the highest device performance of 6.21% with a donor/acceptor ratio of 1/0.66 and annealing of the absorber layer at 135 °C.

Kurzfassung

In den letzten Jahrzehnten hat sich die Zahl neuer Solarzellentechnologien vervielfacht, womit auch das Potential die Energiegewinnung zu steigern und eine Kostenreduktion im Vergleich zu bereits bestehenden Technologien zu erzielen, anstieg. Unter diese Kategorie fallen auch Perowskitsolarzellen und organische Solarzellen welche aufgrund ihrer hohen Effizienz als vielversprechend angesehen werden.

Durch intensive Forschung an bleibasierten Perowskitsolarzellen wurden in den letzten Jahren große Fortschritte erzielt und Wirkungsgrade im Bereich der Siliziumsolarzellen erreicht. Jedoch ist die hohe Toxizität von Blei ein großes Hindernis und macht eine Vermarktung schwierig. Deshalb wird bereits an bleifreien Alternativen geforscht.

Der erste Teil dieser Arbeit untersucht antimon- und zinnbasierte Perowskitsolarzellen. Durch Substitution des Halogens kann man die Eigenschaften der Perowskite verändern. Dabei zeigt sich, dass ein Austausch von Iodid mit Bromid die Bandlücke vergrößert und die Einheitszelle verkleinert. Die Änderungen durch Einführung des Halogens in den Perowskit folgen dabei Vegard's Gesetz.

In Antimonperowskiten wurde ein Rubidium-Antimon-Halogenid Perowskit als Grundmaterial eingesetzt. Dabei konnte allen Perowskiten ein monoklines Kristallsystem zugeordnet werden. Solarzellen mit Rubidium-Antimon-Bromid als Absorberschicht führen zu geringer Leerlaufspannung und zu niedrigen Kurschlussströmen woraus sich nur geringe Effizienzen ergeben. Mit steigendem Iodidgehalt verbessern sich diese Parameter. Für einen reinen Rubidium-Antimon-Iodid Perowskit wurde dabei die höchste Effizienz von 1.37% gemessen.

Für zinnbasierte Perowskite konnte man unter denselben Substitutionsbedingungen eine Erhöhung der Effizienz beobachten. Hierbei wurde für das A-Kation eine Mischung aus Methylammonium, Formamidinium, und Phenethylammonium verwendet um den Zinn-Halogenid Perowskit zu formen. Der iodidbasierte Perowskit wurde dann stufenweise mit Bromid substituiert ($x = 0 – 0.33$). Schon ein kleiner Anteil von Bromid ($x = 0.25$) im Perowskit führt zu einer höheren Leerlaufspannung und zusätzlich zu einer Erhöhung des Kurzschlussstromes und somit zu einer Steigerung des Wirkungsgrades auf 4.63% im Vergleich zu 2.97% für den rein iodierten Perowskit ($x = 0$).

Im zweiten Teil dieser Arbeit wurden neue *Non-Fulleren*-Akzeptoren für organische Solarzellen untersucht. Organische Solarzellen zeichnen sich durch ihr geringes Gewicht, zahlreiche Applikationen sowie unterschiedliche Prozessierungsmöglichkeiten aus.

In dieser Arbeit wurden *Non-Fulleren*-Akzeptoren mit einer Akzeptor-Donor-Akzeptor Struktur hergestellt. Dabei bildet Perlyen monoimid den Akzeptorteil während verschiedene Fluoreneinheiten als Donoren eingebaut wurden. Die Fluorenderivate (Fluoren, Silafluoren, Carbazol und Indenofluoren) weisen alle ähnliche optoelektronische Eigenschaften wie HOMO/LUMO Lagen, Bandlücken und Elektronenmobilitäten auf. In organischen Solarzellen wurden diese Verbindungen in unterschiedlichen Donor/Akzeptor Verhältnissen und mit unterschiedlicher thermischer Behandlung hergestellt. Dabei erreichte der Akzeptor, der mit Indenofluoren gelinkt wurde, die höchste Effizienz von 6.21% mit einem Donor/Akzeptor Verhältnis 1/0.66 und getempert bei 135 °C.

Acknowledgements

First of all, I want to give my gratitude to my supervisor Gregor Trimmel for his supervision over all the years we spent together. Also, for giving me the opportunity to work on several different topics throughout my thesis which challenged me a lot in a good way.

I also want to thank the Österreichische Forschungsförderungsgesellschaft (FFG) for their financial support in the projects PERMASOL (FFG-No. 848 929) and ALTAFOS (FFG No. 865 072)

My thesis would have never been possible without other people contributing to my research. I want to thank all the students (project laboratory, bachelor and diploma students) whom I had the chance to work with; especially Kathrin Fellner, Bianca Brandl, Jasmin Handl, Corinna Weixler and René Nauschnig.

I also want to thank Petra Kaschnitz for the help with NMR spectroscopy, Josefine Hobisch for DSC measurements, David Pfeifer, Andreas Steinegger and Sergey Borisov for supporting me with synthesis and fluorescence measurements, Birgit Kunert and Roland Resel for their help with XRD measurements and evaluations, Theodoros Dimopoulos for the SEM measurements, Roland Fischer for the single crystal analysis, Michaela Flock for the introduction in DFT and Markus Scharber as well as Jakob Hofinger for all the vast number of measurements concerning organic solar cells, discussions and input.

Next, I want to give my gratitude to my whole working group for all the board game evenings, travels and other activities we did together. I want to especially thank Birgit Ehmann and Marvin Paschek for their help, enthusiasm and good friendship. Also, I want to specifically name Jimmy Mangalam whom I found a very good friend in and have a special connection to. Special thanks also go to Thomas Rath for all the discussions about solar cells and all the help for my publications.

My deepest gratitude goes to my family. They always supported me physically and mentally as well as financially. I could always talk to them and they always had a sympathetic ear for me when necessary.

Last but not least I want to thank the most special person in my life, my girlfriend Sandra for always pushing me and loving me. Thank you for all the discussions, advices and solutions concerning either chemistry or personal things.

Table of Contents

Chapter I

Introduction

Introduction

Electricity is one of the main energy sources of mankind. The electricity generation can be achieved by several sources such as nuclear power or fossil resources but also by renewable resources like wind, water, the sun and others.[1] Because of an increasing population and higher global energy demand CO_2 emissions are constantly rising. To reduce the consequential higher air pollution and greenhouse gas effect the development of renewable energy sources is highly desired. Moreover, the reserves on fossil resources are constantly decreasing. One of the most promising renewable technologies is solar energy. It can be generated on a wide operation range throughout the earth only limited in polar regions. Moreover, the availability of solar energy is endless and there is enough unoccupied area for installation, e.g. rooftops, unused land, agriculture or floating photovoltaic (PV).

Although solar cells were discovered in 1883, the starting point of modern solar cells was the invention of the first silicon solar cell in 1954 by Bell Labs.[2] In the following years silicon solar cells became the primary technology and are classified as first-generation solar cells. Other technologies such as Cadmium telluride (CdTe), Copper Indium Gallium selenide (CIGS) or Gallium arsenide (GaAs) also started to emerge which were later summarized as the second generation solar cells.[3] As the development progressed new materials and material classes emerged which are now summarized in the third-generation solar cells also known as emerging photovoltaics.[3,4] So far, they are mainly produced in lab scale but first technologies are already commercially available and more companies are striving for commercialization of these technologies. Within the group of emerging photovoltaics two technologies particularly stand out – perovskite solar cells and organic solar cells.[3]

The first perovskite solar cell was developed by Kojima et al. in 2009 with a power conversion efficiency (PCE) of 3.8% using methylammonium lead iodide ($MAPbI_3$) as absorber.[5] In the following years research on different lead-based perovskites with various compositions led to a steady improve in device efficiency up to a maximum of 25.2%.[3,6,7,8,9,10,11,12,13] Therewith they can already compete with other commercialized thin film technologies. However, a major drawback is the highly toxic lead which may hinder commercialization in the long-term.[14] Therefore, scientists search for less toxic lead alternatives close to lead in the periodic table. As perovskites can be formed in the composition ABX_3 but also in the perovskite-like $A_3B_2X_9$

(A – monovalent cation, B – di – or trivalent cation and C – monovalent anion), elements like tin, germanium, bismuth and antimony are suitable candidates.

Tin is considered as the most promising alternative to possibly replace lead due to its similar optical and electronical properties.[15] First solar cells consisting of tin perovskites were published in 2014 by Noel et al. and Hao et al. with device efficiencies of 5 to 6%.[16,17,18] In recent years the main issue was to tackle the stability problems. This instability is ascribed to (i) the easy oxidation of Sn^{+II} to Sn^{+IV} in presence of oxygen leading to self p-doping and (ii) a higher Lewis acidity leading to fast crystallization of the perovskite which leads to bad film morphology.[19,20] Yao et al. discussed different strategies to improve the stability of tin perovskites.[21] Herein he mentioned four possible ways that may result in higher stability, namely (i) additive engineering, (ii) deoxidizer, (iii) partial substitution and (iv) reduced dimensions.[21] Considering these effects maximum power conversion efficiencies of >9% have been reached so far.[22,23,24,25,26]

Besides tin and germanium with an ABX_3 crystal structure, antimony and bismuth form $A_3B_2X_9$ perovskites due to their different valence number. Many efforts have been devoted to bismuth as lead alternative due to its high stability. However, they still lack in device efficiency reaching maximum PCE values of around 3%.[27] Contrary, antimony is far less investigated and shows similar stability as bismuth. First antimony-based perovskite solar cells were published in 2016 by Hebig et al. with an efficiency of 0.49%.[28] Increasing the efficiency depends on the perovskite's dimensionality and composition and is an ongoing process.[29,30,31,32,33,34] Up to date, a maximum efficiency of 3.08% with an $MASbSI_2$ perovskite was recorded.[35]

After perovskite solar cells, organic solar cells (OSCs) are the next most promising photovoltaic technology out of all emerging photovoltaics. They offer various advantages like light weight, flexibility and a possible energy efficient production via roll-to-roll processes.[36,37] The absorber layer of OSCs consists of a donor and acceptor material, deposited either separately (bilayer-heterojunction) or mixed (bulk-heterojunction).[38,39] From the beginning, fullerenes like [6,6]-phenyl-C_{61}-butyric acid methyl ester ($PCBM_{60}$) or [6,6]-Phenyl-C_{71}-butyric acid methyl ester ($PCBM_{70}$) were mainly used as acceptor materials in OSCs. In order to maximize the device performance many new donor materials were developed to fit the optoelectronic properties of fullerenes.[40,41,42] As a result solar cells with >10% device efficiency could be fabricated.[43,44] However, the possibilities with fullerenes are limited since their absorption range is narrow and

the formation of large aggregates can hardly be suppressed. Moreover, the production costs remain high and tunability of fullerenes is challenging.[45,46,47,48]

To tackle the drawbacks from fullerenes, so called non-fullerene-acceptors (NFAs) came into focus.[48] They benefit among other things from tunable absorption and higher stability due to easy substitution of additional side groups.[49,50] This led to an increase in power conversion efficiency up to 17.4%.[3] Among the huge variety of used compounds, NFAs based on perylenes are one alternative to fullerenes. Their optoelectronic properties can be adjusted easily by the introduction of side groups at ortho, bay or imide position as well as by ring modulation.[51,52,53,54] So far mainly perylene diimides (PDI) substituted at the bay-position are reported and high power conversion efficiencies of up to 10.58% were reached and can rival fullerene-based OSCs.[52,54,55] Contrary to that, perylene monoimides (PMI) are another possibility in the class of perylenes with an open side at the imide position for further substitution. Only a hand full of research groups worked with PMIs up to date introducing core molecules between two PMI units such as fluorene, thiophene or benzene.[56,57,58] Thereby, the highest device efficiency of 6% was reached with two PMI units linked by a fluorene core.[53]

Aim of this Thesis

Within this thesis two promising emerging photovoltaic technologies (perovskite and organic solar cells) are studied. The thesis is comprised of two sections; first, the development of new lead-free perovskites solar cells and secondly the synthesis of new non-fullerene-acceptors for organic solar cells.

Perovskite Solar Cells

In this part, tin and antimony perovskite were investigated as less toxic alternatives to their lead counterparts. The investigation focuses on the question, how the iodide/bromide ratio influences the optical and electrical, and thus the photovoltaic properties of the material. In order to do this, a stable antimony and tin iodide perovskite, known from literature, has to be selected and stepwise substituted with bromide. The implementation of bromide into the perovskite should be verified by single crystal analysis, optical spectroscopy and X-Ray diffraction measurements. Following, the influence of the iodide/bromide ratio on the photovoltaic performance will be studied by assembling solar cells. Their performance is recorded by current-voltage (J-V) measurements. To verify the accuracy of the J-V measurements maximum power point tracking (m_{pp} tracking) and external quantum efficiency (EQE) measurements should be recorded in addition. The hysteresis behavior of all perovskites has to be researched as well by comparing J-V measurements in normal and reverse scan direction. Exemplarily, on the best solar cells, the stability of the best solar cells should be analyzed.

Organic Solar Cells

The second part comprises of an easily accessible and innovative synthesis route for new NFAs. A material backbone should be selected which offers the possibility to be easily substituted at various positions. The resulting new NFAs should then be investigated in terms of their optical and electronic properties. Theoretical calculations using density functional theory (DFT) will be used as a first insight. Prior to the solar cell fabrication, the optoelectronic properties will be determined by e.g. UV-Vis spectroscopy, fluorescence spectroscopy or cyclic voltammetry (CV). Consequently, a suitable donor material will be selected to assemble organic solar cells. The optimization of such will be achieved by changing the donor/acceptor (D/A) ratio, concentration and annealing conditions. The performance will be recorded by J-V, EQE and m_{pp} tracking measurements.

References

[1] Electricity generation by fuel and scenario, 2018-2040, https://www.iea.org/data-and-statistics/charts, accessed on 18/03/**2020**.

[2] APS News, **2009**, *18*, April 25, 1954: Bell Labs demonstrates the first practical silicon solar cell, https://www.aps.org/publications/apsnews/200904/physicshistory.cfm, accessed on 02.07.**2020**.

[3] Research Cell Record Efficiency Chart, National Renewable Energy Laboratory (NREL), https://www.nrel.gov/pv, accessed on 20/07/**2020**.

[4] M. T. Kibria, A. Ahammed, S. M. Sony, F. Hossain, S.-U.-Islam, A Review: Comparative studies on different generation solar cells technology, Proceedings of 5th International Conference on Environmental Aspects of Bangladesh [ICEAB 2015], **2014**, 51-53.

[5] A. Kojima, K. Teshima, Y. Shirai, T. Miyasaka, Organometal Halide Perovskites as Visible-Light Sensitizers for Photovoltaic Cells, *J. Am. Chem. Soc.* **2009**, *131*, 6050-6051.

[6] H. S. Kim, C. R. Lee, J. H. Im, K. B. Lee, T. Moehl, A. Marchioro, S. J. Moon, R. Humphry-Baker, J. H. Yum, J. E. Moser, M. Grätzel, N. G. Park, Lead iodide perovskite sensitized all-solid-state submicron thin film mesoscopic solar cell with efficiency exceeding 9%, *Sci. Rep.* **2012**, *2*, 591.

[7] J. Burschka, N. Pellet, S.-J. Moon, R. Humphry-Baker, P. Gao, M. K. Nazeeruddin, M. Grätzel, Sequential deposition as a route to high-performance perovskite-sensitized solar cells, *Nature* **2013**, *499*, 316-319.

[8] W. S. Yang, J. H. Noh, N. J. Jeon, Y. C. Kim, S. Ryu, J. Seo, S. I. Seok, High-performance photovoltaic perovskite layers fabricated through intramolecular exchange, *Science* **2015**, *348*, 1234-1237.

[9] H. Zhou, Q. Chen, G. Li, S. Luo, T.-B. Song, H.-S. Duan, Z. Hong, J. You, Y. Liu, Y. Yang, Interface engineering of highly efficient perovskite solar cells, *Science* **2014**, *345*, 542-546.

[10] M. Saliba, T. Matsui, K. Domanski, J.-Y. Seo, A. Ummadisingu, S. M. Zakeeruddin, J.-P. Correa-Baena, W. R. Tress, A. Abate, A. Hagfeldt, M. Grätzel, Incorporation of rubidium cations into perovskite solar cells improves photovoltaic performance, *Science* **2016**, *354*, 206-209.

[11] W. S. Yang, B.-W. Park, E. H. Jung, N. J. Jeon, Y. C. Kim, D. U. Lee, S. S. Shin, J. Seo, E. K. Kim, J. H. Noh, S. I. Seok, Iodide management in formamidinium-lead-halide–based perovskite layers for efficient solar cells, *Science* **2017**, *356*, 1376-1379.

[12] N. J. Jeon, H. Na, E. H. Jung, T.-Y. Yang, Y. G. Lee, G. Kim, H.-W. Shin, S. I. Seok, J. Lee, J. Seo, A fluorene-terminated hole-transporting material for highly efficient and stable perovskite solar cells, *Nat. Energy* **2018**, *3*, 682-689.

[13] H. Min, M. Kim, S. U. Lee, H. Kim, G. Kim, K. Choi, J. H. Lee, S. I. Seok, Efficient, stable solar cells by using inherent bandgap of α-phase formamidinium lead iodide, *Science* **2019**, *366*, 749-753.

[14] J. Li, H.-L. Cao, W.-B. Jiao, Q. Wang, M. Wei, I. Cantone, J. Lü, A. Abate, Biological impact of lead from halide perovskites reveals the risk of introducing a safe threshold, *Nat. Comm.* **2020**, *11*, 310.

[15] Q. Chen, N. De Marco, Y. Yang, T.-B. Song, C.-C. Chen, H. Zhao, Z. Hong, H. Zhou, Y. Yang, Under the spotlight: The organic-inorganic hybrid halide perovskite for optoelectronic applications, *Nano Today* **2015**, *10*, 355-396.

[16] N. K. Noel, S. D. Stranks, A. Abate, C. Wehrenfennig, S. Guarnera, A.-A. Haghighirad, A. Sadhanala, G. E. Eperon, S. K. Pathak, M. B. Johnston, A. Petrozza, L. M. Herz, H. J. Snaith, Lead-free organic–inorganic tin halide perovskites for photovoltaic applications, *Energy Environ. Sci.* **2014**, *7*, 3061-3068.

[17] F. Hao, C. C. Stoumpos, R. P. H. Chang, M. G. Kanatzidis, Anomalous Band Gap Behavior in Mixed Sn and Pb Perovskites Enables Broadening of Absorption Spectrum in Solar Cells, *J. Am. Chem. Soc.* **2014**, *136*, 8094-8099.

[18] F. Hao, C. C. Stoumpos, D. H. Cao, R. P. H. Chang, M. G. Kanatzidis, Lead-free solid-state organic-inorganic halide perovskite solar cells, *Nat. Photonics* **2014**, *8*, 489-494.

[19] F. Hao, C. C. Stoumpos, P. Guo, N. Zhou, T. J. Marks, R. P. H. Chang, M. G. Kanatzidis, Solvent-Mediated Crystallization of $CH_3NH_3SnI_3$ Films for Heterojunction Depleted Perovskite Solar Cells, *J. Am. Chem. Soc.* **2015**, *137*, 11445-11452.

[20] S. Gupta, D. Cahen, G. Hodes, How SnF_2 Impacts the Material Properties of Lead-Free Tin Perovskites, *J. Phys. Chem. C* **2018**, *122*, 13926.

[21] H. Yao, F. Zhou, Z. Li, Z. Ci, L. Ding, Z. Lin, Strategies for Improving the Stability of Tin-Based Perovskite ($ASnX_3$) Solar Cells, *Adv. Sci.* **2020**, *7*, 1903540.

[22] X. Liu, K. Yan, D. Tan, X. Liang, H. Zhang, W. Huang, Solvent Engineering Improves Efficiency of Lead-Free Tin-Based Hybrid Perovskite Solar Cells beyond 9%, *ACS Energy Lett.* **2018**, *3*, 2701-2707.

[23] E. Jokar, C.-H. Chien, C.-M. Tsai, A. Fathi, E. W.-G. Diau, Robust Tin-Based Perovskite Solar Cells with Hybrid Organic Cations to Attain Efficiency Approaching 10%, *Adv. Mater.* **2018**, *31*, 1804835.

[24] S. Shao, J. Liu, G. Portale, H.-H. Fang, G. R. Blake, G. H. ten Brink, L. J. A. Koster, M. A. Loi, Highly Reproducible Sn-Based Hybrid Perovskite Solar Cells with 9% Efficiency, *Adv. Mater.* **2017**, *8*, 1702019.

[25] F. Wang, X. Jiang, H. Chen, Y. Shang, H. Liu, J. Wei, W. Zhou, H. He, W. Liu, Z. Ning, 2D-Quasi-2D-3D Hierarchy Structure for Tin Perovskite Solar Cells with Enhanced Efficiency and Stability, *Joule* **2018**, *2*, 2732-2743.

[26] L.-J. Chen, C.-R. Lee, Y.-J. Chuang, Z.-H. Wu, C. Chen, Synthesis and Optical Properties of Lead-Free Cesium Tin Halide Perovskite Quantum Rods with High-Performance Solar Cell Application, *J. Phys. Chem. Lett.* **2016**, *7*, 5028-5035.

[27] S. M. Jain, D. Phuyal, M. L. Davies, M. Li, B. Philippe, C. De Castro, Z. Qiu, J. Kim, T. Watson, W. C. Tsoi, O. Karis, H. Rensmo, G. Boschloo, T. Edvinsson, J. R. Durrant, An effective approach of vapour assisted morphological tailoring for reducing metal defect sites in lead-free, $(CH_3NH_3)_3Bi_2I_9$ Bismuth-

based perovskite solar cells for improved performance and long-term stability, *Nano Energy* **2018**, *49*, 614-624.

[28] J.-C. Hebig, I. Kühn, J. Flohre, T. Kirchartz, Optoelectronic Properties of $(CH_3NH_3)_3Sb_2I_9$ Thin Films for Photovoltaic Applications, *ACS Energy Lett.* **2016**, *1*, 309-314.

[29] J.-P. Correa-Baena, L. Nienhaus, R. C. Kurchin, S. S. Shin, S. Wieghold, N. T. Putri Hartono, M. Layurova, N. D. Klein, J. R. Poindexter, A. Polizzotti, S. Sun, M. G. Bawendi and T. Buonassisi, *A*-Site Cation in Inorganic $A_3Sb_2I_9$ Perovskite Influences Structural Dimensionality, Exciton Binding Energy, and Solar Cell Performance, *Chem. Mater.* **2018**, *30*, 3734-3742.

[30] P. C. Harikesh, H. K. Mulmudi, B. Ghosh, T. W. Goh, Y. T. Teng, K. Thirumal, M. Lockrey, K. Weber, T. M. Koh, S. Z. Li, S. Mhaisalkar and N. Mathews, Rb as an Alternative Cation for Templating Inorganic Lead-Free Perovskites for Solution Processed Photovoltaics, *Chem. Mater.* **2016**, *28*, 7496-7504.

[31] F. Li, Y. Wang, K. Xia, R. L. Z. Hoye, V. Pecunia, Microstructural and photoconversion efficiency enhancement of compact films of lead-free perovskite derivative $Rb_3Sb_2I_9$, *J. Mater. Chem. A* **2020**, *8*, 4396-4406.

[32] K. M. Boopathi, P. Karuppuswamy, A. Singh, C. Hanmandlu, L. Lin, S. A. Abbas, C. C. Chang, P. C. Wang, G. Li, C. W. Chu, Solution-Processable Antimony-Based Light-Absorbing Materials Beyond Lead Halide Perovskites, *J. Mater. Chem. A* **2017**, *5*, 20843-20850.

[33] P. Karuppuswamy, K. M. Boopathi, A. Mohapatra, H. C. Chen, K.-T. Wong, P.-C. Wang, C.-W. Chu, Role of a Hydrophobic Scaffold in Controlling the Crystallization of Methylammonium Antimony Iodide for Efficient Lead-Free Perovskite Solar Cells, *Nano Energy* **2018**, *45*, 330-336.

[34] F. Umar, J. Zhang, Z. Jin, I. Muhammad, X. Yang, H. Deng, K. Jahangeer, Q. Hu, H. Song, J. Tang, Dimensionality Controlling of $Cs_3Sb_2I_9$ for Efficient All-Inorganic Planar Thin Film Solar Cells by HCl-Assisted Solution Method, *Adv. Optical Mater.* **2019**, *7*, 1801368.

[35] R. Nie, A. Mehta, B.-W. Park, H.-W. Kwon, J. Im, S. I. Seok, Mixed Sulfur and Iodide-Based Lead-Free Perovskite Solar Cells, *J. Am. Chem. Soc.* **2018**, *140*, 872-875.

[36] S. Günes, H. Neugebauer, N. S. Sariciftci, Conjugated Polymer-Based Organic Solar Cells, *Chem. Rev.* **2007**, *107*, 1324-1338.

[37] Y. Lin, X. Zhan, Oligomer Molecules for Efficient Organic Photovoltaics, *Acc. Chem. Res.* **2016**, *49*, 175-183.

[38] K. H. Lee, P. E. Schwenn, A. R. G. Smith, H. Cavaye, P. E. Shaw, M. James, K. B. Krueger, I. R. Gentle, P. Meredith, P. L. Burn, Morphology of All-Solution-Processed "Bilayer" Organic Solar Cells, *Adv. Mater.* **2011**, *23*, 766-770.

[39] Y. Cui, H. Yao, J. Zhang, T. Zhang, Y. Wang, L. Hong, K. Xian, B. Xu, S. Zhang, J. Peng, Z. Wei, F. Gao, J. Hou, Over 16% efficiency organic photovoltaic cells enabled by a chlorinated acceptor with increased open-circuit voltages, *Nat. Comm.* **2019**, *10*, 2515.

[40] H.-Y. Chen, J. Hou, S. Zhang, Y. Liang, G. Yang, Y. Yang, L. Yu, Y. Wu, G. Li, Polymer solar cells with enhanced open-circuit voltage and efficiency, *Nat. Photonics* **2009**, *3*, 649-653.

[41] Y. Liang, Y. Wu, D. Feng, S.-T. Tsai, H.-J. Son, G. Li, L. Yu, Development of New Semiconducting Polymers for High Performance Solar Cells, *J. Am. Chem. Soc.* **2009**, *131*, 56-57.

[42] Y. Liang, L. Yu, A New Class of Semiconducting Polymers for Bulk Heterojunction Solar Cells with Exceptionally High Performance, *Acc. Chem. Res.* **2010**, *43*, 1227-1236.

[43] Y. Liu, J. Zhao, Z. Li, C. Mu, W. Ma, H. Hu, K. Jiang, H. Lin, H. Ade, H. Yan, Aggregation and morphology control enables multiple cases of high-efficiency polymer solar cells, *Nat. Comm.* **2014**, *5*, 5293.

[44] J. Zhao, Y. Li, G. Yang, K. Jiang, H. Lin, H. Ade, W. Ma, H. Yan, Efficient organic solar cells processed from hydrocarbon solvents, *Nat. Energy* **2016**, *1*, 15027.

[45] C. B. Nielsen, S. Holliday, H.-Y. Chen, S. J. Cryer, I. McCulloch, Non-Fullerene Electron Acceptors for Use in Organic Solar Cells, *Acc. Chem. Res.* **2015**, *48*, 2803-2812.

[46] T. Heumueller, W. R. Mateker, A. Distler, U. F. Fritze, R. Cheacharoen, W. H. Nguyen, M. Biele, M. Salavador, M. von Delius, H.-J. Egelhaaf, M. D. McGehee, C. J. Brabec, Morphological and electrical control of fullerene dimerization determines organic photovoltaic stability, *Energy Environ. Sci.* **2016**, *9*, 247-256.

[47] A. Distler, T. Sauermann, H.-J. Egelhaar, S. Rodman, D. Waller, K.-S. Cheon, M. Lee, D. M. Guldi, The Effect of PCBM Dimerization on the Performance of Bulk Heterojunction Solar Cells, *Adv. Energy Mater.* **2014**, *4*, 1300693.

[48] C. Yan, S. Barlow, Z. Wang, H. Yan, A. K.-Y. Jen, S. R. Marder, X. Zhan, Non-fullerene acceptors for organic solar cells, *Nat. Rev. Mater.* **2018**, *3*, 18003.

[49] X. Liu, B. Xie, C. Duan, Z. Wang, B. Fan, K. Zhang, B. Lin, F. J. M. Colberts, W. Ma, R. A. J. Janssen, F. Huang, Y. Cao, A high dielectric constant non-fullerene acceptor for efficient bulk-heterojunction organic solar cells, *J. Mater. Chem. A* **2018**, *6*, 395-403.

[50] J. Yang, F. Chen, R. Cong, H. Xiao, Y. Geng, Z. Liao, L. Chen, B. Zhang, R. Zhou, Tuning the optoelectronic properties of vinylene linked perylenediimide dimer by ring annulation at the inside or outside bay positions for fullerene-free organic solar cells, *J. Energy Chem.* **2020**, *40*, 112-119.

[51] P. E. Hartnett, A. Timalsina, H. S. S. R. Matte, N. Zhou, X. Guo, W. Zhao, A. Facchetti, R. P. H. Chang, M. C. Hersam, M. R. Wasielewski, T. J. Marks, Slip-Stacked Perylenediimides as an Alternative Strategy for High Efficiency Nonfullerene Acceptors in Organic Photovoltaics, *J. Am. Chem. Soc.* **2014**, *136*, 16345-16356.

[52] J. Liu, S. Chen, D. Qian, B. Gautam, G. Yang, J. Zhao, J. Bergqvist, F. Zhang, W. Ma, H. Ade, O. Inganäs, K. Gundogdu, F. Gao, H. Yan, Fast charge separation in a non-fullerene organic solar cell with a small driving force, *Nat. Energy* **2016**, *1*, 16089.

[53] Y. Zhang, X. Guo, B. Guo, W. Su, M. Zhang, Y. Li, Nonfullerene Polymer Solar Cells based on a Perylene Monoimide Acceptor with a High Open-Circuit Voltage of 1.3 V, *Adv. Funct. Mater.* **2017**, *27*, 1603892.

[54] H. Zhong, C.-H. Wu, C.-Z. Li, J. Carpenter, C.-C. Chueh, J.-Y. Chen, H. Ade, A. K.-Y. Jen, Rigidifying Nonplanar Perylene Diimides by Ring Fusion Toward Geometry-Tunable Acceptors for High-Performance Fullerene-Free Solar Cells, *Adv. Mater.* **2016**, *28*, 951-958.

[55] J. Zhang, Y. Li, J. Huang, H. Hu, G. Zhang, T. Ma, P. C. Y. Chow, H. Ade, D. Pan, H. Yan, Ring-Fusion of Perylene Diimide Acceptor Enabling Efficient Nonfullerene Organic Solar Cells with a Small Voltage Loss, *J. Am. Chem. Soc.* **2017**, *139*, 16092-16095.

[56] Y. Zhang, Y. Xiao, Y. Xie, L. Zhu, D. Shi, C. Cheng, Fluorene-centered perylene monoimides as potential non-fullerene acceptor in organic solar cells, *Org. Electron.* **2015**, *21*, 184-191.

[57] J. Cremer, P. Bäuerle, Perylene-Oligothiophene–Perylene Triads for Photovoltaic Applications, *Eur. J. Org. Chem.* **2005**, 3715-3723.

[58] Y. Hu, S. Chen, L. Zhang, Y. Zhang, Z. Yuan, X. Zhao, Y. Chen, Facile Approach to Perylenemonoimide with Short Side Chains for Nonfullerene Solar Cells, *J. Org. Chem.* **2017**, *82*, 5926-5931.

Chapter II

Theoretical Section

1 Photovoltaic Technology Classifications

Solar cell technologies are often assigned to a certain photovoltaic generation depending on their time of discovery. Crystalline silicon solar cells form the first-generation solar cells, whereas thin film technologies such as amorphous silicon (a-Si:H), GaAs, CdTe or CIGS form the second-generation photovoltaics. The main difference between these two technologies is the thickness of the absorber layer. Silicon solar cells require a thick absorber layer of >100µm while the other absorbers can be deposited within a few microns or less. Out of all technologies within the second generation only GaAs can surpass silicon solar cells in terms of efficiency, however, GaAs solar cells are more expensive and therefore mainly used in space applications. The third solar cell generation, called emerging photovoltaics, contains other thin film technologies like dye-sensitized solar cells, perovskite solar cells (PSCs), organic solar cells, quantum dot solar cells and copper zinc tin sulfide (CZTS) solar cells. Compared to first and second generation, they are still under research and only a few are commercialized to certain extent. The power output of PSCs can already rival the ones from CdTe or CIGS which makes PSCs the most promising technology to be commercialized soon.[1,2,3,4]

2 General Background about Solar Cells

Within this chapter the different working principles of PSCs and OSCs are described and also the possible device configurations (normal and inverse) are explained.

2.1 Working Principle

Perovskites are intrinsic semiconductors, meaning their Fermi level is located at the center of valence band and conduction band. Charge extraction occurs only if an additional p-type and n-type semiconductor were deposited to sandwich the perovskite. Upon illumination, photons with an energy equal to the band gap or higher can excite electrons (i), leaving a hole behind. The electrons are then transferred by a so-called electron transport layer (ETL) to the respective electrode (ii) and the holes are transferred via hole-transport layers (HTL) to their respective electrode (iii). However, this only applies in theory as the holes are fictional.[5,6]

Regarding the respective holes, one has to mention that a solar cell is connected to an external power source that constantly passes current through the cell. Constant recombination takes place at the interface between HTL and perovskite.

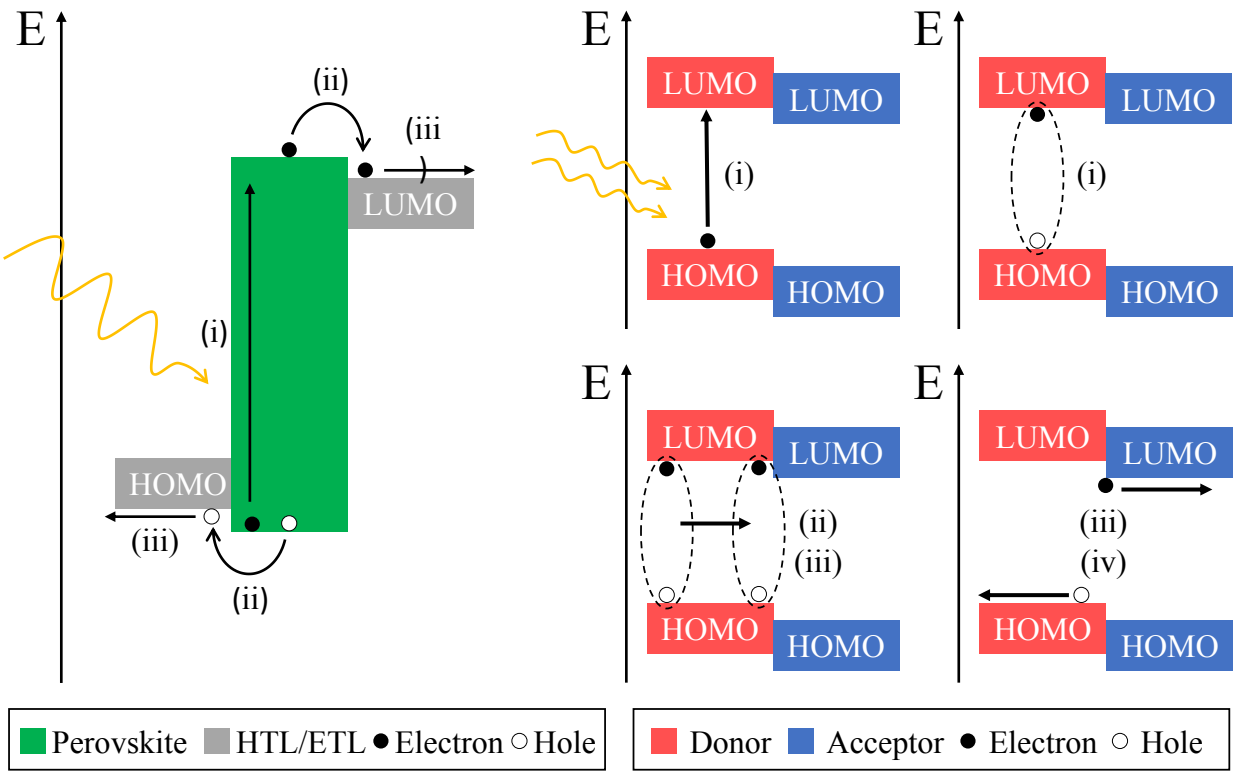

Figure 1: Working principle of perovskite solar cells (left) and organic solar cells (right).[5,7]

In organic solar cells charge generation requires an absorber consisting of two components – donor (p-type material) and acceptor (n-type material). For charge separation, the donor requires a higher lying LUMO level and a higher lying HOMO level than the acceptor. The whole process consists of four steps. Illumination generates an exciton (electron-hole pair) in the donor phase (i). This process can also occur in the acceptor phase. The exciton diffuses within the donor phase (or acceptor phase) to the donor-acceptor interface (ii) where the charges are separated (iii) and further transported to their respective electrodes (iv).[5,7]

2.2 Device Configurations

Organic and perovskite solar cells are often assembled on glass substrates with a precoated transparent conductive oxide (TCO). Thereafter, either a HTL or ETL is deposited to enhance effective charge extraction followed by deposition of the absorber material. On top of the absorber layer the respective counterpart to HTL/ETL is deposited and the cell is completed by a metal electrode.[5,8]

In general, there exist two basic assembling models, usually called normal or inverse. In a normal device set-up, the ETL is directly deposited on the TCO and the HTL on top of the active material and opposite for the inverse set-up (**Figure 2**).[5]

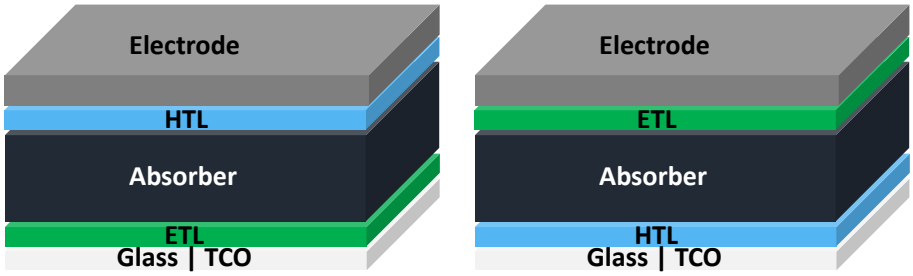

Figure 2: Normal device architecture (left) and inverse architecture (right).

In case of PSCs, the set-ups are also called n-i-p (normal) or p-i-n (inverse) architecture. Moreover, in PSCs mesoporous scaffolds can be introduced instead of a regular HTL or ETL. This increases the surface area of the layer as a certain part of the absorber is able to diffuse into the mesoporous film.[5,8] Organic solar cells can be assembled in a bilayer or bulk heterojunction. In a bilayer heterojunction acceptor and donor are deposited separately while in a bulk heterojunction donor and acceptor are mixed together in order to increase the surface area (**Figure 3**) and enhance the charge separation. One drawback is the possible formation of islands within the bulk material leading to recombination and no charge extraction.[5]

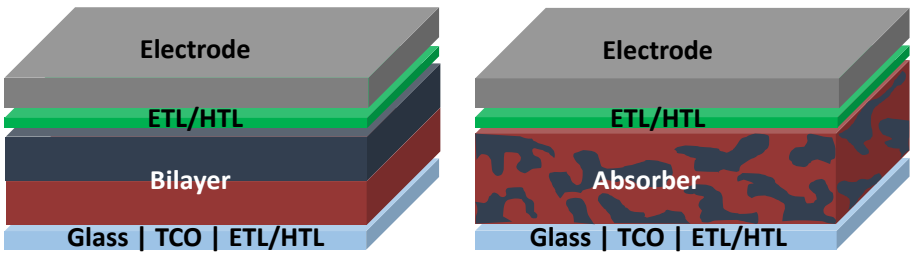

Figure 3: Organic solar cell set-up – bilayer heterojunction (left) and bulk heterojunction (right).

3 Perovskite Solar Cells

3.1 General Aspects about Perovskites

Perovskites are generally formed in an ABX_3 structure. The backbone is formed by BX_6 octahedrons with the A-cation located at the voids between them (see **Figure 4**). Herein the A-cation is either mono- or divalent, the B-cation can be found in oxidation state (+2) or (+4) and the X-anion is usually present in oxidation state (-1) or (-2) to maintain charge neutrality.[9] In solar cells, the perovskite mainly consists of an $A^{+I}B^{+II}X_3^{-I}$ composition.

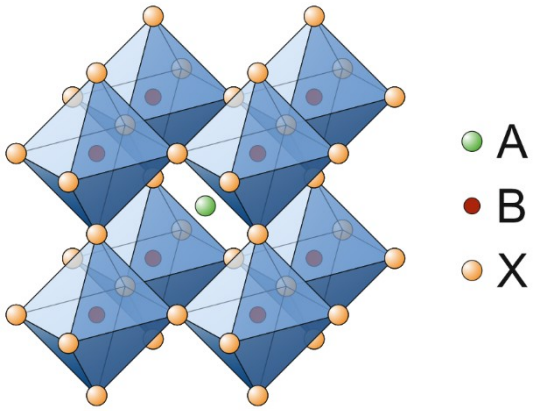

Figure 4: General ABX_3 perovskite structure, reprinted from Hoefler et al.[9]

The ion selection for perovskites in solar cells evolved throughout the last decade from simple $MAPbI_3$ or formamidinium lead iodide ($FAPbI_3$) perovskites to more complex mixed ion perovskites.[10]

Generally, the introduction of larger X-anions (Cl < Br < I) into the perovskite results in an extension of the unit cell thus reducing the band gap. Substitution of the A-cation has the same effect although it is not as pronounced as by anion substitution. They can be organic like methylammonium (MA) or formamidinium (FA) or inorganic (e.g. Cs, Rb).[10,11,12,13]

The mixing of several cations and anions showed a positive effect in the optoelectronic properties and stability of the perovskite.[11,12] In terms of stability, the formation of a cubic crystal structure is desired. It can be calculated via the Goldschmidt tolerance factor and is require to be between 0.8 and 1. Moreover, mixing of the cations was described to provide efficient stabilization as

shown for the perovskite formamidinium lead iodide ($FAPbI_3$). Herein certain amounts of MA were added to obtain the desired black phase.[11]

The toxicity of lead motivated researchers to also investigate lead-free alternatives such as tin, germanium, antimony or bismuth for photovoltaic applications.[9,11] For perovskites where the B-cation has a different oxidation state to (+2), like antimony or bismuth, the composition changes towards a quasi-perovskite with formulas of e.g. $A_3B_2X_9$ or A_3BX_6 crystals.[14]

3.2 Perovskites Types and State of the Art

In this section lead perovskite solar cells and their lead-free alternatives are discussed and their progress (state of the art) is summarized.

3.2.1 Lead Perovskites

Since the first published perovskite solar cell in 2009 the knowledge in lead-based perovskite solar cells increased drastically.[15] Important key parameters like a homogenous layer formation, hysteresis free J-V curves and stability of the cells were tackled.[16] This was achieved by modifying the design of the perovskite composition. From simple ABX_3 perovskites like $MAPbI_3$ mixed perovskites were synthesized.[11] The substitution of the A-cation and X-anion with other organic (MA, FA, PEA) or inorganic (Cs, Rb) species as well as halides (Cl, Br, I) led to an improvement through idealized crystal structures, tunable band gaps and higher stability.[12,13,17,18] Up to date a maximum device efficiency of 25.2% was certified.[2] This technology is closest to be commercialized however, many issues like the production in large scale, long-term stability and the toxicity of lead in connection with their environmental effects still remain a major concern.[16,19] That in return also led to the investigation of lead-free perovskite alternatives for solar cells.

3.2.2 Tin Perovskites

The material closest to substitute lead is tin because of its similar properties.[20] The purpose of using tin is its low toxicity compared to lead, which has been under discussion for years. Hao et al. and Noel et al. were the first to start researching on tin perovskites for solar cells. Both working groups published first tin-based perovskite solar cells in 2014 with approximately 6% using

$MASnI_3$ (Noel et al.) and $MASnIBr_2$ (Hao et al.) as absorber.[21,22] Other working groups also started to investigate tin as lead alternative, however, the lack in stability prevented a rapid increase in efficiency. This is mainly ascribed to two reasons, (i) tin is more prone to oxidation and easily oxidizes to its (+4) state leading to self p-doping, (ii) tin crystallizes readily fast due to its high Lewis-acidity.[23,24] This is supported by the lower thermodynamic stability of tin (+2), compared to lead (+2), due to its lower standard redox potential.[24]

Yao et al. has reviewed the stability concerns and discussed possible candidates to solve these issues.[25] As most promising additive, SnF_2 has been successfully used to suppress oxidation and increase the device efficiency. Herein 10 mol% SnF_2 were reported to be the optimal additive concentration.[26,27] Other tin halide species ($SnCl_2$, $SnBr_2$, SnI_2) were also investigated with positive effects but to a lesser extent.[28,29] Another route to further increase stability and efficiency is ion substitution. Various research groups already fabricated mixed perovskites by substitution of either the A-cation, X-anion or both.[26,30,31] Lee et al. investigated the influence of the iodide to bromide ratio in $FASnX_3$ perovskites and found that already 25% of bromide within the perovskite can increase the efficiency and the stability of the solar cell.[32] By the introduction of large cations such as phenethylammonium (PEA) also the dimensionality of the perovskite can be changed from a 3D to a 2D/3D mixture increasing the stability.[31,33]

Another alternative to improve the stability is the use of other, not tin based, additives. Liu et al. has successfully implemented poly[tetraphenylethene-3,3′-(((2,2-diphenylethene-1,1-diyl)bis(4,1-phenylene))bis(oxy))bis(*N*,*N*-dimethylpropan-1-amine)tetraphenylethene] (PTN-Br) to improve the hole transport. PTN-Br is working as bridge between perovskite and hole transport material (HTM) (PEDOT:PSS) also offering better film coverage and higher stability.[34] Jokar et al. added 1% ethylenediammonium iodide ($EDAI_2$) as additive into a mixed perovskite (guanidinium:formamidinium – 20:80) and reached an efficiency of 9.6%.[30] Also, Kamarudin et al. investigated different concentrations of EDAI as additive and post-treatement of ethylenediamine (EDA), to suppress recombination reactions and reached an astounding device efficiency of 10.18%.[35]

Recently, the main focus of tin perovskites is devoted to improve the crystallinity while also obtain high stability of the Sn (+2) species. Last reports mainly focused on $FASnI_3$ perovskites and some research groups also work on $MASnI_3$ perovskites for solar cells. When working with $MASnI_3$ as absorber, solvent effects, the role of grain boundaries, a displacement approach or

vapor assisted nucleation techniques were investigated and a maximum efficiency of 7.78% was reached.[36,37,38,39] For $FASnI_3$ perovskites different approaches were tested. Shao et al. was able to increase the crystallinity by adding ethylammonium to a 2D/3D perovskite hence reaching a higher efficiency of 8.4% compared to 4.7% ($FASnI_3$) or 7.7% ($PEA_{0.08}FA_{0.92}SnI_3$).[40] Another approach is to retard the crystallization by e.g adding poly (vinyl alcohol) (PVA) to the perovskite precursor reaching efficiencies of 8.82%.[41]

To counter the high Lewis-acidity of tin, Wu et al. used π-conjugated Lewis-bases in $FASnI_3$ perovskites to control the perovskite crystallization. Furthermore, they also help to stabilize the perovskite film to reach 10.1% power conversion efficiency.[42] Alternatively, one can also use an antioxidant capping layer to prevent oxygen permeation for higher stability. He et al. deposited 4-fluororbenzohydrazine (FBH) on top of an $FASnI_3$ perovskite film using a solution-based process. Resulting solar cells can also be fabricated under high oxygen fabrication conditions of 100 ppm oxygen (PCE = 9.03%) compared to low-oxygen conditions (9.47%).[43]

Up to date a maximum device efficiency of 12.4% (certified) was reported by Jiang et al. using a 2D/3D mixed perovskite ($PEA_{0.08}FA_{0.92}SnI_3$) with an ammoniumthiocyanat (NH_4SCN) additive and indene-C_{60} bis adduct (IBCA) as new ETL.[44]

3.2.3 Germanium Perovskites

Another lead-free alternative to tin is germanium (Ge) which also forms perovskites in its (+2) oxidation state. There exist several publications on theoretical calculations of different germanium perovskites providing promising data to substitute germanium with lead.[45,46,47,48,49,50] However, there exist only a hand full of reports on fabricated germanium perovskite solar cells. This is ascribed to the low stability of (Ge^{+II}) which is even lower than the stability of tin.[20] The highest efficiencies reported up to date were realized with $CsGeI_3$ and $MAGeI_{2.7}Br_{0.3}$ as absorber and exhibit efficiencies of 0.58% and 0.57%, respectively.[51,52] A more investigated field are mixed perovskites with germanium and either tin or lead to enhance the stability of PSCs. Researchers also predicted high efficiencies and favorable properties through theoretical calculations and experiments when using a B-side mixed perovskite.[53,54,55] Fabricated solar cells with SnGe perovskites show first solar cell results with efficiencies of >7%.[56,57] On the other side, solar cells with mixed PbGe cells reached even higher efficiencies.[58]

3.2.4 Antimony Perovskites

In comparison to lead, tin or germanium perovskites, formed in an ABX_3 crystal structure, antimony can form perovskites in an $A_3B_2X_9$ crystal structure due to its different valence number. Moreover, it is considered to be less-toxic than lead. However, as possible lead alternative, antimony perovskite solar cells are less investigated so far. In 2016, the first report on antimony perovskites in solar cells was published by Hebig et al. using a $MA_3Sb_2I_9$ absorber to reach an efficiency of 0.49%.[59] Later studies focused on mainly three different perovskites – $MA_3Sb_2I_9$, $Rb_3Sb_2I_9$ and $Cs_3Sb_2I_9$.[60,61,62,63,64,65,66,67] The crystallization of these perovskites occur either in a 0D dimer or 2D layered phase.

Rubidium antimony iodide perovskites were fabricated via different deposition procedures and always feature a 2D layered phase.[60,61,62] This is ascribed to the smaller ionic radius of Rb compared to e.g. Cs.[60,61] So far, device efficiencies of maximum 1.35% with $Rb_3Sb_2I_9$ were reached.[62] The dimensionality of cesium-based antimony iodide perovskites is reported to be either 0D or 2D and can be tuned depending on their deposition method.[65,66,68] Moreover, Chonamada et al. already studied the degradation properties of $Cs_3Sb_2I_9$ perovskites in both dimensionalities in terms of light, heat and water. He found, that the 0D dimer phase is less stable than its 2D layered perovskite.[68]

The preferred crystallization of $MA_3Sb_2I_9$ is 0D as already reported by Hebig et al. in 2016.[59] Although the size of MA is too small to form 2D layered perovskites, the device performance can still be enhanced by using additives like iodic acid (HI) and/or applying additional interlayers, as reported by Boopathi et al. and Karuppuswamy et al.[63,64] Another approach was reported by Ahmad et al. using a two-step solution processed deposition technique increasing its efficiency fivefold compared to a one-step solution process.[67] Another possibility to improve the efficiency of $MA_3Sb_2I_9$ perovskites is anion substitution. Paul et al. substituted iodide with the much smaller chloride to form 2D layered perovskites when the chloride content is higher than 30%.[69] This led to an improved band gap and higher device performance of 1.55% ($MA_3Sb_2(Cl_{0.3}I_{0.7})_9$ compared to $MA_3Sb_2I_9$ (0.5%).[69]

In general, a higher dimensionality is desired since it improves their optoelectronic properties and stability.[60,63,68] So far, the highest Sb-based perovskite solar cell reported up to date reached a maximum device efficiency of 3.08% and consisted of an $MASbSI_2$ perovskite deposited by chemical bath deposition.[70]

3.2.5 Bismuth Perovskites

Unlike antimony, bismuth perovskites were already studied in multiple compositions. Bismuth itself offers similar properties to lead but cannot be replaced directly which is ascribed to its varying valence state. Consequently, bismuth can form perovskites with different dimensionalities from 0D to 3D. $A_3B_2X_9$ perovskites mainly form 0D dimer or 2D layered structures whereas e.g. ABX_4 or ABX_5 crystal structures form preferably 1D perovskites and double cation perovskites ($A_2B^{+I}B^{+III}X_6$) form 3D perovskite crystals.[9,71]

As one of the first research groups, Lehner et al. investigated BiI_3 as absorber in solar cells and compared its properties to PbI_2 and $MAPbI_3$.[72] Later Lehner et al. performed a detailed study on the experimental and computational properties of $A_3B_2X_9$ (A = Cs, K, Rb). Thereby, the crystal structures including their dimensionality (0D, 2D) as well as thin film processing strategies were described.[73] There exist several other studies on the material properties (experimental and theoretical) of $MA_3Bi_2I_9$, $Cs_2AgBiBr_6$ and $Cs_2AgBiCl_6$ which are among the most studied bismuth perovskites.[74,75,76,77] Especially $MA_3Sb_2I_9$ is intensively studied due to its non-toxic character, high stability and thin film processability. It crystallizes in a hexagonal structure and forms 0D dimer perovskites.[78,79] PSCs with efficiencies from 0.1% to 3.17% were reported up to date.[78,79,80,81,82,83,84] Another 0D perovskite – $Cs_3Bi_2I_9$ – so far less investigated, shows promising device efficiencies in Bi-based PSCs. Herein the device performance reaches a maximum of 3.6% when mixed with $Ag_3Bi_2I_9$ to form a bulk heterojunction ($Cs_3i_2I_9$/$Ag_3Bi_2I_9$ – in a ratio 0.5/1/1 of CsI/AgI/BiI_3).[85] Using an optimized dissolution/recrystallization process for perovskite deposition of bare $Cs_3Bi_2I_9$ perovskites and careful selection of the HTL, a maximum device efficiency of 3.20% could be reached.[86]

Mixed bismuth-perovskites were found to crystallize in a 3D network. Herein, the perovskite composition $Cs_2AgBiBr_6$ was mostly researched. Greul et al. published an efficiency of 2.43% in 2017 using hot temperature annealing to optimize the perovskite film formation. However, a big hysteresis effect of 1.66% (FWD) to 2.43% (BWD) was observed.[87] Later, Zhang et al. tested rubidium doping in $Cs_2AgBiBr_6$ perovskites. He found, that 10% doping of Rb can increase the efficiency from 1.21% (Rb = 0%) to 1.39% (Rb = 10%).[88] Another approach was investigated by Pai et al. who added sulphide to $Cs_2AgBiBr_6$ perovskites forming $Cs_2AgBiBr_{6-2x}S_x$ perovskites. By the addition of sulphide he was able to increase the efficiency from 1.4% ($Cs_2AgBiBr_6$) to 1.9% ($Cs_2AgBiBr_{5.8}S_{0.1}$).[89]

4 Non-Fullerene-Acceptors (NFAs)

Non-fullerene acceptors, also known as post-fullerene acceptors, are a collective term for all fused ring systems excluding fullerene derivatives. In this section the history of fullerenes and the rise of NFAs in OSCs is thoroughly discussed. Their advantages and disadvantages compared to fullerenes are discussed and the state of the art is reviewed.

4.1 The Rise of NFAs in OSCs

The history of organic solar cells goes far back in the 20th century. First OSCs were already published in 1958.[90] The first work using a perylene-based acceptor was published in 1986.[91] In 1992, Sariciftci et al. used C_{60} as acceptor for the first time.[92] The first bulk heterojunction solar cells were discovered in 1995 using polymer-based acceptors.[93,94] However, the dawn of a new era of OSCs started with the use of soluble fullerenes derivatives as acceptors. Fullerenes offer some unique properties such as high electron mobility and high electron affinity which are ascribed to their 3D character in connection with their delocalized LUMO level.[95] Blended with suitable donor materials the most prominent fullerenes are $PCBM_{60}$ and $PCBM_{70}$ (**Figure 5**). As a result, bulk-heterojunction solar cells with power conversion efficiencies of >10% were reported.[96,97,98,99,100] Although fullerenes seemed promising for a long time period, they have several disadvantages like their limited absorption range, photochemical and thermal instability as well as degradation when exposed to oxygen. The HOMO and LUMO levels of fullerenes are limited by the fullerene core and can only be slightly shifted by functionalization.[95,101,102,103,104,105]

To tackle the above mentioned obstacles and to improve the device efficiency, the motif of researchers switched towards non-fullerene-acceptors. Over the past few years an infinite number of materials have been tested in OSCs (incl. polymer solar cells – PSCs). Efficiencies surpassing fullerene-based OSCs >17% have been published highlighting the potential of NFAs.[106] Thereby two classes of NFAs emerged, namely (i) rylenes consisting of perylenes, naphtalenes and terylenes and (ii) fused ring electron acceptors (FREA) which can be summarized in a second group, consisting e.g. azo, oxo or thio-heterocycles.

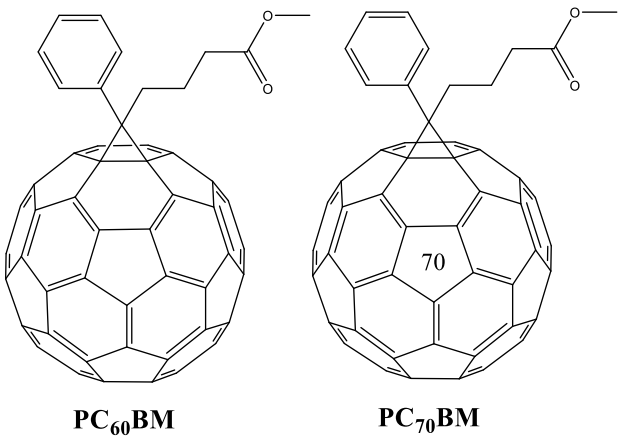

Figure 5: Fullerene acceptors – $PC_{60}BM$ (left) and $PC_{70}BM$ (right).

Beside the acceptor, careful selection of the donor is a prerequisite to high device performance. In recent years, various new donor materials were synthesized and implemented in solar cells. Upon the huge variety of compounds, a selection of the most prominent and important donor materials is given in **Figure 6**.

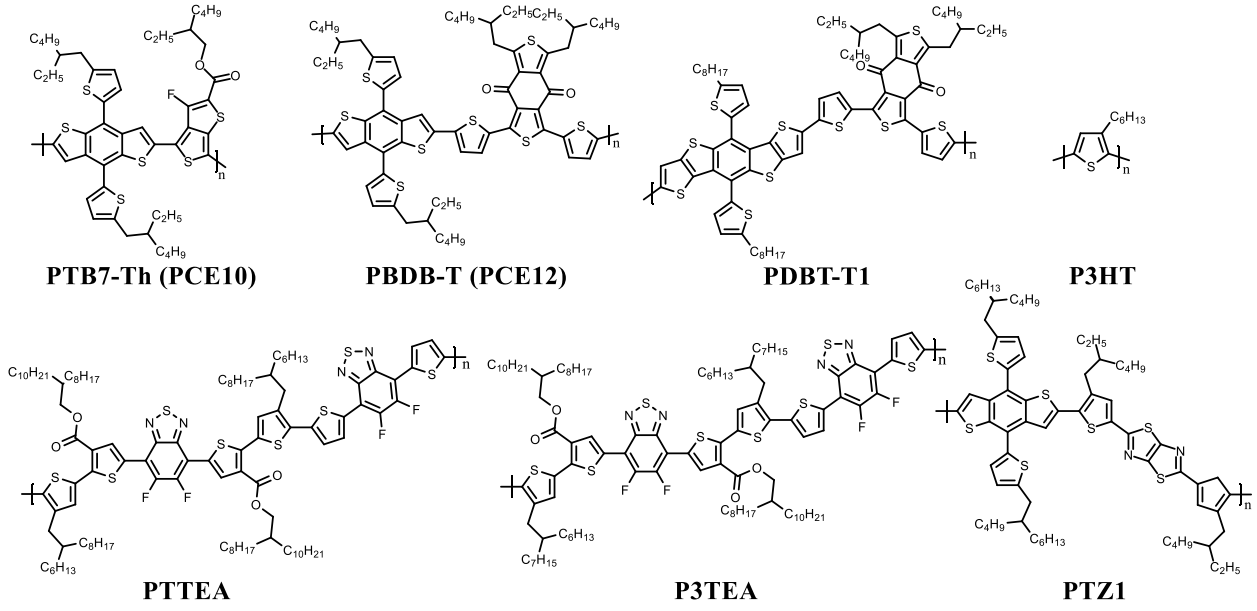

Figure 6: Chemical structures of selected donor materials implemented in OSCs and mentioned in this thesis.

4.2 Rylenes as NFAs

Within the class of rylenes, perylenes are the superior material when it comes to material testing and design in OSCs. As starting material, perylene-3,4,9,10-tetracarboxylic anhydride (PTCDA) is converted to soluble perylene diimides (PDI) which are further processed at the *ortho* (2,5,8,11) or *bay*-position (1,6,7,12) (**Figure 7**). The synthetic procedures to PDIs have be known for decades as PDIs were used as dyes in industry prior to their discovery as acceptors in solar cells.[107,108,109,110,111] PDIs offer high electron mobilities, thermal, chemical and photochemical stability which is advantageous for OSCs. They are also cost effective in terms of synthesis (high yields) and their optical and electronic properties can be readily tuned by simple substitution at *ortho* or *bay*-position.[7,107,110,112] One drawback of PDIs is their tendency to form large aggregates due to π-stacking.[113] However, promising solution methods have already been developed and reported by introducing side-groups that twist the PDI-derivative limiting the π-stacking significantly.[114] They can be further divided in two subsections, either being classified as small molecule acceptor (SMA) or as monomeric unit in polymer-based acceptor.

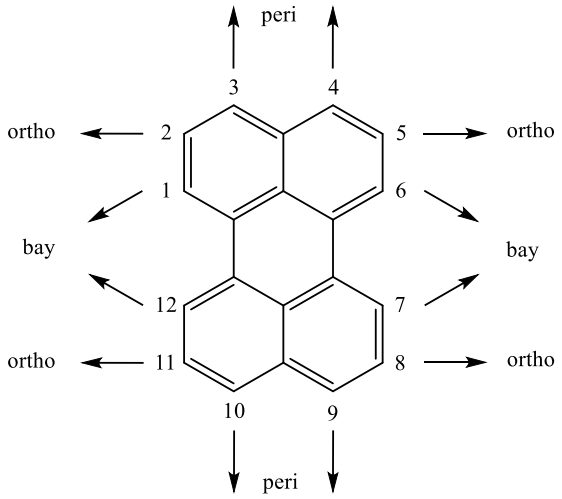

Figure 7: Perylene structure with given functional sites.[108]

Perylene monoimides (PMI) are so far less investigated in solar cells albeit various synthesis procedures have been reported. This may stem from the lower yields of PMIs compared to PDIs.[115,116,117] Nevertheless, PMIs offer an alternative optimization route with additional substitution options at the *peri*-position (9,10) (**Figure 7**) for solar cells and open up the possibility to formulate A-D-A-type acceptors. Their optoelectronic properties can also be enhanced identical to PDIs and, moreover they feature another open side for improvement compared to PDIs.[118]

Regarding their π-stacking, reports showed that substitution of the *peri*-position can already twist the molecule to counter that issue.[119]

Naphthalene diimides (NDI) are also within the group of rylenes and are mostly applied as monomeric units in polymers with alternating donor-acceptor units. They can also be tuned by substitution on their active sites to improve solubility, optoelectronic properties or better film morphology. In solar cells, NDIs are mainly present as conjugated polymers, whereas the most studied one is N2200 (NDI-bithiophene copolymer) and its derivatives.[7,120] They can rival fullerene-based OSCs as well as perylene-based OSCs with efficiencies >11%.[121]

Terrylenes are another subgroup of rylenes, composed of a large conjugated π-system than perylenes or naphthalenes. In solar cells only a few reports exist so far. Herein, the functionalization at the bay-position of terrylene diimides was investigated.[122,123,124] The highest efficiency of 5.29% was reached by using two terrylene diimides linked with a fluorine derivated bithiophene linker (*o*-F_2T_2-TDI_2).[122]

4.3 State of the Art of Perylenes as NFAs

Within the last years several different types of perylene derivatives have been reported. Thereby perylene diimides substituted or fused at the bay position were synthesized and implemented in solar cells. This led to all kind of PDIs which were used a building block for monomeric, dimeric, trimeric and tetrameric based acceptors.

Yin et al. investigated the influence of the number of perylene units fused to a porphyrin core. He proved that higher numbers of PDI units attached to a core is favorable for the device performance. This is supported by reducing the energetic disorder and reaching balanced electron/hole mobilities with a higher amount of PDI units linked to the core to reach a maximum efficiency of 8.40% for 4PDI-ZnP compared to its lower linked PDI counterparts (5.33% – 2PDI-ZnP, 3.10% – 1PDI-ZnP). Moreover, he also tested a plain PDI molecule with PTB7-Th to reach 1.95% efficiency.[125]

4.3.1 Perylene Monomers

The generally low efficiencies for PDIs without the introduction of side groups is well explained in literature and ascribed to π-stacking and thus the formation of agglomerates in thin films.[113] One approach to twist the PDI molecules is the introduction of bulky substituents. Kozma et al. introduced a naphthyl and acenaphthenyl side group at the bay-position to twist the core around 19° leading to slightly higher efficiencies of 0.91% (PDI-3) (**1c**) and 0.91% (PDI-2) (**1b**) compared to a plain PDI molecule (0.13% – PDI-1) (**1a**).[126] Moreover, it was found that slightly modified PDIs can also function as cathodic interfacial layers for polymer solar cells.[127]

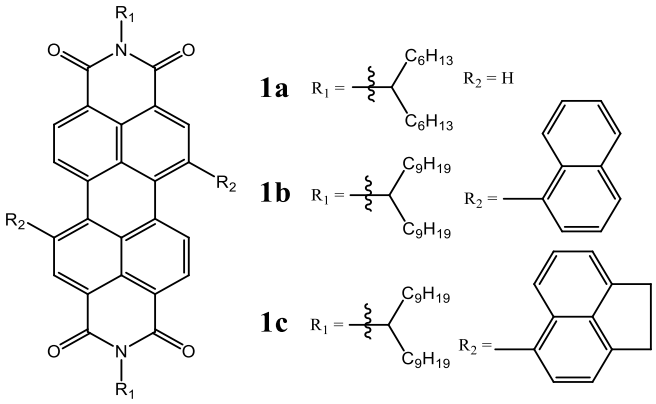

Figure 8: Chemical structures of selected PDI monomers implemented in OSCs.

4.3.2 Perylene Dimers

To avoid aggregation and at the same time retain the unique properties of PDIs, dimer strategies with linked core molecules or linkage via ring fusion were reported. Herein, the π-system can be increased by ring fusion of sulfur or selenide to form outer fused rings on PDIs as reported by several groups.[114,128,129,130,131] In 2016, Sun et al. and Meng et al. synthesized first dimer-based fused acceptors with sulfur (SdiPBI-S) (**2a**) and selenide (SdiPBI-Se) (**2b**). Blended with an optical complementary polymer (PDBT-T1) efficient solar cells with 7.16% (SdiPBI-S) and 8.42% (SdiPBI-Se) were fabricated.[130,131] Three years later sulfur annulated fused PDIs were investigated again by Li et al. He optimized the HOMO/LUMO levels of the acceptor by changing the number of sulfur atoms, linked via outer ring fusion, on fused PDIs to improve the open circuit voltage. Herein, two fused sulfur atoms led to higher lying HOMO/LUMO levels and thus higher efficiencies.[128] Only recently Qureshi et al. used an *N*-annulated core as linker and additionally

fused two sulfur/selenide atoms to the PDI dimer. Using this approach, the A-D-A based acceptors can be effectively twisted and outer fusing increased the molar extinction coefficient, mobility and in turn the efficiencies. This is clearly given as the *N*-annulated PDI-dimer acceptor showed a maximum device efficiency of 4.73% (**3a**) whereas their sulfur and selenide annulated acceptors reached 6.11% (**3b**) and 6.25% (**3c**), respectively.[129] Yang et al. formulated different vinylene linked perylenes by inner and outer ring annulation based on the dimer (V-PDI$_2$) (**4a**). Thereby outer fused rings were synthesized with sulfur (V-PDIS$_2$) (**4b**) or selenide (V-PDISe$_2$) (**4c**) to reach a device efficiency of 5.76% and 6.51%, respectively. On the other side, inner ring annulation with thianaphthene (V-TDI$_2$) (**4d**) and benzofuran (V-FDI$_2$) (**4e**) led to 3.84% and 3.76% device efficiency, respectively. The better performance for the former NFAs, with the selected donor (PBDB-T), was in this case ascribed to a wider light absorption and better morphology.[114]

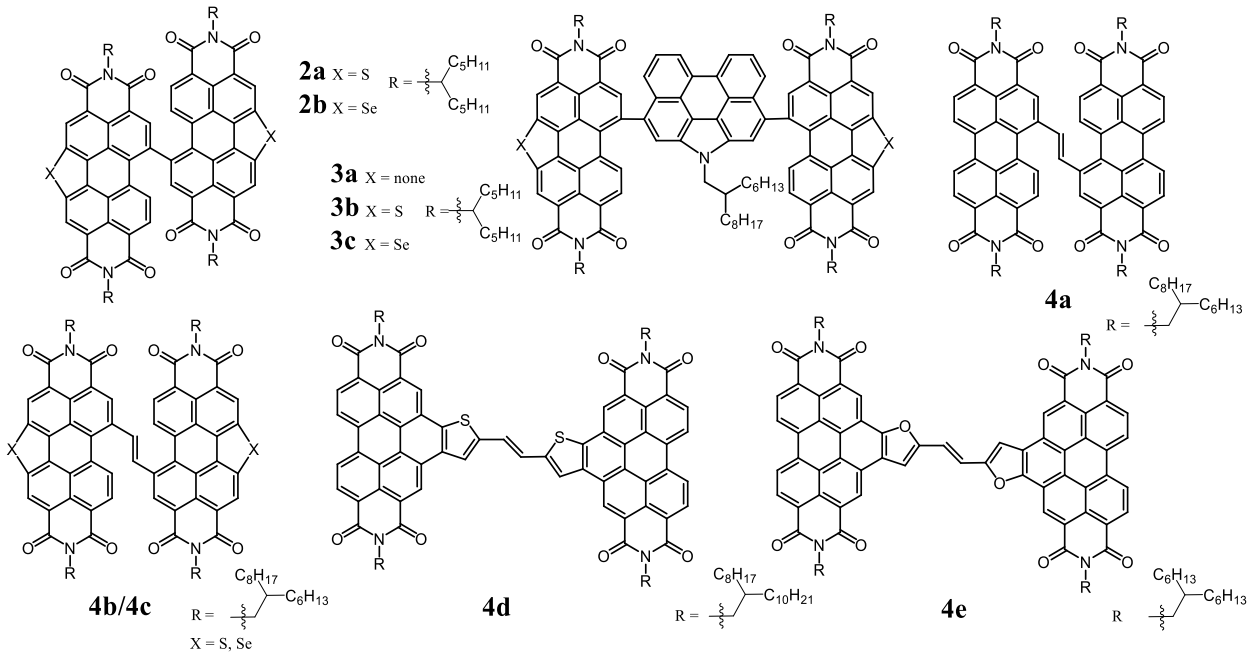

Figure 9: Chemical structures of selected PDI dimers implemented in OSCs.

The linkage of perylene units over fused rings is another approach to twist the PDI skeleton and improve the material properties. Li et al. fused benzodithiophene with two PDI units to form two isomeric NFAs (BPDI-1 and BPDI-2) (**5a** and **5b**). He showed that depending on the isomer-core, the molecules are twisted differently which affects aggregation and thus the device performance.[132] Zhong et al. investigated the fusion of furan, thiophene and selenophene with two

PDI-units. Thereby the size of the heteroatom and the increased π-system play a key role in fabricating efficient solar cells. The three NFAs FPDI-F (**6a**), FPDI-T (**6b**) and FPDI-Se (**6c**) were blended with PTB7-Th and displayed efficiencies of 3.29%, 6.72% and 5.77%, respectively.[133] When two-PDIs are fused with an indacenodithieno[3,2-b]thiophene (IDTT) core and implemented in solar cells with PTB7-Th an even higher efficiency of 7.33% was reported.[134] To go on a step further, Yin et al. linked already fused PDI dimers with a 9,9'-spirobi[fluorene] core to form the NFA – SF-FPDI (**7**) - and reached an efficiency of 6.24% when blended with PTB7-Th.[135] The highest efficiency with PDI-dimer structures up to date was reported by Liu et al. In his work he linked two-PDI units with an 9,9'-spirobi[fluorene] core (**8**) and blended it with the donor P3TEA to a record efficiency of 9.5%.[136]

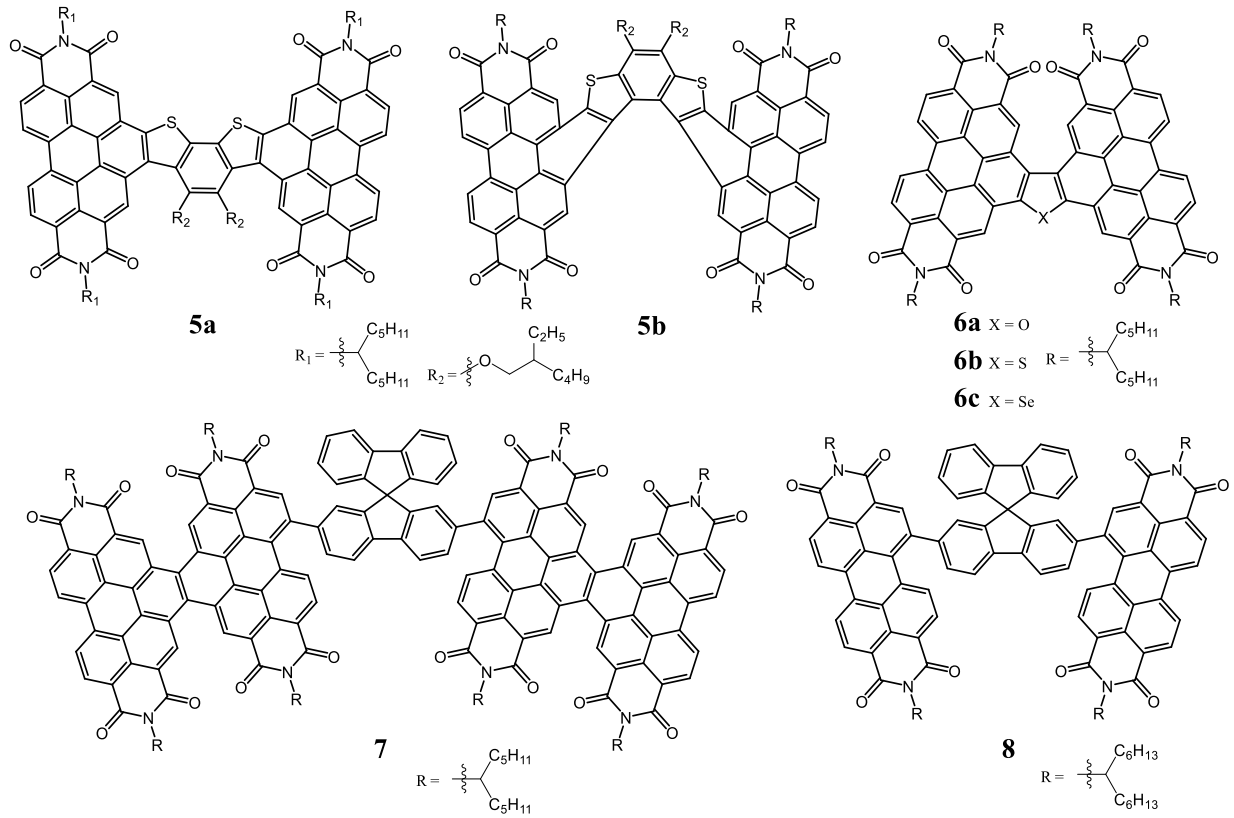

Figure 10: Chemical structures of selected PDI dimers implemented in OSCs.

4.3.3 Perylene Trimers

Perylene trimers form propeller-like structures when three PDI units are linked to one core molecule. In literature, benzene is one of the most investigated core molecules in this field. It can be linked via single-bonds (**9**) or fused together which increases their π-system. Blended with PTB7-Th efficiencies of 5.65% and 5.57% were reported by Li et al. (2016) and Duan et al. (2017), respectively.[137,138] For comparison, Duan et al. also examined 1,3,5-triazine as core molecule (**10**) and could increase the efficiency to 9.15% due to superior crystallinity, electronic properties and greater π-stacking.[138] The photovoltaic performance of three PDI dimers, which were fused to a benzene core, was reported to a maximum efficiency of 6.95% in non-halogenated solvents.[139] Three perylene units were also linked with a benzene core (TPH) by ring fusion (**11a**) and additionally extended by outer ring fusion of selenide atoms (TPH-Se) (**11b**) to reach efficiencies of 8.28% (TPH) and 9.28% (TPH-Se), blended with the donor PDBT-T1.[140] The highest reported trimer-based PDI was published recently by Zhang et al. using triphenylphosphine derivatives as cores molecules. The introduction of a monoxide or sulfide at the phosphorus atom compared to its lone pair modifies the molecular conformation thus leading to remarkable high device performances of 11.01% (TPO-PDI) (**12a**) and 9.67% (TPS-PDI) (**12b**) compared to 6.19% (TPP-PDI) (**12c**) when blended with PTTEA as donor.[141]

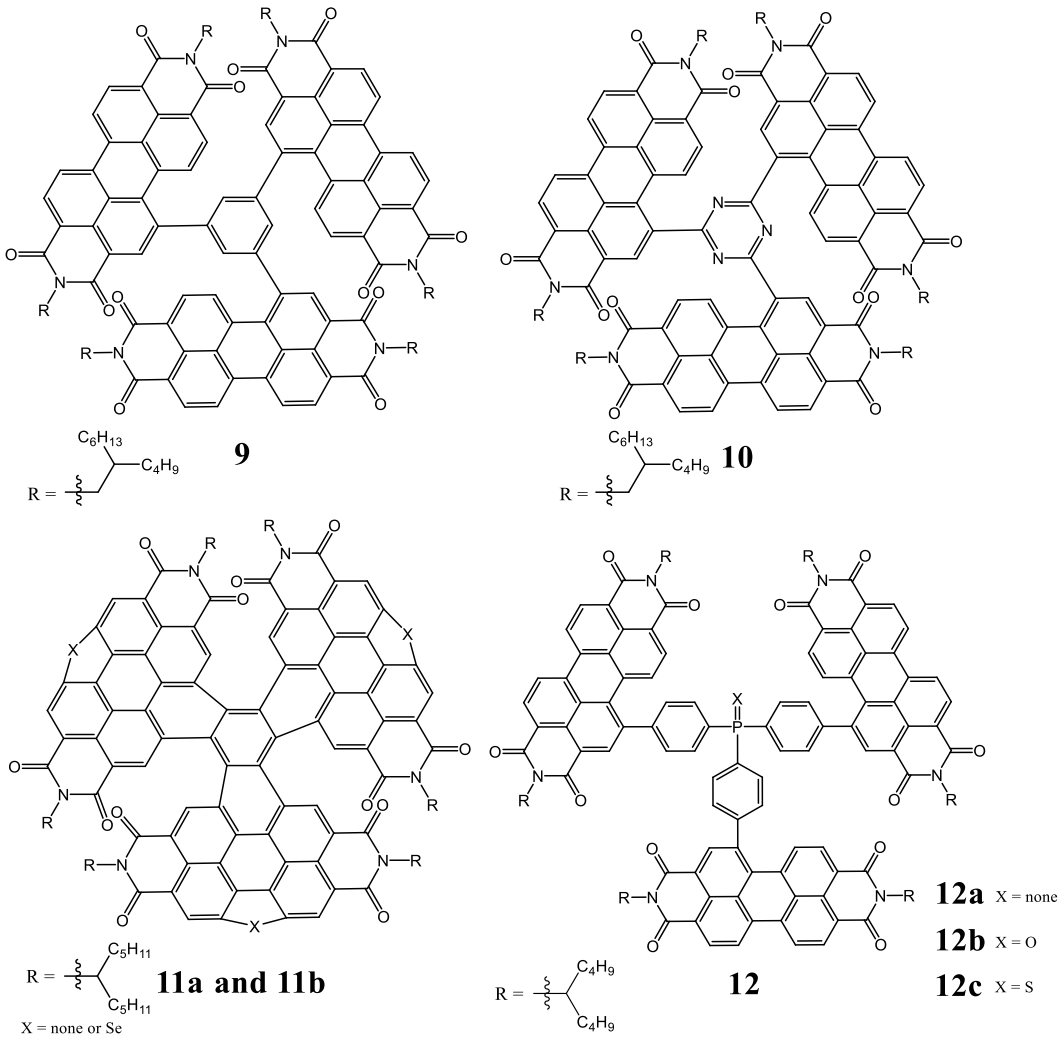

Figure 11: Chemical structures of selected PDI trimers implemented in OSCs.

4.3.4 Perylene Tetramers

Perylene diimides can be linked with different core molecules, e.g. pyrene, 4,8-di(thiophen-2-yl)benzo[1,2-b:4,5-b']dithiophene (BDT-Th), tetrathienylbenzene, 9,9'-spirobi[fluorene], to form tetrameric NFAs.[142,143,144,145] Thereby the influence of linked vs. fused ring tetramers was researched. Ding et al. fabricated four different tetramers, two non-fused (PDI4-DTC, PDIF4-DTC) (**13a & 13b**) and two fused tetramers (FPDI4-DTC, FPDIF4-DTC) (**14a & 14b**). He found, that fused ring acceptors increase the efficiency from e.g. 1.27% (PDI4-DTC) to 4.29% (FPDI4-DTC) when blended with PTB7-Th. Additionally, fluorine atoms at the outer bay-positions of the PDI units can enhance the optical properties and even higher efficiencies of 5.10% (FPDIF4-DTC) compared to 1.78% (FDPI4-DTC) could be reached.[146] Zhang et al. observed the same behavior in solar cells when the non-fused TTB-PDI_4 (**15**) and fused FTTB-PDI_4 (**16**) were mixed with P3TEA to fabricate solar cells with 7.11% and 10.58%, respectively.[144]

Introducing a BDT-Th core, the PDI tetramer (**17**) exhibited one of the highest efficiencies in 2016 with 8.47% (PTB7-Th:TBP).[145] On the other side, Wu et al. enhanced the already mentioned dimer fused 9,9'-spirobi[fluorene] to a dimer-fused PDI which is further linked to the 9,9'-spirobi[fluorene] core (SF-4PDI2) . By optimizing the deposition methods he reached a device efficiency of 7.69%.[142] Tang et al. used an acetylene-linked method to form the PDI tetramer (B-4TPDI) (**18**) and tested it with the donor materials PBDB-T and PTB7-Th. Due to better optoelectronic properties with the acceptor, PTB7-Th:B-4TPDI performed better (7.71%) than PBDB-T:B-4TPDI (6.84%).[143]

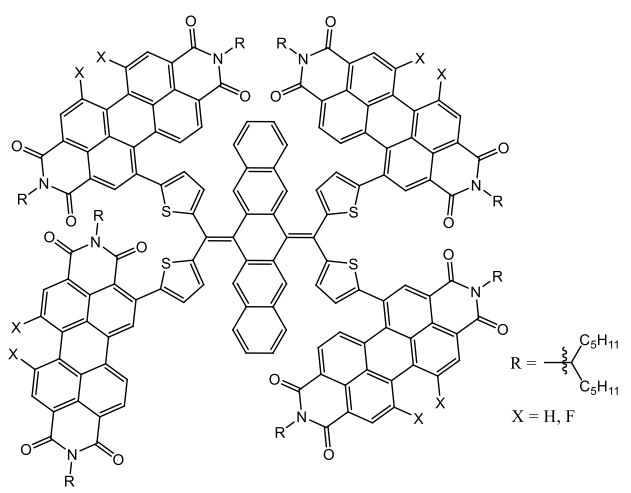

13a and 13b

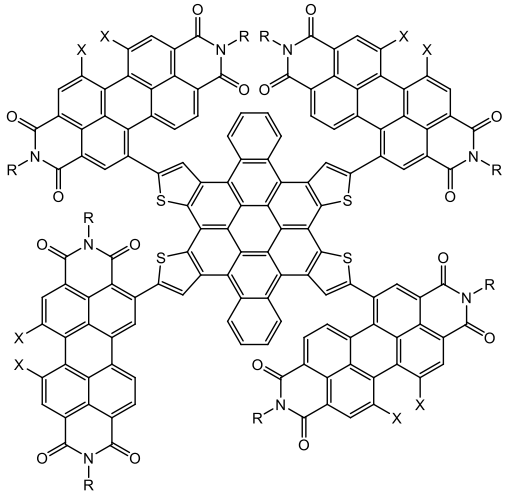

14a and 14b

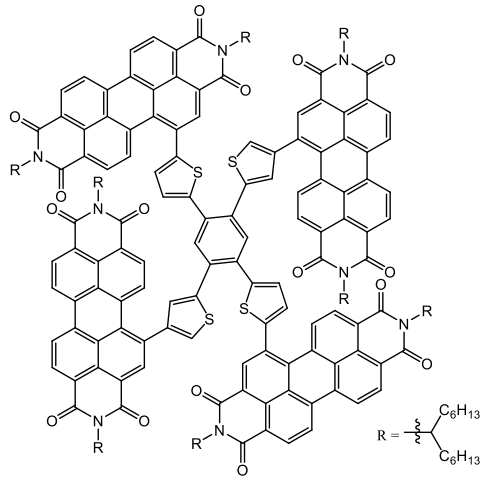

15

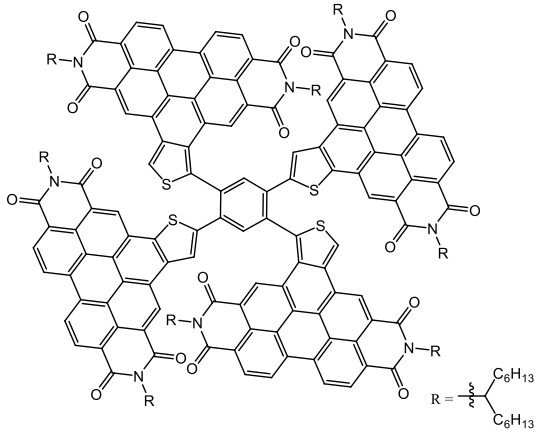

16

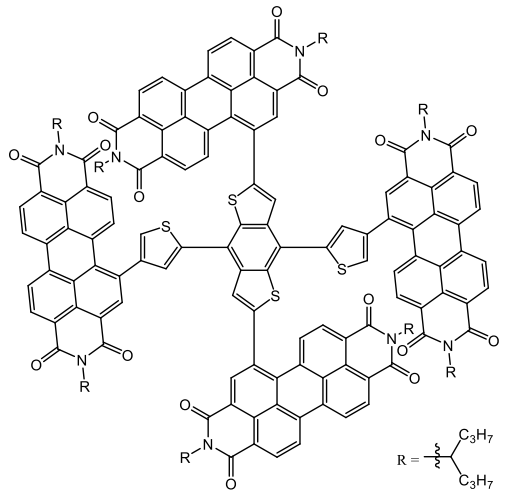

17

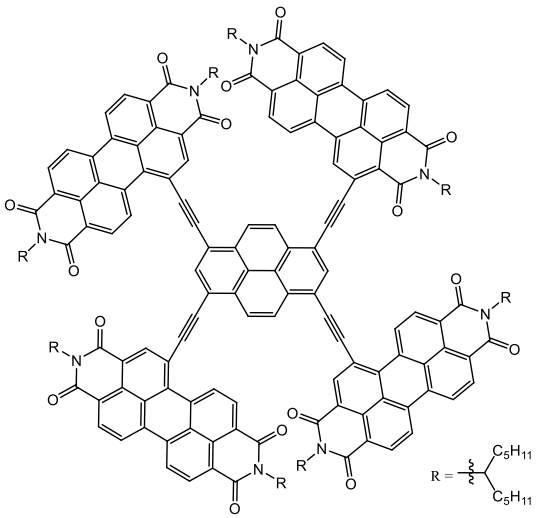

18

Figure 12: Chemical structures of selected PDI tetramers implemented in OSCs.

4.3.5 Perylene Monoimides

The branch of PMIs in OSCs is up to date barely investigated. Reports focus on mainly A-D-A structured NFAs based on two PMI units linked with different core molecules like fluorene (**19**), benzene (**20a**) or thiophene (**20b**). In 2015, Zhang et al. published the first work on PMIs by linking it with a fluorene core to create an A-D and A-D-A acceptor. The resulting solar cell performance displayed that P3HT:PMI-F-based cells reached 1.35% and P3HT:PMI-F-PMI-based cells reached 2.30%.[147] In 2017, he published a second work on PMI-F-PMI acceptors, blended with the donor PTZ1 and the addition of additives to reach an efficiency of 6%.[119] Hu et al. synthesized different A-D-A acceptors with various core molecules. The fabricated solar cells were blended with PTB7-Th to reach an efficiency of 1.3% with PMI-bithiophene-PMI (**20c**) as NFA.[118] In 2019, the last report on PMIs was published by Qin et al. who implemented alkyne bridges between two PMI units. The size of the alkyne bridge was varied (n = 0-2) and the solar cell performance was studied with PBDB-T.[148]

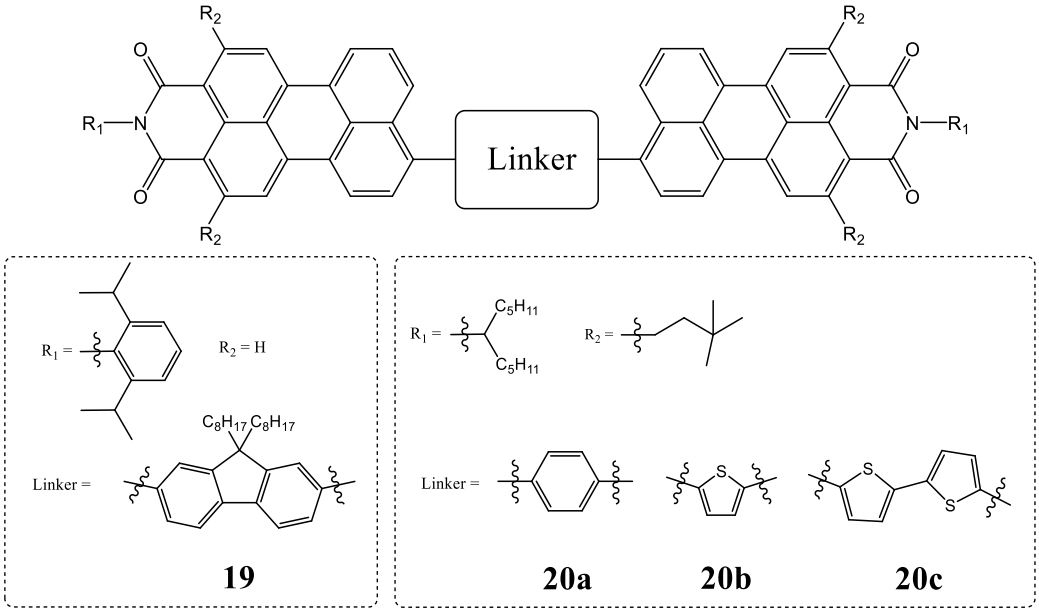

Figure 13: Chemical structures of selected PMI-X-PMI acceptors implemented in OSCs.

4.4 State of the Art of Acceptor Polymers in Polymer Solar Cells (PSCs)

Rylenes, especially NDIs and PDIs are reported as excellent polymer acceptor materials in PSCs. Li et al. reviewed the progress of rylene acceptors. Herein he stated that the NDI-based polymer N2200 (**21a**), featuring NDI-bithiophene alternating units, is the most studied and best performing structure in this class.[149] Solar cells with the acceptor N2200 and PTzBl-Si as donor reached efficiencies of 11% in single junction cells and 11.2% in tandem cells.[121,150] Other synthesized NDI-based polymers varied in either their imide side groups or substituted *bay*-position, e.g. thiophene (**21b**), selenophene (**21c**), biselenophene (**21d**).[151,152,153]

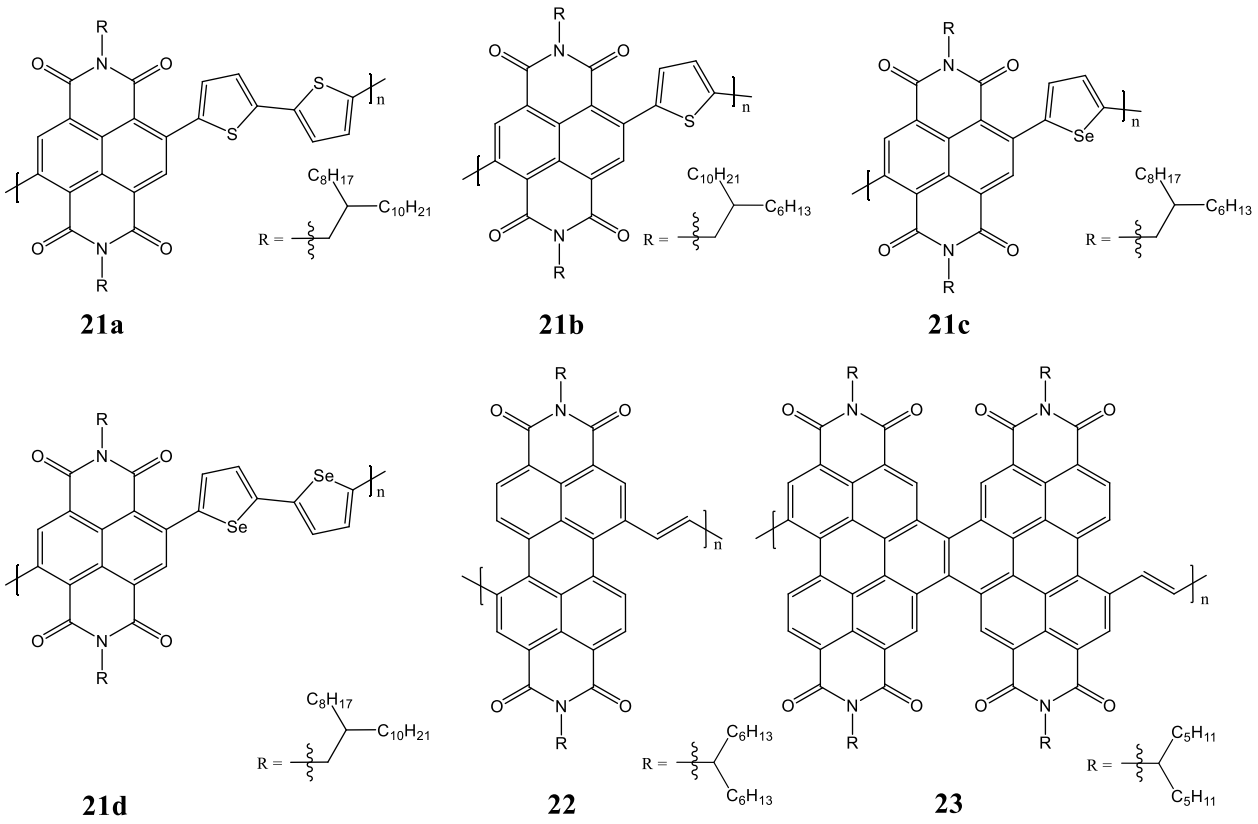

Figure 14: Chemical structures of selected NDI and PDI-based polymer acceptors for PSCs.

The first PDI-based polymer solar cell was published in 2007 by Zhan et al. with a rather low device performance of over 1%.[154] Within the next years, several new polymer-based acceptors were developed, however no breakthrough was accomplished and the device performance remained low.[149] In 2016, Guo et al. synthesized a vinylene-bridged PDI-based acceptor (PDI-V)

(**22**) and blended it with PTB7-Th in order to fabricate PSCs with 7.57% efficiency. The improved performance is ascribed to higher crystallinity and higher electron mobility compared to e.g. PDI-thiophene.[155] Later, Guo et al. was able to improve the device efficiency even further by the synthesis from PDI-V to NDP-V (**23**) blended with PTB7-Th to 8.59% which is among the highest reported so far.[156]

4.5 Evolution of Fused Ring Electron Acceptors (FREAs)

Beside rylene-based NFAs, various other A-D-A structured SMAs were synthesized and implemented in solar cells. In 2014, one of the first fluorene and carbazole-based A-D-A structured acceptors were synthesized for OSCs. Their structure included thiophenes which were included into the system between the accepting and donating unit owing to develop a compound with improved LUMO level and solubility.[157] Fluorenes were further developed by replacing the accepting unit and/or "spacer" and acceptor unit to enhance their material properties.[158,159,160] Hereby the fluorene-based NFA DICTF (**24**) stands out as it is the predecessor of one of the most well know indacenodithiophene (IDT) based NFAs called indaceno[1,2-b:5,6-b']dithiophene and 2-(3-oxo-2,3- dihydroinden-1-ylidene)malononitrile (IEIC) (**25**). IDT-based acceptors were developed to improve the morphology issues and optoelectronic properties (e.g. lower band gap) that fluorene-based NFAs lacked when blending with available donors. Lin et al. reported the synthesis of IEIC with a band gap of 1.57 eV.[161] The further developed modification of IEIC is ITIC (**26**) which is composed of an IDTT donating core, also reported by Lin et al.[162] In comparison to IEIC, ITIC derivatives exhibit a ring fused thiophene attached to its core thus shifting the HOMO/LUMO levels around 0.1 eV and keeping the band gap in a similar range (1.59 eV).[162]

In order to arrange their HOMO/LUMO levels and inter- and intramolecular interactions with available donor materials, e.g. PTB7-Th or PBDB-T, the above-mentioned IDT and IDTT derivatives can be enhanced by (i) donating unit (core) modification, (ii) spacer modification, (iii), accepting unit (terminal) modification and (iv) introduction of additional side chains at the core.

One example for core engineering was published by Dai et al. who extended IEIC into fused 6-ring, 8-ring and 10-ring cores.[163] The spacer of IEIC molecules were also modified by the introduction of an alkoxy group (IEICO) instead of an alkyl group or by using a selenophene

derivative (IDSe-T-IC) instead of a thiophene derivative.[164,165] Substitution on the terminal section by methyl (IT-M) or dimethyl (IT-DM) led to an upshift in HOMO/LUMO levels to achieve higher open circuit voltages in solar cells while fluorination (ITIC-4F) led to a downshift of HOMO and LUMO levels.[166,167] Moreover, fluorination results in a redshift and higher absorption coefficient and slightly higher electron mobility.[167] The probably most known compounds in literature concerning the introduction of side chains are O-IDTBR (**28a**) and EH-IDTBR (**28b**) which are derived from the fluorene-based NFA FBR (**27**) in which the fluorene donor was substituted by IDT with different side chains.[168]

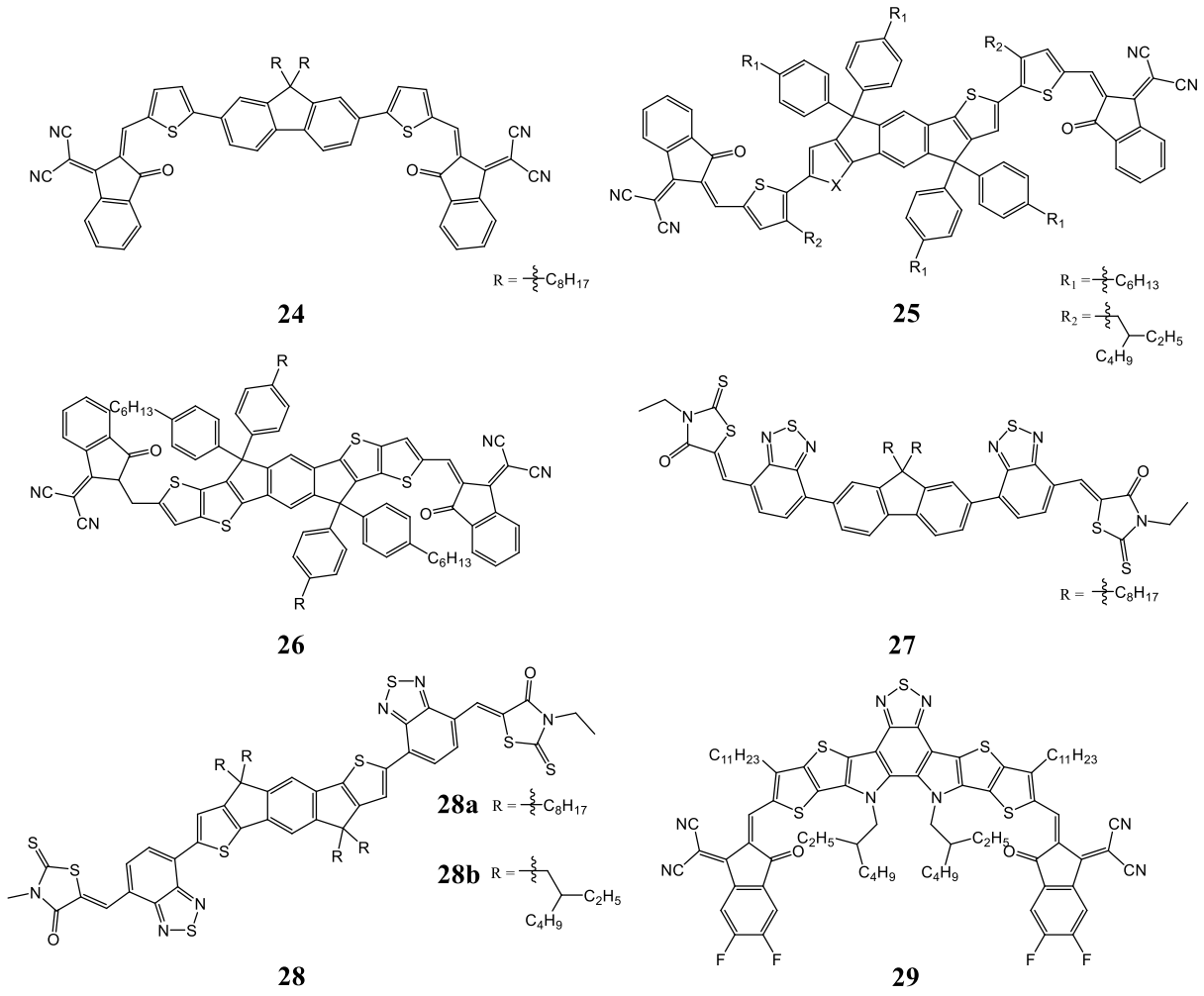

Figure 15: Chemical structures of selected SMAs for OSCs.

One of the most promising new SMA is Y6 (**29**), synthesized by Yuan et al. in 2019.[169] The compound is composed of a fused ring dithienothiophen[3.2-b]- pyrrolobenzothiadiazole core and two (5,6-difluoro-3-oxo-2,3-dihydro-1H-inden-1-ylidene)malononitrile (INCN derivative) terminal units. Y6 features a low band gap (1.34 eV), high absorption coefficient ($9 \cdot 10^4$ cm^{-1}) and suitable HOMO/LUMO levels for available donors.[170]

4.6 State of the Art of FREAs in OSCs

As thoroughly discussed in the previous chapter, SMAs evolved over time and were developed and optimized step by step which in turn also increased their PCEs. The early synthesized fluorene (Flu-RH) and carbazole-based (Cz-RH) NFAs were blended with P3HT and displayed PCEs of 3.08 and 2.56%, respectively.[157] By optimizing the material properties different terminal groups, DICTF and FDICTF were synthesized. Blended with present donors like PTB7-Th and PBDB-T, even higher efficiencies of 7.93% (PTB7-Th:DICTF) and 10.06% (PBDB-T:FDICTF) could be reached.[160,171] Later, Chen et al. investigated the influence of an extended conjugation and different halogens on carbazole-based NFAs.[172] The increased π-system resulted in upshifted HOMO/LUMO levels and a redshift in absorption leading to an increased efficiency of 13.89% (DTTC-4F). Substitution of fluorine with chlorine boosted the performance up to 15.42% (DTTC-4Cl) due to its enhanced π-π interaction and absorption window.

One of the first IDT-based NFAs reported was IEIC in 2014.[161] However, the bad mismatch of donor (PTB7-Th) and acceptor led to only 6.31% efficiency, which was at the current time still one of the highest reported. Later, Lin et al. used a different donor (PffT2-FTAZ-2DT) to improve the device performance up to 7.3%.[173] One approach to narrow the band gap is the substitution of alkyl with alkoxy groups leading to the NFA IEICO. Yao et al. found, that compared to IEIC, IEICO features a higher HOMO level and broader spectral absorption range which resulted in an efficiency of 8.40%.[164] Later, Xie et al. studied different donors with three different IEICO derivatives. Herein, he could reach 9.82% efficiency with PMOT39 as donor and *i*-IEICO-4F as acceptor.[174] Other IDT-core-based NFAs are O-IDTBR and EH-IDTBR with devices performances of 7.80% and 11.70%, respectively.[175,176]

In 2015, Lin et al. published ITIC for the first time with an efficiency of 6.80%.[162] The low efficiency is ascribed to the bad donor/acceptor mismatch. Therefore, other research groups tested

different donor materials and improved the efficiency up to 11.34%.[167,177] There have been several attempts to change the ITIC structure slightly in order to improve their optoelectronic properties. Substituting the phenyl groups with thienyl groups leads to ITIC-Th to lower the HOMO/LUMO levels, however the efficiencies remained low at ~10%.[178,179] A more promising route towards higher V_{OC}s and thus higher efficiencies is the introduction of methyl or dimethyl at the phenyl group of the terminal sides. IT-M and IT-DM raised the LUMO level 0.04 eV and 0.09 eV, respectively, which enhanced their V_{OC}s of 0.94 V and 0.97 V compared to 0.90 V (ITIC). The resulting efficiencies within this study were increased from 11.22% (PBDB-T:ITIC) to 12.05% (PBDB-T:IT-M) and 11.29% (PBDB-T:IT-DM).[166] Contrary to that, introduction of fluorine or chlorine atoms leads to a downshift of the HOMO/LUMO levels. In combination with a new developed donor (PBDB-T-SF) IT-4F featured a certified efficiency of 13.1%.[167] Liao et al. developed new donor materials and reached an even higher efficiency of 13.8% using a non-halogenated solvent when blended with IT-4F. Furthermore, he could boost the efficiency up to 14.4% when an additional anti-reflective coating was applied.[180] When chlorine-based ITIC derivatives (IT-2Cl, IT-4Cl) were derived by Zhang et al. also high efficiencies of 13.45% (IT-4Cl) and 13.16% (IT-2Cl) blended with PBDB-T-2F were reported. Moreover, he fabricated ternary solar cells in which a mixture of 80% IT-4Cl and 20% IT-2Cl led to 14.18% device efficiency.[181]

The up to date best performing SMAs were fabricated with the acceptor Y6. Herein, binary as well as ternary blend systems were developed. Yuan et al. was the first one to report Y6 as NFA. Blended with PBDB-T-2F (PM6) he reached a device efficiency of 15.7% using both inverted and normal device set-ups.[169] Other reports used different donor materials to form binary blends to reach efficiencies between 10% and 17% efficiency.[170,182,183,184] Ternary blend systems with Y6 were composed of either two donors or two acceptors, one of them being Y6, and one donor. Xie et al. mixed the two donors PM6 and J71 with Y6 to an astounding efficiency of 16.5% attributed to enlarged optical window, better morphology leading to better charge transport capability and a lower E_{loss}.[185] On the other side, Wang et al. mixed Y6 with the acceptor IT-M and the donor PBDB-T and achieved a device performance of 12.5%.[186] The highest device performance was reported by Zhan et al. by mixing Y6 with BTP-M (acceptor) and PBDB-T-2F (donor) to an efficiency of 17.03%.[106]

References

[1] M. T. Kibria, A. Ahammed, S. M. Sony, F. Hossain, S.-U.-Islam, A Review: Comparative studies on different generation solar cells technology, Proceedings of 5th International Conference on Environmental Aspects of Bangladesh [ICEAB 2015], **2014**, 51-53.

[2] Research Cell Record Efficiency Chart, National Renewable Energy Laboratory (NREL), https://www.nrel.gov/pv, accessed on 18/03/**2020.**

[3] B. Parida, S. Iniyan, R. Goic, A review of solar photovoltaic technologies, *Renew. Sustain. Energy Rev.* **2011**, *15*, 1625-1636.

[4] T. Pavlović, D. Milosavlijević, I. Radonjić, L. Pantić, A. Radivojević, Application of solar cells made of different Materials in 1 MW PV solar plants in Banja Luka, *Contemp. Mater. (Renewable energy sources)* **2011**, *2*, 155-163.

[5] N. Marinova, S. Valero, J. L. Delgado, Organic and perovskite solar cells: Working principle, materials and interfaces, *J. Colloid Interface Sci.* **2017**, *488*, 373-389.

[6] I. Mora-Seró, How Do Perovskite Solar Cells Work?, *Joule* **2018**, *2*, 585-587.

[7] C. Yan, S. Barlow, Z. Wang, H. Yan, A. K.-Y. Jen, S. R. Marder, X. Zhan, Non-fullerene acceptors for organic solar cells, *Nat. Rev. Mater.* **2018**, *3*, 18003.

[8] S. S. Mali, C. K. Hong, p-i-n/n-i-p type planar hybrid structure of highly efficient perovskite solar cells towards improved air stability: synthetic strategies and the role of p-type hole transport layer (HTL) and n-type electron transport layer (ETL) metal oxides, *Nanoscale* **2016**, *8*, 10528.

[9] S. F. Hoefler, G. Trimmel, T. Rath, Progress on Lead-Free Metal Halide Perovskites for Photovoltaic Applications: a Review, *Monatsh. Chem.* **2017**, *148*, 795-826.

[10] J.-P. Correa-Baena, A. Abate, M. Saliba, W. Tress, T. J. Jacobsson, M. Grätzel, A. Hagfeldt, The rapid evolution of highly efficient perovskite solar cells, *Energy Environ. Sci.* **2017**, *10*, 710-727.

[11] T. J. Jacobsson, J.-P. Correa-Baena, M. Pazoki, M. Saliba, K. Schenk, M. Grätzel, A. Hagfeldt, Exploration of the compositional space for mixed lead halogen perovskites for high efficiency solar cells, *Energy Environ. Sci.* **2016**, *9*, 1706-1724.

[12] M. Saliba, T. Matsui, J.-Y. Seo, K. Domanski, J. P. Correa-Baena, M. K. Nazeeruddin, S. M. Zakeeruddin, W. Tress, A. Abate, A. Hagfeldt, M. Grätzel, Cesium-containing triple cation perovskite solar cells: improved stability, reproducibility and high efficiency, *Energy Environ. Sci.* **2016**, *9*, 1989-1997.

[13] M. Saliba, T. Matsui, K. Domanski, J.-Y. Seo, A. Ummadisingu, S. M. Zakeeruddin, J.-P. Correa-Baena, W. R. Tress, A. Abate, A. Hagfeldt, M. Grätzel, Incorporation of rubidium cations into perovskite solar cells improves photovoltaic performance, *Science* **2016**, *354*, 206-209.

[14] A. K. Baranwal, H. Masutani, H. Sugita, H. Kanda, S. Kanaya, N. Shibayama, Y. Sanehira, M. Ikegami, Y. Numata, K. Yamada, T. Miyasaka, T. Umeyama, H. Imahori, S. Ito, Lead-free perovskite solar cells using Sb and Bi-based $A_3B_2X_9$ and A_3BX_6 crystals with normal and inverse cell structures, *Nano Converg.* **2017**, *4*, 26.

[15] A. Kojima, K. Teshima, Y. Shirai, T. Miyasaka, Organometal Halide Perovskites as Visible-Light Sensitizers for Photovoltaic Cells, *J. Am. Chem. Soc.* **2009**, *131*, 6050-6051.

[16] A. K. Jena, A. Kulkarni, T. Miyasaka, Halide Perovskite Photovoltaics: Background, Status, and Future Prospects, *Chem. Rev.* **2019**, *119*, 3036-3103.

[17] J. Rodríguez-Romero, B. C. Hames, I. Mora-Seró, E. M. Barea, Conjugated Organic Cations to Improve the Optoelectronic Properties of 2D/3D Perovskites, *ACS Energy Lett.* **2017**, *2*, 1969-1970.

[18] N. Li, Z. Zhu, C.-C. Chueh, H. Liu, B. Peng, A. Petrone, X. Li, L. Wang, A. K.-Y. Jen, Mixed Cation $FA_xPEA_{1-x}PbI_3$ with Enhanced Phase and Ambient Stability toward High-Performance Perovskite Solar Cells, *Adv. Mater.* **2017**, *7*, 1601307.

[19] J. Li, H.-L. Cao, W.-B. Jiao, Q. Wang, M. Wei, I. Cantone, J. Lü, A. Abate, Biological impact of lead from halide perovskites reveals the risk of introducing a safe threshold, *Nat. Comm.* **2020**, *11*, 310.

[20] Q. Chen, N. De Marco, Y. Yang, T.-B. Song, C.-C. Chen, H. Zhao, Z. Hong, H. Zhou, Y. Yang, Under the spotlight: The organic-inorganic hybrid halide perovskite for optoelectronic applications, *Nano Today* **2015**, *10*, 355-396.

[21] N. K. Noel, S. D. Stranks, A. Abate, C. Wehrenfennig, S. Guarnera, A.-A. Haghighirad, A. Sadhanala, G. E. Eperon, S. K. Pathak, M. B. Johnston, A. Petrozza, L. M. Herz, H. J. Snaith, Lead-free organic-inorganic tin halide perovskites for photovoltaic applications, *Energy Environ. Sci.* **2014**, *7*, 3061-3068.

[22] F. Hao, C. C. Stoumpos, D. H. Cao, R. P. H. Chang, M. G. Kanatzidis, Lead-free solid-state organic-inorganic halide perovskite solar cells, *Nat. Photonics* **2014**, *8*, 489-494.

[23] F. Hao, C. C. Stoumpos, P. Guo, N. Zhou, T. J. Marks, R. P. H. Chang, M. G. Kanatzidis, Solvent-Mediated Crystallization of $CH_3NH_3SnI_3$ Films for Heterojunction Depleted Perovskite Solar Cells, *J. Am. Chem. Soc.* **2015**, *137*, 11445-11452.

[24] S. Gupta, D. Cahen, G. Hodes, How SnF_2 Impacts the Material Properties of Lead-Free Tin Perovskites, *J. Phys. Chem. C* **2018**, *122*, 13926.

[25] H. Yao, F. Zhou, Z. Li, Z. Ci, L. Ding, Z. Lin, Strategies for Improving the Stability of Tin-Based Perovskite ($ASnX_3$) Solar Cells, *Adv. Sci.* **2020**, *7*, 1903540.

[26] Z. Zhao, F. Gu, Y. Li, W. Sun, S. Ye, H. Rao, Z. Liu, Z. Bian, C. Huang, Mixed-Organic-Cation Tin Iodide for Lead-Free Perovskite Solar Cells with an Efficiency of 8.12%, *Adv. Sci.* **2017**, *4*, 1700204.

[27] X. Liu, K. Yan, D. Tan, X. Liang, H. Zhang, W. Huang, Solvent Engineering Improves Efficiency of Lead-Free Tin-Based Hybrid Perovskite Solar Cells beyond 9%, *ACS Energy Lett.* **2018**, *3*, 2701-2707.

[28] K. P. Marshall, M. Walker, R. I. Walton, R. A. Hatton, Enhanced stability and efficiency in hole-transport-layer-free $CsSnI_3$ perovskite photovoltaics, *Nat. Energy* **2016**, *1*, 16178.

[29] J. H. Heo, J. Kim, H. Kim, S. H. Moon, S. H. Im, K.-H. Hong, Roles of SnX_2 (X = F, Cl, Br) Additives in Tin-Based Halide Perovskites toward Highly Efficient and Stable Lead-Free Perovskite Solar Cells, *J. Phys. Chem. Lett.* **2018**, *9*, 6024-6031.

[30] E. Jokar, C.-H. Chien, C.-M. Tsai, A. Fathi, E. W.-G. Diau, Robust Tin-Based Perovskite Solar Cells with Hybrid Organic Cations to Attain Efficiency Approaching 10%, *Adv. Mater.* **2018**, *31*, 1804835.

[31] Y. Liao, H. Liu, W. Zhou, D. Yang, Y. Shang, Z. Shi, B. Li, X. Jiang, L. Zhang, L. N. Quan, R. Quintero-Bermudez, B. R. Sutherland, Q. Mi, E. H. Sargent, Z. Ning, Highly Oriented Low-Dimensional Tin Halide Perovskites with Enhanced Stability and Photovoltaic Performance, *J. Am. Chem. Soc.* **2017**, *139*, 6693-6699.

[32] S. J. Lee, S. S. Shin, J. Im, T. K. Ahn, J. H. Noh, N. J. Jeon, S. I. Seok, J. Seo, Reducing Carrier Density in Formamidinium Tin Perovskites and Its Beneficial Effects on Stability and Efficiency of Perovskite Solar Cells, *ACS Energy Lett.* **2018**, *3*, 46-53.

[33] S. Shao, J. Liu, G. Portale, H.-H. Fang, G. R. Blake, G. H. ten Brink, L. J. A. Koster, M. A. Loi, Highly Reproducible Sn-Based Hybrid Perovskite Solar Cells with 9% Efficiency, *Adv. Mater.* **2017**, *8*, 1702019.

[34] C. Liu, J. Tu, X. Hu, Z. Huang, X. Meng, J. Yong, X. Duan, L. Tan, Z. Li, Y. Chen, Enhanced Hole Transportation for Inverted Tin-Based Perovskite Solar Cells with High Performance and Stability, *Adv. Funct. Mater* **2019**, *29*, 1808059.

[35] M. A. Kamarudin, D. Hirotani, Z. Wang, K. Hamada, K. Nishimura, Q. Shen, T. Toyoda, S. Iikubo, T. Minemoto, K. Yoshino, S. Hayase, Suppression of Charge Carrier Recombination in Lead-Free Tin Halide Perovskite via Lewis Base Post-treatment, *J. Phys. Chem. Lett.* **2019**, *10*, 5277-5283.

[36] B. P. Nguyen, D. Shin, H. R. Jung, J. Kim, T. T. T. Nguyen, S. Yoon, Y. Yi, W. Jo, Phase formation and local charge transport of lead-free $CH_3NH_3Sn(I_{1-x}Br_x)_3$ ($0 \leq x \leq 1$) perovskite solar cells fabricated by solvent optimization, *Sol. Energy* **2019**, *186*, 136-144.

[37] B. P. Nguyen, H. R. Jung, J. Kim, W. Jo, Enhanced carrier transport over grain boundaries in lead-free $CH_3NH_3Sn(I_{1-x}Br_x)_3$ ($0 \leq x \leq 1$) perovskite solar cells, *Nanotechnology* **2019**, *30*, 314005.

[38] P. Wang, F. Li, K.-J. Jiang, Y. Zhang, H. Fan, Y. Zhang, Y. Miao, J.-H. Huang, C. Gao, X. Zhou, F. Wang, L.-M. Yang, C. Zhan, Y.L. Song, Ion Exchange/Insertion Reactions for Fabrication of Efficient Methylammonium Tin Iodide Perovskite Solar Cells, *Adv. Sci.* **2020**, *7*, 1903047.

[39] F. Li, C. Zhang, J.-H. Huang, H. Fan, H. Wang, P. Wang, C. Zhan, C.-M. Liu, X. Li, L.-M. Yang, Y. Song, K.-J. Jiang, A Cation-Exchange Approach for the Fabrication of Efficient Methylammonium Tin Iodide Perovskite Solar Cells, *Angew. Chem. Int. Ed.* **2019**, *58*, 6688-6692.

[40] S. Shao, J. Dong, H. Duim, G. H. ten Brink, G. R. Blake, G. Portale, M. A. Loi, Enhancing the crystallinity and perfecting the orientation of formamidinium tin iodide for highly efficient Sn-based perovskite solar cells, *Nano Energy* **2019**, *60*, 810-816.

[41] X. Meng, J. Lin, X. Liu, X. He, Y. Wang, T. Noda, T. Wu, X. Yang, L. Han, Highly Stable and Efficient $FASnI_3$-Based Perovskite Solar Cells by Introducing Hydrogen Bonding, *Adv. Mater.* **2019**, *31*, 1903721.

[42] T. Wu, X. Liu, X. He, Y. Wang, X. Meng, T. Noda, X. Yang, L. Han, Efficient and stable tin-based perovskite solar cells by introducing π-conjugated Lewis base, *Sci. China Chem.* **2020**, *63*, 107-115.

[43] X. He, T. Wu, X. Liu, Y. Wang, X. Meng, J. Wu, T. Noda, X. Yang, Y. Morimoto, H. Segawa, L. Han, Highly efficient tin perovskite solar cells achieved in a wide oxygen concentration range, *J. Mater. Chem. A* **2020**, *8*, 2760-2768.

[44] X. Jiang, F. Wang, Q. Wei, H. Li, Y. Shang, W. Zhou, C. Wang, P. Cheng, Q. Cheng, Q. Chen, L. Chen, Z. Ning, Ultra-high open-circuit voltage of tin perovskite solar cells via an electron transporting layer design, *Nat. Comm.* **2020**, *11*, 1245.

[45] T. Krishnamoorthy, H. Ding, C. Yan, W. L. Leong, T. Baikie, Z. Zhang, M. Sherburne, S. Li, M. Asta, N. Mathews, S. G. Mhaisalkar, Lead-free germanium iodide perovskite materials for photovoltaic applications, *J. Mater. Chem. A* **2015**, *3*, 23829-23832.

[46] M. Roknuzzaman, K. Ostrikov, H. Wang, A. Du, T. Tesfamichael, Towards lead-free perovskite photovoltaics and optoelectronics by ab-initio simulations, *Sci Rep.* **2017**, *7*, 14025.

[47] Q. Mahmood, M. Yaseen, M. Hassan, M. S. Rashid, I. Tlili, A. Laref, The first-principle study of mechanical, optoelectronic and thermoelectric properties of $CsGeBr_3$ and $CsSnBr_3$ perovskites, *Mater. Res. Express* **2019**, *6*, 045901.

[48] D. Umadevi, G. W. Watson, Quasiparticle GW Calculations on Lead-Free Hybrid Germanium Iodide Perovskite $CH_3NH_3GeI_3$ for Photovoltaic Applications, *ACS Omega* **2019**, *4*, 5661-5669.

[49] A.-A. Kanoun, M. B. Kanoun, A. E. Merad, S. Goumri-Said, Toward development of high-performance perovskite solar cells based on $CH_3NH3GeI_3$ using computational approach, *Sol. Energy* **2019**, *182*, 237-244.

[50] X. Chang, D. Marongiu, V. Sarritzu, N. Setsu, Q. Wang, S. Lai, A. Mattoni, A. Filippetti, F. Congiu, A. G. Lehmann, F. Quochi, M. Saba, A. Mura, G. Bongiovanni, Layered Germanium Hybrid Perovskite Bromides: Insights from Experiments and First-Principles Calculations, *Adv. Funct. Mater.* **2019**, *29*, 1903528.

[51] I. Kopacic, B. Friesenbichler, S. F. Hoefler, B. Kunert, H. Plank, T. Rath, G. Trimmel, Enhanced Performance of Germanium Halide Perovskite Solar Cells through Compositional Engineering, *ACS Appl. Energy Mater.* **2018**, *1*, 343-347.

[52] K. A. Montiel, C. Yang, C. H. Andreasen, M. S. Gottlieb, M. R. Pfefferkorn, L. G. Wilson, J. L. W. Carter, I. T. Martin, Lead-free perovskite thin film solar cells from binary sources, *Conference Record of the IEEE Photovoltaic Specialists Conference* **2019**, *8980512*, 1183-1186.

[53] Raghvendra, R. R. Kumar, S. K. Pandey, Performance evaluation and material parameter perspective of eco-friendly highly efficient $CsSnGeI_3$ perovskite solar cell, *Superlattice Microstruc*. **2019**, *135*, 106273.

[54] P. Cheng, T. Wu, J. Liu, W.-Q. Deng, K. Han, Lead-Free, Two-Dimensional Mixed Germanium and Tin Perovskites, *J. Phys. Chem. Lett.* **2018**, *9*, 2518-2522.

[55] M.-G. Ju, J. Dai, L. Ma, X. C. Zeng, Lead-Free Mixed Tin and Germanium Perovskites for Photovoltaic Application, *J. Am. Chem. Soc.* **2017**, *139*, 8038-8043.

[56] M. Chen, M.-G. Ju, H. F. Garces, A. D. Carl, L. K. Ono, Z. Hawash, Y. Zhang, T. Shen, Y. Qi, R. L. Grimm, D. Pacifici, X. C. Zeng, Y. Zhou, N. P. Padture, Highly stable and efficient all-inorganic lead-free perovskite solar cells with native-oxide passivation, *Nat. Comm.* **2019**, *10*, 16.

[57] C. H. Ng, K. Nishimura, N. Ito, K. Hamada, D. Hirotani, Z. Wang, F. Yang, S. Iikubo, Q. Shen, K. Yoshimo, T. Minemoto, S. Hayase, Role of GeI_2 and SnF_2 additives for SnGe perovskite solar cells, *Nano Energy* **2019**, *58*, 130-137.

[58] F. Yang, D. Hirotani, G. Kapil, M. A. Kamarudin, C. H. Ng, Y. Zhang, Q. Shen, S. Hayase, All-Inorganic $CsPb_{1-x}Ge_xI_2Br$ Perovskite with Enhanced Phase Stability and Photovoltaic Performance, *Angew. Chem. Int. Ed.* **2018**, *57*, 12745-12749.

[59] J.-C. Hebig, I. Kühn, J. Flohre, T. Kirchartz, Optoelectronic Properties of $(CH_3NH_3)_3Sb_2I_9$ Thin Films for Photovoltaic Applications. *ACS Energy Lett.* **2016**, *1*, 309-314.

[60] J.-P. Correa-Baena, L. Nienhaus, R. C. Kurchin, S. S. Shin, S. Wieghold, N. T. Putri Hartono, M. Layurova, N. D. Klein, J. R. Poindexter, A. Polizzotti, S. Sun, M. G. Bawendi and T. Buonassisi, *A*-Site Cation in Inorganic $A_3Sb_2I_9$ Perovskite Influences Structural Dimensionality, Exciton Binding Energy, and Solar Cell Performance, *Chem. Mater.* **2018**, *30*, 3734-3742.

[61] P. C. Harikesh, H. K. Mulmudi, B. Ghosh, T. W. Goh, Y. T. Teng, K. Thirumal, M. Lockrey, K. Weber, T. M. Koh, S. Z. Li, S. Mhaisalkar and N. Mathews, Rb as an Alternative Cation for Templating Inorganic Lead-Free Perovskites for Solution Processed Photovoltaics, *Chem. Mater.* **2016**, *28*, 7496-7504.

[62] F. Li, Y. Wang, K. Xia, R. L. Z. Hoye, V. Pecunia, Microstructural and photoconversion efficiency enhancement of compact films of lead-free perovskite derivative $Rb_3Sb_2I_9$, *J. Mater. Chem. A* **2020**, *8*, 4396-4406.

[63] K. M. Boopathi, P. Karuppuswamy, A. Singh, C. Hanmandlu, L. Lin, S. A. Abbas, C. C. Chang, P. C. Wang, G. Li, C. W. Chu, Solution-Processable Antimony-Based Light-Absorbing Materials Beyond Lead Halide Perovskites, *J. Mater. Chem. A* **2017**, *5*, 20843-20850.

[64] P. Karuppuswamy, K. M. Boopathi, A. Mohapatra, H. C. Chen, K.-T. Wong, P.-C. Wang, C.-W. Chu, Role of a Hydrophobic Scaffold in Controlling the Crystallization of Methylammonium Antimony Iodide for Efficient Lead-Free Perovskite Solar Cells, *Nano Energy* **2018**, *45*, 330-336.

[65] F. Umar, J. Zhang, Z. Jin, I. Muhammad, X. Yang, H. Deng, K. Jahangeer, Q. Hu, H. Song, J. Tang, Dimensionality Controlling of $Cs_3Sb_2I_9$ for Efficient All-Inorganic Planar Thin Film Solar Cells by HCl-Assisted Solution Method, *Adv. Optical Mater.* **2019**, *7*, 1801368.

[66] A. Singh, K. M. Boopathi, A. Mohapatra, Y. F. Chen, G. Li, C. W. Chu, Photovoltaic Performance of Vapor-Assisted Solution-Processed Layer Polymorph of $Cs_3Sb_2I_9$, *ACS Appl. Mater. Interfaces* **2018**, *10*, 2566-2573.

[67] K. Ahmad, P. Kumar, S. M. Mobin, A Two-Step Modified Sequential Deposition Method-based Pb-Free $(CH_3NH_3)_3Sb_2I_9$ Perovskite with Improved Open Circuit Voltage and Performance, *Chem. Electro. Chem.* **2020**, *7*, 946-950.

[68] T. D. Chonamada, A. B. Dey, P. K. Santra, Degradation Studies of $Cs_3Sb_2I_9$: A Lead-Free Perovskite, *ACS Appl. Energy Mater.* **2020**, *3*, 47-55.

[69] G. Paul, A. J. Pal, Defect Passivation and Layered-Phase Formation in an Antimony Based Hybrid Iodide Perovskite Derivative through Chlorine Incorporation, *J. Phys. Chem. C* **2019**, *123*, 13500-13507.

[70] R. Nie, A. Mehta, B.-W. Park, H.-W. Kwon, J. Im, S. I. Seok, Mixed Sulfur and Iodide-Based Lead-Free Perovskite Solar Cells, *J. Am. Chem. Soc.* **2018**, *140*, 872-875.

[71] L. Liang, P. Gao, Lead-Free Hybrid Perovskite Absorbers for Viable Application: Can We Eat the Cake and Have It too?, *Adv. Sci.* **2018**, *5*, 1700331.

[72] A. J. Lehner, H. Wang, D. H. Fabini, C. D. Liman, C.-A. Hébert, E. E. Perry, M. Wang, G. C. Bazan, M. L. Chabinyc, R. Seshadri, Electronic structure and photovoltaic application of BiI_3, *Appl. Phys. Lett.* **2015**, *107*, 131109.

[73] A. J. Lehner, D. H. Fabini, H. A. Evans, C.-A. Hébert, S. R. Smock, J. Hu, H. Wang, J. W. Zwanziger, M. L. Chabinyc, R. Seshadri, Crystal and Electronic Structures of Complex Bismuth Iodides $A_3Bi_2I_9$ (A = K, Rb, Cs) Related to Perovskite: Aiding the Rational Design of Photovoltaics, *Chem. Mater.* **2015**, *27*, 7137-7148.

[74] K. Eckhardt, V. Bon, J. Getzschmann, J. Grothe, F. M. Wisser, S. Kaskel, Crystallographic insights into $(CH_3NH_3)_3(Bi_2I_9)$: a new lead-free hybrid organic–inorganic material as a potential absorber for photovoltaics, *Chem. Commun.* **2016**, *52*, 3058-3060.

[75] G. Volonakis, M. R. Filip, A. A. Haghighirad, N. Sakai, B. Wenger, H. J. Snaith, F. Giustino, Lead-Free Halide Double Perovskites via Heterovalent Substitution of Noble Metals, *J. Phys. Chem. Lett.* **2016**, *7*, 1254-1259.

[76] A. H. Slavney, T. Hu, A. M. Lindenberg, H. I. Karunadasa, A Bismuth-Halide Double Perovskite with Long Carrier Recombination Lifetime for Photovoltaic Applications, *J. Am. Chem. Soc.* **2016**, *138*, 2138-2141.

[77] Z. Xiao, W. Meng, J. Wang, Y. Yan, Thermodynamic Stability and Defect Chemistry of Bismuth-Based Lead-Free Double Perovskites, *Chem. Sus. Chem.* **2016**, *9*, 2628-2633.

[78] M. Lyu, J.-H. Yun, M. Cai, Y. Jiao, P. V. Bernhardt, M. Zhang, Q. Wang, A. Du, H. Wang, G. Liu, L. Wang, Organic–inorganic bismuth (III)-based material: A leadfree, air-stable and solution-processable light-absorber beyond organolead perovskites, *Nano Res.* **2016**, *9*, 692-702.

[79] S. Öz, J.-C. Hebig, E. Jung, T. Singh, A. Lepcha, S. Olthof, J. Flohre, Y. Gao, R. German, P. H. M. van Lossdrecht, K, Meerholz, T. Kirchartz, S. Mathur, Zero-dimensional $(CH_3NH_3)_3Bi_2I_9$ perovskite for optoelectronic applications, *Sol. Energy Mater. Sol.* **2016**, *158*, 195-201.

[80] H. Wang, J. Tian, K. Jiang, Y. Zhang, H. Fan, J. Huang, L.-m. Yang, B. Guan, Y. Song, Fabrication of methylammonium bismuth iodide through interdiffusion of solution-processed BiI_3/CH_3NH_3I stacking layers, *RSC Adv.* **2017**, *7*, 43826-43830.

[81] S. S. Mali, H. Kim, D.-H. Kim, C. K. Hong, Anti-Solvent Assisted Crystallization Processed Methylammonium Bismuth Iodide Cuboids towards Highly Stable Lead-Free Perovskite Solar Cells, ChemistrySelect **2017**, *2*, 1578-1585.

[82] Z. Zhang, X. Li, X. Xia, Z. Wang, Z. Huang, B. Lei, Y. Gao, High-Quality $(CH_3NH_3)_3Bi_2I_9$ Film-Based Solar Cells: Pushing Efficiency up to 1.64%, *J. Phys. Chem. Lett.* **2017**, *8*, 4300-4307.

[83] S. M. Jain, D. Phuyal, M. L. Davies, M. Li, B. Philippe, C. De Castro, Z. Qiu, J. Kim, T. Watson, W. C. Tsoi, O. Karis, H. Rensmo, G. Boschloo, T. Edvinsson, J. R. Durrant, An effective approach of vapour assisted morphological tailoring for reducing metal defect sites in lead-free, $(CH_3NH_3)_3Bi_2I_9$ bismuth-based perovskite solar cells for improved performance and long-term stability, *Nano Energy* **2018**, *49*, 614-624.

[84] S. M. Jain, T. Edvinsson, J. R. Durrant, Green fabrication of stable lead-free bismuth based perovskite solar cells using a non-toxic solvent, *Commun. Chem.* **2019**, *2*, 91.

[85] W. Hu, X. He, Z. Fang, W. Lian, Y. Shang, X. Li, W. Zhou, M. Zhang, T. Chen, Y. Lu, L. Zhang, L. Ding, S. Yang, Bulk heterojunction gifts bismuth-based lead-free perovskite solar cells with record efficiency, *Nano Energy* **2020**, *68*, 104362.

[86] F. Bai, Y. Hu, Y. Hu, T. Qiu, X. Miao, S. Zhang, Lead-free, air-stable ultrathin $Cs_3Bi_2I_9$ perovskite nanosheets for solar cells, *Sol. Energy Mater. Sol. Cells* **2018**, *184*, 15-21.

[87] E. Greul, M. L. Petrus, A. Binek, P. Docampo, T. Bein, Highly stable, phase pure $Cs_2AgBiBr_6$ double perovskite thin films for optoelectronic applications, *J. Mater. Chem. A* **2017**, *5*, 19972-19981.

[88] Z. Zhang, C. Wu, D. Wang, G. Liu, Q. Zhang, W. Luo, X. Qi, X. Guo, Y. Zhang, Y. Lao, B. Qu, L. Xiao, Z. Chen, Improvement of $Cs_2AgBiBr_6$ double perovskite solar cell by rubidium doping, *Org. Electron.* **2019**, *74*, 204-210.

[89] N. Pai, J. Lu, M. Wang, A. S. R. Chesman, A. Seeber, P. V. Cherepanov, D. C. Senevirathna, T. R. Gengenbach, N. V. Medhekar, P. C. Andrews, U. Bach, A. N. Simonov, Enhancement of the intrinsic light harvesting capacity of $Cs_2AgBiBr_6$ double perovskite via modification with sulphide, *J. Mater. Chem. A* **2020**, *8*, 2008-2020.

[90] D. Kearns, M. Clavin, Photovoltaic Effect and Photoconductivity in Laminated Organic Systems, *J. Chem. Phys.* **1958**, *29*, 950-951.

[91] C. W. Tang, Two-layer organic photovoltaic cell, *Appl. Phys. Lett.* **1986**, *48*, 183-185.

[92] N. S. Sariciftci, L. Smilowitz, A. J. Heeger, F. Wudl, Photoinduced Electron Transfer from a Conducting Polymer to Buckminsterfullerene, *Science* **1992**, *258*, 1474-1476.

[93] J. J. M. Halls, C. A. Walsh, N. C. Greenham, E. A. Marseglia, R. H. Friend, S. C. Moratti, A. B. Holmes, Efficient photodiodes from interpenetrating polymer networks, *Nature* **1995**, *376*, 498-500.

[94] G. Yu, A. J. Heeger, Charge separation and photovoltaic conversion in polymer composites with internal donor/acceptor heterojunctions, *J. Appl. Phys.* **1995**, *78*, 4510-4515.

[95] C. B. Nielsen, S. Holliday, H-Y. Chen, S. J. Cryer, I. McCulloch, Non-Fullerene Electron Acceptors for Use in Organic Solar Cells, *Acc. Chem. Res.* **2015**, *48*, 2803-2812.

[96] J. Zhao, Y. Li, G. Yang, K. Jiang, H. Lin, H. Ade, W. Ma, H. Yan, Efficient organic solar cells processed from hydrocarbon solvents, *Nat. Energy* **2016**, *1*, 15027.

[97] Y. Liu, J. Zhao, Z. Li, C. Mu, W. Ma, H. Hu, K. Jiang, H. Lin, H. Ade, H. Yan, Aggregation and morphology control enables multiple cases of high-efficiency polymer solar cells, *Nat. Comm.* **2014**, *5*, 5293.

[98] D. Deng, Y. Zhang, J. Zhang, Z. Wang, L. Zhu, J. Fan, B. Xia, Z. Wang, K. Lu, W. Ma, Z. Wei, Fluorination-enabled optimal morphology leads to over 11% efficiency for inverted small-molecule organic solar cells, *Nat. Commun.* **2016**, *7*, 13740.

[99] T. Kumari, S. M. Lee, S.-H. Kang, S. Chen, C. Yang, Ternary solar cells with a mixed face-on and edge-on orientation enable an unprecedented efficiency of 12.1%, *Energy Environ. Sci.* **2017**, *10*, 258-265.

[100] J. Huang, H. Wang, K. Yan, X. Zhang, H. Chen, C.-Z. Li, J. Yu, Highly Efficient Organic Solar Cells Consisting of Double Bulk Heterojunction Layers, *Adv. Mater.* **2017**, *29*, 1606729.

[101] A. Distler, T. Sauermann, H.-J. Egelhaar, S. Rodman, D. Waller, K.-S. Cheon, M. Lee, D. M. Guldi, The Effect of PCBM Dimerization on the Performance of Bulk Heterojunction Solar Cells, *Adv. Energy Mater.* **2014**, *4*, 1300693.

[102] Y. He, H.-Y. Chen, J. Hou, Y. Li, Indene-C_{60} Bisadduct: A New Acceptor for High-Performance Polymer Solar Cells, *J. Am. Chem. Soc.* **2010**, *132*, 1377-1382.

[103] C.-Z. Li, S.-C. Chien, H-L. Yip, C.-C. Chueh, F.-C. Chen, Y. Matsuo, E. Nakamura, A. K.-Y. Jen, Facile synthesis of a 56π-electron 1,2-dihydromethano-[60]PCBM and its application for thermally stable polymer solar cells, *Chem. Commun.* **2011**, *47*, 10082-10084.

[104] Y. He, Y. Li, Fullerene derivative acceptors for high performance polymer solar cells, *Phys. Chem. Chem. Phys.* **2011**, *12*, 1970-1983.

[105] E. M. Speller, A. J. Clarke, J. Luke, H. K. H. Lee, J. R. Durrant, N. Li, T. Wang, H. C. Wong, J.-S. Kim, W. C. Tsoi, Z. Li, From fullerene acceptors to non-fullerene acceptors: prospects and challenges in the stability of organic solar cells, *J. Mater. Chem. A* **2019**, *7*, 23361.

[106] L. Zhan, S. Li, T.-K. Lau, Y. Cui, X. Lu, M. Shi, C.-Z. Li, H. Li, J. Hou, H. Chen, Over 17% efficiency ternary organic solar cells enabled by two non-fullerene acceptors working in an alloy-like model, *Energy Environ. Sci.* **2020**, *13*, 635-645.

[107] L. Feiler, H. Langhals, K. Polborn, Synthesis of Perylene-3,4-dicarboximides – Novel Highly Photostable Fluorescent Dyes, *Liebigs Ann. Chem.* **1995**, 1229-1244.

[108] C. Li, H. Wonneberger, Perylene Imides for Organic Photovoltaics: Yesterday, Today, and Tomorrow, *Adv. Mater.* **2012**, *24*, 613-636.

[109] L. Q. Fan, Y. P. Xu, H. Tian, 1,6-Disubstituted perylene bisimides: concise synthesis and characterization as near-infrared fluorescent dyes, *Tetrahedron Lett.* **2005**, *46*, 4443-4447.

[110] S. Nakazono, Y. Imazaki, H. Yoo, J. Yang, T. Sasamori, N. Tokitoh, T. Cédric, H. Kageyama, D. Kim, H. Shinokubo, A. Osuka, Regioselective Ru-Catalyzed Direct 2,5,8,11-Alkylation of Perylene Bisimides, *Chem. Eur. J.* **2009**, *15*, 7530-7533.

[111] C. Huang, S. Barlow, S. R. Marder, Perylene-3,4,9,10-tetracarboxylic Acid Diimides: Synthesis, Physical Properties, and Use in Organic Electronics, *J. Org. Chem.* **2011**, *76*, 2386-2407.

[112] P. S. Marqués, F. Tintori, J. M. A. Castán, P. Josse, C. Dalinot, M. Allain, G. Welch, P. Blanchard, C. Cabanetos, Indeno[1,2-b]thiophene Endcapped perylene Diimide: Should the 1,6-Regioisomers be systematically considered as a byproduct?, *Sci. Rep.* **2020**, *10*, 3262.

[113] S. Rajaram, R. Shivanna, S. K. Kandappa, K. S. Narayan, Nonplanar Perylene Diimides as Potential Alternatives to Fullerenes in Organic Solar Cells, *J. Phys. Chem. Lett.* **2012**, *3*, 2405-2408.

[114] J. Yang, F. Chen, P. Cong, H. Xiao, Y. Geng, Z. Liao, L. Chen, B. Zhang, E. Zhou, Tuning the optoelectronic properties of vinylene linked perylenediimides dimer by ring annulation at the inside or outside bay positions for fullerene-free organic solar cells, *J. Energy Chem.* **2020**, *40*, 112-119.

[115] R. T. Cheriya, J. Joy, S. K. Rajagopal, K Kalaivanan, M. Hariharan, DNA-Enforced Conformational Restriction of an Atropisomer, *J. Phys. Chem. C* **2012**, *116*, 22631-22636.

[116] L. Chen, K. Zhang, L. Zhu, Y. Xiao, New and Efficient Approach to the Versatile Building Block of 3,4-Perylenedicarboxylic Monoanhydride, *Ind. Eng. Chem. Res.* **2015**, *54*, 12699-12703.

[117] K.-Y. Tomizaki, P. Thamyongkit, R. S. Loewe, J. S. Lindsey, Practical synthesis of perylene-monoimide building blocks that possess features appropriate for use in porphyrin-based light-harvesting arrays, *Tetrahedron* **2003**, *59*, 1191-1207.

[118] Y. Hu, S. Chen, L. Zhang, Y. Zhang, Z. Yuan, X. Zhao, Y. Chen, Facile Approach to Perylenemonoimide with Short Side Chains for Nonfullerene Solar Cells, *J. Org. Chem.* **2017**, *82*, 5926-5931.

[119] Y. Zhang, X. Guo, B. Guo, W. Su, M. Zhang, Y. Li, Nonfullerene Polymer Solar Cells based on a Perylene Monoimide Acceptor with a High Open-Circuit Voltage of 1.3 V, *Adv. Funct. Mater.* **2017**, *27*, 1603892.

[120] A. Wadsworth, M. Moser, A. Marks, M. S. Little, N. Gasparini, C. J. Brabec, D. Baran, I. McCulloch, Critical review of the molecular design progress in non-fullerene electron acceptors towards commercially viable organic solar cells, *Chem. Soc. Rev.* **2019**, *48*, 1596-1625.

[121] Z. Li, L. Ying, P. Zhu, W. Zhong, N. Li, F. Liu, F. Huang, Y. Cao, A generic green solvent concept boosting the power conversion efficiency of all-polymer solar cells to 11%, *Energy Environ. Sci.* **2019**, *12*, 157-163.

[122] F. Tang, D. Zhu, N. Liang, J. Hou, Z. Wang, Terrylene diimide-based middle-low bandgap electron acceptors for organic photovoltaics, *J. Mater. Chem. C* **2020**, *8*, 4441-4446.

[123] N. Liang, K. Sun, J. Feng, Y. Chen, D. Meng, W. Jiang, Y. Li, J. Hou, Z. Wang, Near-infrared electron acceptors based on terrylene diimides for organic solar cells, *J. Mater. Chem. A* **2018**, *6*, 18808-18812.

[124] J. Feng, N. Liang, W. Jiang, D. Meng, R. Xin, B. Xu, J. Zhang, Z. Wei, J. Hou, Z. Wang, Twisted terrylene dyes: synthesis and application in organic solar cells, *Org. Chem. Front.* **2017**, *4*, 811-816.

[125] H. Yin, S. Chen, P. Bi, X. Xu, S. H. Cheung, X. Hao, Q. Peng, X. Zhu, S. K. So, Rationalizing device performance of perylenediimide derivatives as acceptors for bulk-heterojunction organic solar cells, *Org. Electron.* **2019**, *65*, 156-161.

[126] E. Kozma, D. Kotowski, M. Catellani, S. Luzzati, A. Famulari, F. Bertini, Synthesis and characterization of new electron acceptor perylenediimides molecule for photovoltaic applications, *Dyes Pigments* **2013**, *99*, 329-338.

[127] Y. Li, M. Han, W. Yang, J. Guo, K. Chang, J. Wang, J. Min, Q. Li, Z. Li, Perylene diimide-based cathode interfacial materials: adjustable molecular structures and conformation, optimized film morphology, and much improved performance of non-fullerene polymer solar cells, *Mater. Chem. Front.* **2019**, *3*, 1840-1848.

[128] X. Li, H. Wang, H. Nakayama, Z. Wei, J. A. Schneider, K. Clark, W.-Y. Lai, W. Huang, J. G. Labram, J. Read de Alaniz, M. L. Chabinyc, F. Wudl, Y. Zheng, Multi-Sulfur-Annulated Fused Perylene Diimides for Organic Solar Cells with Low Open-Circuit Voltage Loss, *ACS Appl. Energy Mater.* **2019**, *2*, 3805-3814.

[129] M. B. A. Qureshi, M. Li, H. Wang, J. Song, Z. Bo, Nonfullerene acceptors with an N-annulated perylene core and two perylene diimide units for efficient organic solar cells, *Dyes Pigments* **2020**, *173*, 107970.

[130] D. Sun, D. Meng, Y. Cai, B. Fan, Y. Li, W. Jiang, L. Huo, Y. Sun, Z. Wang, Non-Fullerene-Acceptor-Based Bulk-Heterojunction Organic Solar Cells with Efficiency over 7%, *J. Am. Chem. Soc.* **2015**, *137*, 11156-11162.

[131] D. Meng, D. Sun, C. Zhong, T. Liu, B. Fan, L. Huo, Y. Li, W. Jiang, H. Choi, T. Kim, J. Y. Kim, Y. Sun, Z. Wang, A. J. Heeger, High-Performance Solution-Processed Non-Fullerene Organic Solar Cells Based on Selenophene-Containing Perylene Bisimide Acceptor, *J. Am. Chem. Soc.* **2016**, *138*, 375-380.

[132] X. Li, K. Wu, L. Zheng, Y. Deng, S. Tan, H. Chen, Synthesis and characterization of novel benzodithiophene-fused perylene diimide acceptors: Regulate photovoltaic performance via structural isomerism, *Dyes Pigments* **2019**, *168*, 59-67.

[133] H. Zhong, C.-H. Wu, C.-Z. Li, J. Carpenter, C.-C. Chueh, J.-Y. Chen, H. Ade, A. K.-Y. Jen, Rigidifying Nonplanar Perylene Diimides by Ring Fusion Toward Geometry-Tunable Acceptors for High-Performance Fullerene-Free Solar Cells, *Adv. Mater.* **2016**, *28*, 951-958.

[134] S. Li, W. Liu, C.-Z. Li, T.-K. Lau, X. Lu, M. Shi, H. Chen, A non-fullerene acceptor with a fully fused backbone for efficient polymer solar cells with a high open-circuit voltage, *J. Mater. Chem. A* **2016**, *4*, 14983-14987.

[135] Y. Lin, Z. Zheng, M. Liu, S. Gao, F. Guo, G. T. Mola, J. Wang, L. Zhao, Y. Zhang, A novel quasi-two-dimensional fused-perylenediimide electron acceptor for solvent additive-free non-fullerene organic solar cells, *Dyes Pigments* **2020**, *175*, 108119.

[136] J. Liu, S. Chen, D. Qian, B. Gautam, G. Yang, J. Zhao, J. Bergqvist, F. Zhang, W. Ma, H. Ade, O. Inganäs, K. Gundogdu, F. Gao, H. Yan, Fast charge separation in a non-fullerene organic solar cell with a small driving force, *Nat. Energy* **2016**, *1*, 16089.

[137] S. Li, W. Liu, C.-Z. Li, F. Liu, Y. Zhang, M. Shi, H. Chen, T. P. Russell, A simple perylene diimide derivative with a highly twisted geometry as an electron acceptor for efficient solar cells, *J. Mater. Chem. A* **2016**, *4*, 10659-10665.

[138] Y. Duan, X. Hu, H. Yan, W. Wu, Z. Li, Q. Peng, Pronounced Effects of a Triazine Core on Photovoltaic Performance-Efficient Organic Solar Cells Enabled by a PDI Trimer-Based Small Molecular Acceptor, *Adv. Mater.* **2017**, *29*, 1605115.

[139] P. Xia, M. Wu, S. Zhang, J. Hu, L. Chen, T. Bu, J. Yi, D. Wu, J. Xia, High performance PDI based ternary organic solar cells fabricated with nonhalogenated solvent, *Org. Electron.* **2019**, *73*, 205-211.

[140] D. Meng, H. Fu, C. Xiao, X. Meng, T. Winands, W. Ma, W. Wei, B. Fan, L. Huo, N. L. Doltsinis, Y. Li, Y. Sun, Z. Wang, Three-Bladed Rylene Propellers with Three-Dimensional Network Assembly for Organic Electronics, *J. Am. Chem. Soc.* **2016**, *138*, 10184-10190.

[141] G. Zhang, J. Feng, X. Xu, W. Ma, Y. Li, Q. Peng, Perylene Diimide-Based Nonfullerene Polymer Solar Cells with over 11% Efficiency Fabricated by Smart Molecular Design and Supramolecular Morphology Optimization, *Adv. Funct. Mater.* **2019**, *29*, 1906587.

[142] M. Wu, P. Xia, H. Huang, Z. Lin, X. You, K. Wang, H. Lu, D. Wu, J. Xia, p-Extension improves the photovoltaic performance: a helical perylene diimide oligomer based three-dimensional non-fullerene acceptor, *Mater. Chem. Front.* **2019**, *3*, 2414-2420.

[143] F. Tang, K. Wu, Z. Zhou, G. Wang, B. Zhao, S. Tan, Alkynyl-Functionalized Pyrene-Cored Perylene Diimide Electron Acceptors for Efficient Nonfullerene Organic Solar Cells, *ACS Appl. Energy Mater.* **2019**, *2*, 3918-3926.

[144] J. Zhang, Y. Li, J. Huang, H. Hu, G. Zhang, T. Ma, P. C. Y. Chow, H. Ade, D. Pan, H. Yan, Ring-Fusion of Perylene Diimide Acceptor Enabling Efficient Nonfullerene Organic Solar Cells with a Small Voltage Loss, *J. Am. Chem. Soc.* **2017**, *139*, 16092-16095.

[145] Q. Wu, D. Zhao, A. M. Schneider, W. Chen, L. Yu, Covalently Bound Clusters of Alpha-Substituted PDI-Rival Electron Acceptors to Fullerene for Organic Solar Cells, *J. Am. Chem. Soc.* **2016**, *138*, 7248-7251.

[146] K. Ding, Y. Wang, T. Shan, J. Xu, Q. Bao, F. Liu, H. Zhong, Propeller-like acceptors with difluoride perylene diimides for organic solar cells, *Org. Electron.* **2020**, *78*, 105569.

[147] Y. Zhang, Y. Xiao, Y. Xie, L. Zhu, D. Shi, C. Cheng, Fluorene-centered perylene monoimides as potential non-fullerene acceptor in organic solar cells, *Org. Electron.* **2015**, *21*, 184-191.

[148] R. Qin, D. Guo, T. Y. Gopalakrishna, G. Li, J. Yang, Y. Jiang, One step to perylene monoimides and derived alkynyl bridged photovoltaic acceptors, *Dyes Pigments* **2019**, *160*, 540-545.

[149] Z. Li, C.-C. Chueh, A. K.-Y. Jen, Recent Advances in Molecular Design of Functional Conjugated Polymers for High-Performance Polymer Solar Cells, *Prog. Polym. Sci.* **2019**, *99*, 101175.

[150] K. Zhang, R. Xia, B. Fan, X. Liu, Z. Wang, S. Dong, H.-L. Yip, L. Ying, F. Huang, Y. Cao, 11.2% All-Polymer Tandem Solar Cells with Simultaneously Improved Efficiency and Stability, *Adv. Mater.* **2018**, *30*, 1803166.

[151] C. Lee, H. Kang, W. Lee, T. Kim, K.-H. Kim, H. Y. Woo, C. Wang, B. J. Kim, High-Performance All-Polymer Solar Cells Via Side-Chain Engineering of the Polymer Acceptor: The Importance of the Polymer Packing Structure and the Nanoscale Blend Morphology, *Adv. Mater.* **2015**, *27*, 2466-2471.

[152] N. B. Kohle, H. Lee, D. Kuzuhara, N. Yoshimoto, T. Koganezawa, S. A. Jenekhe, All-Polymer Solar Cells with 9.4% Efficiency from Naphthalene Diimide-Biselenophene Copolymer Acceptor, *Chem. Mater.* **2018**, *30*, 6540-6548.

[153] J. Oh, K. Kranthiraja, C. Lee, K. Gunasekar, S. Kim, B. Ma, B. J. Kim, S.-H. Jin, Side-Chain Fluorination: An Effective Approach to Achieving High-Performance All-Polymer Solar Cells with Efficiency Exceeding 7%, *Adv. Mater.* **2016**, *28*, 10016-10023.

[154] X. Zhan, Z. Tan, B. Domercq, Z. An, X. Zhang, S. Barlow, Y. Li, D. Zhu, B. Kippelen, S. R. Marder, A High-Mobility Electron-Transport Polymer with Broad Absorption and Its Use in Field-Effect Transistors and All-Polymer Solar Cells, *J. Am. Chem. Soc.* **2007**, *129*, 7246-7247.

[155] Y. Guo, Y. Li, O. Awartani, J. Zhao, H. Han, H. Ade, D. Zhao, H. Yan, A Vinylene-Bridged Perylenediimide-Based Polymeric Acceptor Enabling Efficient All-Polymer Solar Cells Processed under Ambient Conditions, *Adv. Mater.* **2016**, *28*, 8483-8489.

[156] Y. Guo, Y. Li, O. Awartani, H. Han, J. Zhao, H. Ade, H. Yan, D. Zhao, Improved Performance off All-Polymer Solar Cells Enabled by Naphthodiperylenetetraimide-Based Polymer Acceptor, *Adv. Mater.* **2017**, *29*, 1700309.

[157] Y. Kim, C. E. Song, S.-J. Moon, E. Lim, Rhodanine dye-based small molecule acceptors for organic photovoltaic cells, *Chem. Commun.* **2014**, *50*, 8235-8238.

[158] H. Shi, W. Fu, M. Shi, J. Ling, H. Chen, A solution-processable bipolar diketopyrrolopyrrole molecule used as both electron donor and acceptor for efficient organic solar cells, *J. Mater. Chem. A* **2015**, *3*, 1902-1905.

[159] S. Holliday, R. S. Ashraf, C. B. Nielsen, M. Kirkus, J. A. Röhr, C.-H. Tan, E. Collado-Fregoso, A.-C. Knall, J. R. Durrant, J. Nelson, I. McCulloch, A Rhodanine Flanked Nonfullerene Acceptor for Solution-Processed Organic Photovoltaics, *J. Am. Chem. Soc.* **2015**, *137*, 898-904.

[160] M. Li, Y. Liu, W. Ni, F. Liu, H. Feng, Y. Zhang, T. Liu, H. Zhang, X. Wan, B. Kan, Q. Zhang, T. P. Russell, Y. Chen, A simple small molecule as an acceptor for fullerene-free organic solar cells with efficiency near 8%, *J. Mater. Chem. A* **2016**, *4*, 10409.

[161] Y. Lin, Z.-G. Zhang, H. Bai, J. Wang, Y. Yao, Y. Li, D. Zhu, X. Zhan, High-performance fullerene-free polymer solar cells with 6.31% efficiency, *Energy Environ. Sci.* **2015**, *8*, 610-616.

[162] Y. Lin, J. Wang, Z.-G. Zhang, H. Bai, Y. Li, D. Zhu, X. Zhan, An Electron Acceptor Challenging Fullerenes for Efficient Polymer Solar Cells, *Adv. Mater.* **2015**, *27*, 1170-1174.

[163] S. Dai, T. Li, W. Wang, Y. Xiao, T.-K. Lau, Z. Li, K. Liu, X. Lu, X. Zhan, Enhancing the Performance of Polymer Solar Cells via Core Engineering of NIR-Absorbing Electron Acceptors, *Adv. Mater.* **2018**, *30*, 1706571.

[164] H. Yao, Y. Chen, Y. Qin, R. Yu, Y. Cui, B. Yang, S. Li, K. Zhang, J. Hou, Design and Synthesis of a Low Bandgap Small Molecule Acceptor for Efficient Polymer Solar Cells, *Adv. Mater.* **2016**, *28*, 8283-8287.

[165] Y. Li, L. Zhong, F.-P. Wu, Y. Yuan, H.-J. Bin, Z.-Q. Jiang, Z. Zhang, Z.-G. Zhang, Y. Li, L.-S. Liao, Non-fullerene polymer solar cells based on a selenophene-containing fused-ring acceptor with photovoltaic performance of 8.6%, *Energy Environ. Sci.* **2016**, *9*, 3429-3435.

[166] S. Li, L. Ye, W. Zhao, S. Zhang, S. Mukherjee, H. Ade, J. Hou, Energy-Level Modulation of Small-Molecule Electron Acceptors to Achieve over 12% Efficiency in Polymer Solar Cells, *Adv. Mater.* **2016**, *28*, 9423-9429.

[167] W. Zhao, S. Li, H. Yao, S. Zhang, Y. Zhang, B. Yang, J. Hou, Molecular Optimization Enables over 13% Efficiency in Organic Solar Cells, *J. Am. Chem. Soc.* **2017**, *139*, 7148-7151.

[168] S. Holliday, R. S. Ashraf, A. Wadsworth, D. Baran, S. A. Yousaf, C. B. Nielsen, C.-H. Tan, S. D. Dimitrov, Z. Shang, N. Gasparini, M. Alamoudi, F. Laquai, C. J. Brabec, A. Salleo, J. R. Durrant, I. McCulloch, High-efficiency and air-stable P3HT-based polymer solar cells with a new non-fullerene acceptor, *Nat. Commun.* **2016**, *7*, 11585.

[169] J. Yuan, Y. Zhang, L. Zhou, G. Zhang, H.-L. Yip, T.-K. Lau, X. Lu, C. Zhu, H. Peng, P. A. Johnson, M. Leclerc, Y. Cao, J. Ulanski, Y. Li, Y. Zou, Single-Junction Organic Solar Cell with over 15% Efficiency Using Fused-Ring Acceptor with Electron-Deficient Core, *Joule* **2019**, *3*, 1140-1151.

[170] B. Fan, D. Zhang, M. Li, W. Zhong, Z. Zeng, L. Ying, F. Huang, Y. Cao, Achieving over 16% efficiency for single-junction organic solar cells, *Sci. China Chem.* **2019**, *62*, 746-752.

[171] N. Qiu, H. Zhang, X. Wan, C. Li, X. Ke, H. Feng, B. Kan, H. Zhang, Q. Zhang, Y. Lu, Y. Chen, A New Nonfullerene Electron Acceptor with a Ladder Type Backbone for High-Performance Organic Solar Cells, *Adv. Mater.* **2017**, *29*, 1604964.

[172] T.-W. Chen, K.-L. Peng, Y.-W. Lin, Y.-J. Su, K.-J. Ma, L. Hong, C.-C. Chang, J. Hou, C.-S. Hsu, A chlorinated nonacyclic carbazole-based acceptor affords over 15% efficiency in organic solar cells, *J. Mater. Chem. A* **2020**, *8*, 1131-1137.

[173] H. Lin, S. Chen, Z. Li, J. Y. L. Lai, G. Yang, T. McAfee, K. Jiang, Y. Li, Y. Liu, H. Hu, J. Zhao, W. Ma, H. Ade, H. Yan, High- Performance Non- Fullerene Polymer Solar Cells Based on a Pair of Donor–Acceptor Materials with Complementary Absorption Properties, *Adv. Mater.* **2015**, *27*, 7299-7304.

[174] Y. Xie, W. Wang, W. Huang, F. Lin, F. Li, S. Liu, X. Zhan, Y. Liang, C. Gao, H. Wu, Y. Cao, Assessing the energy offset at the electron donor/acceptor interface in organic solar cells through radiative efficiency measurements, *Energy Environ. Sci.* **2019**, *12*, 3556-3566.

[175] D. Baran, R. S. Ashraf, D. A. Hanifi, M. Abdelsamie, N. Gasparini, J. A. Röhr, S. Holliday, A. Wadsworth, S. Lockett, M. Neophytou, C. J. M. Emmott, J. Nelson, C. J. Brabec, A. Amassian, A. Salleo, T. Kirchartz, J. R. Durrant, I. McCulloch, Reducing the efficiency–stability–cost gap of organic photovoltaics with highly efficient and stable small molecule acceptor ternary solar cells, *Nat. Mater.* **2017**, *16*, 363-369.

[176] A. Wadsworth, R. S. Ashraf, M. Abdelsamie, S. Pont, M. Little, M. Moser, Z. Hamid, M. Neophytou, W. Zhang, A. Amassian, J. R. Durrant, D. Baran, I. McCulloch, Highly Efficient and Reproducible Nonfullerene Solar Cells from Hydrocarbon Solvents, *ACS Energy Lett.* **2017**, *2*, 1494-1500.

[177] Z. Zheng, O. M. Awartani, B. Gautam, D. Liu, Y. Qin, W. Li, A. Bataller, K. Gundogdu, H. Ade, J. Hou, Efficient Charge Transfer and Fine-Tuned Energy Level Alignment in a THF-Processed Fullerene-Free Organic Solar Cell with 11.3% Efficiency, *Adv. Mater.* **2017**, *29*, 1604241.

[178] Y. Lin, F. Zhao, Q. He, L. Huo, Y. Wu, T. C. Parker, W. Ma, Y. Sun, C. Wang, D. Zhu, A. J. Heeger, S. R. Marder, X. Zhan, High-Performance Electron Acceptor with Thienyl Side Chains for Organic Photovoltaics, *J. Am. Chem. Soc.* **2016**, *138*, 4955-4961.

[179] Z. Li, K. Jiang, G. Yang, J. Y. L. Lai, T. Ma, J. Zhao, W. Ma, H. Yan, Donor polymer design enables efficient non-fullerene organic solar cells, *Nat. Comm.* **2016**, *7*, 13094.

[180] C.-Y. Liao, Y. Chen, C.-C. Lee, G. Wang, N.-W. Teng, C.-H. Lee, W.-L. Li, Y.-K. Chen, C.-H. Li, H.-L. Ho, P. H.-S. Tan, B. Wang, Y.-C. Huang, R. M. Young, M. R. Wasielewski, T. J. Marks, Y.-M. Chang, A. Facchetti, Processing Strategies for an Organic Photovoltaic Module with over 10% Efficiency, *Joule* **2020**, *4*, 189-206.

[181] H. Zhang, H. Yao, J. Hou, J. Zhu, J. Zhang, W. Li, R. Yu, B. Gao, S. Zhang, J. Hou, Over 14% Efficiency in Organic Solar Cells Enabled by Chlorinated Nonfullerene Small-Molecule Acceptors, *Adv. Mater.* **2018**, *30*, 1800613.

[182] Y. Wu, Y. Zheng, H. Yang, C. Sun, Y. Dong, C. Cui, H. Yan, Y. Li, Rationally pairing photoactive materials for high-performance polymer solar cells with efficiency of 16.53%, *Sci. China Chem.* **2020**, *63*, 265-271.

[183] J. Ge, L. Xie, R. Peng, B. Fanady, J. Huang, W. Song, T. Yan, W. Zhang, Z. Ge, 13.34%Efficiency Non-Fullerene All-Small-Molecule Organic Solar Cells Enabled by Modulating the Crystallinity of Donors via a Fluorination Strategy, *Angew. Chem. Int. Ed.* **2020**, *59*, 2808-2815.

[184] Y. Cui, H. Yao, J. Zhang, T. Zhang, Y. Wang, L. Hong, K. Xian, B. Xu, S. Zhang, J. Peng, Z. Wei, F. Gao, J. Hou, Over 16% efficiency organic photovoltaic cells enabled by a chlorinated acceptor with increased open-circuit voltages, *Nat. Comm.* **2019**, *10*, 2515.

[185] G. Xie, Z. Zhang, Z. Su, X. Zhang, J. Zhang, 16.5% efficiency ternary organic photovoltaics with two polymer donors by optimizing molecular arrangement and phase separation, *Nano Energy* **2020**, *69*, 104447.

[186] Y. Wang, C. Zhuang, Y. Fang, H. D. Kim, H. Yu, B. Wang, H. Ohkita, Improvement of Exciton Collection and Light-Harvesting Range in Ternary Blend Polymer Solar Cells Based on Two Non-Fullerene Acceptors, *Nanomaterials* **2020**, *10*, 241.

Chapter III

Influence of the Iodide to Bromide Ratio on Crystallographic and Optoelectronic Properties of Rubidium Antimony Halide Perovskites

This chapter has been published in:

S. Weber, T. Rath, K. Fellner, R. Fischer, R. Resel, B. Kunert, T. Dimopoulos, A. Steinegger, G. Trimmel, *ACS Appl. Energy Mater.* **2019***, 2*, 539-547.

Abstract

Rubidium antimony halides are a promising low toxic alternative to organo-lead halide perovskites as photovoltaic material. In this contribution we systematically investigate the influence of varying the bromide to iodide ratio on the structural, optical and photovoltaic properties of $Rb_3Sb_2Br_{9-x}I_x$ (x = 0 – 9). Single crystal data reveal that all compounds crystallize in a 2D-layered monoclinic crystal structure. Sequential substitution of iodide with the smaller bromide does not change the crystal system; however, increasing the bromide content results in a shrinkage of the unit cell as well as in a blue shift of the absorption onset, increasing the band gap from 2.02 eV to 2.46 eV. Whereas the photovoltaic properties of bromide rich compounds are limited due to a preferential orientation of the layered structure parallel to the substrate, which is detrimental to charge transport, solar cells with $Rb_3Sb_2I_9$ as absorber material display power conversion efficiencies of 1.37%. Moreover, the devices exhibit low hysteresis properties and are stable for more than 150 days stored under inert atmosphere.

Introduction

Metal halide perovskites are the latest development in photovoltaic materials. They have been shown to provide impressive power conversion efficiencies (PCEs) up to 23.3%[1–3] and are already in a similar range as the PCEs of silicon, CdTe, or CIGS thin film solar cells;[1,2] however, metal halide perovskites can be prepared very energy-efficiently, either via solution-based routes or by vapor deposition processes.

Because of toxicity issues with lead halide perovskites, which are the so far best performing compounds in this material class, there is now growing endeavor to study lead-free perovskite materials with regard to their photovoltaic and optoelectronic properties.[4–13] Among lead-free perovskites, tin perovskites are the most thoroughly studied materials to date, and remarkable PCE values up to 9% have been reported recently.[14,15]

However, tin halide perovskites also suffer from limited stability in ambient conditions due to the oxidation of Sn^{2+} to Sn^{4+}. Perovskites containing elements like Bi and Sb with a stable 3+ oxidation state were found to be significantly more stable than lead or tin halide perovskites. Bismuth halide perovskites have already been studied in detail in past years, and PCEs of up to

1.09% with a pure bismuth perovskite ($Cs_3Bi_2I_9$)[16] and 2.4% with the mixed silver−bismuth perovskite $Cs_2AgBiBr_6$[17] were obtained.

Compared to the research effort devoted to bismuth halide perovskites, antimony halide perovskites are so far much less investigated and the first paper reporting on antimony perovskite-based solar cells was published in 2016.[18] Computational calculations for the optoelectronic properties of antimony perovskites predict promising band gaps for $Rb_3Sb_2I_9$ and $Rb_3Sb_2Br_9$.[19] Moreover, as shown by Baranwal et al.,[20] both common device architectures (n−i−p and p−i− n) can be applied for antimony-based perovskites. To date, encouraging efficiencies of up to 2.77% have been reported recently for solar cells with a $MA_3Sb_2I_9$ absorber layer (MA: methylammonium).[21,22] A mixed sulfur/iodide antimony perovskite even led to a PCE of approximately 3%.[23,24] In recent studies on antimony halide perovskites, materials with different dimensionality (0D and 2D) have been synthesized and discussed. For example, for $Cs_3Sb_2I_9$, it has been shown that the formed structure and dimensionality are strongly dependent on the conditions during synthesis. Solution-based synthesis primarily leads to 0D structures, while preferably 2D-layered structures were obtained by solid-state or gas phase syntheses.[25] The change in dimensionality also has a significant impact on the optical and electronic properties of these materials. Typically, the absorption spectra are blue-shifted for 0D compared to 2D perovskites, and charge carrier mobilities are lower in 0D antimony halide perovskites. Furthermore, the dimensionality can be tuned by compositional engineering. Upon a change from Cs to Rb in the $Cs_3Sb_2I_9$ perovskites, the formation of 2D-layered perovskites is facilitated due to the smaller ionic radius of Rb.[26] In contrast to that, when organic cations like methylammonium (MA) are introduced, the formation of a 0D dimer structure is very likely.[27,28]

However, the opinions in the literature regarding the influence of the dimensionality of the antimony halide perovskites on the solar cell performances are not fully consistent, and this topic is not yet entirely understood. While several reports claim that the dimer structure limits the efficiency of the solar cells,[29] Boopathi et al.[21] obtained PCEs of 2.04% with a zero-dimensional $MA_3Sb_2I_9$ absorber layer. Moreover, the absorption properties of the antimony halide perovskites as well as partly the dimensionality can be tuned by varying the X-site anions, which was already shown for $MA_3Sb_2(I,Cl)_9$ or $(NH_4)_3Sb_2(I,Br)_9$ perovskite materials.[28,30] Hereby, bromide substitution resulted in a blue shift leading to higher band gaps and reduced photovoltaic performance. Also, the energy difference between the 0D dimer and 2D-layered phase was reported to be lower for bromide incorporation compared to chloride incorporation.[28,30] Jiang et

al. predicted the formation of a 2D-layered structure when introducing chloride to cesium antimony perovskites by energy calculations and have successfully proven the formation of a 2D film with $MA_3Sb_2I_{9-x}Cl_x$ perovskites.[28]

In this study, we systematically studied mixed rubidium antimony halide perovskites with the nominal composition ($Rb_3Sb_2Br_{9-x}I_x$) (x = 0 – 9) and investigated their crystallographic and optoelectronic properties. Moreover, the morphological properties of thin films were determined and their photovoltaic performance was thoroughly investigated.

Experimental Section

Materials

All chemicals and solvents were used as purchased without further purification unless otherwise noted. The solvents dimethylformamide (DMF), toluene and chlorobenzene (CB) were dried using molecular sieves (Carl Roth, 3Å type 562 C). Antimony iodide, antimony bromide and rubidium bromide were purchased from abcr and toluene from Carl Roth, TiO_2 nanoparticle paste (30NR-D) was purchased from Greatcell Solar and gold (purity > 99.99%) from Ögussa. All the other chemicals were purchased from Sigma Aldrich.

Caution! In the below described procedures, hazardous chemicals and solvents are used {(DMF, chlorobenzene, toluene, SbI_3, $SbBr_3$ titanium (IV) isopropoxide, ethanolamine, 4-tert-butylpyridine, 2-methoxyethanol, terpineol, lithium bis(trifluoromethanesulfonyl)imide (LiTSFI), tris(2-(1H-pyrazol-1-yl)-4-tert-butylpyridine)cobalt(III) tri[bis(trifluoromethane)sulfo nimide] (FK 209 Co (III) TFSI salt)}. Precautions have to be taken. All reactions must be undertaken under a fume hood or glove box, and protection clothing must be used.

Single Crystal Growth

Perovskite precursor solutions (0.2 M) were prepared by dissolving corresponding amounts of SbI_3, $SbBr_3$, RbI, and RbBr in DMF in a Sb:Rb molar ratio of 2:3 and a Br:I molar ratio necessary to obtain the respective perovskites ($Rb_3Sb_2Br_{9-x}I_x$, denoted as PX-(9-x):x from PX-0-9 to PX-9-0 according to the Br:I ratio in the precursor solution, e.g., PX-2-7 corresponds to a Br:I ratio of 2:7). The precursor solutions were stirred for 2 h at 70 °C under a nitrogen atmosphere, followed by filtration through a 0.45 μm PTFE filter. Single crystals were grown by an antisolvent vapor diffusion crystallization method by evaporation of the antisolvent (dichloromethane or

chloroform) and condensation into the perovskite precursor solution, followed by slow precipitation of single crystals after several days.

Thin Film and Solar Cell Fabrication

Patterned glass/ITO substrates (15 × 15 × 1.1 mm^3) (15 Ω/sq) from Luminescence Technology Corp. were precleaned with acetone, put in an isopropyl alcohol bath, and placed into an ultrasonic bath at 40 °C for 30 min. The substrates were then dried with N_2 and further plasma etched for 3 min. For the preparation of the crystalline TiO_2-layer (c-TiO_2, thickness approximately 30 nm), a solution containing titanium (IV) isopropoxide (70 µL), ethanolamine (55 µL), and 2-methoxyethanol (1 mL) was spin coated on the precleaned glass/ITO substrates at 4000 rpm for 20 s followed by an annealing step at 500 °C for 30 min in a tube furnace. For the preparation of the mesoporous TiO_2-layer (mp-TiO_2, thickness approximately 250 nm), the TiO_2-nanoparticle paste was mixed with terpineol (1:2.5 wt %) and spin coated at 10 000 rpm for 20 s followed by a first annealing step at 200 °C for 5 min and a second annealing at 500 °C for 30 min in a tube furnace. Preparation of the antimony perovskite precursor solutions was performed as described above in the Single Crystal Growth section. The precursor solutions were spin coated on the glass/ITO/c-TiO_2/ mp-TiO_2 substrates at 4000 rpm for 60 s. A 50 µL portion of a SbI_3/ $SbBr_3$ (10 mg/mL) solution in toluene was dropped onto the spinning substrate 5 s after the start of the spinning process followed by antisolvent dripping (toluene) after 30 s, analogous to the process in the paper of Harikesh et al.[26] The perovskite films were annealed at 120 °C for 10 min. All steps were carried out inside a glovebox under nitrogen atmosphere.

The spiro-OMeTAD hole transport layer was prepared by dissolving 2,2′,7,7′-tetrakis[N,N-di(4-methoxyphenyl)amino]-9,9′- spirobifluorene (86 mg) (spiro-OMeTAD), 4-tert-butylpyridine (6.7 µL), FK 209 Co(III) TFSI salt (3.0 mg), and LiTSFI (10 mg) in chlorobenzene (1 mL). The solution was stirred overnight at room temperature under nitrogen atmosphere and spin coated onto the perovskite film at 4000 rpm for 20 s. Afterwards, the top electrode (80 nm Au) was deposited by thermal evaporation under high vacuum conditions (<1x10-5 mbar) using a shadow mask (active area of 0.09 cm^2).

Characterization

Suitable single crystals of compounds were immersed in silicone oil, mounted using a glass fiber, and frozen in the cold nitrogen stream (100 K). X-ray diffraction data were collected at low

temperature on a Bruker Kappa APEX II diffractometer using Mo Kα radiation (λ = 0.71073 Å) generated by an INCOATEC microfocus source. The data reduction and absorption correction were performed with the Bruker SMART[31] and Bruker SADABS,[32] respectively. The structures were solved with SHELXT[33] by Patterson methods and refined with SHELXL[34] by least-squares minimization against F^2 using first isotropic and later anisotropic thermal parameters for all atoms. Mixed perovskites $Rb_3Sb_2Br_{9-x}I_x$ were treated as occupational disorder;[35] for details, see the description in the Supporting Information (SI). The space group assignments and structural solutions were evaluated using PLATON.[36,37] For the graphical representation of the obtained crystal structures, Vesta[38] was employed.

The $Rb_3Sb_2Br_{9-x}I_x$ perovskite thin films were characterized by X-ray diffraction (XRD) with a PANalytical Empyrean system, which uses Cu Kα radiation. UV-Vis measurements of the perovskites were performed using a PerkinElmer Lambda 35 UV−vis spectrometer equipped with an integrating sphere. The optical data were recorded in the wavelength range 350−1000 nm. Photoluminescence spectra were measured in ambient atmosphere on a FluoroLog 3 spectrofluorometer from Horiba Scientific equipped with an NIR-sensitive R2658 photomultiplier from Hamamatsu (300−1050 nm).

Top view SEM images of the $Rb_3Sb_2Br_{9-x}I_x$ perovskites on glass/ITO/c-TiO_2/mp-TiO_2 were acquired on a Zeiss- Supra 40 scanning electron microscope with an in-lens detector and 5 kV acceleration voltage.

J-V curves of all devices were recorded inside a glove box (nitrogen atmosphere) with a scan rate of 100 mV/s using a Keithley 2400 source meter connected to a LabView-based software. Illumination (100 mW/cm^2) was provided by a Dedolight DLH400 lamp, calibrated using a monocrystalline silicon WPVS reference solar cell Fraunhofer ISE. External quantum efficiency (EQE) measurements were acquired in inert atmosphere using a MuLTImode 4-AT monochromator (Amko) equipped with a 75 W xenon lamp (LPS 210-U, Amko), a lock-in amplifier (Stanford Research Systems, Model SR830), and a Keithley 2400 source meter. The monochromatic light was chopped at a frequency of 30 Hz and constant background illumination was provided by white light LEDs. The EQE spectra were measured in the wavelength range of 380−1000 nm (increment: 10 nm). The measurement setup was spectrally calibrated with a silicon photodiode (Newport Corporation, 818-UV/DB).

Results and Discussion

Single Crystal Analysis

Rubidium antimony halide perovskite single crystals ($Rb_3Sb_2Br_{9-x}I_x$) with different iodide/bromide ratios (denoted as PX-(9-x):x from PX-0-9 to PX-9-0 according to the Br:I ratio in the precursor solution) were prepared by a vapor diffusion crystallization technique with either dichloromethane or chloroform as antisolvent from perovskite precursor solutions as described in the Experimental Section. Invariably with constitution, all samples crystallized in the monoclinic space group $P2_1/n$ and cell parameters for $Rb_3Sb_2I_9$ (PX-0-9) and $Rb_3Sb_2Br_9$ (PX-9-0) prepared by the above stated protocol match literature data.[39] The Br/I ratio of the mixed samples $Rb_3Sb_2Br_{9-x}I_x$ was determined by refinement of the mixed occupancies against the diffraction data; for details see Supporting Information. In agreement with Vegard's law,[40-42] the thus obtained Br/I ratios show strictly linear correlation with the cell axes and hence unit cell volume. Crystallographic parameters are summarized in Table 1. Plotting the lattice constants a, b and c as a function of the iodide content shows a linear correlation. The BX_6 octahedra size decreases constantly with increasing bromide content (Figure 1A). Also, the overall cell volume decreases (Figure 1B). In this context, it should also be noted that for some compositions, the bromide/iodide-ratio in the single crystals displays a deviation of up to 12% from its expected composition based on the chemical composition of the precursor solution, as given in Table 1. The highest deviations were observed for the samples PX-4-5, PX-3-6 and PX-2-7. In these samples, in addition to the perovskite single crystals also colorless cubic RbBr crystals were found in small amounts.

Generally, a 3D structure leads to high electronic dimensionality of the perovskite absorber material, which is beneficial for good photovoltaic performance. However, in some perovskites (e.g., tin perovskites)[14] promising solar cell properties were found with 2D or mixed 2D/3D structures. Also, for antimony perovskites, the dimensionality is an important factor regarding the performance in solar cells and has already been discussed in the literature. Harikesh et al. investigated $Rb_3Sb_2I_9$ for the first time in solar cells and described the perovskite as a 2D-layered structure using a solution processed deposition technique.[26] Recently, CorreaBaena et al. also described $Rb_3Sb_2I_9$ as a 2D material.[43] This is also in accordance with our data for $Rb_3Sb_2I_9$ (Figure 1C), and there is no visible change in dimensionality in all mixed halide compounds as well as in $Rb_3Sb_2Br_9$ (Figure S1).

Table 1: Crystallographic data of $Rb_3Sb_2Br_{9-x}I_x$ single crystals.

Sample	**PX-0-9**	**PX-1-8**	**PX-2-7**	**PX-3-6**	**PX-4-5**	**PX-5-4**	**PX-6-3**	**PX-7-2**	**PX-8-1**	**PX-9-0**
Actual formula	$Rb_3Sb_2I_9$	$Rb_3Sb_2Br_{0.75}I_{8.25}$	$Rb_3Sb_2Br_{1.67}I_{7.33}$	$Rb_3Sb_2Br_{2.28}I_{6.72}$	$Rb_3Sb_2Br_{3.35}I_{5.65}$	$Rb_3Sb_2Br_{5.06}I_{3.94}$	$Rb_3Sb_2Br_{5.57}I_{3.43}$	$Rb_3Sb_2Br_{7.22}I_{1.78}$	$Rb_3Sb_2Br_{7.7}I_{1.3}$	$Rb_3Sb_2Br_9$
Space group	P 2_1/n (14)	P 2_1/n (14)	P 2_1/n (14)	P 2_1/n (14)	P 2_1/n (14)	P 2_1/n (14)	P 2_1/n (14)	P 2_1/n (14)	P 2_1/n (14)	P 2_1/n (14)
a [Å]	14.4899	14.4345	14.3122	14.2430	14.1036	13.9281	13.8815	13.7382	13.6522	13.5645
b [Å]	8.0589	8.0571	8.0326	8.0094	7.9652	7.8762	7.8442	7.7600	7.6948	7.6250
c [Å]	20.5787	20.4408	20.2651	20.1205	19.9187	19.6307	19.5972	19.368	19.308	19.186
α [°]	90	90	90	90	90	90	90	90	90	90
β [°]	90.218	90.424	90.390	90.381	90.375	90.237	90.127	90.314	90.214	90.209
γ [°]	90	90	90	90	90	90	90	90	90	90
Volume [$Å^3$]	2403.01	2377.2	2329.71	2295.25	2237.58	2153.48	2133.96	2064.76	2028.31	1984.38
Formula weight	1642.01	1606.85	1563.49	1534.98	1484.64	1402.97	1380.48	1302.92	1280.41	1219.10
Z	4	4	4	4	4	4	4	4	4	4
Temperature (K)	100	100	100	100	100	100	100	100	100	100
R-Factor (%)	4.16	4.18	4.44	4.10	8.43	5.42	8.62	9.41	6.16	9.74

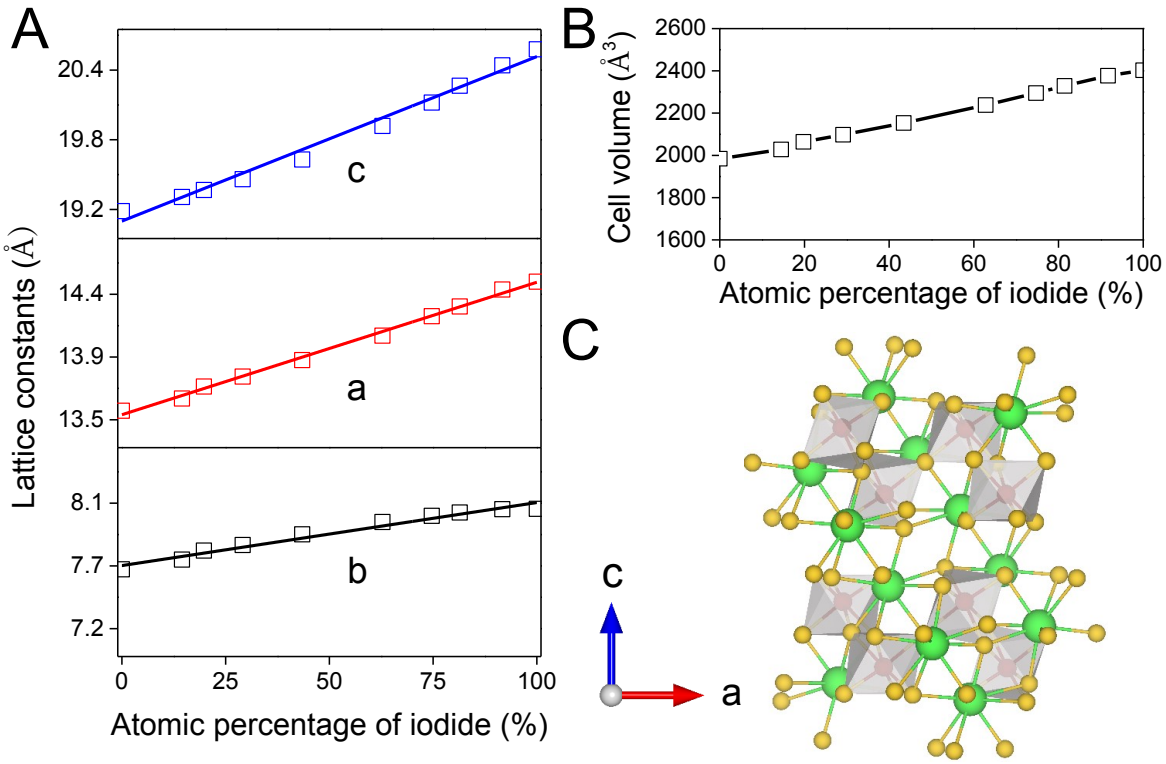

Figure 1: (A, B) Lattice constants and cell volume of $Rb_3Sb_2Br_{9-x}I_x$ plotted as a function of the iodide content, (C) crystal structure of $Rb_3Sb_2I_9$ showing a 2D structure (red: Sb, green: Rb, yellow: I).

Thin film analysis

In a next step, thin films of the Rb3Sb2Br9−xIx perovskites were deposited on glass substrates using spin coating. The perovskite deposition was enhanced by a two-step antisolvent treatment, already reported in the literature.[18,26] In a first step, a solution of antimony iodide/ bromide in toluene (10 mg/mL) was dropped onto the substrate after 5 s of spinning time to reduce the number of iodine and bromine vacancies.[26] After 30 s of spinning, toluene was dripped on the spinning substrate to expedite the perovskite precipitation.

X-ray diffraction measurements of the perovskite thin films revealed a clear influence of the introduction of bromide in $Rb_3Sb_2I_9$ (Figure 2). As already discussed above, the introduction of bromide into the perovskite crystal structure causes the unit cell to compress. In the XRD measurements of the thin films, this is observable by the shift of the diffraction peaks to higher diffraction angles (compare the two reference diffraction patterns of $Rb_3Sb_2I_9$ to $Rb_3Sb_2Br_9$).

Additionally, the diffraction patterns reveal that the preferential orientation of the perovskite crystallites is changing from $Rb_3Sb_2I_9$ to $Rb_3Sb_2Br_9$. While the $Rb_3Sb_2I_9$ thin film almost shows no preferential orientation and the measured pattern matches well with the reference pattern,[44] the $Rb_3Sb_2Br_9$ layer crystallizes in a preferred orientation of the (001) plane parallel to the substrate surface indicated by the significantly increased intensity of the diffraction peaks at 18.5° and 27.0° 2θ corresponding to the (004) and (006) plane, respectively. In Figure S2, the hkl-values for the thin film patterns of $Rb_3Sb_2I_9$ and $Rb_3Sb_2Br_9$ are given. No RbBr or RbI secondary phases were found in the XRD patterns of the thin film samples.

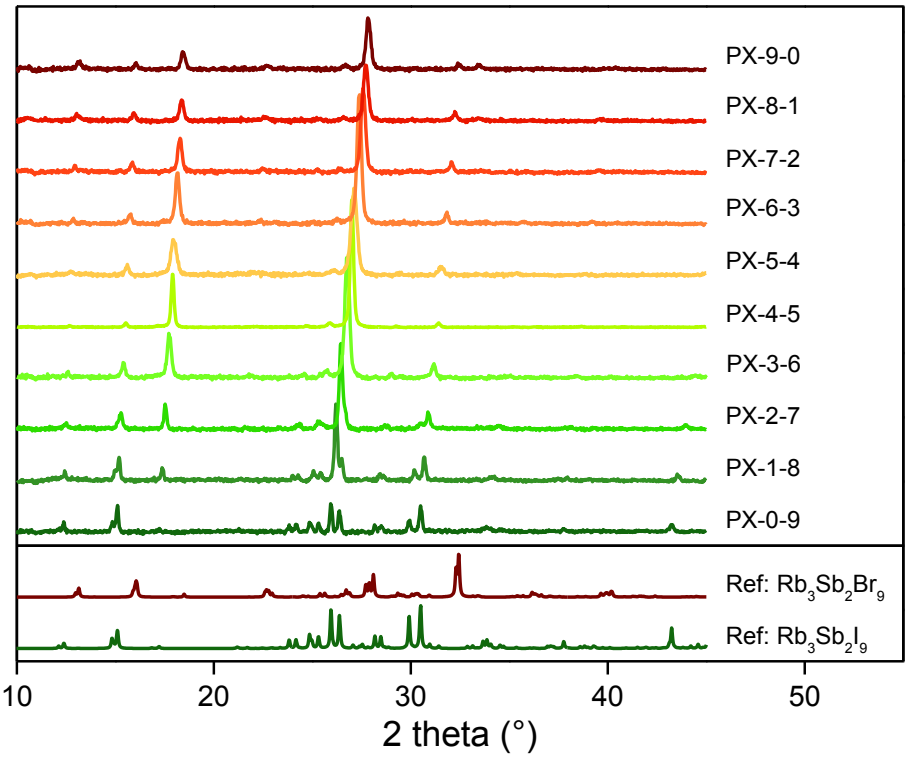

Figure 2: X-ray diffraction patterns of $Rb_3Sb_2Br_{9-x}I_x$ perovskite thin films prepared on glass. The reference patterns were calculated based on the following data from the ICSD database: $Rb_3Sb_2I_9$: ICSD 243727;[44] $Rb_3Sb_2Br_9$: ISCD 431322.[39] The patterns are shifted vertically for better visibility.

To investigate the optical properties of the $Rb_3Sb_2Br_{9-x}I_x$ layers, UV-Vis absorption spectra were recorded and are shown in Figure 3A. $Rb_3Sb_2I_9$ shows an absorption onset at approx. 600 nm. The nature of the band gap is ambiguously described and both, an indirect and a direct band gap are claimed in literature.[26,43] In these studies, it was shown by DFT-calculations that the conduction band edge is rather flat and without any clear minimum, and consequently the energies of indirect

and direct transitions are very similar. Using the Tauc-plot we determined an indirect band gap of 2.02 eV and a first direct transition of 2.24 eV (see Figure S3). By substitution of $Rb_3Sb_2I_9$ towards $Rb_3Sb_2Br_9$, a blue shift of the absorption onset can be recognized. The absorption onset of the $Rb_3Sb_2Br_9$ film is approx. 460 nm and the Tauc plot reveals an indirect band gap of 2.46 eV and a direct band transition of 2.76 eV. The results of the band gap determinations for all mixed compounds can be found in the supporting information (see Figure S3). Similar to the lattice constants and the cell volume, also for the optical band gaps, a linear correlation with respect to the Br/I ratio is found (see Figure S4). The absorption coefficients for $Rb_3Sb_2I_9$ (1.8×10^5 cm^{-1}) and $Rb_3Sb_2Br_9$ (1.2×10^5 cm^{-1}) at 400 nm are comparable to the absorption coefficients of lead perovskites, e.g. methylammonium lead iodide (5.7×10^4 cm^{-1}).[45] The observed blue shift with increasing bromide content in $Rb_3Sb_2Br_{9-x}I_x$ was also found for the analogue ammonium compounds.[30] In contrast to that, a redshift is observed during chloride substitution in ($Rb_3Sb_2I_{9-x}Cl_x$) compounds caused by a change from a 0D dimer towards a 2D layered structure.[28] However, in our case we observe a 2D structure for all compounds.

Moreover, an absorption spectrum of a $Rb_3Sb_2I_9$ perovskite thin film was measured after an ageing time of 18 h in ambient atmosphere (see Figure S5). There is no visible change in absorption behavior, indicating a good stability of Sb-perovskite materials in ambient conditions. Furthermore, the photoluminescence (PL) spectra of the $Rb_3Sb_2Br_{9-x}I_x$ perovskite thin films are depicted in Figure 3B. The emission maximum is shifting from 639 nm for $Rb_3Sb_2I_9$ to 525 nm for $Rb_3Sb_2Br_9$, which matches well with the shift of the band gap to higher energies with increasing Br-content. The peak maximum of the $Rb_3Sb_2I_9$ film is in good agreement with the PL data reported by Correa-Baena et al. (635 nm).[43] The intensity of the photoemission, which was measured at room temperature, is relatively low for the investigated perovskite samples, which is also in line with reported data in literature for $Rb_3Sb_2I_9$.[43] However, it is observed that the photoemission is significantly more intense for the samples with high I-contents, especially the pure iodide compound $Rb_3Sb_2I_9$ and the PX-1-8 sample. It strongly decreases towards parity of I and Br and increases again towards the pure bromide compound. However, the intensity of the pure $Rb_3Sb_2Br_9$ is far lower than for the pure iodide analogue. It is also interesting to note that the emission of the $Rb_3Sb_2Br_9$ is much narrower compared to the pure iodide analogue. We suspect that this effect is related to the higher orientation in the $Rb_3Sb_2Br_9$ thin films. Moreover, PL

spectra of $Rb_3Sb_2Br_{9-x}I_x$ single crystals were recorded, which show a similar trend regarding intensity and the shift of the emission peak as observed in the thin film spectra (see Figure S6).

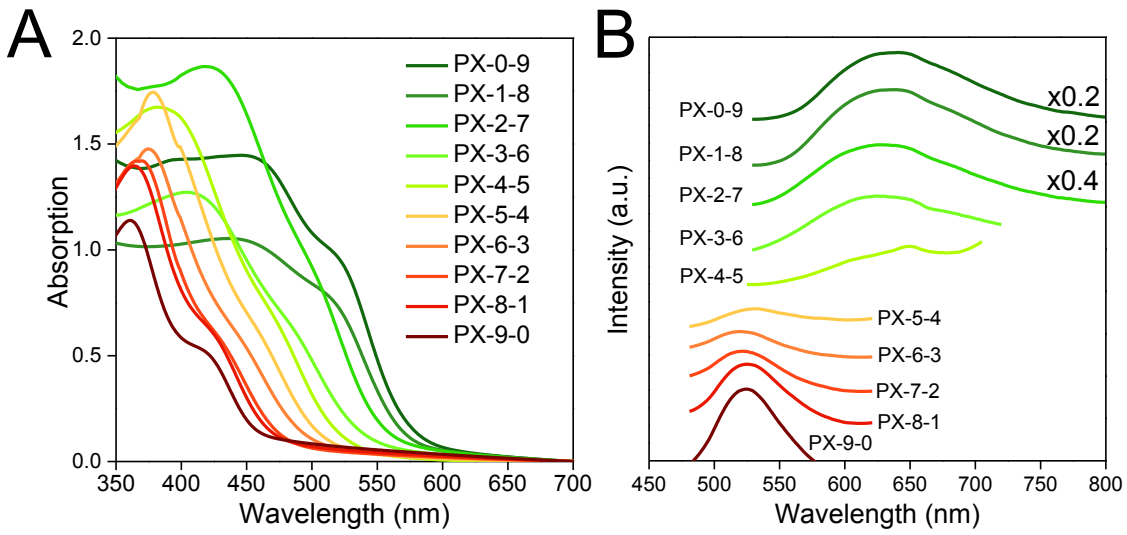

Figure 3: (A) UV-Vis absorption spectra and (B) photoluminescence spectra of $Rb_3Sb_2Br_{9-x}I_x$ perovskite thin films on glass (the PL spectra of the three samples with the highest iodide contents are multiplied by the factor shown in the figure). The excitation wavelengths are given in the SI – Table S1).

In a next step, the film quality of the $Rb_3Sb_2Br_{9-x}I_x$ perovskites on glass/ITO/c-TiO_2/mp-TiO_2 substrates was investigated by scanning electron microscopy (SEM). Although an optimized deposition procedure adopted from Harikesh et al.[26] (including dripping with SbI_3/$SbBr_3$ dissolved in toluene) was used, the perovskites do not form a continuous overlayer on the mp-TiO_2 film and the homogeneity differs for every perovskite (Figure 4). Similar morphologies for antimony halide perovskite thin films have also been reported by other groups.[18,26] In this study, the perovskite sample PX-5-4 (Figure 4F) shows highest coverage of the mp-TiO_2 film. However, in this sample also larger voids are observed compared to the perovskite films of e.g. PX-0-9 to PX-3-6 (Figure 4A-D) and PX-7-2 (Figure 4H), which show similar homogeneity and grain size.

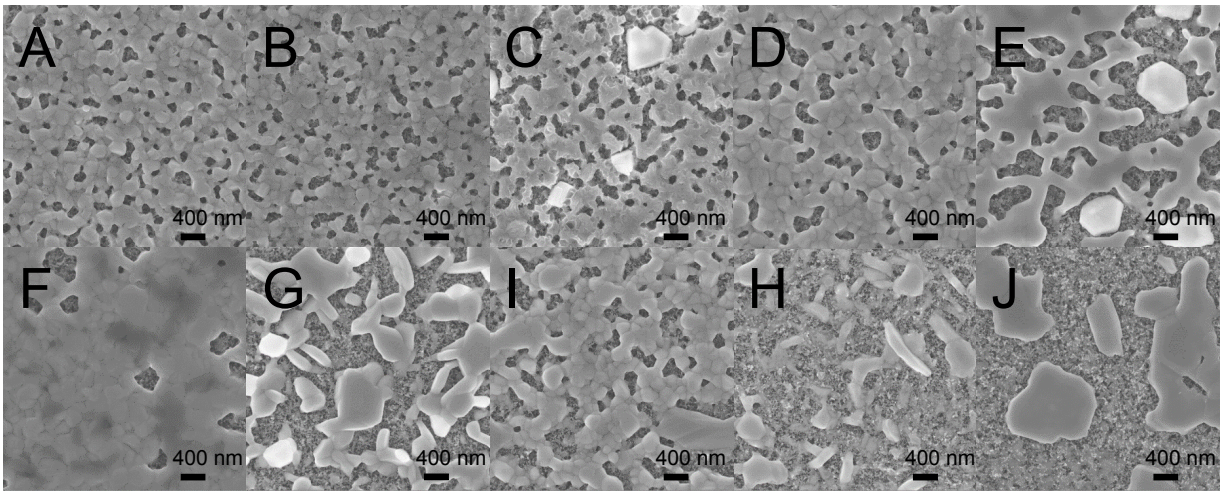

Figure 4: Top-view SEM images of $Rb_3Sb_2Br_{9-x}I_x$ films on mp-TiO_2 layers, PX-0-9 (A), PX-1-8 (B), PX-2-7 (C), PX-3-6 (D), PX-4-5 (E), PX-5-4 (F), PX-6-3 (G), PX-7-2 (H), PX-8-1 (I), PX-9-0 (J).

Solar cell performance

Solar cells with a n-i-p device set up were fabricated having the structure: glass/ITO/c-TiO_2/mp-TiO_2/$Rb_3Sb_2Br_{9-x}I_x$/spiro-OMeTAD/Au. The current-voltage curves (J-V curves) of the best devices, measured after light soaking for 30 minutes, are shown in Figure 5A and the corresponding parameters are summarized in Table 2. A maximum PCE of 1.37% was reached for unmasked solar cells with $Rb_3Sb_2I_9$ (PX-0-9) as absorber showing a V_{OC} of 0.55 V, a J_{SC} of 4.25 mA/cm^2 and a FF of 59.5%. Using a shadow mask, the PCE was slightly reduced to a value of 1.11% caused by a slightly reduced J_{SC} (3.54 mA/cm², for the solar cell characteristics measured with shadow mask, see Table S2). The obtained PCEs for the solar cells with $Rb_3Sb_2I_9$ absorber layer are significantly higher than these reported up to now (~ 0.7%),[26,43] which is mainly based on a higher photocurrent. On the basis of the band gap of 2.03 eV of $Rb_3Sb_2I_9$, a higher V_{OC} would also seem feasible. However, the V_{OC} found here matches with the study by Harikesh et al., in which the loss in V_{OC} was ascribed to defect levels in the perovskite absorber layer.[26] The highest V_{OC} obtained so far for $Rb_3Sb_2I_9$-based solar cells is 0.66 V and was reported by Correa-Baena et al.[43] With increasing bromide content the PCE decreased to 0.01% for $Rb_3Sb_2Br_9$ (PX-9-0). Herein, the current density decreased with increasing bromide content, most likely due to a larger band gap for the bromide-based compounds. In general, this should in turn increase the photovoltage; however, the photovoltage decreased. As discussed above, the increased intensity of the (006) reflection in the XRD-patterns with increasing bromide content revealed a stronger

orientation of the ab-planes, i.e., the connected SbI_6-octaeder containing planes, parallel to the substrate, which is detrimental to an efficient charge transport.

Table 2: Summarized J-V characteristics (best and average) for the $Rb_3Sb_2Br_{9-x}I_x$ perovskite solar cells. For $Rb_3Sb_2I_9$ (PX-0-9)-based solar cells, the best 30 devices and for the other perovskite absorber layers the best 12 solar cells were used for the calculation of the average values and standard deviations, respectively.

		V_{OC} (V)	**J_{SC} (mA/cm^2)**	**FF (%)**	**PCE (%)**
PX-0-9	Best	0.55	4.25	59.5	1.37 (1.11*)
	Average	0.51 ± 0.03	3.80 ± 0.44	55.1 ± 3.8	1.06 ± 0.12
PX-1-8	Best	0.48	3.20	62.1	0.96 (0.81*)
	Average	0.45 ± 0.03	3.34 ± 0.32	59.0 ± 3.3	0.88 ± 0.05
PX-2-7	Best	0.37	2.45	57.6	0.53 (0.44*)
	Average	0.37 ± 0.01	2.42 ± 0.12	56.0 ± 1.5	0.49 ± 0.03
PX-3-6	Best	0.37	0.57	61.2	0.13 (0.10*)
	Average	0.34 ± 0.02	0.50 ± 0.06	56.8 ± 4.6	0.10 ± 0.02
PX-4-5	Best	0.31	0.43	55.1	0.07
	Average	0.28 ± 0.03	0.38 ± 0.06	51.2 ± 3.5	0.05 ± 0.01
PX-5-4	Best	0.29	0.42	51.2	0.06
	Average	0.28 ± 0.02	0.36 ± 0.04	46.2 ± 3.9	0.05 ± 0.01
PX-6-3	Best	0.27	0.23	44.5	0.03
	Average	0.24 ± 0.02	0.17 ± 0.04	43.8 ± 6.2	0.017 ± 0.004
PX-7-2	Best	0.25	0.06	50.0	0.01
	Average	0.27 ± 0.03	0.05 ± 0.01	49.4 ± 4.2	0.007 ± 0.001
PX-8-1	Best	0.31	0.04	46.8	0.01
	Average	0.24 ± 0.05	0.03 ± 0.01	44.2 ± 6.0	0.003 ± 0.001
PX-9-0	Best	0.29	0.05	51.7	0.01
	Average	0.25 ± 0.05	0.05 ± 0.01	49.9 ± 5.9	0.006 ± 0.002

*illumination through a shadow mask (2.65 x 2.65 cm)

An investigation of the hysteresis behavior of the $Rb_3Sb_2Br_{9-x}I_x$ based solar cells by measuring the devices in forward and reverse scan directions with a scan rate of 100 mV/s showed only slight hysteresis for $Rb_3Sb_2I_9$ (PX-0-9), whereas no hysteresis was observed for solar cells prepared with bromide rich perovskite absorber layers (Figure S7). The corresponding J-V parameters are summarized in Table S3. As it is known that in perovskite solar cells scan rates and bias conditions can significantly influence the hysteresis properties,[46−51] we investigated this in more detail for a $Rb_3Sb_2I_9$- based solar cell. The J−V curves measured in forward and backward directions using different scan rates (1000 to 10 mV/s) and bias conditions are shown in Figures S8 and S9 with their characteristic solar cell parameters summarized in Tables S4 and S5. For all these measurements, the solar cells were illuminated through a 2.65 × 2.65 mm^2 shadow mask.

Herein, changing the scan rate reveals no significant change in the overall power conversion efficiency. The V_{OC} decreases 30 mV from a scan rate of 1000 mV/s to 10 mV/s, whereas on the other side the fill factor increases slightly from 54.9 % to 60.8 % (Table S4). However, this change may arise from repeated scanning rather than changing the scan rate. The temporary V_{OC} change recovers after storage in the dark under inert conditions and most likely stem from light soaking during the measurement. There is also no significant change in V_{OC} and J_{SC} (backward and forward scans) when changing the starting voltage closer towards the V_{OC} (Table S5). Only the FF increases slightly for the forward as well as the backward scan. However, this can be most likely also ascribed to the multiple scans performed on the solar cell, as a repeated measurement using the initial bias conditions also showed an increased FF. In addition, maximum power point (MPP) tracking measurements confirm the PCE values extracted from the J−V curves (see Figure 5B). At the start of the MPP tracking, the PCE was at 1.02%, and after several minutes, it stabilized at 0.94%.

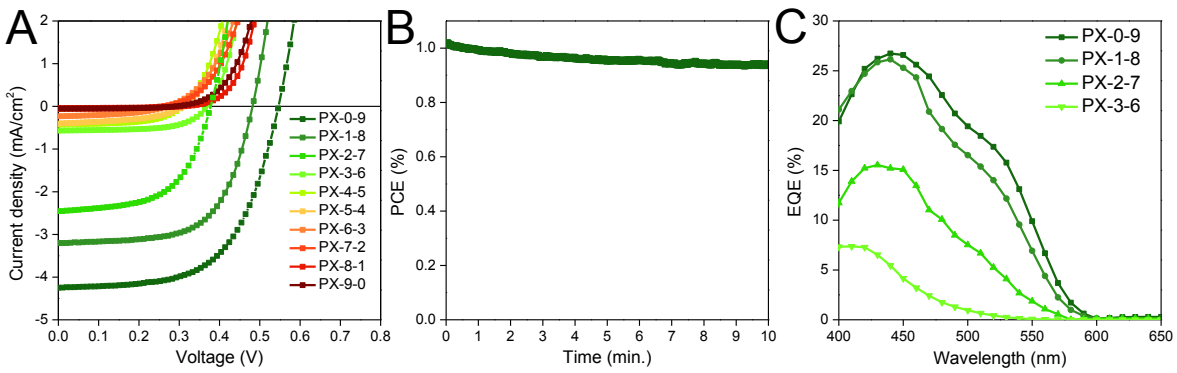

Figure 5: J-V curves of $Rb_3Sb_2Br_{9-x}I_x$-based solar cells measured in backward direction from 1000 mV to 0 mV with a scan rate of 100 mV/s (A), maximum power point tracking measurement of a $Rb_3Sb_2I_9$-based solar cell (B), and EQE spectra of the solar cells prepared with rubidium antimony halide perovskite layers with compositions from $Rb_3Sb_2I_9$ (PX-0-9) to PX-3-6 (C).

The external quantum efficiency (EQE) spectra of the best performing $Rb_3Sb_2Br_{9-x}I_x$ based devices (PX-0-9 to PX-3-6) were measured and the spectra are depicted in Figure 5C. The PX-0-9 based solar cells display highest EQE values of 26.7%, whereas the solar cells based on PX-1-8, PX-2-7 and PX-3-6 absorber layers show maximum EQE values of 26.1%, 16.8% and 7.4%, respectively. The shapes of the EQE spectra are very similar to the absorption spectra of the corresponding perovskite films (cf. Figure 3A) and the increased band gap of the perovskites with increasing Br-content is also reflected in the EQE spectra.

We further investigated the stability of the $Rb_3Sb_2I_9$ based devices under inert conditions (nitrogen atmosphere). The cells were stored in the glovebox in the dark and measured periodically at an illumination of 100 mW/cm^2. After more than 150 days of storage, the devices still exhibit 84% of their initial efficiency (Figure S10). It has to be noted that the V_{OC} as well as FF stay relatively constant over time, whereas the J_{SC} is steadily reduced and therefore responsible for the efficiency loss.

Conclusion

The crystal system of $Rb_3Sb_2Br_{9-x}I_x$ was determined to be monoclinic, showing a P $2_1/n$ space group. Increasing bromide content compresses the BX_6 octahedron, thus reducing the perovskite volume from 2403.01 $Å^3$ to 1984.38 $Å^3$ from $Rb_3Sb_2I_9$ to $Rb_3Sb_2Br_9$. The single crystals reveal a layered structure for all perovskites. In thin films, $Rb_3Sb_2I_9$ shows no preferential orientation. However, increasing the bromide content in the perovskite led to preferential growth alongside the (001) plane. When they are implemented in a n-i-p solar cell structure using TiO_2 as electron transport layer and spiro-OMeTAD as corresponding hole transport layer, a maximum PCE of 1.37% for devices using the perovskite $Rb_3Sb_2I_9$ was recorded. With increasing bromide content, the device efficiency decreased significantly. The higher photovoltaic performance of the antimony perovskite absorber layers with higher iodide/bromide ratio is supported by a red shift of the absorption onset and in addition by less orientation of the layered structure parallel to the substrate surface. Moreover, $Rb_3Sb_2I_9$-based solar cells feature good stability; after more than 150 days, still approx. 85% of the initial PCE values are retained.

Acknowledgements

This work was carried out within the project “Permasol” (FFG No. 848 929) funded by the Austrian Climate and Energy Fund within the program Energy Emission Austria.

References

[1] Green, M. A.; Hishikawa, Y.; Dunlop, E. D.; Levi, D. H.; Hohl-Ebinger, J.; Ho-Baillie, A. W. H. Solar Cell Efficiency Tables (version 51). *Prog. Photovolt: Res. Appl.* **2018**, *26*, 427-436.

[2] Research Cell Record Efficiency Chart, National Renewable Energy Laboratory (NREL), https://www.nrel.gov/pv/, accessed on 14/09/2018.

[3] Yang, W. S.; Noh, J. H.; Jeon, N. J.; Kim, Y. C.; Ryu, S.; Seo, J.; Seok, S. I. High-Performance Photovoltaic Perovskite Layers Fabricated through Intramolecular Exchange. *Science* **2015**, *348*, 1234-1237.

[4] Liang, L.; Gao, P. Lead-Free Hybrid Perovskite Absorbers for Viable Application: Can We Eat the Cake and Have It too? *Adv. Sci.* **2018**, *5*, 1700331.

[5] Giustino, F.; Snaith, H. J. Toward Lead-Free Perovskite Solar Cells. *ACS Energy Lett.* **2016**, *1*, 1233-1240.

[6] Shi, Z.; Guo, J.; Chen, Y.; Li, Q.; Pan, Y.; Zhang, H.; Xia, Y.; Huang, W. Lead-Free Organic-Inorganic Perovskites for Photovoltaic Applications: Recent Advances and Perspectives. *Adv. Mater.* **2017**, *29*, 1605005.

[7] Hoefler, S. F.; Trimmel, G.; Rath, T. Progress on Lead-Free Metal Halide Perovskites for Photovoltaic Applications: a Review. *Monatsh. Chem.* **2017**, *148*, 795-826.

[8] Hu, H.; Dong, B.; Zhang, W. Low-Toxic Metal Halide Perovskites: Opportunities and Future Challenges. *J. Mater. Chem. A* **2017**, *5*, 11436-11449.

[9] Jodlowski, A. D.; Rodríguez-Padrón, D.; Luque, R.; de Miguel, G. Alternative Perovskites for Photovoltaics. *Adv. Energy Mater*. **2018**, *8*, 1703120.

[10] Nakajima, T.; Sawada, K. Discovery of Pb-Free Perovskite Solar Cells via High-Throughput Simulation on the K Computer. *Phys. Chem. Lett.* **2017**, *8*, 4826-4831.

[11] Koliogiorgos, A.; Baskoutas, S.; Galanakis, I. Electronic and Gap Properties of Lead-Free Perfect and Mixed Hybrid Halide Perovskites: An Ab-Initio Study. *Comp. Mater. Sci*. **2017**, *138*, 92-98.

[12] Ono, L. K.; Qi, Y. Research Progress on Organic–Inorganic Halide Perovskite Materials and Solar Cells. *J. Phys. D: Appl. Phys.* **2018**, *51*, 093001.

[13] Chen, H.; Xiang, S.; Li, W.; Liu, H.; Zhu L.; Yang, S. Inorganic Perovskite Solar Cells: A Rapidly Growing Field. *Solar RRL* **2018**, *2*, 1700188.

[14] Shao, S.; Liu, J.; Portale, G.; Fang, H.-H.; Blake, G. R.; ten Brink, G. H.; Koster, L. J. A.; Loi, M. A. Highly Reproducible Sn-Based Hybrid Perovskite Solar Cells with 9% Efficiency. *Adv. Energy Mater.* **2017**, *8*, 1702019.

[15] Zhao, Z.; Gu, F.; Li, Y.; Sun, W.; Ye, S.; Rao, H.; Liu, Z.; Bian, Z.; Huang, C. Mixed-Organic-Cation Tin Iodide for Lead-Free Perovskite Solar Cells with an Efficiency of 8.12%. *Adv. Sci.* **2017**, *4*, 1700204.

[16] Park, B.-W.; Philippe, B.; Zhang, X.; Rensmo, H.; Boschloo, G.; Johansson, E. M. J. Bismuth Based Hybrid Perovskites $A_3Bi_2I_9$ (A: Methylammonium or Cesium) for Solar Cell Application. *Adv. Mater.* **2015**, *27*, 6806-6813.

[17] Greul, E.; Petrus, M. L.; Binek, A.; Docampo, P.; Bein, T. Highly Stable, Phase Pure $Cs_2AgBiBr_6$ Double Perovskite Thin Films for Optoelectronic Applications. *J. Mater. Chem. A* **2017**, *5*, 19972-19981.

[18] Hebig, J.-C.; Kühn, I.; Flohre, J.; Kirchartz, T. Optoelectronic Properties of $(CH_3NH_3)_3Sb_2I_9$ Thin Films for Photovoltaic Applications. *ACS Energy Lett.* **2016**, *1*, 309-314.

[19] Koliogiorgos, A.; Baskoutas, S.; Galanakis, I. Electronic and Gap Properties of Sb and Bi Based Halide Perovskites: An *Ab-Initio* Study. *Comput. Condensed Matter* **2018**, *14*, 161-168.

[20] Baranwal, A. K.; Masutani, H.; Sugita, H.; Kanda, H.; Kanaya, S.; Shibayama, N.; Sanehira, Y.; Ikegami, M.; Numata, Y.; Yamada, K.; Miyasaka, T.; Umeyama, T.; Imahori, H.; Ito, S. Lead-Free Perovskite Solar Cells using Sb and Bi-Based $A_3B_2X_9$ and A_3BX_6 Crystals with Normal and Inverse Cell Structures. *Nano Convergence* **2017**, *4*, 26.

[21] Boopathi, K. M.; Karuppuswamy, P.; Singh, A.; Hanmandlu, C.; Lin, L.; Abbas, S. A.; Chang, C. C.; Wang, P. C.; Li, G.; Chu, C. W. Solution-Processable Antimony-Based Light-Absorbing Materials Beyond Lead Halide Perovskites. *J. Mater. Chem. A* **2017**, *5*, 20843-20850.

[22] Karuppuswamy, P.; Boopathi, K. M.; Mohapatra, A.; Chen, H.-C.; Wong, K.-T.; Wang, P.-C.; Chu, C.-W. Role of a Hydrophobic Scaffold in Controlling the Crystallization of Methylammonium Antimony Iodide for Efficient Lead-Free Perovskite Solar Cells. *Nano Energy* **2018**, *45*, 330-336.

[23] Nie, R.; Mehta, A.; Park, B.-W.; Kwon, H.-W.; Im, J.; Seok, S. I. Mixed Sulfur and Iodide-Based Lead-Free Perovskite Solar Cells. *J. Am. Chem. Soc.* **2018**, *140*, 872-875.

[24] Nie, R.; Yun, H.-S.; Paik, M.-J.; Mehta, A.; Park, B.-W.; Choi, Y. C.; Seok, S. I., Efficient Solar Cells Based on Light-Harvesting Antimony Sulfoiodide. *Adv. Energy. Mater*. **2018**, *8*, 1701901.

[25] Saparov, B.; Hong, F.; Sun, J.-P.; Duan, H.-S.; Meng, W.; Cameron, S.; Hill, I. G.; Yan, Y.; Mitzi, D. B. Thin-Film Preparation and Characterization of $Cs_3Sb_2I_9$: A Lead-Free Layered Perovskite Semiconductor. *Chem. Mater*. **2015**, *27*, 5622−5632.

[26] Harikesh, P. C.; Mulmudi, H. K.; Ghosh, B.; Goh, T. W.; Teng, Y. T.; Thirumal, K.; Lockrey, M.; Weber, K.; Koh, T. M.; Li, S.; Mhaisalkar, S.; Mathews, N. Rb as an Alternative Cation for Templating Inorganic Lead-Free Perovskites for Solution Processed Photovoltaics. *Chem. Mater.* **2016**, *28*, 7496-7504.

[27] Bator, G.; Baran, J.; Jakubas, R.; Ratajczak, H. Infrared Studies on Structural Phase Transitions in $[NH_2(CH_3)_2]_3Sb_2Br_9$ and $[NH_2(CH_3)_2]_3Sb_2I_9$. *Vib. Spectrosc.* **1994**, *6*, 193-204.

[28] Jiang, F.; Yang, D.; Jiang, Y.; Liu, T.; Zhao, X.; Ming, Y.; Luo, B.; Qin, F.; Fan, J.; Han, H.; Zhang, L.; Zhou, Y. Chlorine-Incorporation-Induced Formation of the Layered Phase for Antimony-Based Lead-Free Perovskite Solar Cells. *J. Am. Chem. Soc.* **2018**, *140*, 1019-1027.

[29] Singh, A.; Boopathi, K. M.; Mohapatra, A.; Chen, Y. F.; Li, G.; Chu, C. W. Photovoltaic Performance of Vapor-Assisted Solution-Processed Layer Polymorph of $Cs_3Sb_2I_9$. *ACS Appl. Mater. Interfaces* **2018**, *10*, 2566-2573.

[30] Zuo, C.; Ding, L. Lead-Free Perovskite Materials $(NH_4)_3Sb_2I_xBr_{9-x}$. *Angew. Chem. Int. Ed.* **2017**, *56*, 6528-6532.

[31] Bruker (**2007**). SMART. Bruker AXS Inc., Madison, Wisconsin, USA.

[32] Bruker (**2001**). SADABS. Bruker AXS Inc., Madison, Wisconsin, USA.

[33] Sheldrick, G. M. SHELXT - Integrated Space-Group and Crystal-Structure Determination. *Acta Crystallogr. Sect. A Found. Crystallogr.* **2015**, *71*, 3-8.

[34] Sheldrick, G. M. Crystal Structure Refinement with SHELXL. *Acta Crystallogr. Sect. C Struct. Chem.* **2015**, *71*, 3-8.

[35] Müller, P.; Herbst-Irmer, R.; Spek, A.; Schneider, T.; Sawaya, M. Crystal Structure Refinement: A Crystallographer's Guide to SHELXL, International Union of Crystallography Texts on Crystallography, Oxford, United Kingdom, **2006**.

[36] Spek, A. L. Single-Crystal Structure Validation with the Program PLATON. *Journal of Applied Crystallography* **2003**, *36*, 7-13.

[37] Spek, A. L. Structure Validation in Chemical Crystallography. *Acta Crystallographica Section D* **2009**, *65*, 148-155.

[38] Momma, K.; Izumi, F. Vesta 3 for Three-Dimensional Visualization of Crystal, Volumetric and Morphology Data. *J. Appl. Crystallogr.* **2011**, *44*, 1272-1276.

[39] Chang, J.-H.; Doert, T.; Ruck, M. Structural Variety of Defect Perovskite Variants $M_3E_2X_9$ (M = Rb, Tl, E = Bi, Sb, X = Br, I). *Z. Anorg. Chem.* **2016**, *642*, 736-748.

[40] Vegard, L. Die Konstitution der Mischkristalle und die Raumfüllung der Atome. *Z. Phys*. **1921**, *5*, 17-26.

[41] Vegard, L. Die Röntgenstrahlen im Dienste der Erforschung der Materie. *Z. Kristallogr.* **1928**, *67*, 239-259.

[42] Denton, A. R.; Ashcroft, N. W. Vegard's Law. *Phys. Rev. A* **1991**, *43*, 3161-3164.

[43] Correa-Baena, J.-P.; Nienhaus, L.; Kurchin, R. C.; Shin, S. S.; Wieghold, S.; Hartono, N. T. P.; Layurova, M.; Klein, N. D.; Poindexter, J. R.; Polizzotti, A.; Sun, S.; Bawendi, M. G.; Buonassisi, T. A-Site Cation in Inorganic $A_3Sb_2I_9$ Perovskite Influences Structural Dimensionality, Exciton Binding Energy, and Solar Cell Performance. *Chem. Mater.* **2018**, *30*, 3734-3742.

[44] McCall, K. M.; Stoumpos, C.; Kostina, S. S.; Kanatzidis, M. G.; Wessels, B. W. Strong Electron-Phonon Coupling and Self Trapped Excitons in the Defect Halide Perovskite $A_3M_2I_9$ (A = Cs, Rb; M = Bi, Sb). *Chem. Mater.* **2017**, *29*, 4129-4145.

[45] Xing, G.; Mathews, N.; Sun, S.; Lim, S. S.; Lam, Y. M.; Grätzel, M.; Mhaisalkar, S.; Sum, T. C. Long-Range Balanced Electron- and Hole-Transport Lengths in Organic-Inorganic $CH_3NH_3PbI_3$. *Science* **2013**, *342*, 344-347.

[46] Nemnes, G. A.; Besleaga, C.; Tomulescu, A. G.; Palici, A.; Pintilie, L.; Manolescu, A.; Pintilie, I. How Measurement Protocols Influence the Dynamic J-V Characteristics of Perovskite Solar Cells: Theory and Experiment. *Sol. Energy* **2018**, *173*, 976−983.

[47] Rong, Y.; Hu, Y.; Ravishankar, S.; Liu, H.; Hou, X.; Sheng, Y.; Mei, A.; Wang, Q.; Li, D.; Xu, M.; Bisquert, J.; Han, H. Tunable Hysteresis Effect for Perovskite Solar Cells. *Energy Environ. Sci.* **2017**, *10*, 2383−2391.

[48] Wu, F.; Bahrami, B.; Chen, K.; Mabrouk, S.; Pathak, R.; Tong, Y.; Li, X.; Zhang, T.; Jian, R.; Qiao, Q. Bias-Dependent Normal and Inverted J−V Hysteresis in Perovskite Solar Cells. *ACS Appl. Mater. Interfaces* **2018**, *10*, 25604−25613.

[49] Nemnes, G. A.; Besleaga, C.; Stancu, V.; Dogaru, D. E.; Leonat, L. N.; Pintilie, L.; Torfason, K.; Ilkov, M.; Manolescu, A.; Pintilie, I. Normal and Inverted Hysteresis in Perovskite Solar Cells. *J. Phys. Chem. C* **2017**, *121*, 11207−11214.

[50] Tress, W.; Marinova, N.; Moehl, T.; Zakeeruddin, S. M.; Nazeeruddin, M. K.; Grätzel, M. Understanding the Rate-Dependent J−V Hysteresis, Slow Time Component, and Aging in CH3NH3PbI3 Perovskite Solar Cells: the Role of a Compensated Electric Field. *Energy Environ. Sci.* **2015**, *8*, 995−1004.

[51] Christians, J. A.; Manser, J. S.; Kamat, P. V. Best Practices in Perovskite Solar Cell Efficiency Measurements. Avoiding the Error of Making Bad Cells Look Good. *J. Phys. Chem. Lett.* **2015**, *6*, 852−857.

Supporting Information

Single Crystal X-ray structure analysis:

Suitable single crystals of compounds were immersed in silicone oil, mounted using a glass fiber and frozen in the cold nitrogen stream (100K). X-ray diffraction data were collected at low temperature on a Bruker Kappa APEX II diffractometer using Mo K_a radiation (λ = 0.71073 Å) generated by an INCOATEC micro-focus source.

The data reduction and absorption correction was performed with the Bruker SMART[1] and Bruker SADABS[2], respectively. The structures were solved with SHELXT[3] by direct methods and refined with SHELXL[4] by least-square minimization against F^2 using first isotropic and later anisotropic thermal parameters for all atoms. To assess the Br^-/I^- ratio in the mixed perovskites $Rb_3Sb_2Br_{9-x}I_x$, the halide positions in the crystals were treated as substitutional disorder in SHELXL (Part 1 for bromide and Part 2 for iodide ions) for which a second free variable was refined to give the Br^-/I^- ratio, while their sum accounts to 100% occupancy in total. Halide positions and anisotropic displacements parameters were therefore constrained pairwise to be identical using EADP and EXYZ commands as splitting over two positions remained unsuccessful.

The space group assignments and structural solutions were evaluated using PLATON.[5,6]

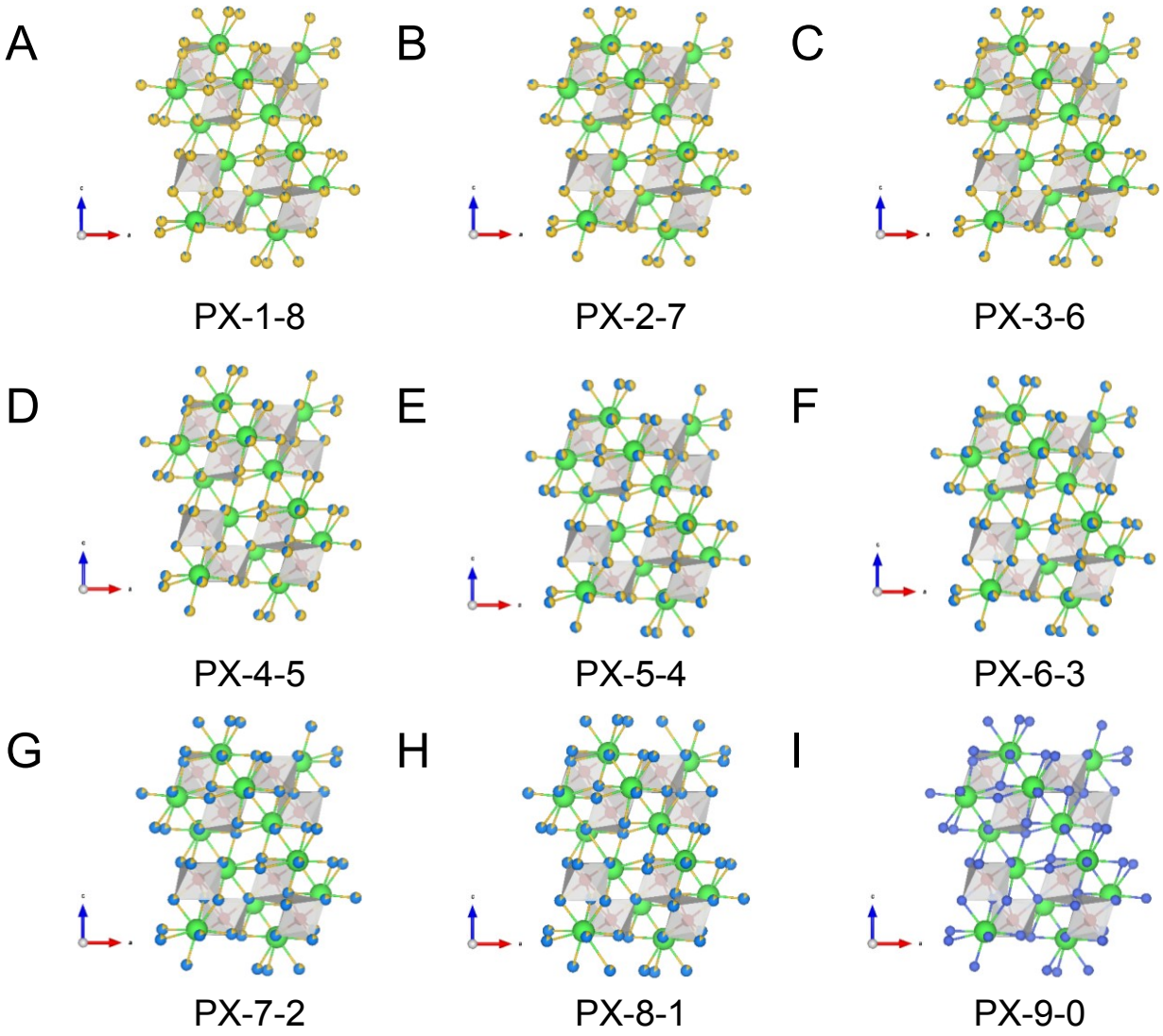

Figure S1: Crystal structures of the prepared $Rb_3Sb_2Br_{9-x}I_x$ samples obtained from single crystal X-ray diffraction: PX-1-8 (A), PX-2-7 (B), PX 3-6 (C), PX-4-5 (D), PX-5-4 (E), PX-6-3 (F), PX-7-2 (G), PX-8-1 (H), and PX-9-0 (I). Green: Rb, red: Sb, yellow: I, blue: Br. The crystal structure of the $Rb_3Sb_2I_9$ sample is shown in the main part of the manuscript.

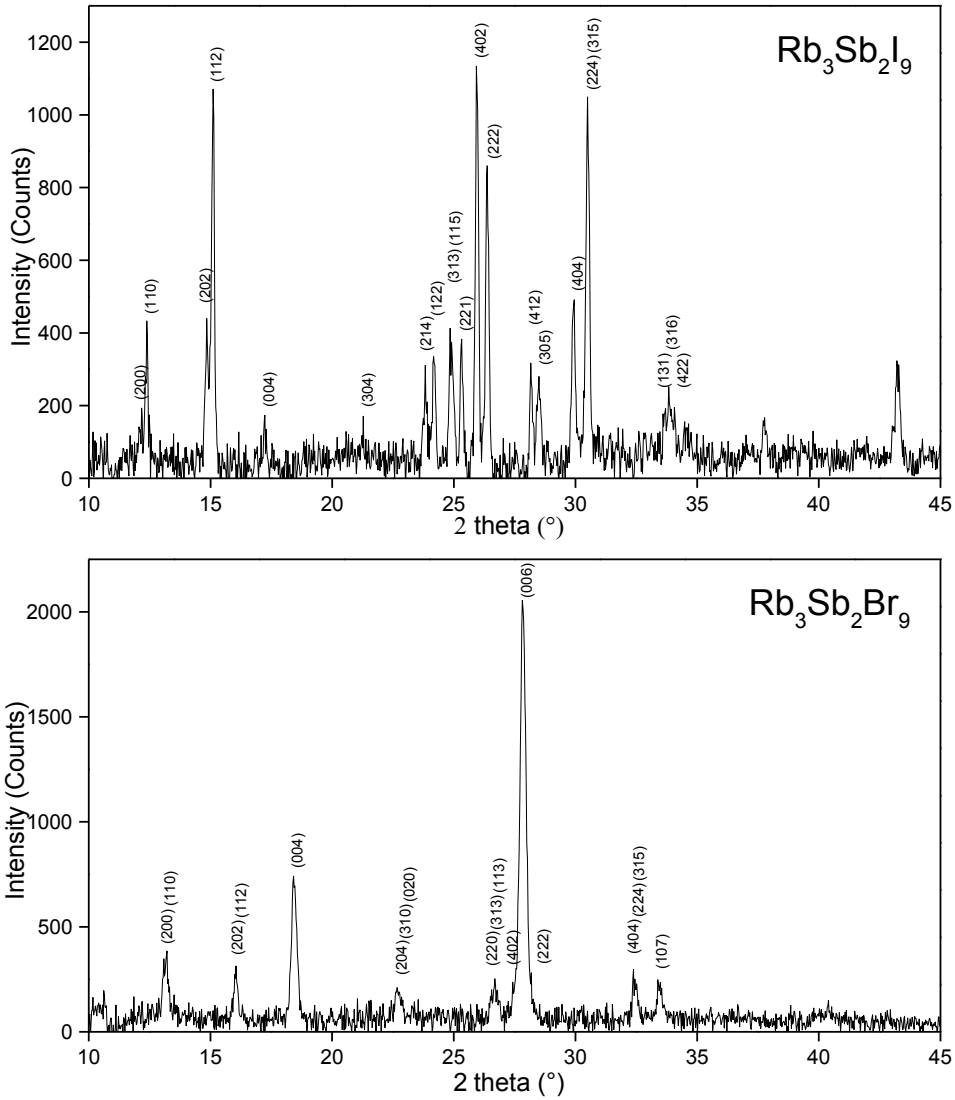

Figure S2: XRD patterns of $Rb_3Sb_2I_9$ and $Rb_3Sb_2Br_9$ thin films with assigned (hkl) values. The hkl values have been calculated via PowderCell 2.0 from the crystal structure data ($Rb_3Sb_2I_9$: ICSD 243727;[7] $Rb_3Sb_2Br_9$: ISCD 431322[8]) from the ICSD database.

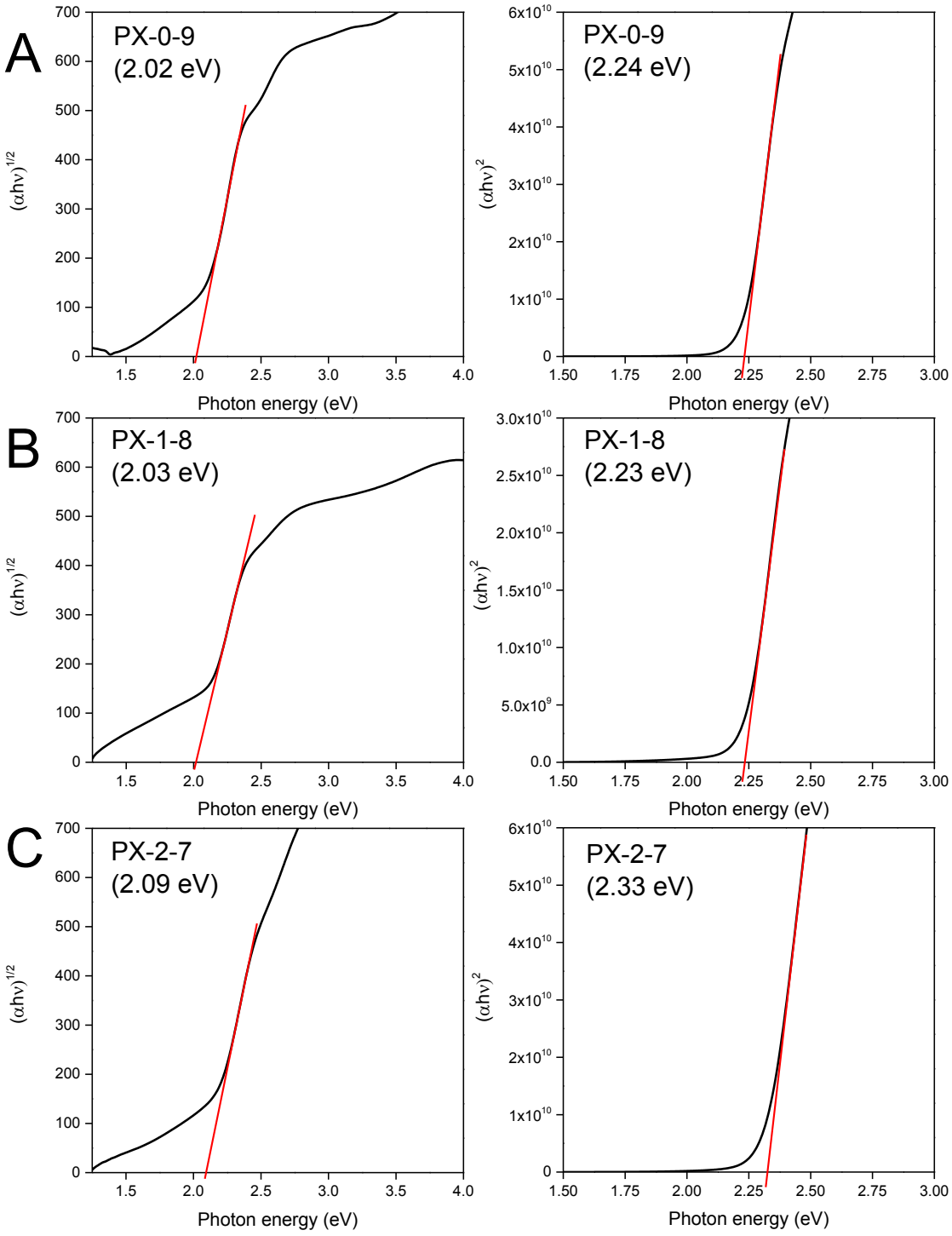
A
PX-0-9
(2.02 eV)
(αhν)^1/2
Photon energy (eV)
PX-0-9
(2.24 eV)
(αhν)^2
Photon energy (eV)
B
PX-1-8
(2.03 eV)
(αhν)^1/2
Photon energy (eV)
PX-1-8
(2.23 eV)
(αhν)^2
Photon energy (eV)
C
PX-2-7
(2.09 eV)
(αhν)^1/2
Photon energy (eV)
PX-2-7
(2.33 eV)
(αhν)^2
Photon energy (eV)

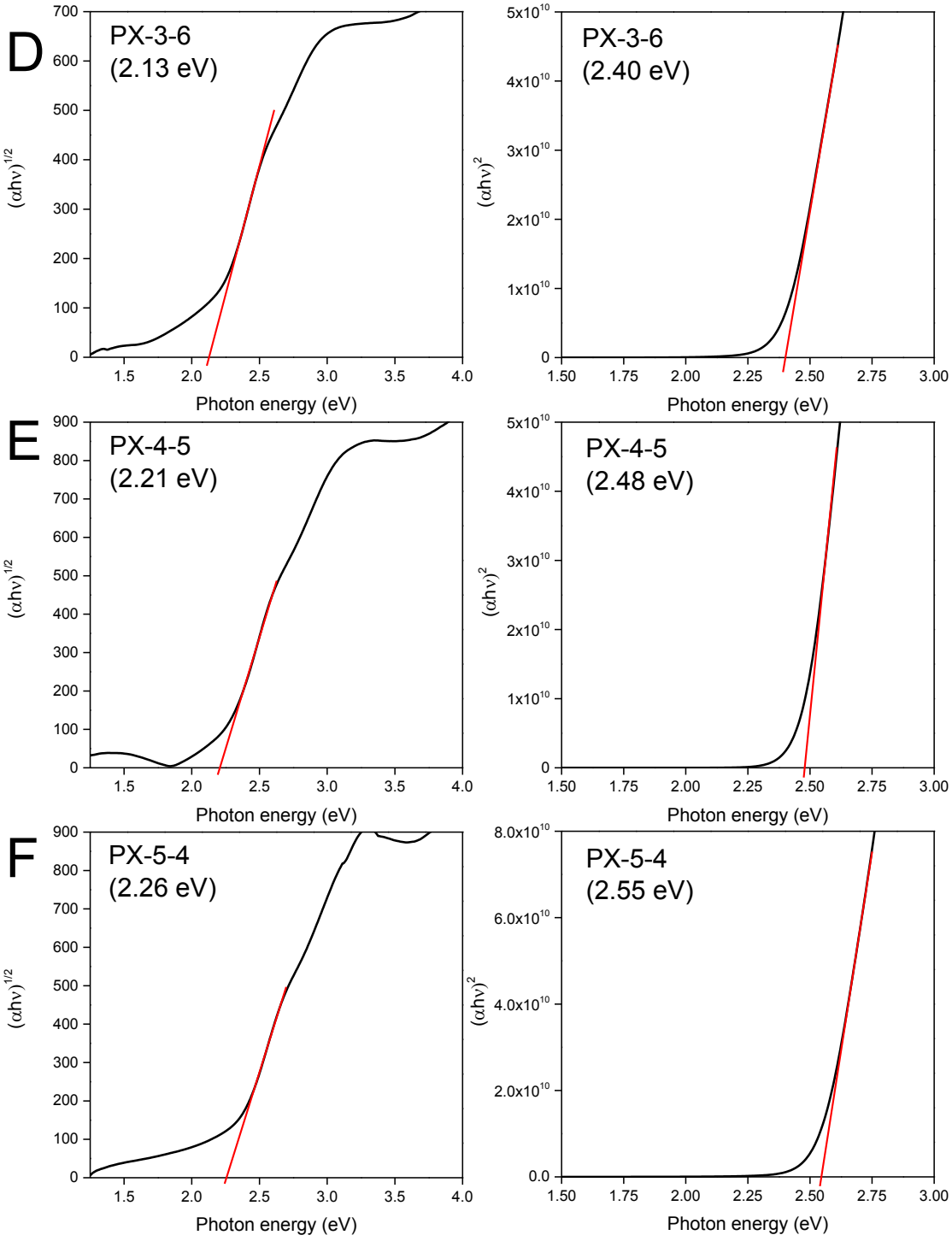
D
PX-3-6
(2.13 eV)
(αhν)^1/2
Photon energy (eV)
PX-3-6
(2.40 eV)
(αhν)^2
Photon energy (eV)
E
PX-4-5
(2.21 eV)
(αhν)^1/2
Photon energy (eV)
PX-4-5
(2.48 eV)
(αhν)^2
Photon energy (eV)
F
PX-5-4
(2.26 eV)
(αhν)^1/2
Photon energy (eV)
PX-5-4
(2.55 eV)
(αhν)^2
Photon energy (eV)

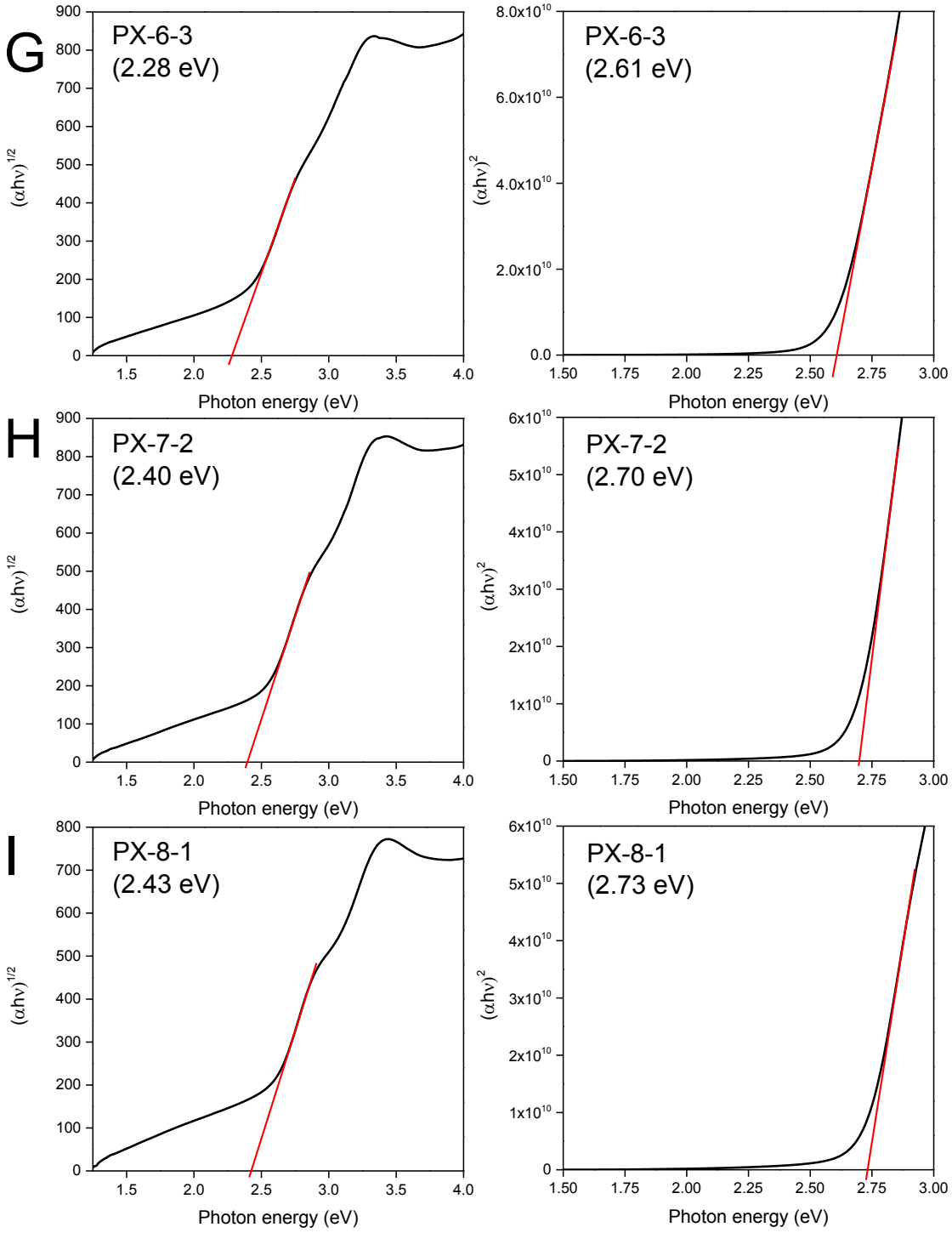
G
PX-6-3
(2.28 eV)
(αhν)^1/2
Photon energy (eV)
PX-6-3
(2.61 eV)
(αhν)^2
Photon energy (eV)
H
PX-7-2
(2.40 eV)
(αhν)^1/2
Photon energy (eV)
PX-7-2
(2.70 eV)
(αhν)^2
Photon energy (eV)
I
PX-8-1
(2.43 eV)
(αhν)^1/2
Photon energy (eV)
PX-8-1
(2.73 eV)
(αhν)^2
Photon energy (eV)

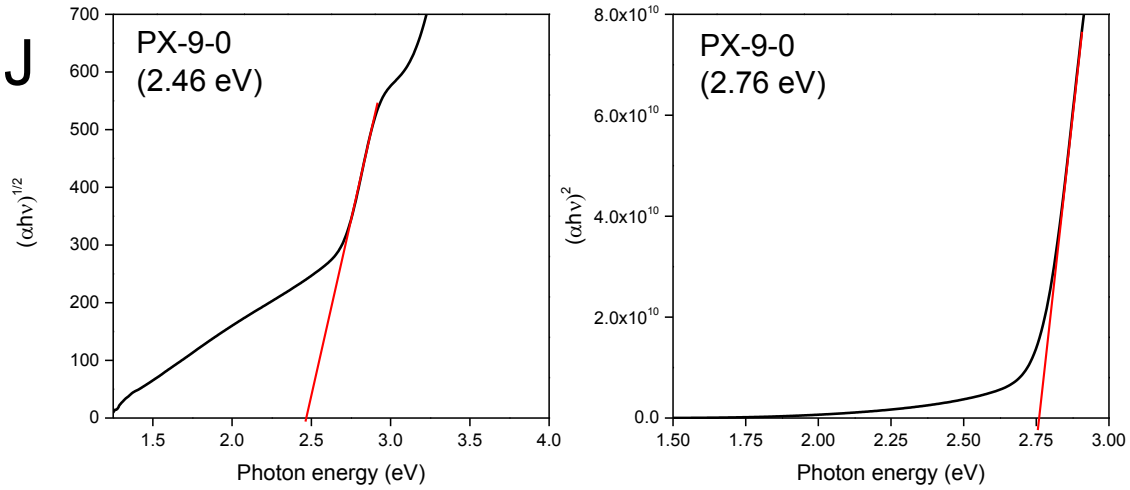

Figure S3: Tauc plots for indirect (left side) and direct (right side) allowed transitions and the corresponding band gaps of the following $Rb_3Sb_2Br_{9-x}I_x$ samples: PX-0-9 (A), PX-1-8 (B), PX-2--7 (C), PX-3-6 (D), PX-4-5 (E), PX-5-4 (F), PX-6-3 (G), PX-7-2 (H), PX-8-1 (I), PX-9-0 (J).

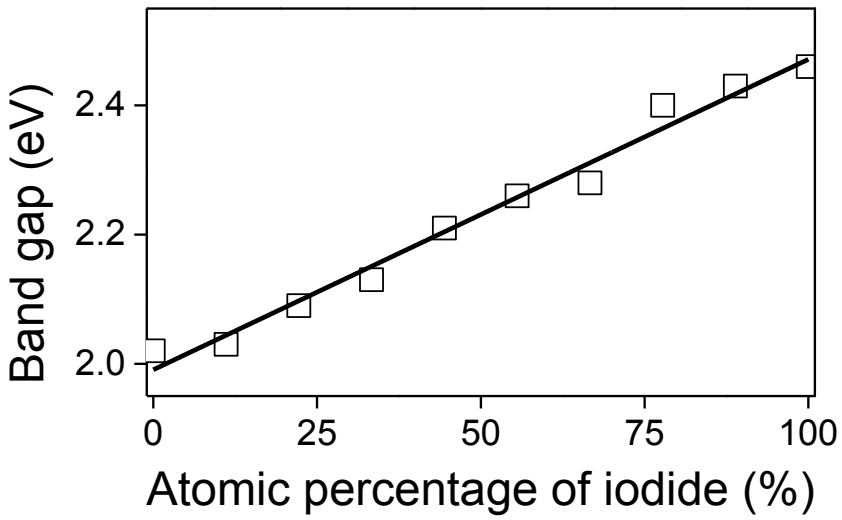

Figure S4: Correlation of the band gap of the $Rb_3Sb_2Br_{9-x}I_x$ samples with the atomic percentage of iodide. All samples showed an indirect band gap.

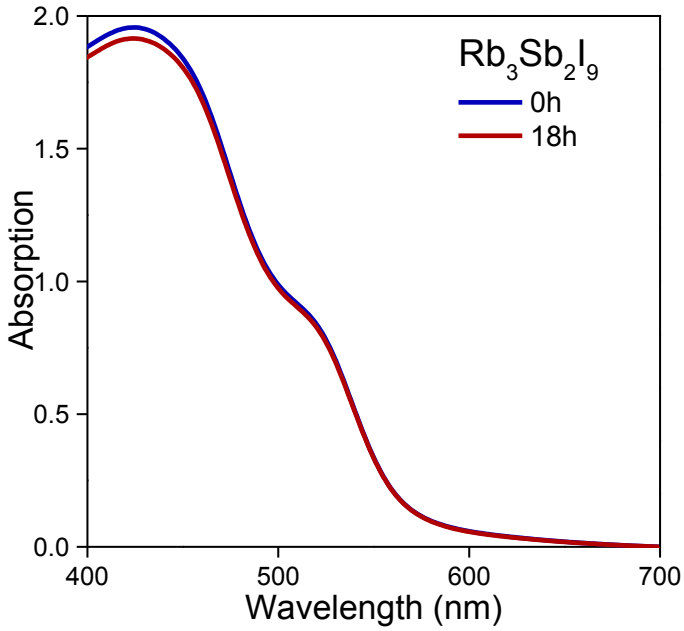

Figure S5: UV-Vis absorption spectra of a $Rb_3Sb_2I_9$ thin film before and after ageing for 18 h under ambient conditions.

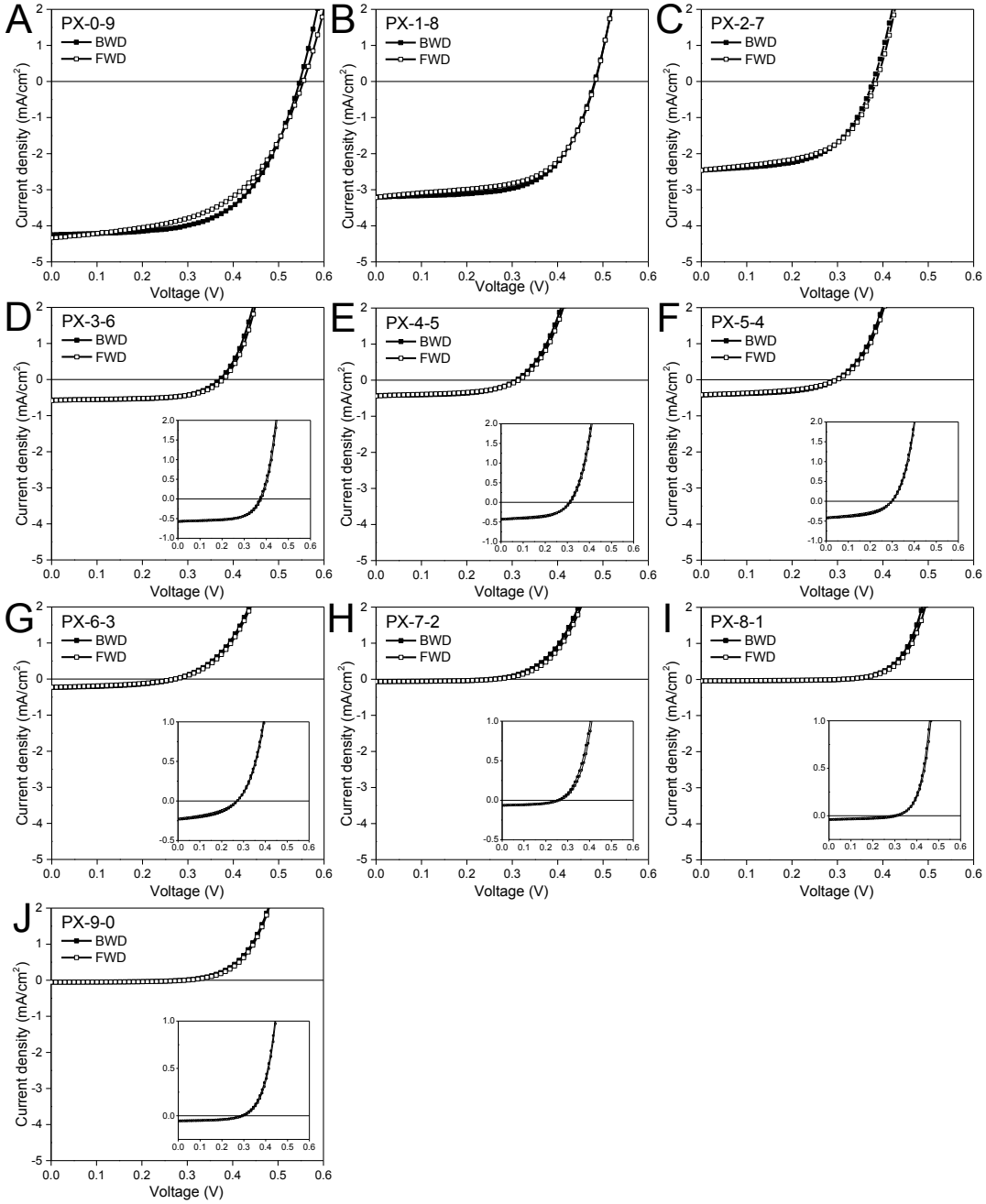

Figure S6: J-V curves of $Rb_3Sb_2I_{9-x}Br_x$ –based solar cells measured in forward (hollow symbols) and backward (solid symbols) scan direction (scan rate 100 mV/s). PX-0-9 (A), PX-1-8 (B), PX-2-7 (C), PX-3-6 (D), PX-4-5 (E), PX-5-4 (F), PX-6-3 (G), PX-7-2 (H), PX-8-1 (I), PX-9-0 (J).

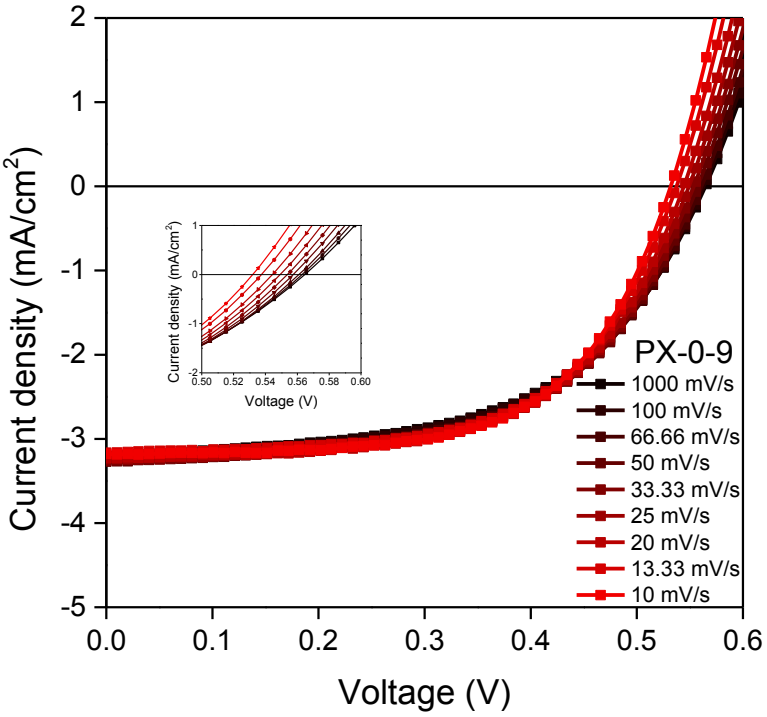

Figure S7: J-V curves – measured in backward direction – of a $Rb_3Sb_2I_9$ perovskite-based solar cell using a 2.65x2.65 mask, whereas the scan rate was varied from 1000 mV/s to 10 mV/s.

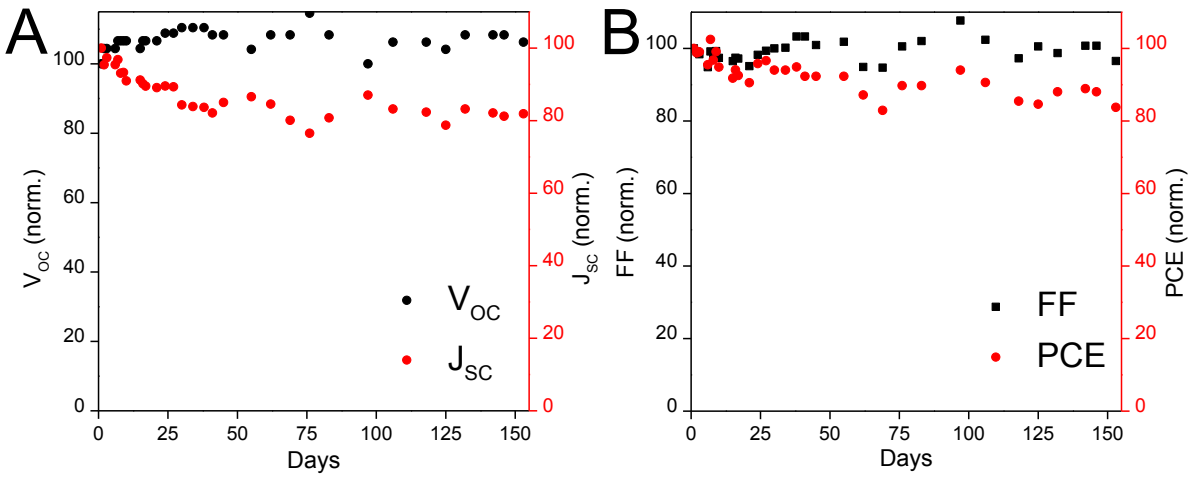

Figure S8: Stability data of a $Rb_3Sb_2I_9$ perovskite-based solar cell tested for more than 150 days (storage under inert conditions). The values were normalized with V_{OC} and J_{SC} shown in (A) and FF and PCE shown in (B).

Table S1: Excitation wavelengths used for the photoluminescence measurements of the $Rb_3Sb_2Br_{9-x}I_x$ perovskite films.

Sample	Excitation wavelength (nm) (Thin film)	Excitation wavelength (nm) (Single crystal)
PX-0-9	475	425
PX-1-8	475	425
PX-2-7	475	425
PX-3-6	425	425
PX-4-5	400	425
PX-5-4	425	425
PX-6-3	425	425
PX-7-2	425	425
PX-8-1	425	425
PX-9-0	425	425

Table S2: Characteristic parameters of the solar cells used for the measurements of the EQE spectra (measured with a 2.65x2.65 mm² shadow mask).

	V_{OC} (V)	J_{SC} (mA/cm^2)	FF (%)	PCE (%)
PX-0-9	0.52	3.54	61.2	1.11
PX-1-8	0.45	2.76	64.6	0.81
PX-2-7	0.41	1.88	57.2	0.44
PX-3-6	0.39	0.43	60.7	0.11

Table S3: Characteristic parameters of $Rb_3Sb_2Br_{9-x}I_x$-based solar cells measured in backward (BWD) and forward (FWD) scan direction. The corresponding J-V curves are shown in figure S6.

		V_{OC} (V)	J_{SC} (mA/cm^2)	FF (%)	PCE (%)
PX-0-9	BWD	0.55	4.25	59.5	1.37
	FWD	0.56	4.33	53.1	1.27
PX-1-8	BWD	0.48	3.20	62.1	0.96
	FWD	0.48	3.22	59.5	0.92
PX-2-7	BWD	0.37	2.45	57.6	0.53
	FWD	0.38	2.46	54.9	0.52
PX-3-6	BWD	0.37	0.57	61.8	0.13
	FWD	0.37	0.58	60.2	0.13
PX-4-5	BWD	0.31	0.43	55.1	0.07
	FWD	0.31	0.44	51.2	0.07
PX-5-4	BWD	0.29	0.42	51.2	0.06
	FWD	0.30	0.42	45.0	0.06
PX-6-3	BWD	0.27	0.23	44.5	0.028
	FWD	0.27	0.23	40.5	0.025
PX-7-2	BWD	0.25	0.06	50.0	0.008
	FWD	0.26	0.07	45.2	0.008
PX-8-1	BWD	0.31	0.04	46.8	0.006
	FWD	0.30	0.04	37.0	0.005
PX-9-0	BWD	0.29	0.05	51.7	0.007
	FWD	0.29	0.06	50.5	0.008

Table S4: Characteristic parameters of a $Rb_3Sb_2I_9$-based solar cell measured in backward (BWD) and forward (FWD) scan direction whereas the scan rate was varied from 1000 mV/s to 10 mV/s. The corresponding (BWD) J-V curves are shown in figure S7.

Scan rate		**V_{OC} (V)**	**J_{SC} (mA/cm^2)**	**FF (%)**	**PCE (%)**
1000 mV/s	BWD	0.57	3.20	54.9	0.99
	FWD	0.56	3.19	53.6	0.95
100 mV/s	BWD	0.57	3.22	55.0	1.00
	FWD	0.56	3.17	54.1	0.96
66.66 mV/s	BWD	0.57	3.25	55.4	1.02
	FWD	0.56	3.21	54.4	0.97
50 mV/s	BWD	0.56	3.27	56.7	1.02
	FWD	0.56	3.22	54.8	0.97
33.33 mV/s	BWD	0.56	3.26	57.1	1.03
	FWD	0.55	3.22	55.9	0.98
25 mV/s	BWD	0.55	3.24	58.6	1.03
	FWD	0.55	3.21	56.0	0.97
20 mV/s	BWD	0.55	3.23	59.0	1.03
	FWD	0.55	3.21	55.9	0.97
13.33 mV/s	BWD	0.54	3.16	60.2	1.01
	FWD	0.54	3.17	56.9	0.96
10 mV/s	BWD	0.54	3.18	60.8	1.02
	FWD	0.53	3.16	57.7	0.96

Table S5: Characteristic parameters of a $Rb_3Sb_2I_9$-based solar cell measured in backward (BWD) and forward (FWD) scan direction whereas the starting voltage was varied from 1000 mV to 600 mV in 100 mV steps.

Starting voltage		**V_{OC} (V)**	**J_{SC} (mA/cm^2)**	**FF (%)**	**PCE (%)**
0 – 1000 mV	BWD	0.57	3.46	53.8	1.06
	FWD	0.56	3.44	54.6	1.05
0 – 900 mV	BWD	0.55	3.52	57.3	1.11
	FWD	0.55	3.49	56.6	1.07
0 – 800 mV	BWD	0.55	3.49	57.6	1.10
	FWD	0.54	3.44	57.2	1.06
0 – 700 mV	BWD	0.54	3.47	58.2	1.10
	FWD	0.54	3.44	56.9	1.06
0 – 600 mV	BWD	0.55	3.43	58.3	1.08
	FWD	0.54	3.42	57.3	1.05
0 – 1000 mV (02)	BWD	0.54	3.47	59.7	1.10
	FWD	0.54	3.45	58.1	1.06

References

[1] Bruker (**2007**). SMART. Bruker AXS Inc., Madison, Wisconsin, USA.

[2] Bruker (**2001**). SADABS. Bruker AXS Inc., Madison, Wisconsin, USA.

[3] Sheldrick, G. M. SHELXT - Integrated Space-Group and Crystal-Structure Determination. *Acta Crystallogr. Sect. A Found. Crystallogr*. **2015**, *71*, 3-8.

[4] Sheldrick, G. M. Crystal Structure Refinement with SHELXL. *Acta Crystallogr. Sect. C Struct. Chem.* **2015**, *71*, 3-8.

[5] Spek, A. L. Single-Crystal Structure Validation with the Program PLATON. *Journal of Applied Crystallography* **2003**, 36, 7-13.

[6] Spek, A. L. Structure Validation in Chemical Crystallography. *Acta Crystallographica Section D* **2009**, *65*, 148-155.

[7] McCall, K. M.; Stoumpos, C.; Kostina, S. S.; Kanatzidis, M. G.; Wessels, B. W. Strong Electron-Phonon Coupling and Self Trapped Excitons in the Defect Halide Perovskite $A_3M_2I_9$ (A = Cs, Rb; M = Bi, Sb). *Chem. Mater.* **2017**, *29*, 4129-4145.

[8] Chang, J.-H.; Doert, T.; Ruck, M. Structural Variety of Defect Perovskite Variants $M_3E_2X_9$ (M = Rb, Tl, E = Bi, Sb, X = Br, I). *Z. Anorg. Chem.* **2016**, *642*, 736-748.

Chapter IV

Dependence of Material Properties and Photovoltaic Performance of Triple Cation Tin Perovskites on the Iodide to Bromide Ratio

This chapter has been published in:

S. Weber, T. Rath, B. Kunert, R. Resel, T. Dimopoulos, G. Trimmel, *Monatsh. Chem.* **2019**, *150*, 1921–1927.

Abstract

In this work, the influence of a partial introduction of bromide (x = 0 – 0.33) into the $MA_{0.75}FA_{0.15}PEA_{0.1}Sn(Br_xI_{1-x})_3$ (MA: methylammonium, FA: formamidinium, PEA: phenylethylammonium) triple cation tin perovskite on the material properties and photovoltaic performance is investigated and characterized. The introduction of bromide shifts the optical band gap of the perovskite films from 1.29 eV for the iodide-based perovskite to 1.50 eV for the perovskite with a bromide content of x = 0.33. X-ray diffraction measurements reveal that also the size of the unit cell is gradually reduced based on the incorporation of bromide. Regarding the photovoltaic performance of the perovskite films, it is shown that already small amounts of bromide (x = 0.08) in the perovskite system increase the open circuit voltage, short circuit current density and fill factor. The maximum power conversion efficiency of 4.63% was obtained with a bromide content of x = 0.25, which can be ascribed to the formation of homogeneous thin films in combination with higher values of the open circuit voltage. Upon introduction of a higher amount of bromide (x = 0.33), the perovskite absorber layers form pinholes, thus reducing the overall device performance.

Introduction

Intensive studies on lead halide perovskites within the past years have shown their great potential as absorber materials in photovoltaics. Lead halide perovskite solar cells are exhibiting high power conversion efficiencies (PCEs) up to 24.2% and are already catching up with conventional thin film solar cell technologies, such as CdTe or CIGS in terms of efficiency.[1,2] Nevertheless, the toxicity of lead itself, in particular, affiliated with the good solubility of lead halide species in water is one of the biggest hindrances for a swift commercialization.[3] Therefore, there is growing endeavor to substitute lead with alternative elements showing less toxicity but similar properties to lead.[4,5] The most promising upon these elements is tin due to its similar electronic structure and ionic radius to lead (Pb^{2+}: 119 pm; Sn^{2+}: 110 pm).[6]

In 2014, first studies on tin perovskite solar cells in n-i-p device architecture with perovskites based on methylammonium (MA^+) as *A*-cation, have been reported, already showing PCEs of 5 to 6%.[7-9] However, a major drawback for tin perovskite solar cells is the easy oxidation of Sn^{2+} to Sn^{4+} in the presence of oxygen which leads to a self p-doping. The standard redox potentials for

tin (E_0 of Sn^{2+}/Sn^{4+} = + 0.15 V) and lead (E_0 of Pb^{2+}/Pb^{4+} = +1.67 V) indicate that Sn^{2+} is thermodynamically less favorable compared to Pb^{2+} which corroborates the sensitivity of Sn^{2+} towards oxidation.[10] One common approach to reduce the oxidation of Sn^2 is the use of SnF_2 as reducing agent. Several research groups investigated different SnF_2 concentrations and found that approximately 10 mol% of the reducing agent is ideal to improve the perovskite film formation and also the power conversion efficiency.[11-13] Gupta et al. recently highlighted several possible effects of SnF_2 on the solar cell properties[10], however, the role of SnF_2 in these devices is still not fully elucidated. Song et al. demonstrated that hydrazine vapor during the perovskite deposition can further diminish the Sn^{4+} concentration and also lowers the defect concentration.[14]

In the last years, tin perovskites with various compositions were investigated and efficiencies up to 9.6% have been obtained.[13,15,16] Jokar et al. realized pinhole-free $FASnI_3$ (FA: formamidinium) perovskite thin films by the addition of 1% ethylenediammonium diiodide (enI_2), reaching a maximum efficiency of 8.9% in the corresponding solar cells.[17] In a further step, the incorporation of 20% guanidinium (GA^+) into the ($FASnI_3$ + 1% enI_2) perovskite resulted in the current record power conversion efficiency of 9.6% (8.3% certified) for tin perovskite solar cells.[16] On the other hand, Wang et al. fabricated 2D-quasi-2D-3D tin perovskite solar cells based on $PEA_{0.15}FA_{0.85}SnI_3$ (PEA: phenylethylammonium) and the usage of NH_4SCN to tailor the tin perovskite structure and reached efficiencies of 9.41%.[18]

This introduction of large *A*-cations in the perovskite lattice such as PEA^+ became attractive to form 2D/3D perovskites.[11,15] Bigger cations are able to break up the 3D structure to form mixed 2D/3D crystal structures. Thereby the perovskites gain higher stability, which is ascribed to the hydrophobic character of these cations.[19] In other reports, the authors claim that the PEA *A*-cation is able to block oxygen diffusion paths making the perovskite less sensible against degradation and, furthermore, a reduction of background carrier density was found, which improves the carrier transport due to longer lifetime of the respective charge carriers.[11,15] Promising solar cells with FA and PEA ions have already been fabricated and efficiencies of 5.94%[11] and 9.0%[15] were obtained. In our previous study, we have shown that solar cells with the triple cation perovskite $MA_{0.75}FA_{0.15}PEA_{0.1}SnI_3$ exhibit an excellent shelf life of more than 5000 hours and also remarkable stability under operation.[20]

An alternative method for tailoring the perovskite absorber layer is the introduction of smaller *X*-anions.[9,21-25] In an early study on lead-free tin perovskites, Hao et al. already investigated the substitution of iodide with bromide in $MASnI_{3-x}Br_x$ perovskite solar cells.[9] The wider optical band

gap due to the introduction of bromide led to an increase in open circuit voltage and overall better device performance. When using $CsSnI_{3-x}Br_x$ as perovskite material, in addition to the expected changes in the optical characteristics, also a change in the crystal structure from orthorhombic to cubic was observed.[22] Later, Lee et al. reported that the introduction of bromide in $FASnI_3$ perovskite solar cells increases the perovskite stability as well as the recombination lifetime and by using an n-i-p device architecture, a maximum PCE of 5.5% with 25% bromide in the perovskite absorber was reached.[21]

In this study, $MA_{0.75}FA_{0.15}PEA_{0.1}Sn(Br_xI_{1-x})_3$ (x = 0, 0.08, 0.17, 0.25, 0.33) perovskite films are investigated and solar cells using a p-i-n planar device set up were fabricated and characterized. The perovskite films were analyzed by optical spectroscopy and X-ray diffraction to substantiate the introduction of bromide into the crystal structure. Moreover, the surface morphology and layer thicknesses were investigated by scanning electron microscopy (SEM) and surface profilometry, respectively. The tin perovskite films were applied in solar cells with the device structure glass/ITO/PEDOT:PSS/perovskite/$PC_{60}BM$/Al, which were analyzed in terms of J-V characteristics, power output at the maximum power point (MPP tracking), hysteresis properties and external quantum efficiency (EQE).

Results and Discussion

Perovskite films with the composition $MA_{0.75}FA_{0.15}PEA_{0.1}Sn(Br_xI_{1-x})_3$, whereby x was set to 0, 0.08, 0.17, 0.25 and 0.33, were fabricated by dissolving the respective amounts of iodide and bromide salts in DMSO/DMF (4/1 vol%) followed by a one-step solution process using anti-solvent treatment to initiate the perovskite crystallization. For simplicity, the perovskite compositions are labelled according to their bromide content (e.g. $MA_{0.75}FA_{0.15}PEA_{0.1}Sn(Br_{0.25}I_{0.75})_3$ is labelled as x = 0.25). The fast crystallization of tin perovskites when using the anti-solvent dripping method is a major challenge in the fabrication of efficient solar cells. Therefore, a solvent ratio of DMF/DMSO (4/1 vol%) was chosen to slow down the crystallization process during spin-coating through the formation of a $SnI_2{\cdot}3DMSO$ intermediate state.[26] Wu et al. have shown that DMSO can also retard the crystallization in lead perovskite solar cells.[27] Liu et al. reported that bigger perovskite grains can be observed when DMSO is present during the annealing procedure thus leading to more homogenous films and less pinholes.[28]

Optical Properties

Fig. 1A shows the UV/Vis absorption spectra of $MA_{0.75}FA_{0.15}PEA_{0.1}Sn(Br_xI_{1-x})_3$ thin films with layer thicknesses of 220, 200, 180, 175 and 170 nm for x = 0, 0.08, 0.17, 0.25 and 0.33, respectively. The films were prepared by the same deposition parameters as used for the solar cell fabrication. In the graph (Fig. 1A), a clear blueshift of the absorption onset with increasing bromide content of the perovskite films can be observed. The absorption onset changes from approximately 1000 nm (x = 0) to approximately 835 nm for the composition with the highest bromide content (x = 0.33), correlating well with other reports.[9,21] The corresponding band gaps were determined using Tauc plots (Fig. S1). Herein, direct transitions were found with band gap values of 1.29 eV, 1.32 eV, 1.38 eV, 1.45 eV and 1.50 eV for the absorber layers with x = 0, 0.08, 0.17, 0.25 and 0.33, respectively. By plotting these values versus the bromide content, a linear correlation (R^2: 0.981) can be observed (Fig. 1B).

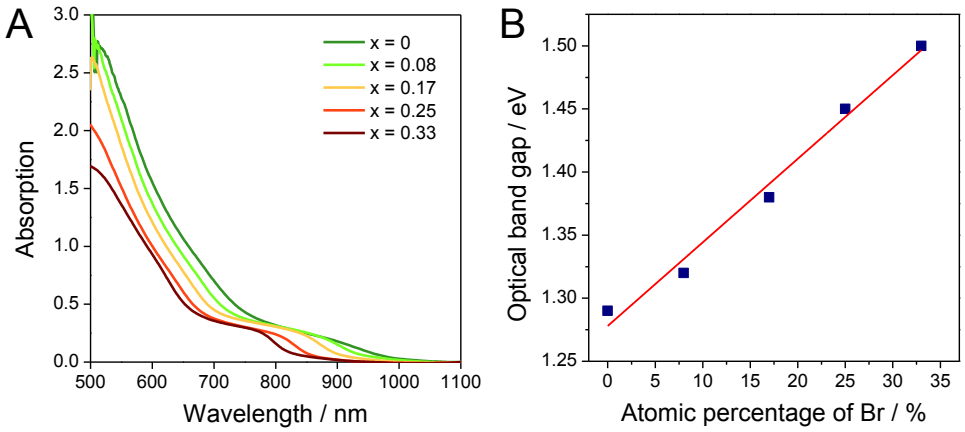

Figure 1: (A) UV/Vis absorption spectra of $MA_{0.75}FA_{0.15}PEA_{0.1}Sn(Br_xI_{1-x})_3$ (x = 0 – 0.33) thin films deposited on glass/PEDOT:PSS substrates; (B) band gap values plotted as a function of the bromide content.

Crystallographic Properties

To further investigate the introduction of bromide into the crystal lattice, X-ray diffraction patterns were recorded (Fig. 2A). The diffractograms show two distinct peaks at approx. 14 ° and 28 ° 2θ which can be assigned to the 100 and 200 peaks of a typical diffraction pattern for a mixed 2D/3D tin perovskite with quasi-cubic/orthorhombic crystal structure.[11,15,19] The very pronounced 100 and 200 peaks indicate a preferred orientation of the (h00) planes of the perovskite crystals parallel to the substrate. Upon the introduction of bromide, no change in the crystal structure or

the preferred orientation is noticed. However, all peaks gradually shift to higher diffraction angles with increasing bromide content of the samples ($x = 0$ to $x = 0.33$), as can be clearly seen in Fig. 2B for the 100 reflex and in Fig. S2 for the 200 reflex. This indicates a decrease of the size of the unit cell due to the incorporation of bromide instead of the larger iodide ions. The peak positions and corresponding d values of all the samples are summarized in Table S1. As observed in the case of the optical data, also the quasi-cubic lattice constant a exhibits a linear correlation (R^2: 0.996) with the bromide content and decreases from $a = 6.250$ Å for $x = 0$ to $a = 6.152$ Å for $x = 0.33$ (Fig. 2C). This is in accordance with Vegard's law[29], and similar linear correlations have been also observed e.g. for mixed halide lead or antimony perovskites.[30-33]

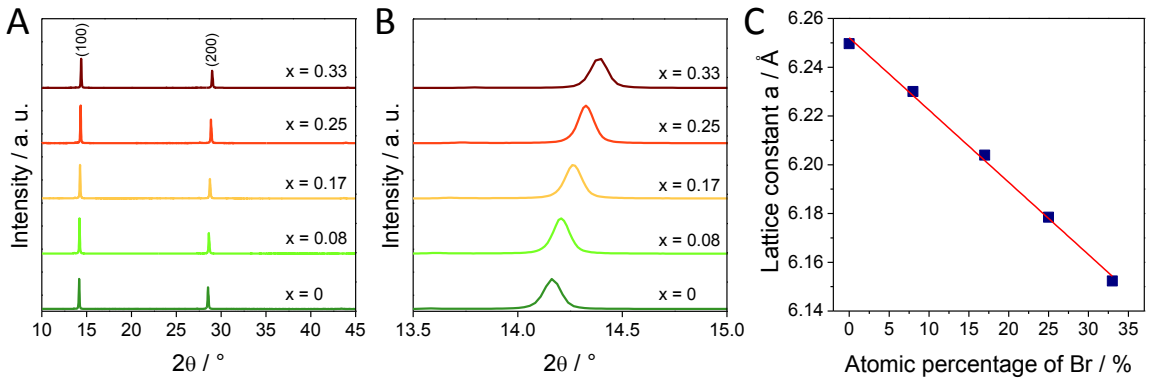

Figure 2: X-ray diffraction patterns of $MA_{0.75}FA_{0.15}PEA_{0.1}Sn(Br_xI_{1-x})_3$ ($x = 0 – 0.33$) thin films prepared on glass substrates showing (A) the whole patterns and (B) a zoom-in between 13.5 and 15.0 ° 2θ to illustrate the shift of the 100 reflex with increasing bromide content. The diffraction patterns are shifted vertically for better visibility. (C) The lattice constants plotted as a function of the bromide content.

Film Morphology and Solar Cells

In a next step, we investigated the morphology of the perovskite films by recording top-view SEM images (Fig. 3, Fig. S3). The films with a bromide content of $x = 0$ to $x = 0.25$ display full coverage without any pinholes. In particular, the films with a bromide content of $x = 0.17$ and $x = 0.25$ appear very flat and show a low roughness. However, by further increasing the bromide content to $x = 0.33$, the perovskite film exhibits pinholes.

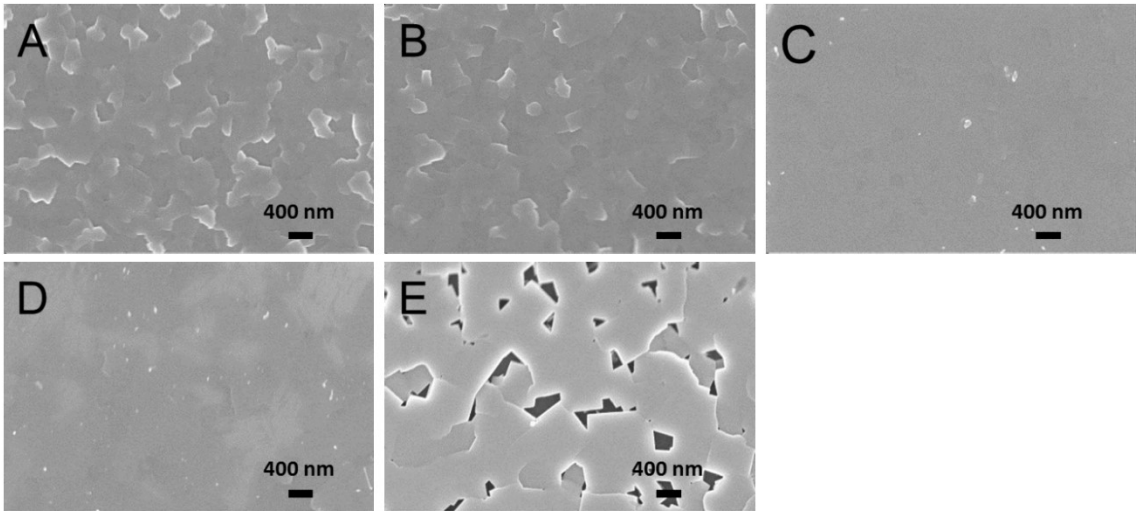

Figure 3: Top view SEM images of $MA_{0.75}FA_{015}PEA_{0.1}Sn(Br_xI_{1-x})_3$ (x = 0 – 0.33) perovskite thin films deposited on glass/ITO/PEDOT:PSS; (A) x = 0, (B) x = 0.08, (C) x = 0.17, (D) x = 0.25, (E) x = 0.33.

Furthermore, solar cells with the device structure glass/ITO/PEDOT:PSS/perovskite/$PC_{60}BM$/Al were fabricated (Fig. 4A). J-V curves of typical solar cells measured in backward scan direction are presented in Fig. 4B and their characteristic parameters are shown in Table 1. All measurements were recorded using a shadow mask (area of 0.07 cm^2) for the illumination.

As expected, the V_{OC} of the solar cells increases with the introduction of bromide into the perovskite absorber layer from 0.37 to 0.49 V because of the widening of the band gap with higher bromide content. However, a higher band gap typically leads to a lower current density due to the narrower absorption range. In contrast to that, we observed that slight amounts of bromide ($x = 0.08 – 0.25$) have a positive effect on the current density of the solar cells. This can be ascribed to the reduced roughness of the perovskite films and thereby an improved interface between absorber and electron transport layer. Moreover, based on previous studies on related tin perovskite materials an improved electron extraction due to a raised conduction band of the perovskite absorber based on the incorporation of bromide is expected.[9,21] In addition, reduced defect concentrations have been found by Lee et al. for mixed iodide/bromide formamidinium tin halide perovskite films.[21]

The solar cells based on perovskites with a bromide content of $x = 0$ showed an efficiency of 2.97%. The PCE is lower compared to previously published values for solar cells with a $MA_{0.75}FA_{0.15}PEA_{0.1}SnI_3$ absorber layer.[20] This originates from an intended simplification of the

solar cell fabrication process by omitting an additional purification of the SnI_2 precursor and applying a single anti-solvent dripping instead of as two-step anti-solvent dripping procedure. Already little amounts of bromide (x = 0.08 and x = 0.17) increase the efficiency, showing maximum PCEs of 4.52% and 4.15%, respectively. The highest PCE of 4.63% was reached with a solar cell comprising a tin perovskite absorber layer with a bromide content of x = 0.25. This solar cell showed a V_{OC} of 0.49 V, a J_{SC} of 16.45 mA/cm^2 and a FF of 63.3%. Further increasing the bromide content to x = 0.33 decreases the efficiency of the solar cells and PCEs of up to 3.34% were obtained. This reduced PCE originates most likely from the pinholes in the perovskite layer leading to partial short circuiting of the device. Generally, all fabricated perovskite solar cells display high reproducibility, indicated by the low standard deviations for an average of the best 10 devices (see Table 1 and Fig. S4).

To investigate the hysteresis behavior, also J-V curves in forward scan direction were recorded. The corresponding light as well as dark measurements of the five perovskite compositions (x = 0 – 0.33) are given in Fig. S5 with their solar cell characteristics summarized in Table S2. A slight hysteresis was observed for the pure iodide perovskite solar cell (x = 0), whereas the devices fabricated with x = 0.08 – 0.25 are almost hysteresis-free. Upon further increasing the bromide content, a large hysteresis is observed, indicated by a change in open circuit voltage, which can be ascribed to the pin holes in the perovskite films with a bromide content of x = 0.33 as observed in the SEM images (Fig. 3 and Fig. S3).

In addition, maximum power point (MPP) tracking measurements were performed (Fig. S6). Hereby power outputs of approximately 4.0%, 4.3%, 4.4%, 5.0% and 3.0% were recorded for the solar cells prepared with the different bromide contents x = 0 – 0.33. These PCE values are slightly higher compared to the ones extracted from the J-V curves, which is due to a light soaking effect. However, also in the MPP tracking measurements, the solar cell with a bromide content of x = 0.25 showed the highest PCE of slightly above 5%. Moreover, it is interesting to mention that the device with the pure iodide compound $MA_{0.75}FA_{0.15}PEA_{0.1}SnI_3$ as absorber layer showed the most pronounced increase in PCE between initial J-V characterisation and MPP tracking.
The external quantum efficiency spectra (Fig. 4C) nicely show that the onset of photocurrent generation shifts to lower wavelengths for the solar cells prepared with higher bromide content in the absorber layers. While the onset of the EQE spectrum of the pure iodide compound is already

at 1000 nm, the onset of photocurrent generation of the solar cells comprising an absorber layer with a bromide content of $x = 0.33$ is at approx. 840 nm. This also matches well with the onsets of the optical absorption spectra (Fig. 1A). Furthermore, the enhanced light absorption of the thin films with the compositions $x = 0.08$ to 0.25 compared to the pure iodide ($x = 0$) compound is also reflected in the EQE spectra. While the maximum EQE values for the device with the pure iodide tin perovskite absorber layer are at 55%, these values are increased to 62-65% for the solar cells based on the perovskite absorbers with a bromide content of $x = 0.08$ to 0.25.

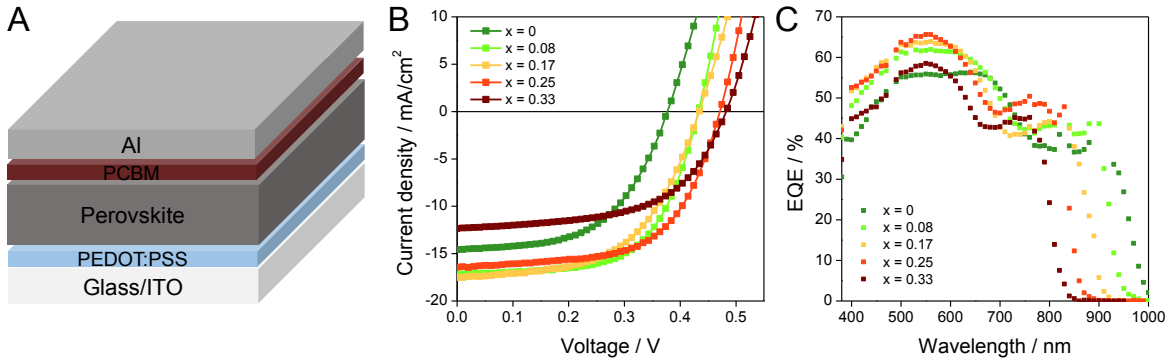

Figure 4: (A) Schematic of the used solar cell architecture, (B) J-V curves of typical tin perovskite solar cells (x = 0 – 0.33) measured in backward scan direction using an illumination mask, (C) EQE spectra of the corresponding solar cells (x = 0 – 0.33)

Table 1: Solar cell characteristics of tin perovskite solar cells for x = 0 – 0.33 showing the best and average (best 10 solar cells) values including the standard deviations. The measurements have been performed one day after fabrication.

Samples		**V_{OC} / V**	**J_{SC} / mA/cm^2**	**FF / %**	**PCE / %**
***x* = 0**	Average	0.37 ± 0.01	13.50 ± 0.77	55.3 ± 1.0	2.70 ± 0.18
	Best	0.39	14.57	57.1	2.97
***x* = 0.08**	Average	0.43 ± 0.01	17.12 ± 0.56	67.2 ± 1.7	3.98 ± 0.25
	Best	0.44	18.10	69.6	4.52
***x* = 0.17**	Average	0.45 ± 0.01	15.65 ± 2.05	64.1 ± 1.0	3.93 ± 0.16
	Best	0.46	18.48	65.8	4.15
***x* = 0.25**	Average	0.48 ± 0.01	15.19 ± 0.94	61.5 ± 1.0	3.88 ± 0.31
	Best	0.49	16.45	63.3	4.63
***x* = 0.33**	Average	0.49 ± 0.02	11.58 ± 0.91	56.0 ± 1.0	2.99 ± 0.23
	Best	0.51	13.06	58.8	3.34

Conclusion

The substitution of iodide with bromide in the $MA_{0.75}FA_{0.15}PEA_{0.1}Sn(Br_xI_{1-x})_3$ perovskite ($x = 0 – 0.33$) leads to an increase of the optical band gap from 1.29 eV to 1.50 eV for $x = 0$ to $x = 0.33$, respectively. X-ray diffraction patterns indicate the bromide introduction by a shift of the diffraction peaks towards higher angles due to a compaction of the unit cell. Both, the optical band gap and the lattice constants show a linear dependence on the bromide content. Thus, in this regard, the herein presented Sn-analogues behave very similar to other perovskite systems e.g. based on lead halides[32,33] or antimony halides[31]. The J-V characteristics of the fabricated perovskite solar cells with $x = 0 – 0.33$ reveal an increase in V_{OC} from 0.37 to 0.49 V as expected due to the increase of the optical band gap. A maximum PCE of 4.63% was reached for the solar cells with a bromide content of $x = 0.25$ in the perovskite absorber layer.

The increased performance of the perovskite solar cells caused by the addition of bromide can be related to a combination of higher open circuit voltages and the formation of more homogeneous thin films as observed in the SEM images. A further increase of the bromide content leads to obvious pinholes the perovskite films resulting in lower device performance and pronounced hysteresis.

Thus, the introduction of bromide does not only influence the optical and structural parameters but also the crystallization and film formation. In order to obtain high-performance perovskite solar cells, a thorough understanding of the crystallization kinetics during the thin film formation is of high importance and will be the topic of further research.

Experimental Section

All chemicals and solvents were used as purchased without further purification unless otherwise noted. The solvents dimethylformamide (DMF), dimethylsulfoxide (DMSO) and chlorobenzene (CB) were dried using molecular sieves (Carl Roth, 3Å type 562 C). PEDOT:PSS was purchased from Heraeus (CLEVIOS^{TM} P VP AI 4083), [6,6]-Phenyl C_{61} butyric acid methyl ester ($PC_{60}BM$) from Solenne, phenylethylammonium iodide (PEAI) from Greatcell Solar and aluminum from Kurt J. Lesker Company. All the other chemicals were purchased from Sigma Aldrich.

Thin Film and Solar Cell Fabrication

Patterned glass/ITO substrates (15 x 15 x 1.1 mm) with a sheet resistance of 15 Ω/sq (Luminescence Technology Corp.) were pre-cleaned with deionized water and acetone, put in an isopropyl alcohol bath and placed into an ultrasonic bath at 40 °C for 30 minutes. The substrates were then dried with N_2 and further plasma etched for 3 minutes (FEMTO, Diener Electronic). PEDOT:PSS (used as purchased) was filtered through a 0.45 μm PVDF filter, then deposited by spin-coating at 3000 rpm for 60 s followed by annealing at 120 °C for 20 minutes. For the annealing step, the substrates were transferred into a N_2 filled glove box.

The perovskite precursor solution (1M) was prepared by dissolving the corresponding amounts of MAI, MABr, FAI, PEAI, SnI_2 and $SnBr_2$ in DMF/DMSO (4/1 vol%) to obtain the theoretical composition $MA_{0.75}FA_{0.15}PEA_{0.1}Sn(Br_xI_{1-x})_3$ (x = 0, 0.08, 0.17, 0.25, 0.33). In Table S3 the corresponding amounts used of each substance to obtain the respective compositions are given. Additionally, 10 mol% SnF_2 were added to the solutions. It should be noted that the SnI_2 (and all

the other precursors) were used as purchased, which is in contrast to our previous study[20], where the SnI_2 was additionally purified based on the different boiling points of SnI_2 and SnI_4 to keep SnI_4 impurities as low as possible. The precursor solutions were stirred overnight at room temperature under nitrogen atmosphere, followed by filtration through a 0.45 µm PTFE filter. For the preparation of the perovskite films, the respective precursor solution was spin-coated on the glass/ITO/PEDOT:PSS substrates at 5000 rpm for 60 s. After 30 s, 100 mm^3 of CB were dropped on the spinning substrates (distance between tip and substrate: 1 cm) to crystallize the perovskite, indicated by color change from yellow to black. The perovskite films were then annealed at 70 °C for 20 minutes. The electron transport layer - $PC_{60}BM$ (20 mg/cm^3 in CB) - was stirred overnight at room temperature under inert conditions and filtered through a 0.45 µm PTFE filter before use. The solution was spin coated at 6000 rpm for 60 s. Afterwards, the top electrode (100 nm Al) was deposited by thermal evaporation under high vacuum conditions ($<1x10^{-5}$ mbar) using a shadow mask (active area of 0.09 cm^2).

Characterization

The $MA_{0.75}FA_{0.15}PEA_{0.1}Sn(Br_xI_{1-x})_3$ perovskite thin films were characterized by X-ray diffraction (XRD) with a PANalytical Empyrean system, which uses Cu K_α radiation. UV-Vis absorption measurements of the perovskites were performed on a Perkin Elmer Lambda 35 UV/Vis spectrometer equipped with an integrating sphere. The optical data were recorded in the wavelength range of 300 to 1100 nm.

Top view SEM images of the perovskite layers prepared on glass/ITO/PEDOT:PSS substrates were acquired on a Zeiss Supra 40 scanning electron microscope with an in-lens detector and 5 kV acceleration voltage. Surface profilometry measurements were performed on a Bruker DektakXT stylus surface profiling system equipped with a 12.5 µm-radius stylus tip. Line scans were recorded over a length of 1000 µm, with a stylus force of 3 mg, and a resolution of 0.33 µm/pt. The layer thicknesses were determined from two-dimensional surface profiles using Vision 64 software (Bruker).

J-V curves of all devices were recorded inside a glovebox (nitrogen atmosphere) with a scan rate of 100 mV/s using a Keithley 2400 source meter connected to a LabView-based software. Illumination (100 mW/cm^2) was provided by a Dedolight DLH400 lamp, calibrated using a monocrystalline silicon WPVS reference solar cell Fraunhofer ISE. External quantum efficiency (EQE) spectra were acquired in inert atmosphere using a MuLTImode 4-AT monochromator

(Amko) equipped with a 75 W xenon lamp (LPS 210-U, Amko), a lock-in amplifier (Stanford Research Systems, Model SR830), and a Keithley 2400 source meter. The monochromatic light was chopped at a frequency of 30 Hz and constant background illumination was provided by white light LEDs. The EQE spectra were measured in the wavelength range of 380−1000 nm (increment: 10 nm). The measurement setup was spectrally calibrated with a silicon photodiode (Newport Corporation, 818-UV/DB).

Acknowledgements

Open access funding provided by Graz University of Technology. This work was carried out within the project “Permasol”, Österreichische Forschungsförderungsgesellschaft (FFG no. 848 929). The authors gratefully acknowledge financial support from the Austrian Climate and Energy Fund within the program Energy Emission Austria.

References

[1] Research Cell Record Efficiency Chart, National Renewable Energy Laboratory (NREL), https://www.nrel.gov/pv/, accessed on 12/06/2019

[2] Green MA, Hishikawa Y, Dunlop ED, Levi DH, Hohl-Ebinger J, Yoshita M, Ho-Baillie AWY (2019) Prog Photovolt Res Appl 27:3

[3] Qiu L, Ono LK, Qi Y (2018) Mater Today Energy 7:169

[4] Hoefler SF, Trimmel G, Rath T (2017) Monatsh Chem 148:795

[5] Ke W, Stoumpos CC, Kanatzidis MG (2018) Adv Mater 1803230, in press, DOI: 10.1002/adma.201803230

[6] Chen Q, De Marco N, Yang Y, Song T-B, Chen C-C, Zhao H, Hong Z, Zhou H, Yang Y (2015) Nano Today 10:355

[7] Noel NK, Stranks SD, Abate A, Wehrenfennig C, Guarnera S, Haghighirad AA, Sadhanala A, Eperon GE, Pathak SK, Johnston MB, Petrozza A, Herz LM, Snaith HJ (2014) Energy Environ Sci 7:3061

[8] Hao F, Stoumpos CC, Chang RPH, Kanatzidis MG (2014) J Am Chem Soc 136:8094

[9] Hao F, Stoumpos CC, Cao DH, Chang RPH, Kanatzidis MG (2014) Nat Photonics 8:489

[10] Gupta S, Cahen D, Hodes G (2018) J Phys Chem C 122:13926

[11] Liao Y, Liu H, Zhou W, Yang D, Shang Y, Shi Z, Li B, Jiang X, Zhang L, Quan LN, Quintero-Bermudez R, Sutherland BR, Mi Q, Sargent EH, Ning Z (2017) J Am Chem Soc 139:6693

[12] Liao W, Zhao D, Yu Y, Grice CR, Wang C, Cimaroli AJ, Schulz P, Meng W, Zhu K, Xiong R-G, Yan Y (2016) Adv Mater 28:9333

[13] Zhao Z, Gu F, Li Y, Sun W, Ye S, Rao H, Liu Z, Bian Z, Huang C (2017) Adv Sci 4:1700204

[14] Song T-B, Yokoyama T, Stoumpos CC, Logsdon J, Cao DH, Wasielewski MR, Aramaki S, Kanatzidis MG (2017) J Am Chem Soc 139:836

[15] Shao S, Liu J, Portale G, Fang H-H, Blake GR, ten Brink GH, Koster LJA, Loi MA (2017) Adv Energy Mater 8:1702019

[16] Jokar E, Chien C-H, Tsai C-M, Fathi A, Diau EW-G (2018) Adv Mater 31:1804835

[17] Jokar E, Chien C-H, Fathi A, Rameez M, Chang Y-H, Diau EW-G (2018) Energy Environ Sci 11:2353

[18] Wang F, Jiang X, Chen H, Shang Y, Liu H, Wei J, Zhou W, He H, Liu W, Ning Z (2018) Joule 2:2732

[19] Tsai H, Nie W, Blancon J-C, Stoumpos CC, Asadpour R, Harutyunyan B, Neukirch AJ, Verduzo R, Crochet JJ, Tretiak S, Pedesseau L, Even J, Alam MA, Gupta G, Lou J, Ajayan PM, Bedzyk MJ, Kanatzidis MG, Mohite AD (2016) Nature 536:312

[20] Rath T, Handl J, Weber S, Friesenbichler B, Fürk P, Troi L, Dimopoulos T, Kunert B, Resel, R, Trimmel G (2019) J Mater Chem A 7:9523

[21] Lee SJ, Shin SS, Im J, Ahn TK, Noh JH, Jeon NJ, Seok SI, Seo J (2018) ACS Energy Lett 3:46

[22] Sabba D, Mulmudi HK, Prabhakar RR, Krishnamoorthy T, Baikie T, Boix PP, Mhaisalkar S, Mathews N (2015) J Phys Chem C 119:1763

[23] Yokohama T, Song T-B, Cao DH, Stoumpos CC, Aramaki S, Kanatzidis MG (2017) ACS Energy Lett 2:22

[24] Saski M, Prochowicz D, Marynowski W, Lewiński J (2019) Eur J Inorg Chem 22:2680

[25] Konstantakou M, Stergiopoulos T (2017) J Mater Chem A 5:11518

[26] Hao F, Stoumpos CC, Guo P, Zhou N, Marks TJ, Chang RPH, Kanatzidis MG (2015) J Am Chem Soc 137:11445

[27] Wu Y, Islam A, Yang X, Qin C, Liu J, Zhang K, Peng W, Han L (2014) Energy Environ Sci 7:2934

[28] Liu J, Ozaki M, Yakumaru S, Handa T, Nishikubo R, Kanemitsu Y, Saeki A, Murata Y, Murdey R, Wakamiya A (2018) Angew Chem Int Ed 57:13221

[29] Vegard L (1921) Z Phys 5:17

[30] Ono LK, Juarez-Perez EJ, Qi Y (2017) ACS Appl Mater Interfaces 9:30197

[31] Weber S, Rath T, Fellner K, Fischer R, Resel R, Kunert B, Dimopoulos T, Steinegger A, Trimmel G (2019) ACS Appl Energy Mater 2:539

[32] Beal RE, Slotcavage DJ, Leijtens T, Bowring AR, Belisle RA, Nguyen WH, Burkhard GF, Hoke ET, McGehee MD (2016) J Phys Chem Lett 7:746

[33] Fedeli P, Gazza F, Calestani D, Ferro P, Besagni T, Zappettini A, Calestani G, Marchi E, Ceroni P, Mosca R (2015) J Phys Chem C 119:21304

Supporting Information

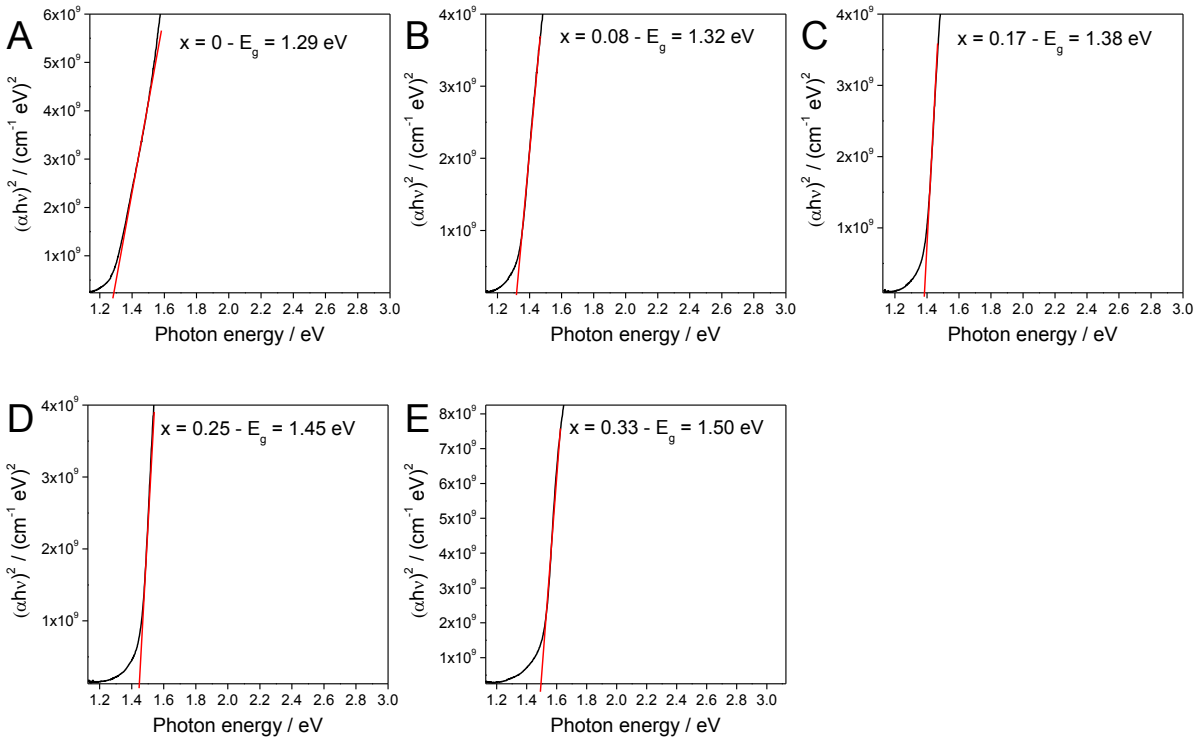

Figure S1: Tauc plots for the band gap determination of the $MA_{0.75}FA_{0.15}PEA_{0.1}Sn(Br_xI_{1-x})_3$ thin films with x = 0 – 0.33; (A) x = 0, (B) x = 0.08, (C) x = 0.17, (D) x = 0.25, (E) x = 0.33

Table S1: Peak positions and corresponding d values of the prepared $MA_{0.75}FA_{0.15}PEA_{0.1}Sn(Br_xI_{1-x})_3$ samples

		100	200
$x = 0$	peak position / ° 2θ	14.16	28.52
	d / Å	6.25	3.13
$x = 0.08$	peak position / ° 2θ	14.2	28.62
	d / Å	6.23	3.12
$x = 0.17$	peak position / ° 2θ	14.26	28.75
	d / Å	6.21	3.1
$x = 0.25$	peak position / ° 2θ	14.33	28.86
	d / Å	6.18	3.09
$x = 0.33$	peak position / ° 2θ	14.4	29.00
	d / Å	6.15	3.08

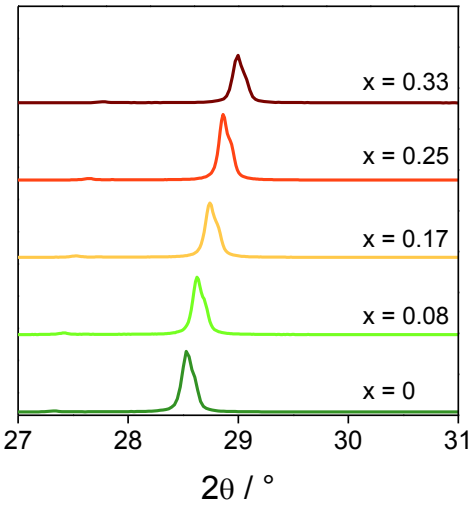

Figure S2: XRD patterns of $MA_{0.75}FA_{0.15}PEA_{0.1}Sn(Br_xI_{1-x})_3$ (x = 0 – 0.33) thin films in the range between 27 and 31 ° 2θ illustrating the shift of the 200 peak with increasing bromide content. The diffraction patterns are shifted vertically for better visibility

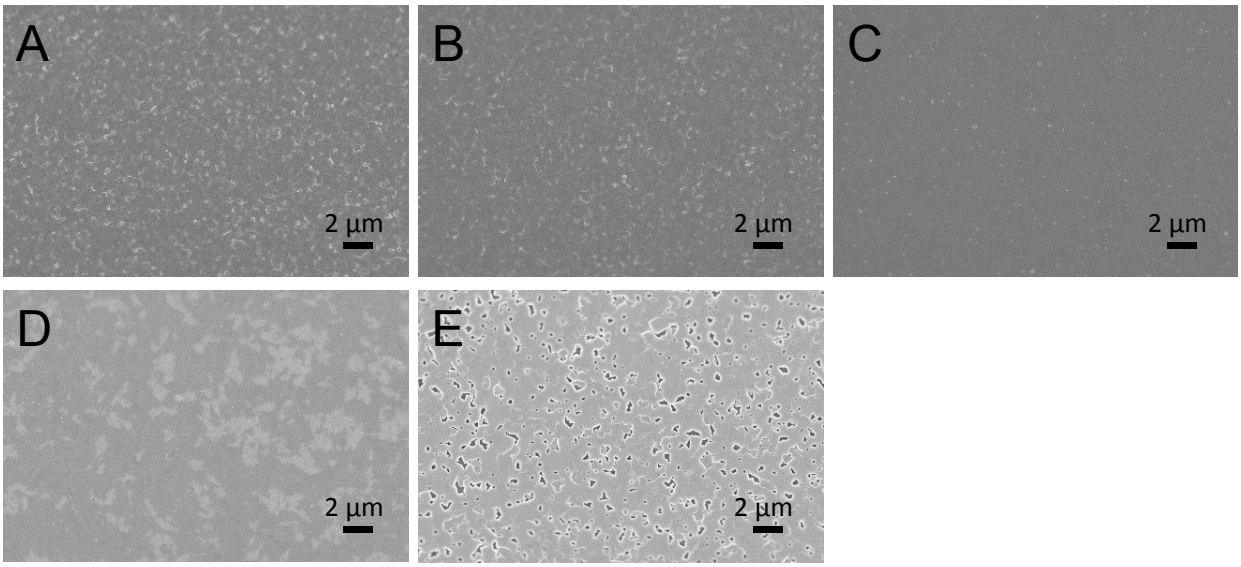

Figure S3: Top view SEM images of $MA_{0.75}FA_{0.15}PEA_{0.1}Sn(Br_xI_{1-x})_3$ perovskite thin films where x = 0 – 0.33 in a lower magnification. (A) x = 0, (B) x = 0.08, (C) x = 0.17, (D) x = 0.25, (E) x = 0.33

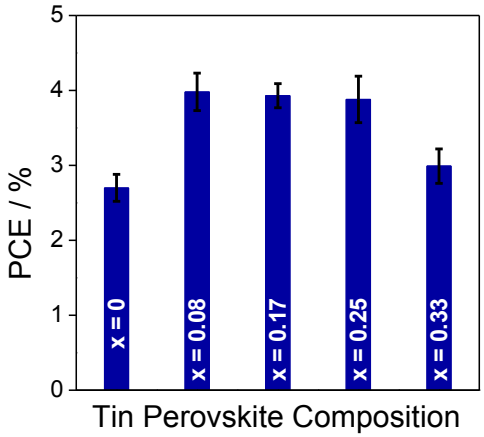

Figure S4: Graphic representation of the average solar cell efficiencies of tin perovskites with x = 0 – 0.33 including their standard deviations

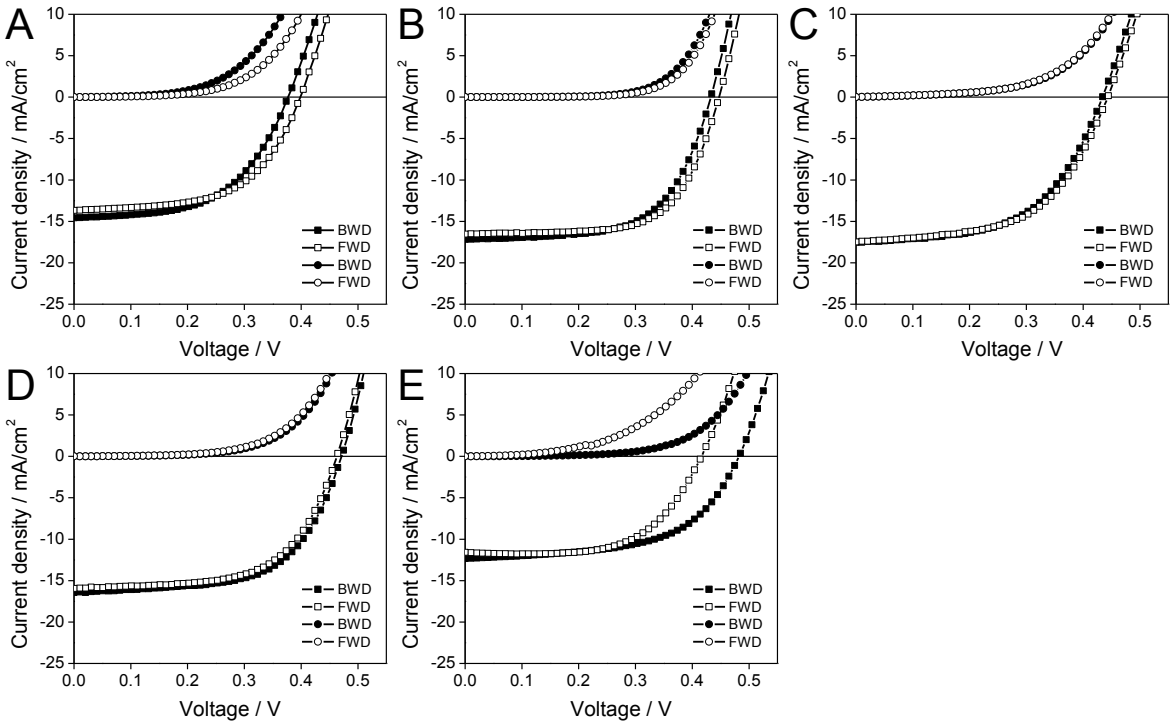

Figure S5: Hysteresis behavior (backward and forward scans) of typical tin perovskite solar cells under light and dark conditions (scan rate: 100 mV/s); (A) x = 0, (B) x = 0.08, (C) x = 0.17, (D) x = 0.25, (E) x = 0.33

Table S2: Solar cell characteristics of typical tin perovskite solar cells measured in backward (bwd) and forward (fwd) scan direction

	V_{OC} / V	J_{SC} / mA/cm^2	FF / %	PCE / %	scan direction
***x* = 0**	0.37	14.57	54.9	2.97	BWD
	0.39	13.68	58.0	3.07	FWD
***x* = 0.08**	0.43	17.17	61.2	4.52	BWD
	0.44	16.54	65.2	4.77	FWD
***x* = 0.17**	0.43	17.53	54.9	4.15	BWD
	0.44	17.49	55.1	4.25	FWD
x = 0.25	0.47	16.44	60.0	4.63	BWD
	0.46	15.95	60.1	4.41	FWD
x = 0.33	0.48	12.34	56.3	3.34	BWD
	0.41	11.58	61.3	2.91	FWD

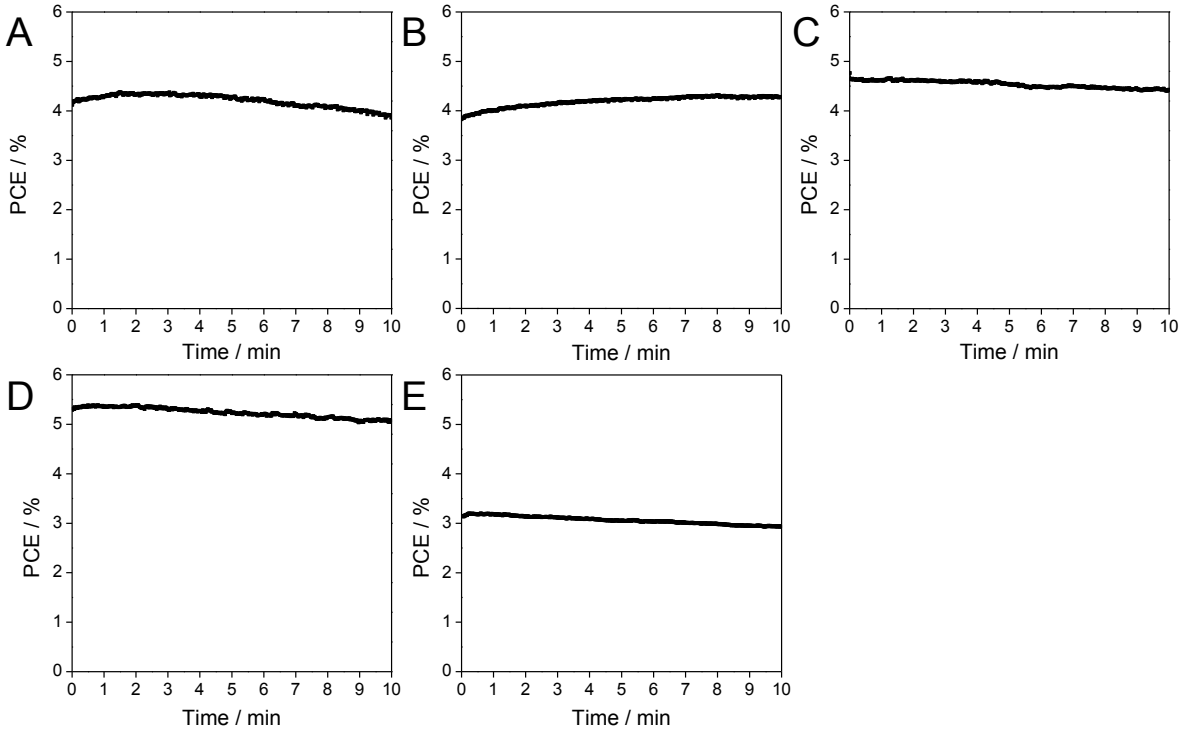

Figure S6: Maximum power point tracking measurements of $MA_{0.75}FA_{0.15}PEA_{0.1}Sn(Br_xI_{1-x})_3$ based solar cells with x = 0 – 0.33 measured with a shadow mask. (A) x = 0, (B) x = 0.08, (C) x = 0.17, (D) x = 0.25, (E) x = 0.33

Table S3: Perovskite precursor compositions for x = 0 – 0.33 with their respective weight portions calculated for 500 mm^3 precursor solution

component	$x = 0$	$x = 0.08$	$x = 0.17$	$x = 0.25$	$x = 0.33$
MAI / mg	59.6	39.8	19.9	-	-
FAI / mg	12.9	12.9	12.9	12.9	12.9
PEAI / mg	12.5	12.5	12.5	12.5	12.5
MABr / mg	-	14.0	28.0	42.0	42.0
SnI_2 / mg	186.3	186.3	186.3	186.3	163.9
$SnBr_2$ / mg	-	-	-	-	16.7
SnF_2 / mg	7.9	7.9	7.9	7.9	7.9

Chapter V

Comparison of Fluorene, Silafluorene and Carbazol as Linkers in Perylene Monoimide Based Non-Fullerene Acceptors

This chapter has been submitted to:

S. Weber, J. Hofinger, T. Rath, M. Reinfelds, D. Pfeifer, S. M. Borisov, P. Fürk, H. Amenitsch, M. C. Scharber, G. Trimmel, *Mat. Adv.* **2020**.

Abstract

Perylene monoimide (PMI) based non-fullerene acceptors are an interesting alternative to perylene diimide acceptors in organic photovoltaics due to an open substitution side allowing chemical modifications of the molecule. In addition, this offers the possibility to twist the molecule to avoid pronounced π-π stacking. At the same time, the good solubility and the well-suited optical properties are maintained. This work provides a new perspective of perylenes using PMI-linker-PMI based acceptors in which the linker is composed of different fluorene derivatives to investigate the influence of heteroatoms on the optical and electronic properties. The three compounds **PMI-F-PMI**, **PMI-FSi-PMI** and **PMI-FN-PMI** were synthesized using a fluorene (F), silafluorene (FSi) and carbazole (FN) linker, respectively, characterized regarding optical, structural and electronic properties and implemented in solar cells using PBDB-T as donor material. The influence of the donor/acceptor ratio as well as thermal annealing on the solar cell properties were studied and maximum device efficiencies of 5.16% and high photovoltages up to 1.14 V were obtained for all three acceptors. Moreover, the solar cells display reasonable stability in inert conditions as it is exemplified by maximum power point tracking experiments under continuous illumination.

Introduction

Bulk heterojunction organic solar cells offer various advantages over conventional photovoltaic technologies such as light weight, flexibility and easy continuous roll-to-roll processability.[1,2] This opens up a broad range of possible commercial applications in the future in the areas of building integrated photovoltaics, mobility, consumer goods and more. Within the era of polymer/fullerene solar cells, a large part of the research was focused on the design of various donor materials to optimize the power output leading to maximum device efficiencies of around 10%.[3,4] However, fullerene derivatives suffer from low absorption in the visible range, aggregation in blend films and high production costs and thus ushered a new era of materials, the so called non-fullerene acceptors (NFAs) or small molecule acceptors (SMAs).[2,5-7] This new material class offers several advantages such as tunable HOMO/LUMO levels and spectral adjustments by molecular design as well as

higher stability in many cases.[8-12] Implemented in bulk heterojunction solar cells, device efficiencies of 16% were already reached with various donor/acceptor material combinations using the SMAs BTP-4X[13] and Y6.[14-16] Recently, PCE values of 17.35% have been reported.[17] Among the broad variety of different structures, NFAs based on perylenes have been in the focus since the beginning of organic solar cell research and were used in the first organic heterojunction solar cell by C.W. Tang back in 1986.[18] So far, mainly perylene diimides (PDI), substituted at the bay position were investigated as NFAs in solar cells.[19-25] The major issue of PDIs is their pronounced agglomeration, which leads to large crystallites within the blend and hence low device performance.[26,27,28] To tackle this issue, twisting the PDI is necessary by introducing side groups or by ring fusion.[29,30] Following these strategies, recently maximum device efficiencies of 10% were reached with PDI based acceptors.[29,31,32]

A very interesting approach is to link two perylene monoimides (PMI) by a conjugated linker, to form a perylene-linker-perylene triad structure (compare **Scheme 1** , e.g. using alkinyl, thiophene or fluorene linkers.[33-38] In the case of electron rich linkers, this results in an acceptor-donor-acceptor structure, a structure realized in most of the high efficient NFAs such as Y6 or BTP-4X. Recently, Zhang et al. demonstrated that a simple fluorene linker, combined with perylene monoimide electron withdrawing groups, reaches in combination with PTZ1 PCEs up to 6%.[37,38] Although the efficiencies are moderate, extremely high open circuit voltages of 1.32 V were reached due to the high lying LUMO level of PMI-F-PMI.[38]

These high V_{OC} values inspired us to investigate this type of NFAs in more detail. Therefore, this study compares a PMI-fluorene-PMI-acceptor molecule with its carbazole and silafluorene analogues in order to investigate the influence of the heteroatom in the fluorene-based core. Their optical, structural and electronic properties were thoroughly characterized and additionally supported by density functional theory (DFT) calculations. Moreover, all three compounds were evaluated in bulk heterojunction solar cells using PBDB-T as donor polymer in an inverted device setup.

Results and discussion

The PMI-aryl-PMI NFAs were synthesized as outlined in **Scheme 1**. The key step for the synthesis of these compounds was a Suzuki coupling reaction, using commercially available diboronic acid esters of the corresponding linker molecules and perylene monoimide bromide to give in the case of the fluorene linker the compound **PMI-F-PMI** (**3a**), of the silafluorene linker **PMI-FSi-PMI (3b**) and of the carbazole linker **PMI-FN-PMI** (**3c**). $Pd(PPh_3)_4$ and aqueous K_2CO_3 in refluxing toluene were used as standard coupling conditions. A detailed synthesis procedure is given in the ESI.

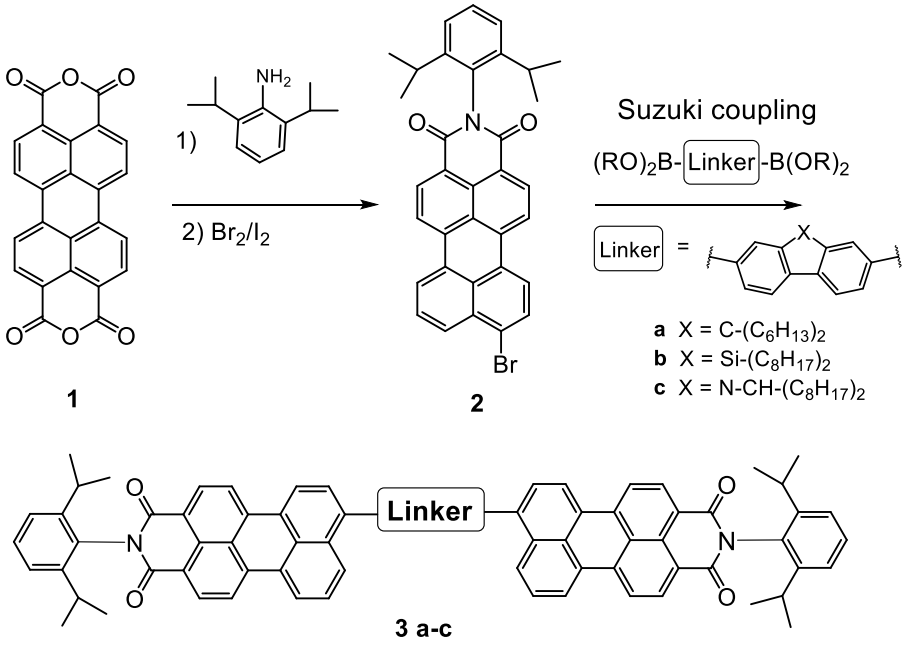

Scheme 1 *Synthesis of perylene-linker-perylene NFAs* ***3a-c.***

The structures were verified by ^{1}H- and ^{13}C-NMR spectroscopy and MALDI-TOF mass spectrometry and are shown in the ESI. Owing to the long alkyl side chains, all three synthesized compounds exhibited good solubility in common organic solvents such as dichloromethane, chloroform, chlorobenzene (CB) or dichlorobenzene. Furthermore, all compounds demonstrated excellent thermal stability. The decomposition temperatures (TGA, see Figure S10) of **PMI-F-PMI**, **PMI-FSi-PMI** and **PMI-FN-PMI** are 441 °C, 471 °C and 465 °C, respectively. The minor mass loss of up to 3% in the PMI-FSi-PMI sample below 400 °C can be assigned to low amounts of residual solvent in the sample.

Computations

Density functional theory (DFT) computations were conducted in order to analyze the influence of the heteroatom on the structure as well as on the optical and electrical properties. The ground state geometries were optimized and the obtained minima were verified by frequencies calculations (B3LYP/6-31G* / Gaussian 09).[39] A representation of the results is shown for all three compounds **3a-c** in Figure S11. In all three cases a twist between the fluorene-type linker and the PMI units is observed with a similar dihedral angle of approximately 55° between the PMI and linker moieties. The frontier molecular orbitals of all three compounds are essentially isolobal. In the HOMO, the electron density is distributed alongside the perylene backbone and fluorene, whereas in the LUMO the electron density is shifted towards the perylene backbone (**Figure 1**). The nodal plane passes through the imide in the HOMO and LUMO orbitals, thus the imide substitution should not influence spectral and electrochemical properties of the molecule. However, due to the bulky isopropyl groups, the phenyl substituent on the imide moiety is oriented perpendicularly to the rest of the molecule. This as well as the aliphatic side chain on the central linker moiety suppress the aggregation of the molecule and increases the solubility. The HOMO and LUMO energy levels of **PMI-F-PMI (3a)** are predicted to be -5.42 and -2.88 eV, respectively (bandgap 2.54 eV). The silafluorene (**3b**) and carbazol (**3c**) based NFAs have values nearly identical to PMI-F-PMI (see Table 1).

Table 1 *DFT (B3LYP/6-31G*) characteristics of* ***PMI-F-PMI (3a)****,* ***PMI-FSi-PMI (3b)*** *and* ***PMI-FN-PMI (3c)***

Material	$HOMO^{DFT}$ (eV)	$LUMO^{DFT}$ (eV)	E_g^{DFT} (eV)
PMI-F-PMI	-5.42	-2.88	2.54
PMI-FSi-PMI	-5.44	-2.88	2.56
PMI-FN-PMI	-5.40	-2.86	2.54

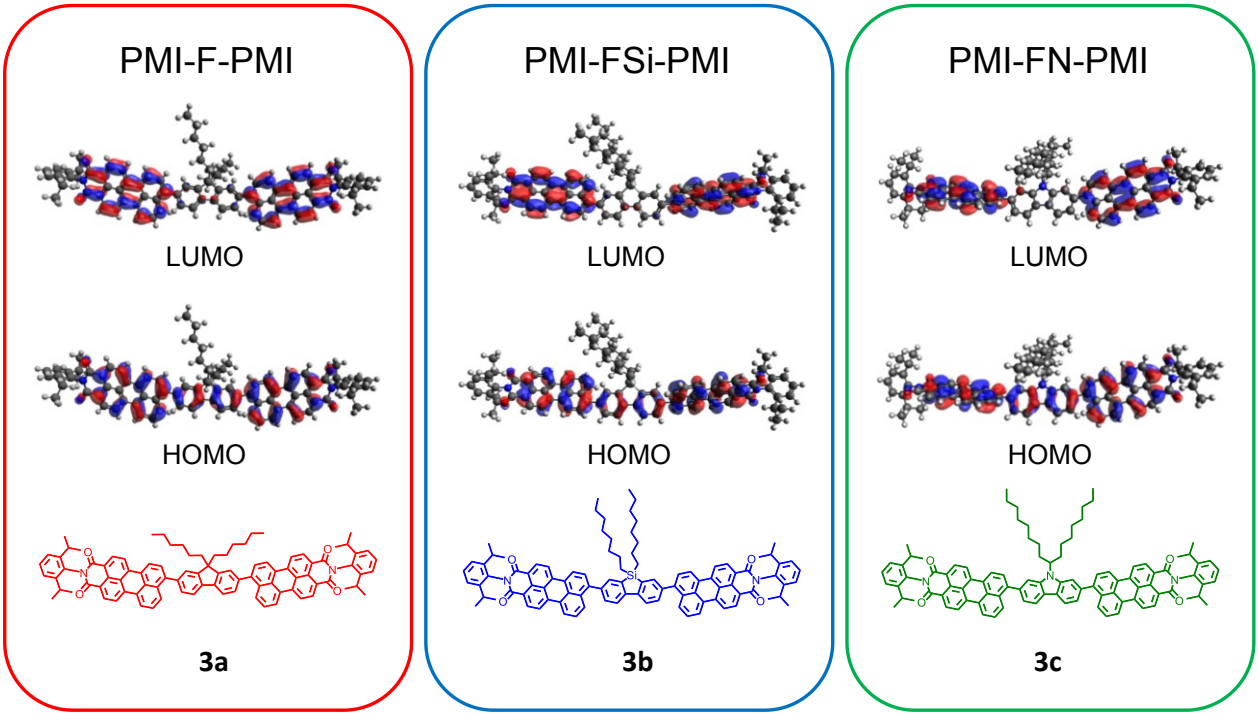

Fig. 1 *DFT (B3LYP/6-31G*) – Molecular geometries and the frontier molecular orbitals of* ***PMI-F-PMI (3a)****,* ***PMI-FSi-PMI (3b)*** *and* ***PMI-FN-PMI (3c)****.*

Optical and electronic properties

UV-Vis absorption spectra of the synthesized NFAs (**PMI-F-PMI**, **PMI-FSi-PMI** and **PMI-FN-PMI**) were compared to those of the monomeric PMI compounds **PMI-Br** (**2**) as well as **PMI-H** (without bromide) in chloroform solution and are depicted in **Figure 2A**. In solution, PMI-H and PMI-Br (2) exhibit two absorption peaks whereas all three acceptors 3a-c have less resolved absorption peaks. Due to the increased π-system of the linked molecules, the absorption spectra are 19 nm redshifted compared to PMI-Br (Table 2). This was also reported by Y. Zhang et al. for **PMI-F-PMI**.[37] Absorption spectra of thin films on glass substrates of **PMI-F-PMI**, **PMI-FSi-PMI**, **PMI-FN-PMI** (see **Figure 2B**) are broadened compared to their spectra in solution which is due to π-π stacking.

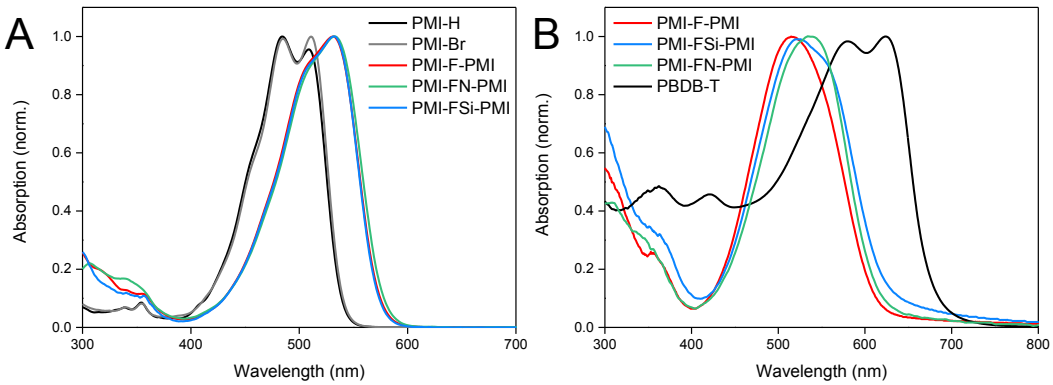

Fig. 2 *(A) Optical absorption spectra of PMI (1), PMI-Br (2),* ***PMI-F-PMI (3a)****,* ***PMI-FSi-PMI (3b)*** *and* ***PMI-FN-PMI (3c)*** *in solution (chloroform); (B) thin film absorption spectra of* ***PMI-F-PMI (3a)****,* ***PMI-FSi-PMI (3b)****,* ***PMI-FN-PMI (3c)*** *and PBDB-T.*

The molar absorption coefficients (in solution) for all compounds were calculated. Herein, the linked molecules, containing two PMI units, show an almost three times higher values of absorption coefficient ($8.9 – 9.0 \cdot 10^4$ M^{-1} cm^{-1}) compared to the starting materials ($3.3 \cdot 10^4$ $M^{-1}cm^{-1}$). This can be ascribed to the extended π-system within the molecules **3a-c**.

All compounds show fluorescence in solution (chloroform) with a Stokes shift of 57 nm, 55 nm and 65 nm and nearly identically fluorescence quantum yields to be 0.74, 0.74 and 0.72 for **PMI-F-PMI**, **PMI-FSI-PMI** and **PMI-FN-PMI**, respectively (Figure S12, Table 2). These values are only slightly lower than those of the PMI-H and PMI-Br (0.81 and 0.86 respectively), indicating that the introduction of the linker with long alkyl side chains does not result in large increase of (unfavorable) non-radiative relaxation pathways from the excited state.

Furthermore, fluorescence excitation and emission scans of the acceptor thin films were performed under ambient conditions (**Figure 3**). The optical band gap energies were determined from the intersection between the excitation and emission spectra, since this method is less sensitive to scattering effects compared to the commonly used method of determining the optical band gap from the onset of the absorption spectrum.[40] The small inset in **Figure 3** depicts an enlarged view of the intersection region around 600 nm and shows that the excitation and emission

spectra intersect at 601, 602 and 601 nm for **PMI-F-PMI**, **PMI-FSi-PMI** and **PMI-FN-PMI**, respectively. This translates to an optical band gap of 2.06 eV for all three materials (**Table 2**).

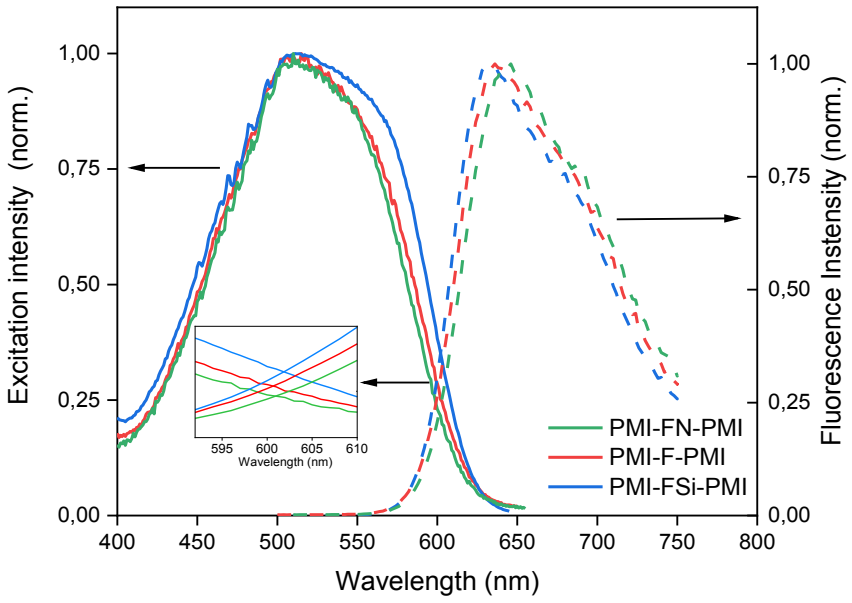

Fig. 3 *Normalized fluorescence excitation (solid lines) and emission (dashed lines) spectra of the PMI-X-PMI in $CHCl_3$ solution.*

Table 2 *Optical and electrical characteristics of PMI, PMI-Br (2),* ***PMI-F-PMI (3a)****,* ***PMI-FSi-PMI (3b)*** *and* ***PMI-FN-PMI (3c)***

Material	$\lambda_{max, sol.}$ (nm)	$\lambda_{onset (sol.)}$ (nm)	$\lambda_{max, (fluor., sol.)}$ (nm)	$\phi_{FL)}$	E_g (eV)	ε ($M^{-1} cm^{-1}$)	$\lambda_{max, film}$ (nm)	HOMO[el.] (eV)	LUMO[el.] (eV)	μ_{e_FET} (saturation) (cm^2/Vs)	μ_{e_FET} (linear) (cm^2/Vs)
PMI	485	539	539	0.81	2.30[1]	$3.3 \cdot 10^4$	-	-	-	-	-
PMI-Br	511	541	541	0.86	2.29[1]	$3.3 \cdot 10^4$	-	-	-	-	-
PMI-F-PMI	530	575	587	0.74	2.16[1]/2.06[2]	$9.0 \cdot 10^4$	516	-6.12	-3.93	$2.4 \cdot 10^{-4}$	$1.9 \cdot 10^{-4}$
PMI-FSi-PMI	530	573	585	0.74	2.16[1]/2.06[2]	$8.9 \cdot 10^4$	523	-6.12	-3.97	$1.3 \cdot 10^{-4}$	$1.1 \cdot 10^{-4}$
PMI-FN-PMI	530	576	595	0.72	2.16[1]/2.06[2]	$8.8 \cdot 10^4$	536	-6.16	-3.94	$1.6 \cdot 10^{-4}$	$1.2 \cdot 10^{-4}$

[1] solution; [2] thin films, [el] determined by CV

In addition to the optical bandgap, the electrochemical bandgap was investigated performing cyclic voltammetry (CV) measurements on drop-casted films of **PMI-F-PMI**, **PMI-FSi-PMI** and **PMI-FN-PMI,** as well as of the donor polymer **PBDB-T**. The oxidation and reduction onsets were determined from CV measurements as shown in Figure S13. HOMO and LUMO energy levels of the investigated materials were calculated according to the equations described in the experimental section and the results are depicted in Table 2. The electrochemical measurements suggest only minor differences between the respective HOMO and LUMO levels of the newly synthesized acceptor materials, which is supported by almost identical optical properties observed in absorbance and fluorescence measurements. Electrochemical bandgaps of 2.19, 2.15 and 2.22 eV were obtained for **PMI-F-PMI**, **PMI-FSi-PMI** and **PMI-FN-PMI** respectively, which are in good agreement with the reported electrochemical bandgap of **PMI-F-PMI** in literature.[38]

For the investigation of the performance of **PMI-F-PMI**, **PMI-FSi-PMI** and **PMI-FN-PMI** in solar cells, PBDB-T was selected as donor material due to its optoelectronic properties, which fit well to the three synthesized NFAs, as well as due to its good solubility and processability.[4] The chemical structure of PBDB-T is shown in Scheme 2. A HOMO level of -5.89 eV and a LUMO level of -3.45 eV were determined from CV measurements of PBDB-T. These values result in a HOMO energy level offset of approximately 0.25 eV and a LUMO level offset of around 0.5 eV compared to the energy levels of **PMI-F-PMI**, **PMI-FSi-PMI** and **PMI-FN-PMI**.

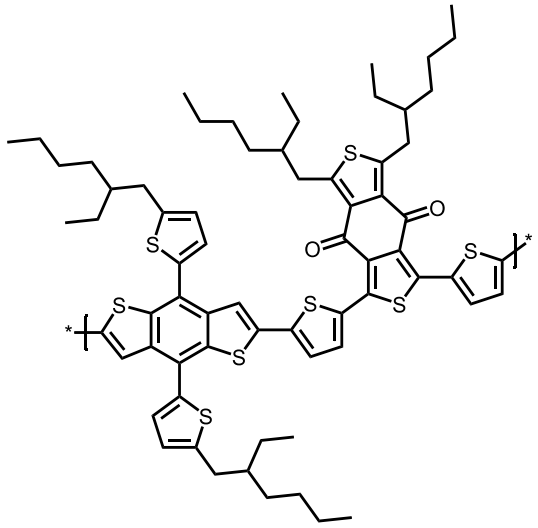

Scheme 2 *Structure of the conjugated polymer PBDB-T.*

In order to investigate the electronic properties of the newly synthesized acceptor materials, organic field effect transistors were fabricated with **PMI-F-PMI**, **PMI-FSi-PMI** and **PMI-FN-PMI** in a bottom-gate, top-contact geometry as shown in Figure S14. The electron mobilities in the linear and saturation regime were extracted from OFET transfer characteristic measurements. The measurements are shown in Figure S15 and the determined electron mobilities are presented in **Table 2**. All three acceptors exhibit similar values of OFET electron mobility in the range of low 10^{-4} cm^2/Vs.

Crystallization properties and molecular packing

In a next step, we performed grazing incidence wide angle X-ray scattering (GIWAXS) measurements to study the crystallinity and molecular packing of the synthesized compounds. **Figure 4** shows the 2D-GIWAXS patterns of pristine **PMI-F-PMI**, **PMI-FSi-PMI** and **PMI-FN-PMI** thin films. In the GIWAXS images of the samples without annealing as well as in the corresponding line cuts in in-plane and out-of-plane direction (**Figure 4 A-D**) only weak features are visible. After annealing of the films at 150 °C, the crystallinity and order of the molecules is enhanced and more distinct signals are revealed (see **Figure 4 E-H**), which are most pronounced for **PMI-FSi-PMI**. This sample shows diffraction peaks at 2.6 and 4.1 nm^{-1} in the in-plane direction, which correlates to distances of 2.4 and 1.5 nm and suggests a two-dimensional order. Moreover, these peaks in the in-plane direction are characteristic for a preferential face-on orientation with respect to the substrate. The signal at 17.9 nm^{-1} in out-of-plane direction corresponds to a d-spacing of 0.35 nm, which indicates π–π stacking. Due to the fact that also for the **PMI-F-PMI** and **PMI-FN-PMI** films a broad diffraction peak around 4 nm^{-1} in in-plane direction is observed, we also assume a preferential, disordered face-on orientation in these samples. However, no pronounced crystallization of the investigated NFAs is suggested by the GIWAXS data.

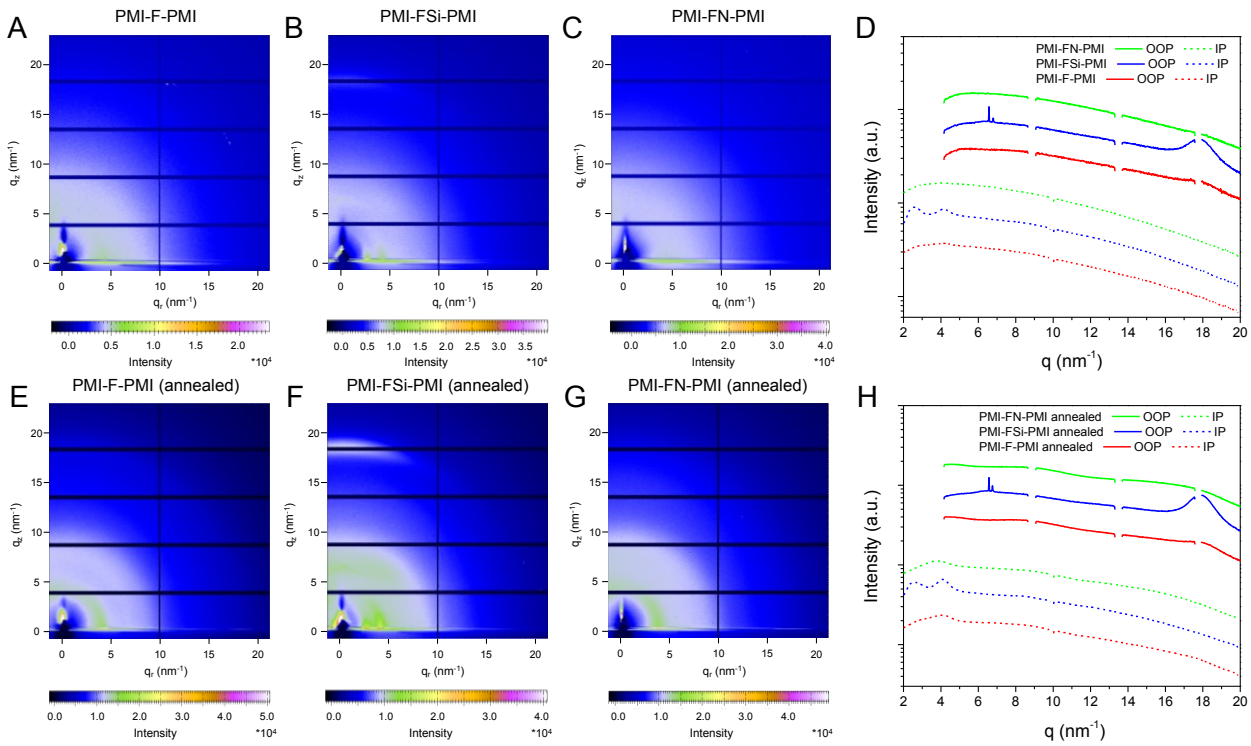

Fig. 4 *2D GIWAXS patterns of: A -* ***PMI-F-PMI (3a)****, B -* ***PMI-FSi-PMI (3b)*** *and C -* ***PMI-FN-PMI (3c)*** *w/o annealing and E -* ***PMI-F-PMI (3a)****, F-* ***PMI-FSi-PMI (3b)*** *and G -* ***PMI-FN-PMI (3c)*** *w. annealing. D, H: The corresponding 1D line cuts in in-plane (IP) and out-of-plane (OOP) direction. The scattering profiles are shifted vertically for better visibility.*

The GIWAXS images of pristine PBDB-T films without and with annealing are depicted in Figure S16. According to previous reports in the literature,[41,42] the GIWAXS images reveal a typical pattern for preferential face-on orientation. The most pronounced features are a diffraction peak in the out-of-plane direction at 17.0 nm^{-1}, corresponding to a π–π stacking distance of 0.37 nm and a lamellar diffraction peak at 2.85 nm^{-1} in in-plane direction corresponding to a lamellar d-spacing of 2.2 nm.

In the blend films of PBDB-T and the investigated NFAs (**Figure 5**), the signals stemming from the individual components are combined in the GIWAXS patterns, which indicates that the preferential face-on orientation found for the pristine materials is also present in the blend. The features of the conjugated polymer are in in-plane direction overlapped by the lamellar diffraction peaks of the NFAs which can be particularly recognized at q = 4.1 nm^{-1}. The relative intensity of this diffraction peak is the highest in the PBDB-T/**PMI-FSi-PMI** film, followed by the

PMI-F-PMI containing blend film, which is in line with the results from the pristine NFA films where the crystallinity also decreased from **PMI-FSi-PMI** to **PMI-F-PMI** to **PMI-FN-PMI**. In the out-of-plane direction, the diffraction peak at 17.5 nm^{-1} is more pronounced in all three blend films compared to the pattern of the pristine polymer and the maximum is slightly shifted towards higher q-values due to an overlap of the peaks of both components of the blend.

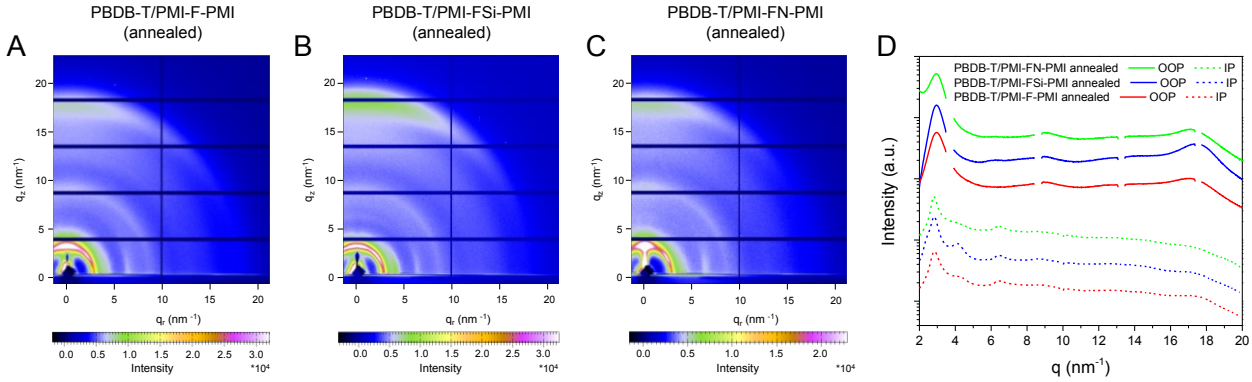

Fig. 5 *2D-GIWAXS patterns of donor/acceptor blends with a ratio of 1/1 for: A -* ***PMI-F-PMI (3a)****, B -* ***PMI-FSi-PMI (3b)*** *and C -* ***PMI-FN-PMI (3c)*** *w. annealing and D - 1D-line cuts in the in-plane (IP) and out-of-plane (OOP) directions. The scattering profiles are shifted vertically for better visibility.*

Photovoltaic performance

Solar cells with the three synthesized NFAs – **PMI-F-PMI**, **PMI-FSi-PMI** and **PMI-FN-PMI** – were fabricated using an inverted device architecture – glass/ITO/ZnO/absorber/MoO_3/Ag (**Figure 6A**).

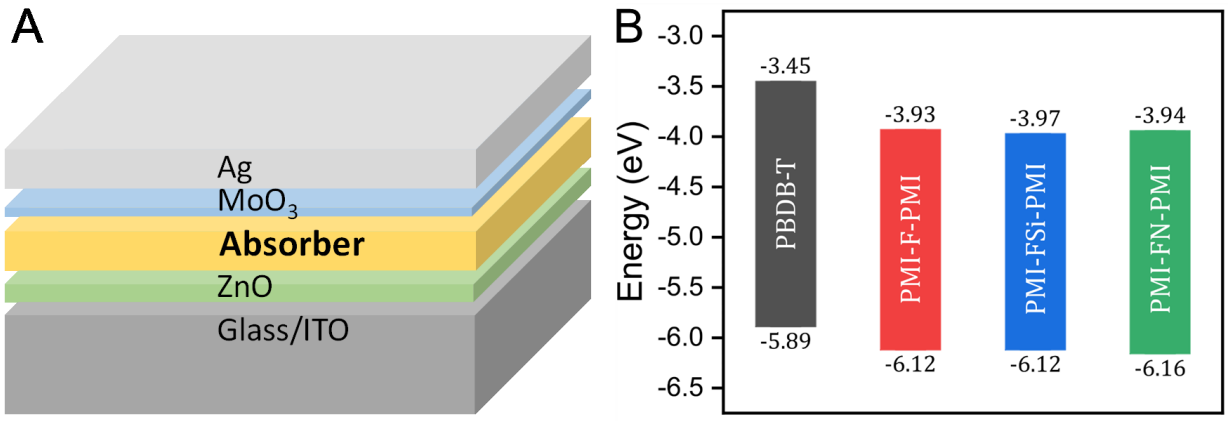

***Fig. 6** (A) Device architecture of the fabricated solar cells and (B) energy diagram of **PMI-F-PMI (3a)**, **PMI-FSi-PMI (3b)**, **PMI-FN-PMI (3c)** and PBDB-T. The HOMO/LUMO levels were determined by cyclic voltammetry.*

The donor/acceptor (D/A) blends were mixed in CB and spin coated at 70 °C in a two-step spin coating process to form a homogenous film. Solar cells with different D/A ratios of 1/0.66, 1/1 and 1/1.5 (w/w) were fabricated and their influence on solar cell performance was investigated. Herein, solar cells with a D/A ratio of 1/0.66 showed the highest power conversion efficiencies of 3.79%, 3.06% and 3.42% for **PMI-F-PMI**, **PMI-FSi-PMI** and **PMI-FN-PMI,** respectively(Table 3). For all solar cells, high V_{OC}s between 1.05 and 1.10 V were obtained.

In addition, the respective J-V curves and the characteristic parameters of solar cells with D/A ratios of 1/1 and 1/1.5 are summarized in the ESI (Figure S17A and B, Table S2). It should be noted that upon increasing the ratio of the acceptor, a decreased current density and fill factor are the main cause for the decrease in device performance, which can be ascribed to an unbalanced charge transport and the slightly thicker absorber layers in these solar cells.

To further increase the device performance, the absorber layers with a D/A ratio of 1/0.66 were thermally annealed directly after spin coating. Two annealing temperatures (135 and 150 °C,

annealing time: 5 min) were chosen, as the glass transition temperature of PBDB-T was found to be in the range of 145 °C (the corresponding DSC data are plotted in Figure S18). Indeed, using such an annealing step leads to an increase of the overall performance. While for **PMI-F-PMI** based solar cells an annealing temperature of 135 °C led to the best PCEs, for the **PMI-FSi-PMI** and **PMI-FN-PMI** based devices, the best performance was obtained upon annealing at 150 °C. J-V curves of the best solar cells (non-annealed and annealed) measured under illumination and in dark conditions are depicted in **Figure 7A-C** and their solar cell characteristics are given in Table 3 and Table S3. Noticeable, the current density increased by 1-2 mA/cm^2 due to the annealing step and the highest current density (10.18 mA/cm^2) was obtained for the PBDB-T/PMI-FN-PMI-based solar cell. Moreover, the fill factors of the solar cells with all three NFAs could also be significantly enhanced due to an increased crystallinity in the absorber layer. This results in maximum device efficiencies of 5.16% for the **PMI-F-PMI**-based solar cells annealed at 135 °C and for the **PMI-FSi-PMI** and **PMI-FN-PMI**-based solar cells annealed at 150 °C.

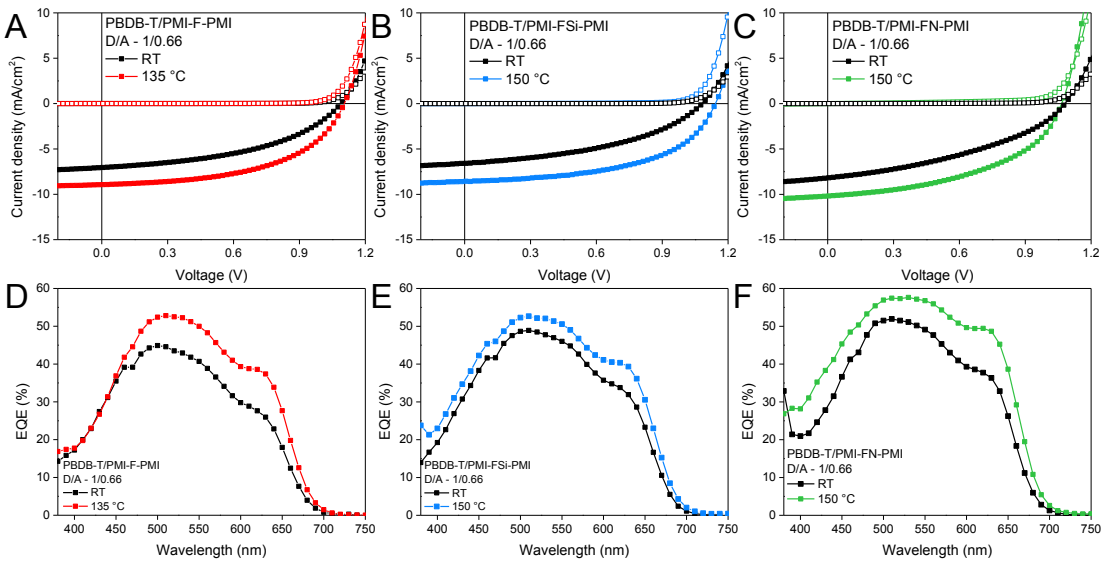

***Fig.** 7 J-V curves (under illumination - solid symbols and under dark conditions - hollow symbols; notice that the hollow curves overlay) and EQE spectra of the best solar cells of PBDB-T: A,D – **PMI-F-PMI (3a)**, B,E - **PMI-FSi-PMI (3b)** and C,F - **PMI-FN-PMI (3c)** with a D/A ratio of 1/0.66 w. and w/o annealing of the absorber.*

Table 3 *Best and average device characteristics of PBDB-T –* ***PMI-F-PMI****,* ***PMI-FSi-PMI*** *and* ***PMI-FN-PMI*** *based solar cells (D/A – 1 /0.66) with and without annealing of the absorber layer. The average values and standard deviations were calculated from the best 15 cells.*

Compound	Annealing temperature	Thickness (nm)	V_{OC} (V)	J_{SC} (mA/cm^2)	FF (%)	PCE (%)
PMI-F-PMI						
best cell	-	93	1.10	7.04	4.54	3.48
average		88 ± 3.7	1.06 ± 0.03	6.54 ± 0.28	44.7 ± 1.7	3.09 ± 0.18
best cell	135 °C	85	1.10	8.94	52.9	**5.16**
average		93 ± 6.7	1.09 ± 0.04	8.13 ± 0.47	48.8 ± 2.9	4.34 ± 0.37
PMI-FSi-PMI						
best cell	-	88	1.08	6.58	43.4	3.06
average		92 ± 13	1.05 ± 0.05	6.08 ± 0.33	42.4 ± 1.7	2.69 ± 0.15
best cell	150 °C	78	1.14	8.55	53.4	**5.16**
average		75 ± 2.4	1.12 ± 0.02	7.88 ± 0.42	53.1 ± 1.5	4.67 ± 0.28
PMI-FN-PMI						
best cell	-	80	1.08	8.17	39.6	3.46
average		90 ± 7.6	1.08 ± 0.03	7.08 ± 0.30	40.1 ± 1.9	3.07 ± 0.15
best cell	150 °C	78	1.06	10.18	48.0	**5.16**
average		81 ± 13	1.11 ± 0.04	9.10 ± 0.62	44.2 ± 2.6	4.45 ± 0.36

External quantum efficiency (EQE) spectra of **PMI-F-PMI**, **PMI-FSi-PMI** and **PMI-FN-PMI** based solar cells with a D/A ratio of 1/0.66 (non-annealed and annealed) are depicted in **Figure 7D-F**. The EQE spectra show an onset of photocurrent generation at 700 nm corresponding to the absorption onset of PBDB-T. Moreover, the photoresponse of the EQE spectra matches well with

the absorption spectra of the blend films revealing a contribution of donor and acceptor component to charge carrier generation. The pronounced broad shoulder around 630 nm matches with the absorption maximum of the conjugated polymer and the maxima of the EQE spectra are in line with the maxima of the absorption spectra of the new acceptors. Moreover, in the EQE spectra of the solar cells prepared with D/A ratios of 1/1 and 1/1.5 (see Figure S17C and D) the increased acceptor content in the absorber layer leads to an increased photocurrent generation in the spectral region in which the PMI-based acceptors show strong absorption, compared to the wavelength region above 600 nm where the photocurrent generation is based on absorption in PBDB-T - the donor component in the absorber layer (cf. absorption spectra in Figure S19).

The current densities calculated from the EQE data match well with current densities from the J-V measurements performed either before or after the EQE measurements (Table S4). As these measurements were performed in ambient atmosphere, slightly reduced J_{SC} values were observed after the EQE measurements. As expected, for the devices annealed at 135 or 150 °C, respectively, increased EQE values were obtained. Herein the annealed solar cells with the **PMI-F-PMI**, **PMI-FSi-PMI** and **PMI-FN-PMI** acceptors (D/A ratio of 1/0.66) showed maximum EQE values of 53%, 53% and 57%, respectively.

Moreover, the stability of the solar cells (D/A ratio 1 /0.66, annealing at 150 °C) was investigated. Therefore, solar cells with device efficiencies close to the average values mentioned in Table 3 were selected for maximum power point (MPP) tracking under continuous illumination and active load for 24 hours. As can be seen in **Figure 8**, the solar cells reveal a stable output over 24 h. The device performance even increased slightly and for all three solar cells more than 100% of their initial device efficiency were found after the testing period. The main part of the increase in PCE occurred during the first 60 minutes, which most likely stems from an increased conductivity of the ZnO layer due to light soaking.[43]

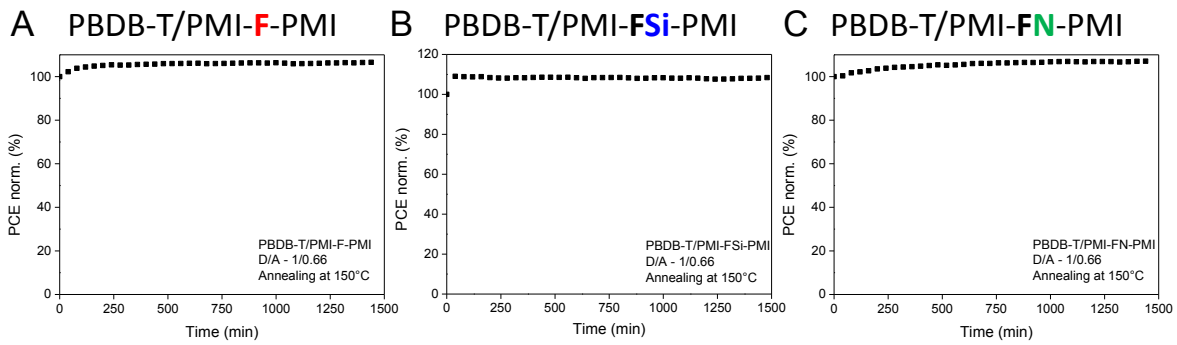

Fig. 8 *Maximum power tracking of solar cells with the PBDB-T/acceptor absorber layers: A -* ***PMI-F-PMI (3a)****, B-* ***PMI-FSi-PMI (3b)*** *and C -* ***PMI-FN-PMI (3c)*** *(D/A – 1/0.66, annealed at 150 °C), measured for 24 h under inert conditions.*

Film morphology

Since annealing of the solar cells strongly improved the photovoltaic performance, AFM measurements were performed on not annealed and annealed samples in order to investigate possible morphological changes of the organic semiconductor surface. The AFM images of the absorber layers of the solar cells with D/A ratios of 1/0.66 processed without annealing, as well as post-annealed devices at 135/150 °C are presented in Figure 9.

The AFM topography images of the PBDB-T/**PMI-F-PMI** and PBDB-T/**PMI-FSi-PMI** samples (**Figure 9A and B)** are characterized by a surface morphology consisting of a spheroidal structure with small domains. In the non-annealed PBDB-T/**PMI-FN-PMI** absorber layer (**Figure 9C**), the spheroidal structure is superimposed by a fiber-like surface morphology. Regarding the surface roughness, R_q values of ~4-6 nm are found in the PBDB-T/**PMI-F-PMI** and PBDB-T/**PMI-FN-PMI** samples and the PBDB-T/**PMI-FSi-PMI** sample, in which the crystallization of the acceptor is more pronounced, exhibited higher R_q values of 7-8 nm.

The AFM images of the absorber layer of the devices, which have been heat treated at 135/150 °C, are shown in **Figure 9D-F**. Morphology-wise there are no significant differences between the annealed and non-annealed absorber layers based on **PMI-F-PMI** and **PMI-FSi-PMI**, However, in the PBDB-T/**PMI-FN-PMI** sample the fiber-like structure is distinctly more pronounced. Regarding the surface roughness, the annealing process tends to reduce the Rq values for all three

absorber layers. However, the change is quite subtle and influences of other effects like local morphology variations cannot be excluded.

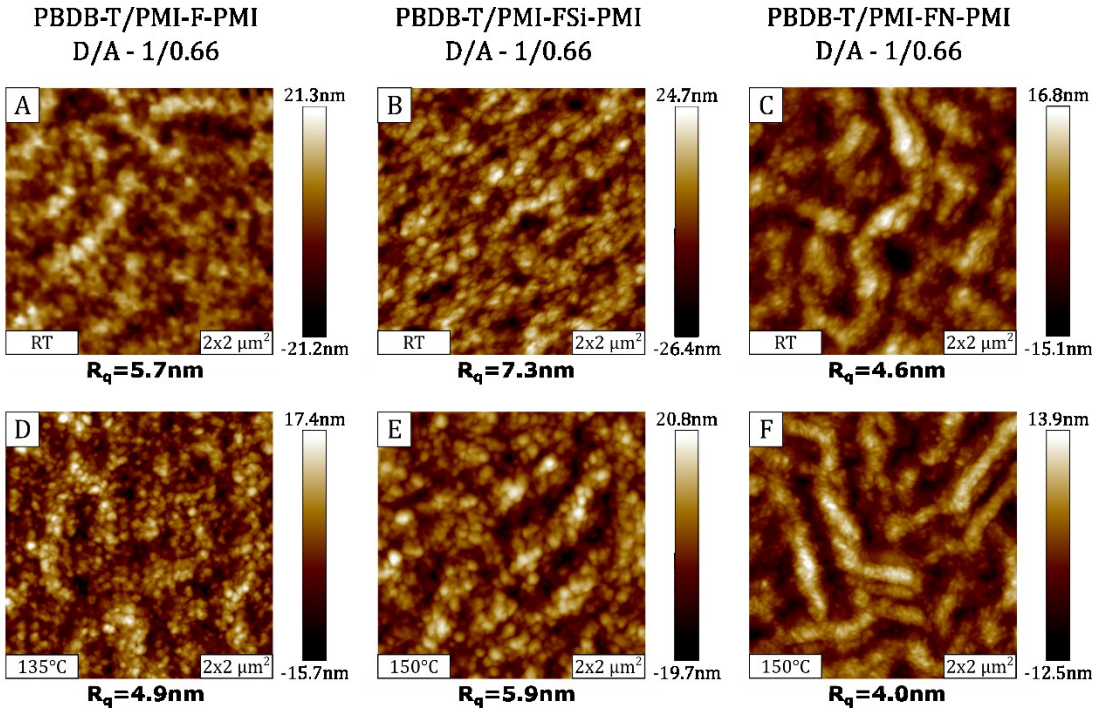

Fig. 9 *2x2µm2 AFM images of as cast and post-annealed solar cell devices. The images in the first row (A, B, C) depict the surface of the absorber layers without thermal annealing, while in the second row (D, E, F) the images of the annealed samples are presented.*

Conclusion

Three different perylene monoimide non-fullerene acceptors bridged via fluorene, silafluorene and carbazole linkers – **PMI-F-PMI**, **PMI-FSi-PMI** and **PMI-FN-PMI** – were synthesized via Suzuki coupling. DFT calculations displayed suitable HOMO/LUMO levels for the application as acceptors in organic solar cells and a 55° dihedral angle between the PMI units and the linkers. This twisting together with the long alkyl chains on the central linker unit as well as the diisopropylphenyl substituents on the PMI part helps to avoid pronounced π-π-stacking and leads to an excellent solubility. The three A-D-A type acceptors exhibit an absorption maximum at around 530 nm, absorption coefficients of $9 \cdot 10^4$ cm^{-1} and good fluorescence quantum yields (~70%). It was found that the introduction of the heteroatoms in the fluorene-derivative linker does not significantly influence the electronic properties such as HOMO/LUMO levels or charge carrier mobilities. A distinct difference was, however, observed regarding structural properties as GIWAXS measurements revealed that the crystallinity of PMI-FSi-PMI is significantly more pronounced compared to the other two investigated acceptors. Interestingly, these differences in crystallinity and molecular packing do not substantially influence the performance of the organic solar cells, which were fabricated in an inverted device setup using the conjugated polymer PBDB-T as donor material. The solar cells based on all three acceptors show similar device performances. The highest PCEs were obtained using a D/A ratio of 1/0.66 (w/w). Thermal annealing of the absorber layers leads to increased crystallinity of the absorber layers, which is also reflected in increased device efficiencies up to 5.16%.

Experimental

Materials and methods

All reagents and solvents were purchased from commercially available sources (Sigma Aldrich, Lumtec, abcr, VWR, Roth) and used as received.

Synthetic procedures

The synthesis of PMI and PMI-Br were performed and verified according to literature procedures.[44,45] PMI-F-PMI, PMI-FSi-PMI and PMI-FN-PMI were synthesized under standard Suzuki-coupling conditions in toluene with $Pd(PPh_3)_4$ catalyst. The detailed synthesis procedures are given in the Supporting Information.

Fabrication of solar cells

Patterned glass/ITO substrates (15 × 15 × 1.1 mm^3) (15 Ω/sq) from Luminescence Technology Corp. were precleaned with acetone, put in an isopropyl alcohol bath, and placed into an ultrasonic bath at 40 °C for 30 min. The substrates were then dried with N_2 and plasma etched for 3 minutes. The zinc oxide precursor solution was prepared by dissolving 500 mg zinc acetate dihydrate in 5 ml 2-methoxyethanol and 150 µl ethanolamine while stirring for 8 hours, followed by filtration (0.45 µm PVDF filter). The precursor solution was spin coated at 4000 rpm for 30 s and afterwards annealed at 150 °C for 15 minutes in air. The donor/acceptor solutions were prepared in an N_2 filled glove box with D/A weight ratios of 1/0.66, 1/1 and 1/1.5. The concentration of the donor PBDB-T was kept constant at 10 mg/ml (solvent: chlorobenzene) and the amount of the acceptor was adjusted according to the envisaged D/A weight ratio. The blend solutions were stirred at 50 °C over night. Before applying the blend, the solution was heated to 70 °C for 30 minutes and then hot spin coated (70 °C) on the zinc oxide layer. A two-step spin coating process was used to achieve layer thicknesses around 100 nm (first step) and to dry the substrate (5000 rpm / 5 s) (second step). A part of the samples was annealed at 135 °C or 150 °C for 5 min. Therefore, the heating plate was thoroughly calibrated using a PT100 temperature sensor mounted on a glass/ITO

substrate prior to the annealing experiments. The solar cells were completed by thermal evaporation of MoO_3 (10 nm) and Ag (100 nm) under high vacuum conditions ($1 \cdot 10^{-5}$ mbar).

Characterization techniques

NMR spectroscopy (^1H, APT) was performed on a Bruker Avance 300 MHz and/or Varian Inova 500 MHz spectrometers. Chemical shifts were referenced to tetramethylsilane (TMS – 0.00 ppm) or a solvent peak ($CDCl_3$ ^{13}C 77.16 ppm). Deuterated chloroform-d with 0.03% TMS was obtained from Cambridge Isotope Laboratories Inc.

MALDI-TOF mass spectrometry was performed on a Micromass TofSpec 2E time-of flight mass spectrometer. The instrument was equipped with a nitrogen laser (l = 337 nm, operated at a frequency of 5 Hz) and a time lag focusing unit. Ions were generated just above the threshold laser power. Positive ion spectra were recorded in reflection mode with an accelerating voltage of 20 kV. The spectra were externally calibrated with a polyethylene glycol standard. Data analysis was done with MassLynx-Software V3.5 (Micromass/Waters, Manchester, UK). Samples were dissolved in dichloromethane (c = 1 mg/ml). The matrix was either trans-2-[3-(4-tert-butylphenyl)-2-methyl-2-propenylidene]malononitrile (DCTB) or Dithranol (c = 10 mg/ml). Sample and matrix were mixed in a ratio of 2:7 and was spotted onto the target and allowed to air-dry.

Decomposition temperatures were determined using a Netzsch Jupiter STA 449C thermogravimetric analyzer in aluminium crucibles under helium atmosphere with a flow rate of 50 mL/min. The operated temperature range was between 20–550 °C with a heating rate of 10 °C/min. Differential scanning calorimetry (DSC) was performed on a DSC 8500 (Perkin Elmer USA) using heating rates of 20 °C/min and 40 °C/min under nitrogen atmosphere, with flowrate of 20 mL/min. Glass-transition temperatures (Tg) from the second heating run were interpreted as the midpoint of change in heat capacity. The samples (3-10 mg) were measured in aluminium pans.

Computations were done using Gaussian09 software.[39] Ground state minimal energy was localized, followed by its verification with frequency calculation (B3LYP level of theory, 6-31G* basis set). Excitation energy was calculated using TD-DFT (B3LYP, 6-31+G*).

Absorption spectra were recorded on a Shimadzu spectrophotometer UV-1800 (300 to 1000 nm). Spectra of solutions were recorded in chloroform and for the measurements of thin film spectra samples on glass substrate were used. Fluorescence measurements were recorded in ambient atmosphere on a FluoroLog 3 spectrofluorometer from Horiba Scientific equipped with an NIR-sensitive R2658 photomultiplier from Hamamatsu (300–1050 nm). Compounds were measured in a solution of chloroform (c = 1 to 4 µmol/l) and on glass substrates. Relative luminescence quantum yields were determined using Lumogen orange (Kremer Pigmente, Germany) as reference compound (ϕ_{fl} = 1.0 in $CHCl_3$).[46] Excitation and emission scans of the acceptor thin films were measured with a PTI QuantaMaster 40.

Cyclic voltammetry (CV) measurements of PBDB-T, PMI-F-PMI, PMI-FSi-PMI and PMI-FN-PMI were performed to determine their respective HOMO-LUMO energy levels using a Jaissle Potentiostat-Galvanostat IMP 88 PC-100. A standard three-electrode setup was used where an Ag/AgCl wire served as quasi-reference electrode and two Pt-plates served as working and counter electrodes. On a hotplate (50 °C) and in nitrogen atmosphere the investigated organic materials were deposited onto the working electrode via drop-casting. All CV measurements were performed in a nitrogen glovebox using 0.1M tetrabutylammoniumhexafluorophosphate ($TBAPF_6$) in acetonitrile (MeCN) as the electrolyte solution. The scan speed was 50 mV/s. Two separate measurements on freshly drop-casted materials were carried out to determine the oxidation and reduction onset, respectively. In order to avoid the effect of possible trapped charges, measurements to determine the oxidation onset were cycled through starting from zero to positive voltages, whereas measurements to determine the reduction onset were cycled through starting from zero to negative voltages. Every measurement was externally calibrated by measuring the half-wave potential of a Fc/Fc^+ redox couple. The HOMO and LUMO energy levels were calculated using the following equations[47]:

$$E_{HOMO} = -(4.75 + E^{ox}_{onset\ vs.\ NHE})\ eV$$
$$E_{LUMO} = -\left(4.75 + E^{red}_{onset\ vs.\ NHE}\right)\ eV$$

The fermi energy level of NHE vs vacuum was taken as -4.75eV, whereas the redox potential of Fc/Fc^+ vs. NHE was taken as 0.64 V.[48]

OFET fabrication and characterization: As a first step, the OFET glass substrates were sonicated for 15 minutes in Hellmanex®, deionized water, acetone and isopropanol, followed by a 5-minute O_2 plasma treatment (50 W). OFET devices were fabricated in a bottom-gate, top-contact geometry with aluminum top electrodes (source and drain) and an aluminum gate electrode covered with a thin, insulating oxide layer. The aluminum bottom-gate electrode was thermally evaporated through a shadow mask onto a pre-cleaned glass substrate under a base pressure of $2 \cdot 10^{-6}$ mbar until a thickness of 100 nm was reached. Subsequently, electrochemical anodization was used to grow a 32 nm dielectric Al_2O_3 layer. The Al gate electrode is immersed into a 0.01M electrolyte solution of citric acid/trisodium citrate in ultrapure 18 MΩ water (0.265 g / 2.57 g in 100 ml H_2O) and serves as working electrode[49]. A Pt-foil is placed parallel to the substrate, which acts as a counter electrode. Applying a constant voltage of 20 V for several minutes leads to the formation of a 32 nm thick oxide layer, due to an oxide formation factor of 1.6 nm/V for this electrolyte system[50].

As a next step, the substrates were rinsed thoroughly with 18 MΩ water, dried and transferred into a nitrogen filled glovebox, where a thin passivation layer of benzocyclobutene (BCB) (1:50 diluted in mesitylene) was spin-coated at 25 rps for 45 seconds. Typical film thicknesses of the BCB layers were between 10-15 nm. Afterwards, the substrates were annealed at 280 °C for 1 hour on a hotplate in nitrogen atmosphere in order to cure the BCB layer.

The organic semiconductor materials (PMI-F-PMI, PMI-FSi-PMI and PMI-FN-PMI) were spin-coated on top of the BCB layer under nitrogen atmosphere with a two-step spin-coating recipe of 20 rps for 10 s followed by 67 rps for 20 s. As a final step, Al source and drain top electrodes were thermally evaporated on top of the semiconductor using a shadow mask. Evaporation conditions were the same as described for the gate electrode. The evaporation mask geometry of source, drain and gate electrodes results in transistors with a channel width W of 2000 µm and a channel length L of 65 µm.

OFET devices were measured in a nitrogen filled glove box with an Agilent B1500A semiconductor device parameter analyzer. Transistor transfer curves were measured by sweeping the gate voltage from 0 to 10 V and back to 0 V in 50 mV steps. After each sweep the drain voltage was increased by 2 V until a final drain voltage of 10 V was reached.

The surface morphology of the active layer of the solar cell devices was characterized with a Brucker Innova AFM. Measurements were carried out in tapping mode and under ambient conditions.

2D grazing incidence wide angle X-ray scattering (GIWAXS) measurements were performed at the Austrian SAXS Beamline 5.2L of the electron storage ring ELETTRA Trieste at a photon energy of 8 keV.[51] For the detection of the GIWAXS images, a Dectris Pilatus3 1M detector was used set to a sample detector distance of 294 mm. The angular calibration of the detector was carried out using silver behenate powder (d-spacing: 58.38 Å). All measurements have been performed with a grazing angle of 0.17°. The in-plane cuts taken at the Yoneda wing (q_r) and out-of-plane cuts (q_z) along the Ewald sphere have been determined with the data evaluation software SAXS Dog.

Surface profilometry measurements were performed on a Bruker DektakXT stylus surface profiling system equipped with a 12.5 µm-radius stylus tip. Line scans were recorded over a length of 500 µm, with a stylus force of 3 mg, and a resolution of 0.33 µm/pt. The layer thicknesses were determined from two-dimensional surface profiles using Vision 64 software (Bruker).
J–V curves of all devices were recorded inside a glovebox (nitrogen atmosphere) with a scan rate of 200 mV/s using a Keithley 2400 source meter connected to a LabView-based software. Illumination (100 mW/cm^2) was provided by a Dedolight DLH400 lamp, calibrated using a monocrystalline silicon WPVS reference solar cell from Fraunhofer ISE. The active area of the solar cells was defined by a shadow mask (2.65 x 2.65 mm) used for the illumination. External quantum efficiency (EQE) measurements were acquired using a MuLTImode 4-AT monochromator (Amko) equipped with a 75 W xenon lamp (LPS 210-U, Amko), a lock-in amplifier (Stanford Research Systems, Model SR830), and a Keithley 2400 source meter. The monochromatic light was chopped at a frequency of 30 Hz, and constant background illumination was provided by white light LEDs. The EQE spectra were measured in the wavelength range of 380–900 nm (increment: 10 nm). The measurement setup was spectrally calibrated with a silicon photodiode (818-UV/DB, Newport Corporation). The MPP tracking tests of the solar cells were performed under continuous illumination with a white light (6500 K) 10 W chip-on-board high power LED.

Acknowledgments

Financial support by the Austrian "Climate and Energy Fund" within the program Energy Emission Austria (Project: ALTAFOS, FFG No. *865 072*) is gratefully acknowledged. The authors thank Efthymia Vakalopoulou, Josefine Hobisch, Petra Kaschnitz and Karin Bartl for experimental support. Moreover, the authors acknowledge the CERIC-ERIC Consortium for the access to experimental facilities (Austrian SAXS beamline at Elettra Sincrotrone Trieste) and financial support.

References

[1] S. Günes, H. Neugebauer and N. S. Sariciftci, *Chem. Rev.,* 2007, **107**, 1324-1338.

[2] Y. Lin and X. Zhan, *Acc. Chem. Res.*, 2016, **49**, 175-183.

[3] Y. Liu, J. Zhao, Z. Li, C. Mu, W. Ma, H. Hu, K. Jiang, H. Lin, H. Ade and H. Yan, *Nat. Comm.*, 2014, **5**, 5293.

[4] J. Zhao, Y. Li, G. Yang, K. Jiang, H. Lin, H. Ade, W. Ma and H. Yan, *Nat. Energy*, 2016, **1**, 15027.

[5] G. Sauvé and R. Fernando, *J. Phys. Chem. Lett.*, 2015, **6**, 3770-3780.

[6] C. B. Nielsen, S. Holliday, H.-Y. Chen, S. J. Cryer and I. McCulloch, *Acc. Chem. Phys.*, 2015, **48**, 2803-2812.

[7] H. Kang, W. Lee, J. Oh, T. Kim, C. Lee and B. J. Kim, *Acc. Chem. Res.*, 2016, **49**, 2424-2434.

[8] X. Liu, B. Xie, C. Duan, Z. Wang, B. Fan, K. Zhang, B. Lin, F. J. M. Colberts, W. Ma, R. A. J. Janssen, F. Huang and Y. Cao, *J. Mater. Chem. A*, 2018, **6**, 395-403.

[9] X. Li, K. Wu, L. Zheng, Y. Deng, S. Tan and H. Chen, *Dyes Pigments*, 2019, **168**, 59-67.

[10] P. S. Rao, V. G. More, A. D. Jangale, S. V. Bhosale, R. S. Bhosale, A. L. Puyad, J-Y. Chen, J.-L. Li, S. V. Bhosale, A. Gupta and G. D. Sharma, *Dyes Pigments*, 2019, **171**, 107677.

[11] J. Yang, F. Chen, P. Cong, H. Xiao, Y. Geng, Z. Liao, L. Chen, B. Zhang and E. Zhou, *J. Energy Chem.*, 2020, **40**, 112-119.

[12] H. Yin, S. Chen, P. Bi, X. Xu, S. H. Cheung, X. Hao, Q. Peng, X. Zhu and S. K. So, *Org. Electron.*, 2019, **65**, 156-161.

[13] Y. Cui, H. Yao, J. Zhang, T. Zhang, Y. Wang, L. Hong, K. Xian, B. Xu, S. Zhang, J. Peng, Z. Wei, F. Gao and J. Hou, *Nat. Comm.*, 2019, **10**, 2515.

[14] G. Xie, Z. Zhang, Z. Su, X. Zhang and J. Zhang, *Nano Energy*, 2020, **69**, 104447.

[15] B. Fan, D. Zhang, M. Li, W. Zhong, Z. Zeng, L. Ying, F. Huang and Y. Cao, *Sci. China Chem.*, 2019, **62**, 746-752.

[16] Y. Wu, Y. Zheng, H. Yang, C. Sun, Y. Dong, C. Cui, H. Yan and Y. Li, *Sci. China Chem.*, 2020, **63**, 265-271.

[17] M. A. Green, E. D. Dunlop, J. Hohl-Ebinger, M. Yoshita, N. Kopidakis and A. W. Y. Ho-Baillie, *Prog. Photovoltaics Res. Appl.*, 2020, **28**, 3-15.

[18] C. W. Tang, *Appl. Phys. Lett.*, 1986, **48**, 183-185.

[19] Z. Luo, K. Wu, Y. Zhao, B. Qiu, Y. Li and C. Yang, *Dyes Pigments*, 2019, **163**, 356-362.

[20] J. Cheng, B. Li, X. Ren, F. Liu, H. Zhao, H. Wang, Y. Wu, W. Chen and X. Ba, *Dyes Pigments*, 2019, **161**, 221-226.

[21] J. Liu, S. Chen, D. Qian, B. Gautam, G. Yang, J. Zhao, J. Bergqvist, F. Zhang, W. Ma, H. Ade, O. Inganäs, K. Gundogdu, F. Gao and H. Yan, *Nat. Energy,* 2016, **1**, 16089.

[22] Y. Yang, Y. Wang, Y. Xie, T. Xiong, Z. Yuan, Y. Zhang, S. Qian and Y. Xiao, *Chem. Commun.*, 2011, **47**, 10749-10751.

[23] X. Lian, L. Zhang, Y. Hu, Y. Zhang, Z. Yuan, W. Zhou, X. Zhao and Y. Chen, *Org. Electron.*, 2017, **47**, 72-78.

[24] M. B. A. Qureshi, M. Li, H. Wang, J. Song and Z. Bo, *Dyes Pigments*, 2020, **173**, 107970.

[25] A. G. Macedo, L. P. Christopholi, A. E. X. Gavim, J. F. de Deus, M. A. M. Teridi, A. R. bin M. Yusoff and W. J. da Silva, *J. Mater. Sci. Mater. Electron.*, 2019, **30**, 15803–15824.

[26] V. Kamm, G. Battagliarin, I. A. Howard, W. Pisula, A. Mavrinskiy, C. Li, K. Müllen and F. Laquai, *Adv. Energy Mater.*, 2011, **1**, 297-302.

[27] A. Wadsworth, M. Moser, A. Marks, M. S. Little, N. Gasparini, C. J. Brabec, D. Baran and I. McCulloch, *Chem. Soc. Rev.,* 2018, **48**, 1596-1625.

[28] J. Zhang, H. S. Tan, X. Guo, A. Facchetti and H. Yan, *Nat. Energy*, 2018, **3**, 720-731.

[29] J. Zhang, Y. Li, J. Huang, H. Hu, G. Zhang, T. Ma, P. C. Y. Chow, H. Ade, D. Pan and H. Yan, *J. Am. Chem. Soc.*, 2017, **139**, 16092-16095.

[30] G. Zhang, J. Feng, X. Xu, W. Ma, Y. Li and Q. Peng, *Adv. Funct. Mater.*, 2019, **29**, 1906587.

[31] F. Tang, K. Wu, Z. Zhou, G. Wang, B. Zhao and S. Tan, *ACS Appl. Energy Mater.*, 2019, **2**, 3918-3926.

[32] Y. Li, M. Han, W. Yang, J. Guo, K. Chang, J. Wang, J. Min, Q. Li and Z. Li, *Mater. Chem. Front.*, 2019, **3**, 1840-1848.

[33] R. Qin, D. Guo, T. Y. Gopalakrishna, G. Li, J. Yang, Y. Jiang and H. Ma, *Dyes Pigments*, 2019, **160**, 540-545.

[34] D. Xia, F. Yang, J. Li, C. Li and W. Li, *Mater. Chem. Front.*, 2019, **3**, 1565-1573.

[35] J. Cremer and P. Bäuerle, *Eur. J. Org. Chem.*, 2005, 3715-3723.

[36] Y. Hu, S. Chen, L. Zhang, Y. Zhang, Z. Yuan, X. Zhao and Y. Chen, *J. Org. Chem.*, 2017, **82**, 5926-5931.

[37] Y. Zhang, Y. Xiao, Y. Xie, L. Zhu, D. Shi and C. Cheng, *Org. Electron.*, 2015, **21**, 184-191.

[38] Y. Zhang, X. Guo, B. Guo, W. Su, M. Zhang and Y. Li, *Adv. Funct. Mater.*, 2017, **27**, 1603892.

[39] Gaussian 09, Revision D.01, M. J. Frisch, G. W. Trucks, H. B. Schlegel, G. E. Scuseria, M. A. Robb, J. R. Cheeseman, G. Scalmani, V. Barone, B. Mennucci, G. A. Petersson, H. Nakatsuji, M. Caricato, X. Li, H. P. Hratchian,

A. F. Izmaylov, J. Bloino, G. Zheng, J. L. Sonnenberg, M. Hada, M. Ehara, K. Toyota, R. Fukuda, J. Hasegawa, M. Ishida, T. Nakajima, Y. Honda, O. Kitao, H. Nakai, T. Vreven, J. A. Montgomery, Jr., J. E. Peralta, F. Ogliaro, M. Bearpark, J. J. Heyd, E. Brothers, K. N. Kudin, V. N. Staroverov, T. Keith, R. Kobayashi, J. Normand, K. Raghavachari, A. Rendell, J. C. Burant, S. S. Iyengar, J. Tomasi, M. Cossi, N. Rega, J. M. Millam, M. Klene, J. E. Knox, J. B. Cross, V. Bakken, C. Adamo, J. Jaramillo, R. Gomperts, R. E. Stratmann, O. Yazyev, A. J. Austin, R. Cammi, C. Pomelli, J. W. Ochterski, R. L. Martin, K.

Morokuma, V. G. Zakrzewski, G. A. Voth, P. Salvador, J. J. Dannenberg, S. Dapprich, A. D. Daniels, O. Farkas, J. B. Foresman, J. V. Ortiz, J. Cioslowski and D. J. Fox, Gaussian, Inc., Wallingford CT, 2013.

[40] J. Gierschner, J. Cornil and H. J. Egelhaaf, *Adv. Mater.,* 2007*,* **19**, 173-191.

[41] H. Wu, H. Fan, S. Xu, C. Zhang, S. Chen, C. Yang, D. Chen, F. Liu and X. Zhu, *Sol. RRL*, 2017, ***1,*** 1700165.

[42] Z. Zhang and X. Zhu, *Chem. Mater.*, 2018, **30**, 587-591.

[43] X. Du, D. He, Z. Xiao and L. Ding, *Synth. Met.*, 2012, **162**, 2302-2306.

[44] R. T. Cheriya, J. Joy, S. K. Rajagopal, K. Nagarajan and M. Hariharan, *J. Phys. Chem. C*, 2012, **116**, 22631-22636.

[45] F. Nolde, W. Pisula, S. Müller, C. Kohl and K. Müllen, *Chem. Mater*., 2006, **18**, 3715-3725.

[46] G.Seybold, G.Wagenblast, *Dyes Pigment*., 1989, **11**, 303-317.

[47] C. M. Cardona, W. Li, A. E. Kaifer, D. Stockdale and G. C. Bazan, *Adv. Mater.,* 2011, **23**, 2367-2371.

[48] N. G. Connelly and W. E. Geiger, *Chem. Rev.*, 1996, **96**, 877–910.

[49] A. I. Mardare, M. Kaltenbrunner, N. S. Sariciftci, S. Bauer and A. W. Hassel, *Phys. Status Solidi A*, 2012, **209**, 813-818.

[50] M. Kaltenbrunner, P. Stadler, R. Schwödiauer, A. W. Hassel, N. S. Sariciftci and S. Bauer, *Adv. Mater*., 2011, **23**, 4892-4896.

[51] H. Amenitsch, M. Rappolt, M. Kriechbaum, H. Mio, P. Laggner and S. Bernstorff, *J. Synchrotron Rad*., 1998, **5**, 506-508.

Electronic Supplementary Information

Detailed synthesis description

Synthesis of **PMI**

In an autoclave, perylene-3,4,9,10-tetracarboxylic dianhydride (4.0 g, 10.2 mmol, 1 equiv.), zinc acetate (1.51 g, 6.86 mmol, 0.67 equiv.) and imidazole (20.4 g) were dispersed in 4.8 ml water. Then 2,6-diisopropylaniline (1.014 ml, 5.38 mmol, 0.53 equiv.) was added and the closed vessel was placed in a muffle furnace at 190 °C for 24 h. After cooling down to room temperature, the reaction mixture was rinsed with water (~ 30 ml) and acidified to a pH of 2 followed by filtration (until completely dry). The filter cake was extracted in chloroform in a Soxhlet extractor for 48 h. The crude product was then purified on SiO_2 (eluent $CHCl_3$) to give the product **2** as a red solid. Yield: 1.03 g (40%). R_f = 0.30-0.36 ($CHCl_3$)

^{1}H NMR (300 MHz, $CDCl_3$) 8.61 (d, *J* = 8.1 Hz, 2H), 8.40-8.35 (m, 4H), 7.87 (d, *J* = 8.1 Hz, 2H), 7.60 (t, *J* = 7.8 Hz, 2H), 7.48 (t, *J* = 7.6 Hz, 1H), 7.35 (d, *J* = 7.6 Hz, 2H), 2.78 (sept, *J* = 6.9 Hz, 2H), 1.20 (d, *J* = 6.9 Hz, 12H). ^{13}C NMR (75 MHz, $CDCl_3$) 164.1, 145.8, 137.6, 134.4, 132.1, 131.2, 131.1, 130.7, 129.6, 129.3, 128.1, 127.2, 124.2, 123.9, 121.1, 120.3, 29.3, 24.2.

Synthesis of **PMI-Br (2)**

In a two-necked flask 3.72 g (7.72 mmol, 1 equiv.) of *N*-(2,6-diisopropylphenyl)-perylene-3,4-dicarboximide were dissolved in 150 ml acetic acid. The reaction mixture was stirred for 30 minutes at room temperature in the dark followed by the addition of iodine (78.4 mg, 0.309 mmol, 0.4 equiv.) and bromine (1.58 ml, 30.9 mmol, 4 equiv.). The mixture was stirred for another 22 h at room temperature and afterwards flushed with N_2 to remove the remaining bromine. The reaction mixture was then diluted with 100 ml MeOH and stirred for another 30 minutes. Afterwards it was poured in deionized water followed by filtration to obtain the product in quantitative yield. Yield: 4.30 g (>99%). R_f = 0.38- 0.54 (toluene/acetone – 39/1)

^{1}H NMR (500 MHz, $CDCl_3$) 8.66 (t, J = 8.03 Hz, 2H), 8.49 (d, J = 3.82 Hz, 1H), 8.46 (d, J = 4.00 Hz, 2H) 8.41 (d, J = 4.00 Hz, 1H), 8.31 (d, J = 4.10 Hz, 1H), 8.24 (d, J = 4.16 Hz, 1H), 7.91 (d, J = 4.10 Hz, 1H), 7.72 (t, J = 8.00 Hz, 1H), 7.48 (t, J = 7.87 Hz, 1H), 7.34 (d, J = 3.88 Hz, 2H), 2.81-2.72 (hept, 2H), 1.18 (d, J = 3.41 Hz, 12H). ^{13}C NMR (75 MHz, $CDCl_3$) 164.0, 145.9, 137.1, 136.9, 133.14, 132.3, 132.2, 131.5, 131.1, 130.6, 130.2, 129.8, 129.7, 129.3, 129.2, 128.5, 126.8, 126.4, 124.6, 124.2, 124.0, 121.6, 120.9, 120.6, 29.3, 24.2.

Synthesis of **PMI-F-PMI (3a)**

In a Schlenk tube, operated under nitrogen, 250 mg (0.45 mmol, 2 equiv.) of 9-bromo-*N*-(2,6-diisopropylphenyl)-perylene-3,4-dicarboximide and 112 mg (0.223 mmol, 1 equiv.) of 9,9-dihexylfluorene-2,7-diboronic acid *bis*(1,3-propanediol) ester (CAS Number 250597-29-6) were dissolved in 25 ml toluene followed by the addition of 1M K_2CO_3 (2.50 ml) and 1 drop of Aliquat 336. Afterwards, $Pd(PPh_3)_4$ (0.022 mmol, 0.1 equiv.) were added and the reaction mixture was heated at 100 °C for 24 h. Upon completion, the reaction mixture was extracted with H_2O, dried over Na_2SO_4 followed by evaporation of the solvent under reduced pressure. The residue was purified by column chromatography (eluent: $CHCl_2$/CH – 10/1 – 20/1 gradient) and further recrystallized using $CHCl_2$/hexane to yield the product as a violet solid. Yield: 211 mg (73%). R_f = 0.45-0.53 (CH_2Cl_2)

^{1}H NMR (500 MHz, $CDCl_3$) 8.71-8.66 (m, 4H), 8.57 (d, *J* = 8.0 Hz, 2H), 8.53 (d, *J* = 7.6 Hz, 2H), 8.51-8.47 (m, 4H), 8.11 (d, *J* = 8.5 Hz, 2H), 7.98 (d, *J* = 7.7 Hz, 2H), 7.73 (d, *J* = 7.7 Hz, 2H), 7.65-7.57 (m, 6H), 7.49 (*t*, *J* = 7.8 Hz, 2H), 7.36 (d, *J* = 7.8 Hz, 4H), 2.80 (hept, *J* = 6.8 Hz, 4H), 2.14-2.08 (m, 4H), 1.24-1.13 (m, 36H), 0.95-0.87 (m, 4H), 0.85-0.80 (m, 6H). ^{13}C NMR (75 MHz, $CDCl_3$) 164.2, 151.6, 145.9, 144.0, 140.7, 139.1, 137.9, 137.8, 133.0, 132.3, 132.2, 131.2, 130.77, 129.7, 129.6, 129.2, 128.7, 128.7, 128.5, 127.2, 127.1, 125.0, 124.17, 124.14, 124.12, 123.8, 121.2, 121.1, 120.5, 120.3, 120.2, 55.7, 40.5, 31.7, 29.9, 29.3, 24.2, 22.8, 14.2. MS (MALDI-TOF) calc. for $C_{93}H_{84}N_2O_4H$ 1293.650, found 1293.647.

Synthesis of **PMI-FSi-PMI (3b)**

In a Schlenk tube, operated under nitrogen, 300 mg (0.535 mmol, 2 equiv.) of 9-bromo-*N*-(2,6-diisopropylphenyl)-perylene-3,4-dicarboximide and 176.3 mg (0.27 mmol, 1equiv.) of 9,9-dioctyl-9H-9-silafluorene-2,7-bis(boronic acid pinacol ester) (CAS Number 958293-23-7) were dissolved in 30 ml toluene followed by the addition of 1 M K_2CO_3 (3 ml) and 1 drop of Aliquat 336. Afterwards, $Pd(PPh_3)_4$ (0.027 mmol, 0.1 equiv.) was added and the reaction mixture was heated at 100 °C for 24 h. Upon completion, the reaction mixture was extracted with H_2O and dried over Na_2SO_4 followed by evaporation of the solvent under reduced pressure. The residue was purified by column chromatography (eluent: CH_2Cl_2/CH – 1/1 – 4/1 – 10/1 gradient) and further recrystallized using CH_2Cl_2/hexane to yield the product as a violet solid. Yield: 136 mg (37%). R_f = 0.47-0.55 (CH_2Cl_2)

^{1}H NMR (500 MHz, $CDCl_3$) 8.69 (dd, *J* = 8.0, 2.0 Hz, 4H), 8.57 (d, *J* = 8.0, 2H), 8.55 (d, *J* = 7.6 Hz, 2H), 8.53-8.49 (m, 4H), 8.15 (d, *J* = 8.4 Hz, 2H), 8.11 (d, *J* = 8.0 Hz, 2H), 7.88-7.84 (m, 2H), 7.73 (d, *J* = 7.8 Hz, 2H), 7.71-7.69 (m, 2H), 7.65 (t, *J* = 8.9 Hz, 2H), 7.49 (t, *J* = 7.8 Hz, 2H), 7.35 (d, *J* = 7.8 Hz, 4H), 2.79 (hept, *J* = 6.8 Hz, 4H), 1.54-1.46 (m, 4H), 1.37-1.30 (m, 4H), 1.29-1.17 (m, 40H), 1.11-1.05 (m, 4H), 0.85-0.80 (m, 6H). ^{13}C NMR (75 MHz, $CDCl_3$) 164.2, 147.8, 145.9, 143.7, 139.0, 138.9, 137.9, 137.7, 135.1, 133.0, 132.3, 132.4, 132.2, 131.2, 130.8, 129.67, 129.6, 128.7, 128.4, 127.2, 127.2, 124.2, 123.8, 121.3, 121.2, 121.1, 120.5, 120.3, 33.5, 32.0, 29.4, 29.3, 24.3, 24.2, 22.8, 14.2, 12.5. MS (MALDI-TOF) calc. for $C_{96}H_{92}N_2O_4SiH$ 1365.6904, found 1365.6947.

Synthesis of **PMI-FN-PMI (3c)**

In a Schlenk tube, operated under nitrogen, 300 mg (0.535 mmol, 2 equiv.) of 9-bromo-*N*-(2,6-diisopropylphenyl)-perylene-3,4-dicarboximide and 176 mg (0.27 mmol, 1 equiv.) of 9-(heptadecan-9-yl)-2,7-bis(4,4,5,5-tetramethyl-1,3,2-dioxaborolan-2-yl)-9H-carbazole (CAS Number 958261-51-3) were dissolved in 30 ml toluene followed by the addition of 1 M aqueous K_2CO_3 (3 ml) and 1 drop of Aliquat 336. Afterwards, $Pd(PPh_3)_4$ (0.027 mmol, 0.1 equiv.) was added and the reaction mixture was heated at 100 °C for 24 h. Upon completion, the reaction mixture was extracted with H_2O and dried over Na_2SO_4 followed by evaporation of the solvent

under reduced pressure. The residue was purified by column chromatography (eluent: CH_2Cl_2/CH – 1/1 – 4/1 – 10/1 gradient) and further recrystallized using CH_2Cl_2/hexane to yield the product as a violet solid. Yield: 205 mg (56%). R_f = 0.47-0.55 (CH_2Cl_2)

^{1}H NMR (500 MHz, $CDCl_3$) 8.69 (t, J = 7.6 Hz, 4H), 8.62-8.55 (m, 2H), 8.56-8.49 (m, 6H), 8.39-8.31 (m, 2H), 8.22-8.14 (m, 2H) 7.83-7.76 (m, 3H), 7.67-7.60 (m, 3H), 7.53-7.46 (m, 4H), 7.35 (d, *J* = 7.8 Hz, 4H), 4.68 (hept, *J* = 5.0 Hz, 1H), 2.80 (hept, *J* = 6.8 Hz, 4H), 2.40-2.30 (m, 2H), 2.00-1.90 (m, 2H), 1.34-1.11 (m, 48H), 0.83-0.78 (m, 6H). ^{13}C NMR (75 MHz, $CDCl_3$) 164.2, 145.9, 144.6, 142.8, 139.43, 139.39, 137.9, 137.8, 137.3, 133.2, 132.3, 132.2, 131.3, 130.8, 129.9, 129.7, 129.6, 128.9, 128.7, 128.6, 127.2, 127.1, 124.2, 124.1, 123.7, 123.5, 122.1, 121.5, 121.2, 121.0, 120.8, 120.5, 120.2, 113.5, 110.8, 56.9, 34.0, 31.9, 29.6, 29.5, 29.4, 29.3, 27.1, 24.2, 22.8, 14.2. MS (MALDI-TOF) calc. for $C_{97}H_{93}N_3O_4H$ 1364.7200, found 1364.7173.

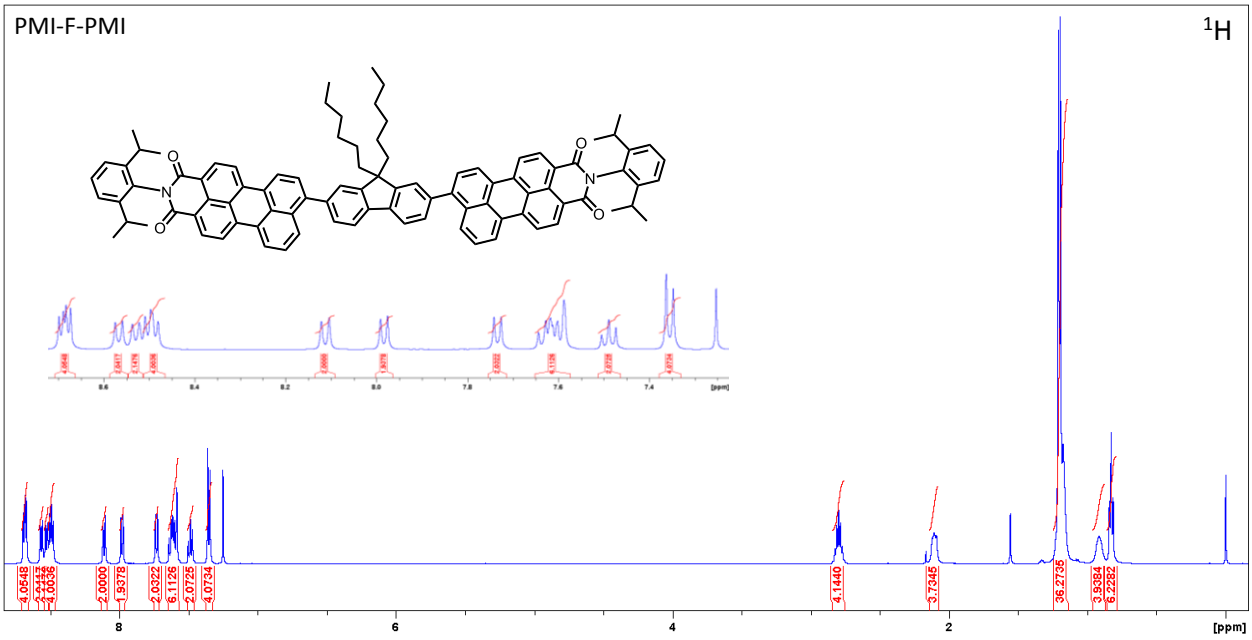

*Figure S1: ^{1}H NMR (500 MHz, $CDCl_3$) spectrum of **PMI-F-PMI (3a)** with an inset of the aromatic region, referenced to TMS.*

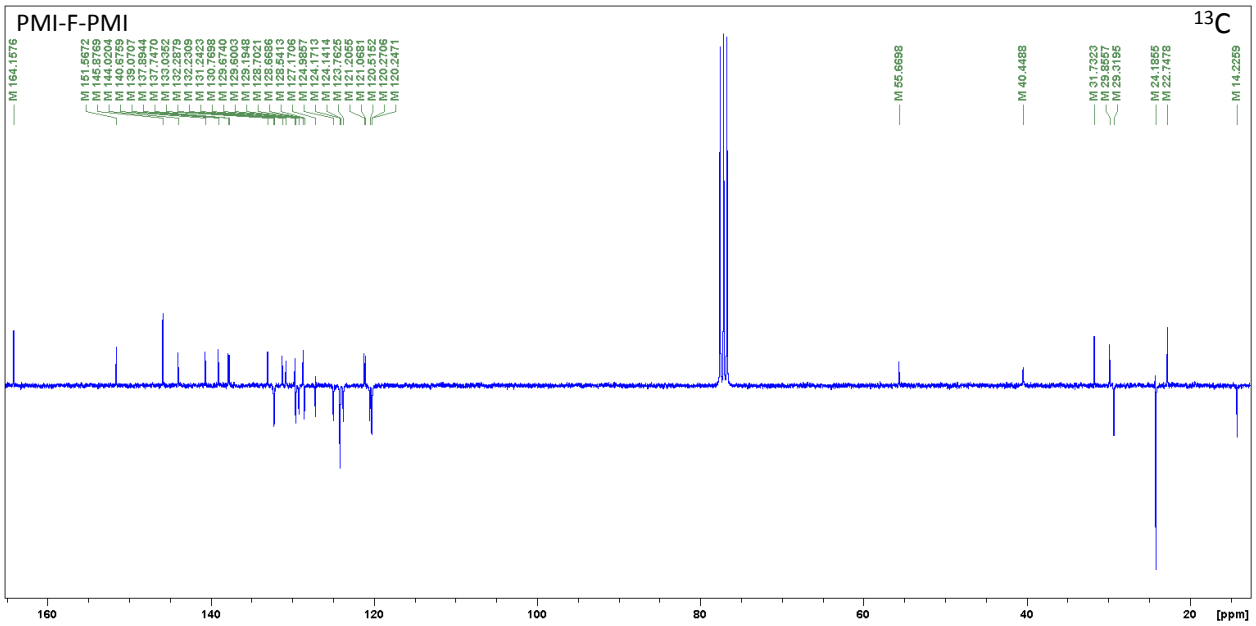

*Figure S2: ^{13}C APT NMR (75 MHz, $CDCl_3$) spectrum of **PMI-F-PMI (3a)**, referenced to $CDCl_3$.*

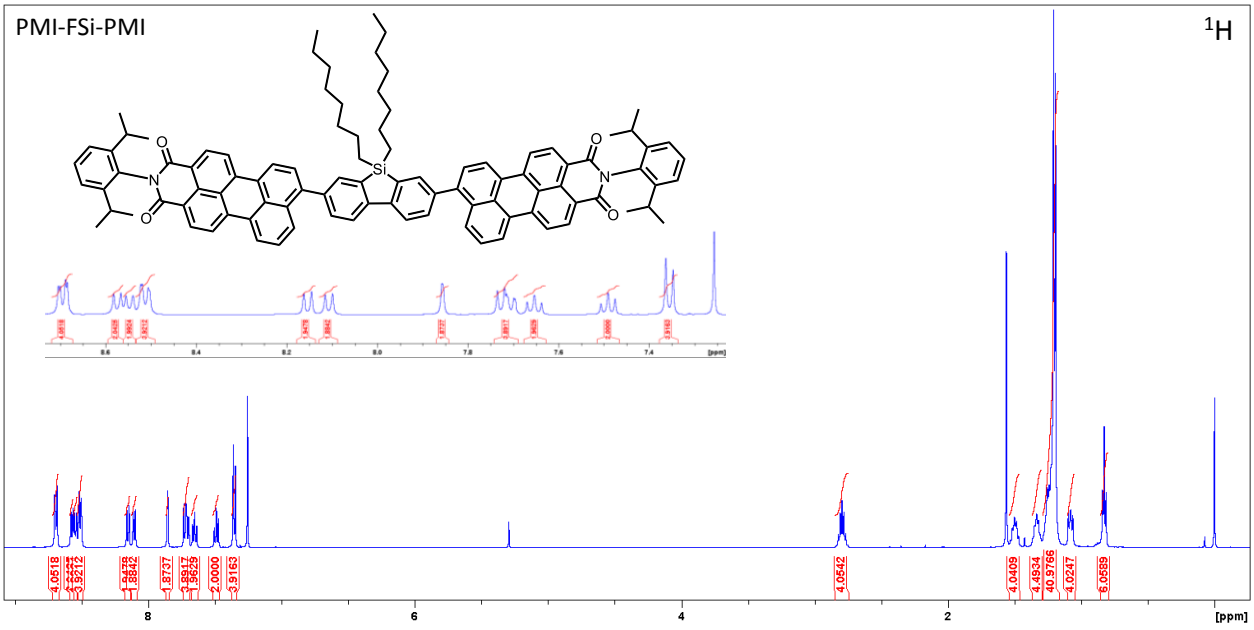

*Figure S3: ^{1}H NMR (500 MHz, $CDCl_3$) of **PMI-FSi-PMI (3b)** with an inset of the aromatic region, referenced to TMS.*

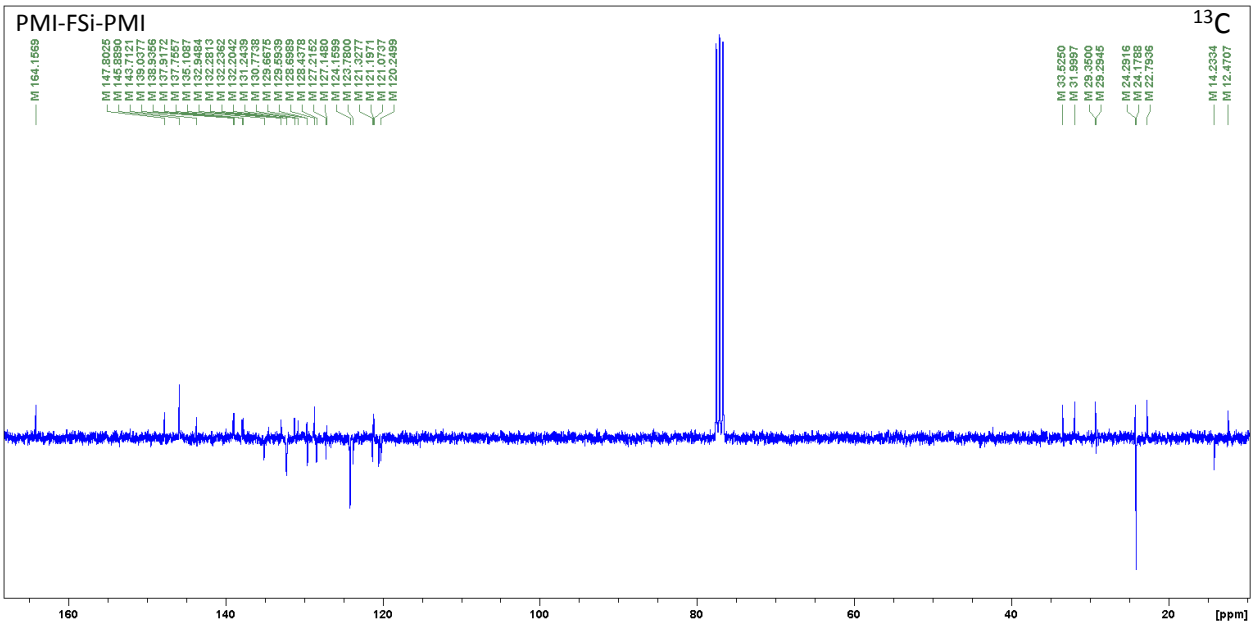

*Figure S4: ^{13}C APT NMR spectrum (75 MHz, $CDCl_3$) of **PMI-FSi-PMI (3b)**, referenced to $CDCl_3$.*

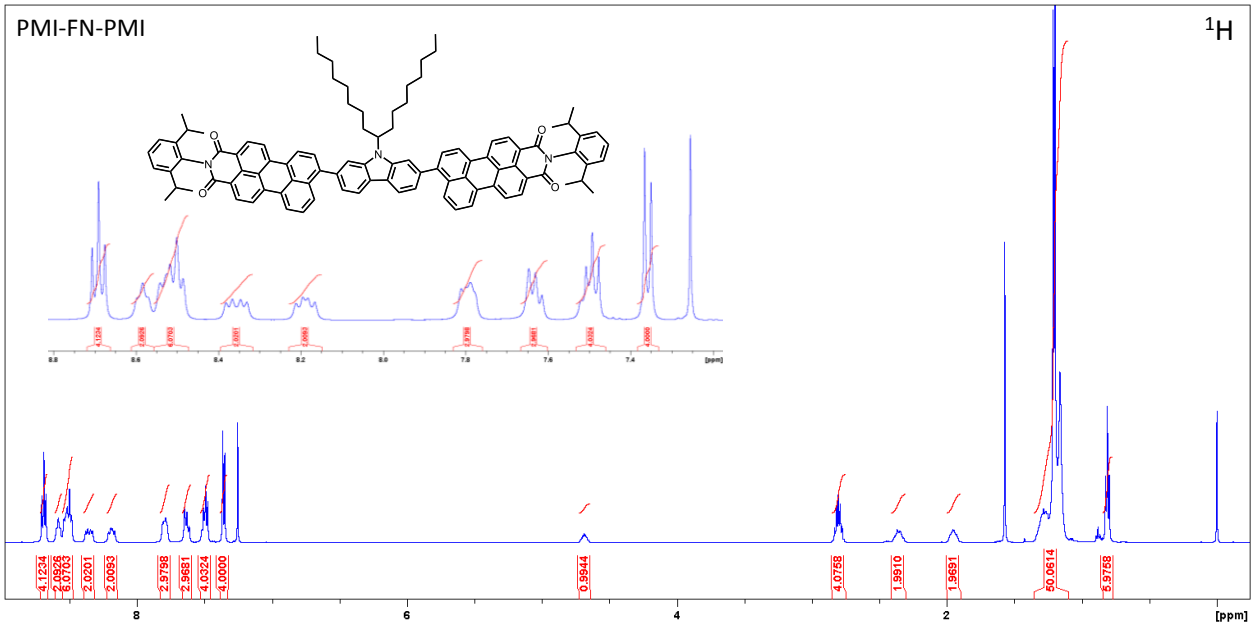

*Figure S5: ^{1}H NMR (500 MHz, $CDCl_3$) spectrum of **PMI-FN-PMI (3c)** with an inset of the aromatic region, referenced to TMS.*

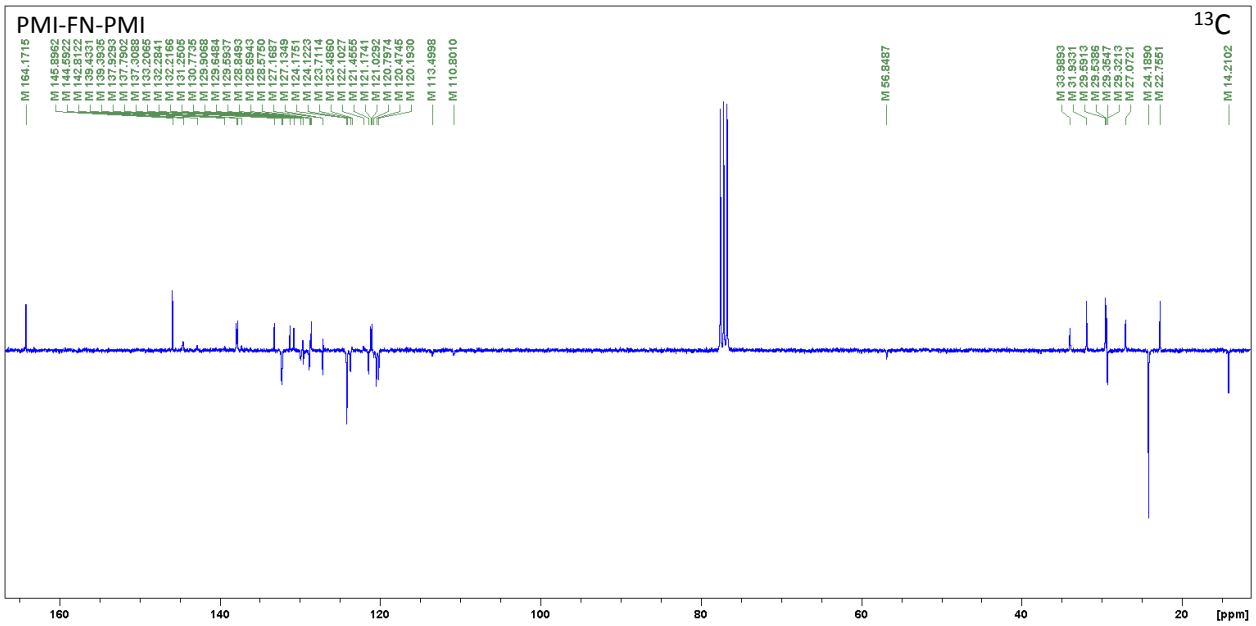

*Figure S6: ^{13}C APT NMR spectrum (75 MHz, $CDCl_3$) of **PMI-FN-PMI (3c)**, referenced to $CDCl_3$.*

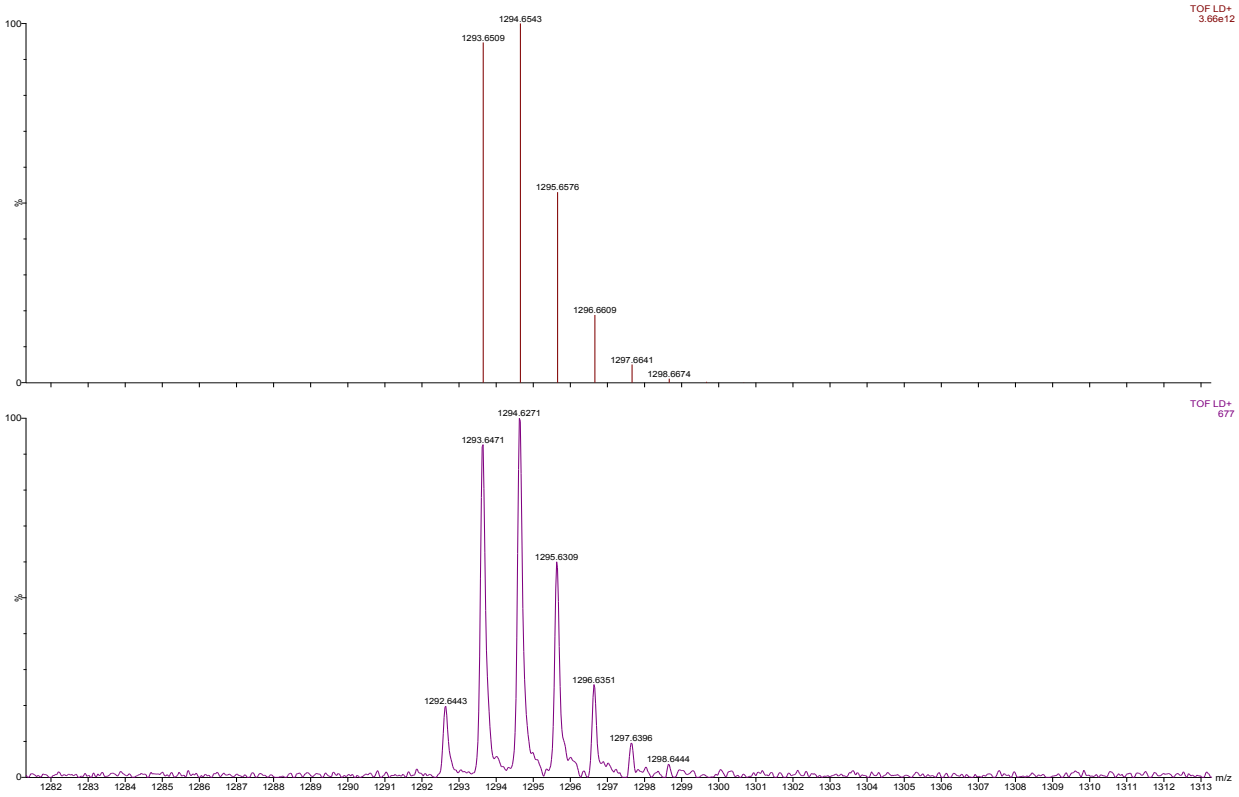

*Figure S7: HRMS (MALDI-TOF, Dithranol matrix) of **PMI-F-PMI (3a)**, upper – simulated, lower - found.*

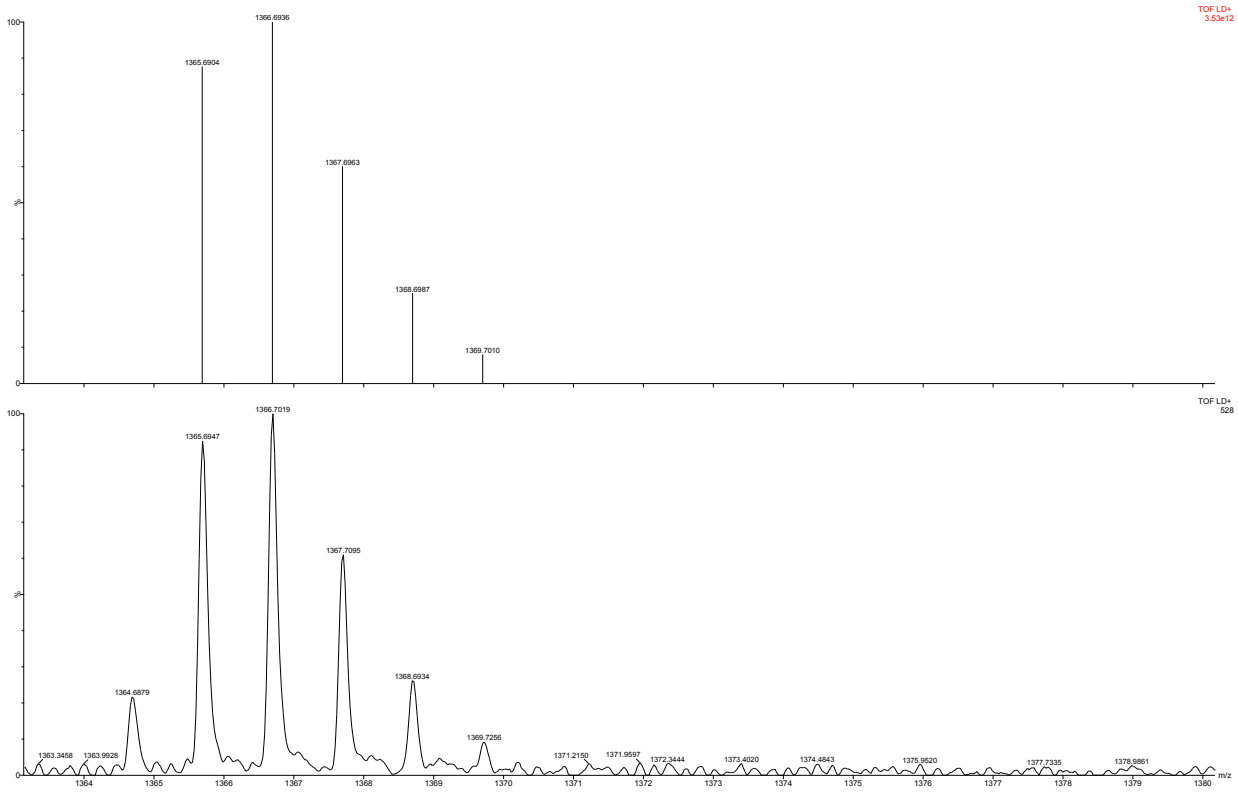

*Figure S8: HRMS (MALDI-TOF, Dithranol matrix) of **PMI-FSi-PMI (3b)**, upper – simulated, lower - found.*

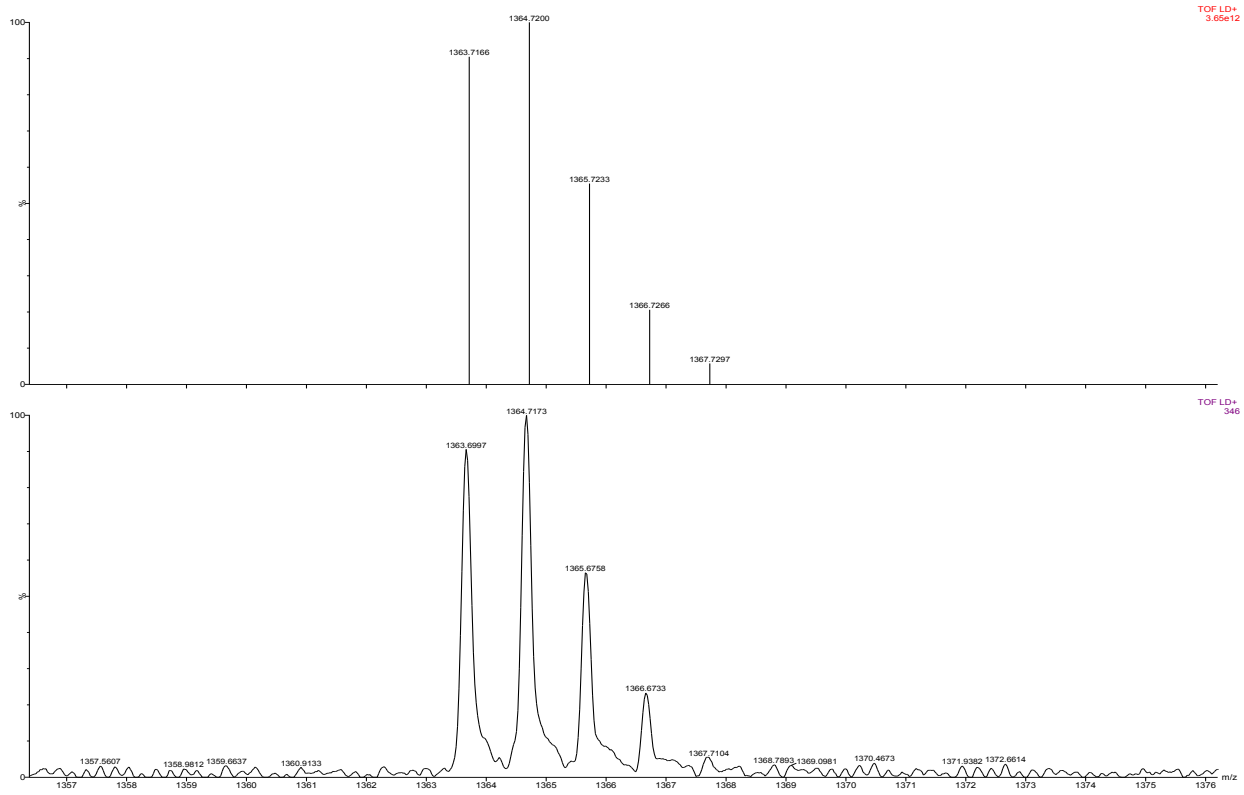

*Figure S9: HRMS (MALDI-TOF, DCTB matrix) of **PMI-FN-PMI (3c)**, upper – simulated, lower - found.*

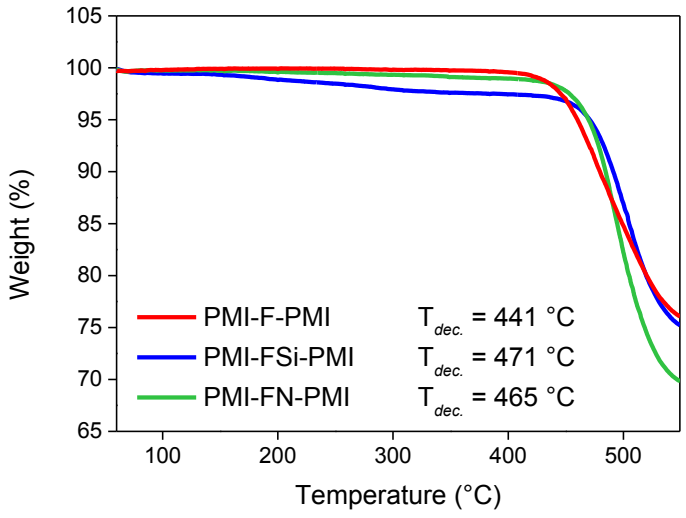

*Figure S10: TGA measurements with the respective decomposition temperatures of: red - **PMI-F-PMI (3a)**, blue - **PMI-FSi-PMI (3b)** and green - **PMI-FN-PMI (3c)**.*

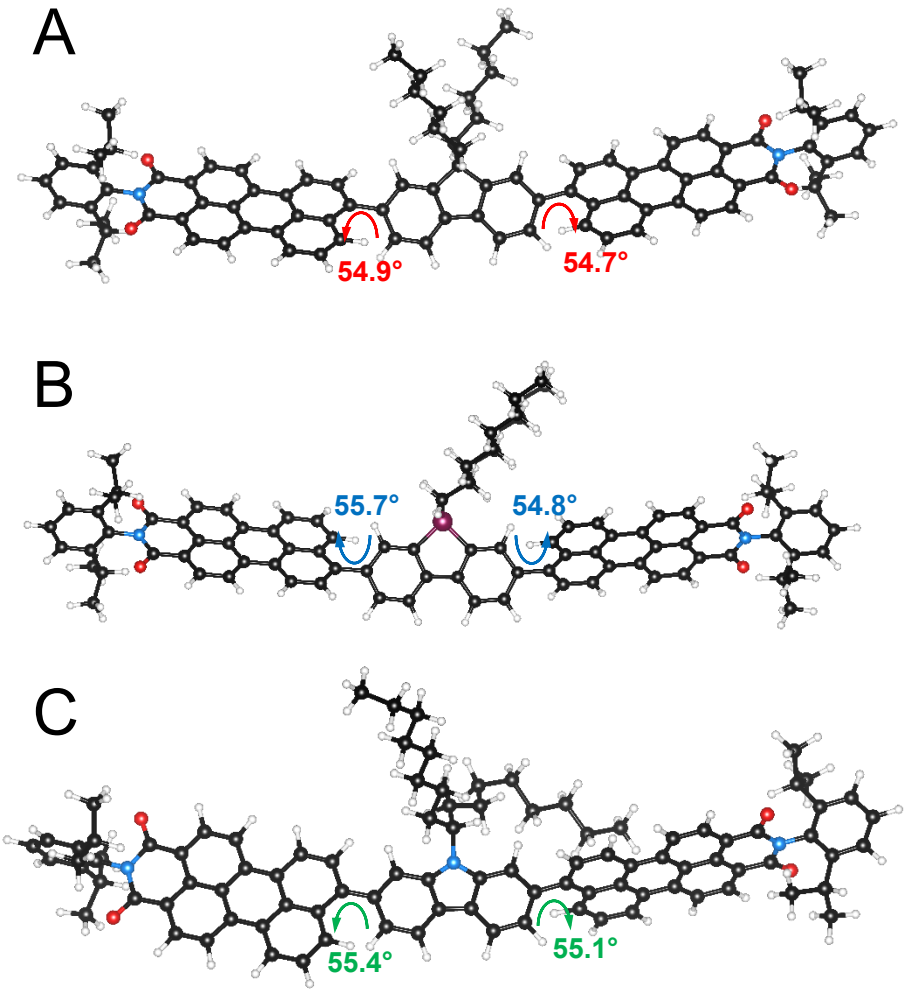

Figure S11: Computed (B3LYP/6-31G) optimal geometries and the dihedral angles of: A -* ***PMI-F-PMI*** *(3a); B -* ***PMI-FSi-PMI*** *(3b); C -* ***PMI-FN-PMI*** *(3c).*

Table S1: Cartesian coordinates for the DFT (B3LYP/6-31G) optimized structures of* ***PMI-F-PMI (3a)****,* ***PMI-FSi-PMI (3b)*** *and* ***PMI-FN-PMI (3c)****.*

PMI-F-PMI (3a)				PMI-Si-PMI (3b)				PMI-FN-PMI (3c)			
C	18.39259	0.87382	-0.43067	C	-12.65472	-0.18179	1.12317	C	-12.48076	-1.32043	-0.23179
C	17.80821	-0.00341	-1.33929	C	-11.98346	-0.71083	2.21286	C	-12.09903	-2.65041	-0.16699
C	16.44534	-0.31448	-1.26972	C	-10.60433	-0.5338	2.35414	C	-10.75132	-3.00919	-0.25847
C	15.68734	0.29078	-0.25229	C	-9.8494	0.17518	1.41652	C	-9.74051	-2.05654	-0.41239
C	16.25169	1.18024	0.67861	C	-10.51857	0.71326	0.27221	C	-10.11296	-0.67772	-0.49418
C	17.61905	1.45764	0.56796	C	-11.93206	0.53473	0.13886	C	-11.4941	-0.3183	-0.39446
C	15.43476	1.83275	1.78782	C	-9.80402	1.42483	-0.74282	C	-9.13361	0.35015	-0.67135
C	15.91772	1.37701	3.17817	C	-10.5221	1.9369	-1.82685	C	-9.56451	1.67905	-0.71387
C	15.42995	3.36771	1.65824	C	-11.90423	1.76648	-1.94492	C	-10.91434	2.02268	-0.60069
C	15.83712	-1.28174	-2.27839	C	-12.61455	1.07145	-0.97976	C	-11.88149	1.0424	-0.44926
C	15.93044	-0.72969	-3.71351	C	-8.39909	0.38383	1.56661	C	-8.31627	-2.42273	-0.49206
C	16.46708	-2.68293	-2.16234	C	-7.67057	1.06035	0.53302	C	-7.33461	-1.40209	-0.71849
N	14.2703	-0.01204	-0.16001	C	-8.34808	1.5866	-0.61403	C	-7.71833	-0.02511	-0.80662
C	13.88682	-1.09666	0.65283	C	-7.71331	-0.05129	2.69692	C	-7.89302	-3.74075	-0.34624
C	12.43656	-1.38086	0.73536	C	-6.33427	0.15609	2.84476	C	-6.53636	-4.08886	-0.41611
C	11.49486	-0.59508	0.02741	C	-5.61329	0.77983	1.85101	C	-5.58212	-3.12659	-0.66047
C	11.94315	0.48025	-0.77767	C	-6.24707	1.22749	0.66293	C	-5.94852	-1.76752	-0.84161
C	13.38317	0.80287	-0.89063	C	-5.50553	1.87702	-0.38117	C	-4.96237	-0.7567	-1.10243
C	10.09746	-0.88673	0.12461	C	-6.20478	2.38661	-1.46455	C	-5.37706	0.56453	-1.1656
C	9.16315	-0.08746	-0.60728	C	-7.59352	2.24989	-1.57656	C	-6.72212	0.92318	-1.01603
C	9.65434	0.96261	-1.38779	C	-14.11664	-0.38189	1.00537	C	-13.91493	-0.97151	-0.12276
C	11.02037	1.24518	-1.47196	C	-14.07666	0.90328	-1.1367	C	-13.30353	1.43703	-0.34036
C	11.99566	-2.43499	1.51793	N	-14.73977	0.18122	-0.12513	N	-14.24619	0.39002	-0.26143
C	10.63199	-2.72361	1.62077	O	-14.76844	-1.00113	1.83603	O	-14.78408	-1.812	0.06871
C	9.66371	-1.97158	0.95026	O	-14.69639	1.35903	-2.08813	O	-13.66406	2.60569	-0.32871
C	8.22356	-2.25874	1.06424	C	-16.17487	0.0039	-0.2595	C	-15.64631	0.76274	-0.13814
C	7.28475	-1.48351	0.30634	C	-4.02591	2.01914	-0.35539	C	-3.52321	-1.06965	-1.31674
C	7.72894	-0.39996	-0.51815	C	-17.0328	0.95534	0.31965	C	-16.4579	0.85131	-1.28722
C	5.88123	-1.78888	0.39212	C	-18.41132	0.76171	0.17612	C	-17.79311	1.23478	-1.09867
C	4.93651	-1.0342	-0.38294	C	-18.91479	-0.33503	-0.51755	C	-18.30693	1.51281	0.16346
C	5.40871	0.02137	-1.14752	C	-18.04257	-1.26127	-1.08114	C	-17.48346	1.41302	1.27839
C	6.77163	0.33445	-1.21081	C	-16.65569	-1.11234	-0.96442	C	-16.14104	1.03918	1.15093
C	7.74448	-3.26257	1.90112	C	-16.51481	2.16577	1.08669	C	-16.04447	0.51792	-2.72541
C	6.37271	-3.52833	2.01952	C	-16.93959	3.48381	0.41137	C	-14.70662	1.0996	-3.21827
C	5.45807	-2.81033	1.28203	C	-16.94079	2.11616	2.56624	C	-16.13077	-0.99831	-3.00091
C	3.48105	-1.3399	-0.40565	C	-15.72763	-2.14392	-1.59506	C	-15.27571	0.94337	2.4035
C	3.00797	-2.6262	-0.72818	C	-15.93514	-3.53942	-0.97666	C	-15.14243	2.3106	3.10111
C	1.64292	-2.89732	-0.79009	C	-15.87622	-2.16904	-3.12797	C	-15.79917	-0.14179	3.36391
C	0.73218	-1.8694	-0.53822	C	-3.43568	3.27806	-0.55911	C	-3.12031	-1.99181	-2.31269

C	1.18287	-0.56692	-0.24205	C	-2.05162	3.43383	-0.58951	C	-1.77693	-2.24376	-2.55709
C	2.54769	-0.31206	-0.16242	C	-1.21464	2.32541	-0.41763	C	-0.80348	-1.57634	-1.80498
C	-0.72994	-1.87768	-0.50682	C	-1.78796	1.04241	-0.21877	C	-1.20249	-0.64577	-0.80899
C	-1.18174	-0.58142	-0.18655	C	-3.17526	0.90803	-0.19188	C	-2.55539	-0.3901	-0.56478
C	-9E-5	0.37894	0.01132	C	0.26987	2.36057	-0.42428	C	0.63774	-1.59904	-1.79416
C	-1.63993	-2.90846	-0.74966	C	0.9068	1.10574	-0.23451	C	1.05616	-0.67897	-0.7937
C	-3.00524	-2.64082	-0.67795	Si	-0.4086	-0.23449	-0.01811	N	-0.06946	-0.11032	-0.19665
C	-3.47909	-1.34908	-0.37931	C	1.05018	3.5095	-0.59647	C	1.5953	-2.30313	-2.53283
C	-2.5467	-0.31856	-0.14519	C	2.44098	3.42131	-0.5839	C	2.94436	-2.08547	-2.28766
C	-4.93397	-1.03882	-0.38681	C	3.09288	2.18978	-0.40682	C	3.36832	-1.16163	-1.30288
C	0.10748	0.92452	1.46961	C	2.2997	1.03926	-0.23005	C	2.41696	-0.46005	-0.54985
C	-0.10986	1.50969	-1.05943	C	4.57676	2.1311	-0.33279	C	4.81391	-0.96815	-1.00642
C	0.97994	2.59041	-1.08232	C	5.36056	1.23911	-1.14021	C	5.77778	-0.63347	-2.01718
C	0.70701	3.65933	-2.1509	C	6.78529	1.16913	-0.95417	C	7.17074	-0.52946	-1.67263
C	1.79002	4.74336	-2.22389	C	7.42004	2.02164	0.00571	C	7.58305	-0.70447	-0.31239
C	1.51926	5.8068	-3.29597	C	6.62518	2.90825	0.7257	C	6.60822	-0.98723	0.63906
C	2.60788	6.8823	-3.36908	C	5.23546	2.95748	0.5636	C	5.25698	-1.12184	0.29812
C	-0.98433	1.88689	1.95745	C	4.76408	0.44748	-2.15603	C	5.38266	-0.35845	-3.35232
C	-0.71605	2.3912	3.38346	C	5.5243	-0.40684	-2.92314	C	6.3159	-0.04236	-4.31432
C	-1.79366	3.35149	3.90287	C	6.90679	-0.51019	-2.71065	C	7.6796	0.00624	-3.99079
C	-1.53053	3.85455	5.32822	C	7.55677	0.25704	-1.74795	C	8.13071	-0.23281	-2.69584
C	-2.60951	4.81532	5.83812	C	9.01136	0.15951	-1.53545	C	9.56244	-0.17889	-2.35539
C	-5.89316	-1.7713	0.39115	C	9.63637	1.01384	-0.57272	C	9.96227	-0.33236	-0.99044
C	-7.29398	-1.46319	0.27636	C	8.87619	1.94792	0.20044	C	9.00395	-0.57591	0.04378
C	-7.72122	-0.40017	-0.583	C	11.05155	0.93135	-0.3765	C	11.34957	-0.24229	-0.65241
C	-6.75057	0.31344	-1.27887	C	11.68949	1.77421	0.56578	C	11.76262	-0.36908	0.69619
C	-5.38984	-0.00155	-1.18547	C	10.93467	2.67371	1.30009	C	10.81557	-0.58492	1.68385
C	-5.48727	-2.77336	1.31065	C	9.55124	2.75544	1.12008	C	9.4601	-0.68906	1.35992
C	-6.4158	-3.46983	2.05142	C	9.81208	-0.74271	-2.2408	C	10.55421	0.01777	-3.31993
C	-7.78454	-3.20056	1.90734	C	11.19312	-0.82083	-2.03999	C	11.90879	0.09221	-2.98355
C	-8.24712	-2.21504	1.03992	C	11.82039	0.00508	-1.12226	C	12.31584	-0.02763	-1.66507
C	-9.68413	-1.92375	0.89889	C	13.28512	-0.09978	-0.93535	C	13.75657	0.06579	-1.34022
C	-10.10106	-0.86091	0.03666	C	13.15237	1.7105	0.78194	C	13.19135	-0.27289	1.07059
C	-9.15277	-0.08639	-0.70381	N	13.86255	0.76944	0.01063	N	14.10474	-0.06033	0.01914
C	-11.49559	-0.56644	-0.08914	O	13.73419	2.42842	1.58401	O	13.58066	-0.37082	2.22647
C	-11.92743	0.48674	-0.93166	O	13.97662	-0.8922	-1.56163	O	14.61686	0.24506	-2.1915
C	-10.99145	1.22699	-1.63494	C	15.29903	0.69144	0.20545	C	15.51217	0.03657	0.36233
C	-9.62804	0.94176	-1.52242	C	16.13382	1.50731	-0.5772	C	16.28033	-1.13958	0.41309
C	-10.66532	-2.65106	1.57782	C	17.51509	1.41327	-0.37129	C	17.63341	-1.01954	0.75027
C	-12.02606	-2.35958	1.4473	C	18.04313	0.54184	0.57645	C	18.19914	0.22224	1.02315
C	-12.45095	-1.32725	0.6277	C	17.19289	-0.25394	1.33846	C	17.41599	1.37104	0.96334
C	-13.89859	-1.03952	0.51592	C	15.80454	-0.19613	1.17037	C	16.05756	1.3036	0.63318
N	-14.26535	0.02328	-0.33274	C	14.90146	-1.08263	2.02008	C	15.22931	2.58169	0.57309

C	-13.36412	0.81244	-1.07414	C	15.15788	-2.57585	1.73998	C	15.18454	3.29	1.94033
C	-15.67944	0.33084	-0.45195	C	15.03472	-0.74903	3.51823	C	15.72926	3.52009	-0.54194
C	-16.25211	1.2435	0.45106	C	15.58886	2.46964	-1.62642	C	15.6921	-2.51545	0.12252
C	-17.6164	1.52474	0.31515	C	15.9326	3.93113	-1.281	C	16.38491	-3.18412	-1.07972
C	-18.37883	0.9224	-0.68106	C	16.06855	2.08746	-3.03975	C	15.72692	-3.41261	1.37475
C	-17.78634	0.02239	-1.5617	C	-0.42629	-1.00553	1.71952	C	-0.09522	0.89233	0.88236
C	-16.42621	-0.2937	-1.46603	C	0.87895	-1.6639	2.20863	C	0.5172	0.35071	2.19006
C	-15.80867	-1.28565	-2.44454	C	0.78387	-2.20353	3.64361	C	0.49845	2.2386	0.40892
C	-16.4527	-2.67903	-2.31325	C	2.08163	-2.85553	4.13816	C	0.16671	3.4276	1.32273
C	-15.87163	-0.76028	-3.8913	C	1.9906	-3.39545	5.57156	C	0.67406	4.76486	0.76541
C	-15.44715	1.91666	1.55658	C	3.2866	-4.05396	6.06175	C	0.34707	5.96393	1.6648
C	-15.43182	3.44823	1.39235	C	-0.42457	-1.51657	-1.42113	C	0.8521	7.30159	1.1079
C	-15.95129	1.49487	2.95006	C	0.84054	-2.3792	-1.59661	C	0.52265	8.49688	2.01314
O	13.80291	1.72489	-1.57659	C	0.75477	-3.34389	-2.78854	C	0.95079	9.86392	1.45394
O	14.7252	-1.75626	1.25215	C	2.01143	-4.20545	-2.96813	C	2.46685	10.05118	1.31973
O	-13.76962	1.71594	-1.79258	C	1.92828	-5.17302	-4.15582	C	-0.17853	-0.90331	2.73642
O	-14.74855	-1.67803	1.12166	C	3.18179	-6.04046	-4.32861	C	0.44425	-1.40143	4.04895
H	19.45297	1.10254	-0.5007	C	3.10139	-7.00685	-5.51727	C	-0.27538	-2.60381	4.68264
H	18.41902	-0.45565	-2.11589	C	4.35509	-7.87264	-5.67885	C	-0.22093	-3.89748	3.85746
H	18.08316	2.14046	1.27439	C	3.19691	-4.59597	7.49427	C	-0.88326	-5.09046	4.55895
H	14.39695	1.50138	1.68513	C	4.49701	-5.2467	7.97774	C	-0.84437	-6.38458	3.73586
H	15.28693	1.81006	3.96403	H	-12.55142	-1.26368	2.9539	C	-1.50924	-7.57067	4.44177
H	15.87733	0.28614	3.26353	H	-10.12708	-0.97172	3.22263	H	-12.86802	-3.40584	-0.04386
H	16.95025	1.6935	3.36763	H	-10.01291	2.48561	-2.61021	H	-10.50616	-4.06341	-0.21026
H	14.78954	3.81392	2.42875	H	-12.44377	2.1724	-2.79437	H	-8.84781	2.48213	-0.83768
H	15.05345	3.67373	0.67654	H	-8.24333	-0.54604	3.50217	H	-11.22871	3.06058	-0.63428
H	16.43596	3.78616	1.78026	H	-5.83861	-0.17298	3.75368	H	-8.6124	-4.52855	-0.1561
H	14.77345	-1.3899	-2.04558	H	-4.55131	0.95199	1.98006	H	-6.24181	-5.12432	-0.27102
H	15.43535	-1.4092	-4.41789	H	-5.6581	2.87792	-2.26427	H	-4.53463	-3.40022	-0.70136
H	15.4497	0.25155	-3.78376	H	-8.06986	2.66403	-2.4576	H	-4.6447	1.33946	-1.37198
H	16.97306	-0.62016	-4.03491	H	-19.09872	1.47975	0.61538	H	-6.97394	1.97464	-1.09214
H	15.97819	-3.38071	-2.85298	H	-19.9889	-0.46775	-0.61891	H	-18.44024	1.31393	-1.96898
H	16.36134	-3.0727	-1.14453	H	-18.44318	-2.11441	-1.62208	H	-19.34649	1.80985	0.27549
H	17.53536	-2.6652	-2.40862	H	-15.42111	2.13549	1.06778	H	-17.88447	1.63165	2.26414
H	8.97405	1.58758	-1.95397	H	-16.50592	4.34182	0.93934	H	-16.81762	0.98753	-3.34785
H	11.38176	2.06548	-2.08332	H	-16.60219	3.5129	-0.63003	H	-14.67942	1.06167	-4.31381
H	12.7313	-3.02996	2.04904	H	-18.02923	3.60675	0.41732	H	-14.58004	2.14132	-2.90881
H	10.34015	-3.56216	2.24157	H	-16.50825	2.96016	3.11734	H	-13.84652	0.52832	-2.85706
H	4.70743	0.59997	-1.74175	H	-16.60258	1.18664	3.03572	H	-15.91535	-1.20263	-4.05711
H	7.06809	1.16531	-1.8404	H	-18.03071	2.17266	2.67328	H	-17.13273	-1.38009	-2.77684
H	8.43088	-3.85136	2.49812	H	-14.6962	-1.84819	-1.3782	H	-15.42307	-1.56343	-2.38851
H	6.03503	-4.30159	2.70364	H	-15.22081	-4.25591	-1.40034	H	-14.26823	0.64096	2.10407
H	4.39884	-3.01004	1.3914	H	-15.792	-3.50859	0.10861	H	-14.46863	2.23504	3.96322

H	3.72173	-3.41495	-0.94687	H	-16.9441	-3.92052	-1.17386	H	-14.73974	3.05892	2.41099
H	1.29932	-3.89893	-1.03546	H	-15.15872	-2.87053	-3.5708	H	-16.11054	2.67218	3.46748
H	2.91714	0.67101	0.11223	H	-15.69559	-1.17565	-3.55162	H	-15.13312	-0.23834	4.23002
H	-1.29581	-3.90635	-1.00899	H	-16.88152	-2.48744	-3.42877	H	-15.85332	-1.11204	2.85951
H	-3.71843	-3.43205	-0.88957	H	-4.07533	4.14847	-0.67819	H	-16.79988	0.10116	3.74046
H	-2.91696	0.67825	0.07329	H	-1.63581	4.42626	-0.7409	H	-3.87818	-2.48725	-2.91126
H	1.07999	1.42474	1.56796	H	-3.62414	-0.07421	-0.06195	H	-1.48642	-2.94631	-3.33379
H	0.14781	0.0605	2.14587	H	0.58462	4.47996	-0.74557	H	-2.87605	0.30584	0.20319
H	-0.15171	1.0287	-2.04561	H	3.03606	4.31897	-0.72942	H	1.28726	-3.0212	-3.2883
H	-1.08269	2.00115	-0.92705	H	2.79787	0.08665	-0.06723	H	3.68978	-2.64741	-2.84147
H	1.05814	3.07788	-0.10096	H	7.06989	3.57546	1.45464	H	2.75412	0.25631	0.18907
H	1.957	2.13301	-1.28165	H	4.65642	3.63661	1.18272	H	6.88233	-1.13398	1.67739
H	0.61366	3.173	-3.13314	H	3.69984	0.53742	-2.33813	H	4.54214	-1.386	1.0719
H	-0.26676	4.13152	-1.95307	H	5.05724	-1.00114	-3.70344	H	4.32971	-0.38264	-3.60616
H	1.88363	5.2331	-1.24304	H	7.46803	-1.19561	-3.3346	H	5.99914	0.17654	-5.33006
H	2.76444	4.27142	-2.42069	H	11.44037	3.31068	2.01836	H	8.38201	0.25702	-4.77701
H	1.42257	5.3162	-4.27498	H	9.00576	3.47209	1.7223	H	11.15034	-0.6753	2.71196
H	0.54778	6.28143	-3.09738	H	9.37018	-1.41417	-2.96718	H	8.75938	-0.86197	2.16805
H	2.38509	7.62518	-4.14328	H	11.7966	-1.5284	-2.59896	H	10.28792	0.11231	-4.3659
H	2.70471	7.41472	-2.41484	H	18.18512	2.03125	-0.96259	H	12.66351	0.2467	-3.7476
H	3.58532	6.44187	-3.60177	H	19.11883	0.48303	0.72164	H	18.25106	-1.91215	0.79969
H	-1.96082	1.38774	1.93787	H	17.6123	-0.93153	2.0772	H	19.25216	0.29479	1.28296
H	-1.06141	2.75113	1.28347	H	13.86382	-0.87876	1.73809	H	17.86492	2.33718	1.17728
H	0.26282	2.89242	3.41455	H	14.46023	-3.19808	2.31367	H	14.19997	2.3073	0.32297
H	-0.63756	1.53038	4.06365	H	15.02534	-2.79861	0.67621	H	14.53446	4.17205	1.89301
H	-2.77318	2.85147	3.87067	H	16.17572	-2.86941	2.02289	H	14.79862	2.61769	2.71382
H	-1.87121	4.21359	3.22348	H	14.3397	-1.3578	4.10937	H	16.1798	3.62791	2.25241
H	-0.55115	4.35283	5.36112	H	14.81138	0.30713	3.70198	H	15.08742	4.40675	-0.61287
H	-1.45571	2.99341	6.00739	H	16.04772	-0.94952	3.8865	H	15.72194	3.00915	-1.51026
H	-2.39295	5.15609	6.85694	H	14.4974	2.39006	-1.62668	H	16.75212	3.86462	-0.34836
H	-3.59532	4.33429	5.85031	H	15.48297	4.61287	-2.01314	H	14.64003	-2.3845	-0.14884
H	-2.6836	5.70354	5.1986	H	15.55565	4.19375	-0.28707	H	15.90522	-4.14264	-1.31217
H	-7.03406	1.12883	-1.93412	H	17.01541	4.10278	-1.28889	H	16.32658	-2.54503	-1.96704
H	-4.67697	0.55983	-1.78235	H	15.61878	2.7499	-3.78926	H	17.44347	-3.38415	-0.87591
H	-4.43052	-2.9752	1.43924	H	15.79015	1.05577	-3.27845	H	15.24881	-4.37789	1.16814
H	-6.09178	-4.22868	2.75793	H	17.15784	2.17345	-3.13122	H	15.19946	-2.93566	2.20726
H	-8.48203	-3.77238	2.50799	H	-1.24834	-1.7369	1.76258	H	16.75617	-3.61276	1.69578
H	-11.34036	2.03033	-2.27537	H	-0.70946	-0.20465	2.4177	H	-1.15816	1.06671	1.07775
H	-8.93697	1.54681	-2.09709	H	1.69752	-0.93246	2.15623	H	1.58488	0.14397	2.04599
H	-10.38637	-3.47191	2.22754	H	1.16202	-2.48809	1.53925	H	0.46127	1.14864	2.94107
H	-12.77184	-2.93539	1.98535	H	-0.03785	-2.93295	3.70183	H	1.58696	2.15664	0.29955
H	-18.08693	2.22527	0.99966	H	0.50765	-1.38097	4.31991	H	0.10393	2.43914	-0.59563
H	-19.43697	1.1545	-0.77102	H	2.90162	-2.12472	4.07673	H	-0.9231	3.48501	1.46485

H	-18.3886	-0.44388	-2.3367
H	-14.75041	-1.39815	-2.19021
H	-15.95743	-3.394	-2.98137
H	-16.36875	-3.0502	-1.28647
H	-17.51615	-2.65745	-2.57925
H	-15.36948	-1.45678	-4.57377
H	-15.3819	0.21572	-3.97113
H	-16.90752	-0.6489	-4.23329
H	-14.40991	1.57759	1.47553
H	-14.8005	3.90849	2.1621
H	-15.03885	3.72982	0.40978
H	-16.43708	3.87492	1.48937
H	-15.32795	1.94124	3.73443
H	-15.91914	0.40595	3.05986
H	-16.98409	1.82199	3.11908

H	2.3561	-3.67674	3.4592
H	1.16706	-4.12258	5.63339
H	1.72122	-2.57435	6.25253
H	4.11013	-3.32664	6.00098
H	3.55707	-4.87482	5.38062
H	-1.29758	-2.17122	-1.2754
H	-0.62189	-0.96679	-2.35268
H	1.71719	-1.72857	-1.72741
H	1.02849	-2.96063	-0.68343
H	-0.12068	-3.99761	-2.66016
H	0.57121	-2.76742	-3.7073
H	2.88693	-3.55049	-3.09364
H	2.19334	-4.77774	-2.04618
H	1.05063	-5.82457	-4.0314
H	1.75214	-4.60099	-5.07902
H	4.0611	-5.38995	-4.44993
H	3.35623	-6.61459	-3.40627
H	2.22175	-7.6552	-5.39727
H	2.93134	-6.43305	-6.43952
H	4.26697	-8.54916	-6.53658
H	5.24752	-7.25356	-5.83352
H	4.53061	-8.48695	-4.78704
H	2.37669	-5.32577	7.55424
H	2.9238	-3.77632	8.17433
H	4.39859	-5.62571	9.00141
H	5.32745	-4.5298	7.96676
H	4.781	-6.09007	7.33608

H	0.59698	3.27198	2.32117
H	1.7626	4.70676	0.6184
H	0.24172	4.92934	-0.23248
H	-0.74156	6.02	1.81398
H	0.78126	5.79891	2.66213
H	1.93788	7.2367	0.95339
H	0.41218	7.46973	0.11322
H	-0.56177	8.5139	2.19361
H	0.99146	8.34625	2.99738
H	0.55273	10.64978	2.10986
H	0.47565	10.01766	0.47425
H	2.70823	11.0607	0.9679
H	2.90628	9.34294	0.60831
H	2.96929	9.907	2.28463
H	-1.24417	-0.68472	2.90281
H	-0.14179	-1.6963	1.98039
H	1.4988	-1.66167	3.87271
H	0.45301	-0.57501	4.77409
H	0.16876	-2.79589	5.66955
H	-1.32615	-2.33754	4.87111
H	-0.70659	-3.74228	2.88421
H	0.82937	-4.14253	3.63802
H	-0.39177	-5.26249	5.52828
H	-1.92961	-4.84071	4.79063
H	-1.33601	-6.21188	2.76779
H	0.20072	-6.63514	3.50444
H	-1.46585	-8.47783	3.82823
H	-1.01621	-7.791	5.39665
H	-2.56504	-7.36353	4.65613

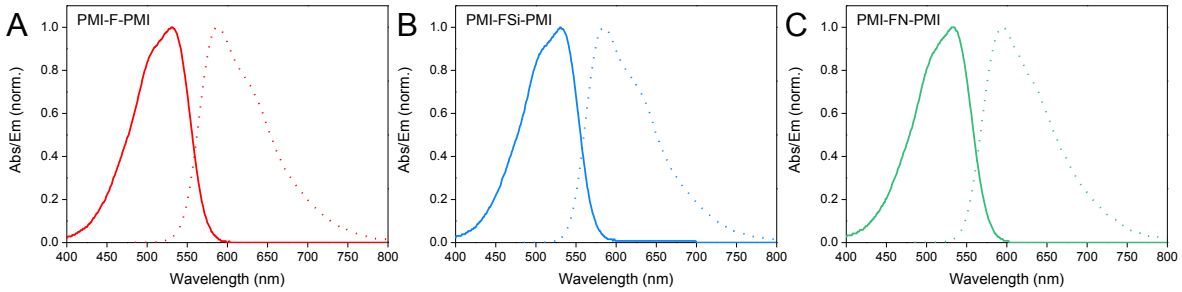

*Figure S12: Normalized absorption and fluorescence spectra (dashed lines) in $CHCl_3$ solution of: A - **PMI-F-PMI (3a)**; B - **PMI-FSi-PMI (3b)**; C - **PMI-FN-PMI (3c)**.*

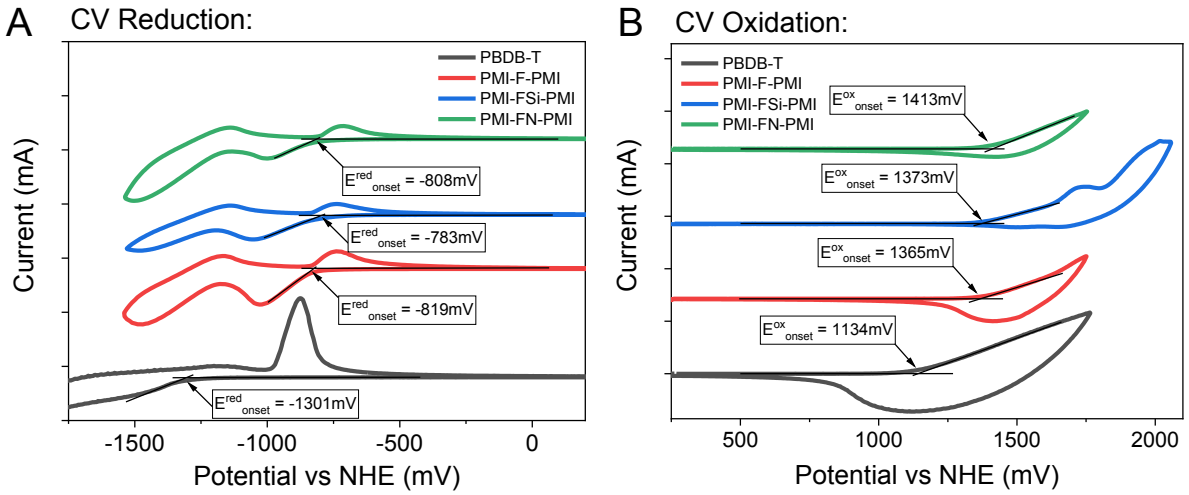

Figure S13: Cyclic voltammetry measurements. Oxidation and reduction were measured separately and with a scan speed of 50 mV/s. Each measurement was calibrated with a Fc/Fc^+ redox couple and the presented data is plotted against NHE.

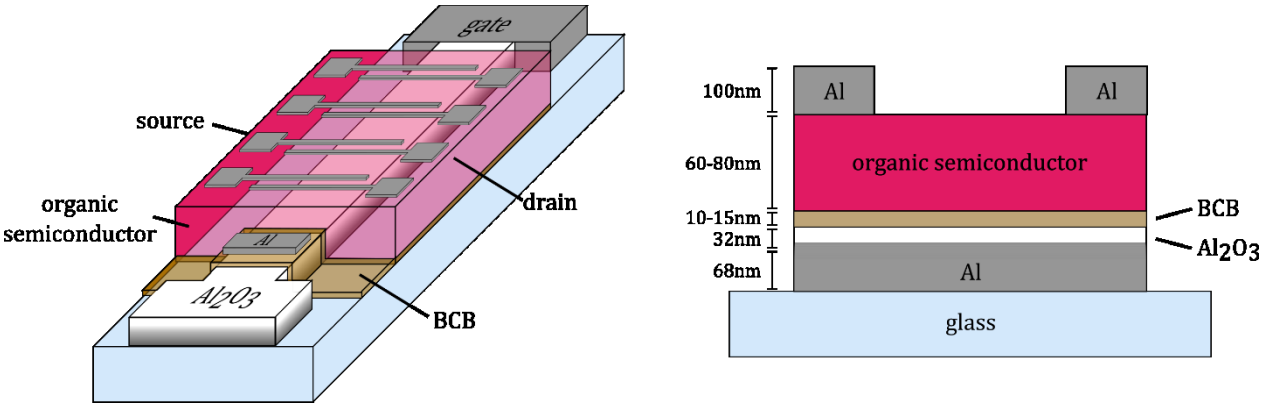

Figure S14: OFET device structure in bottom-gate, top-contact geometry.

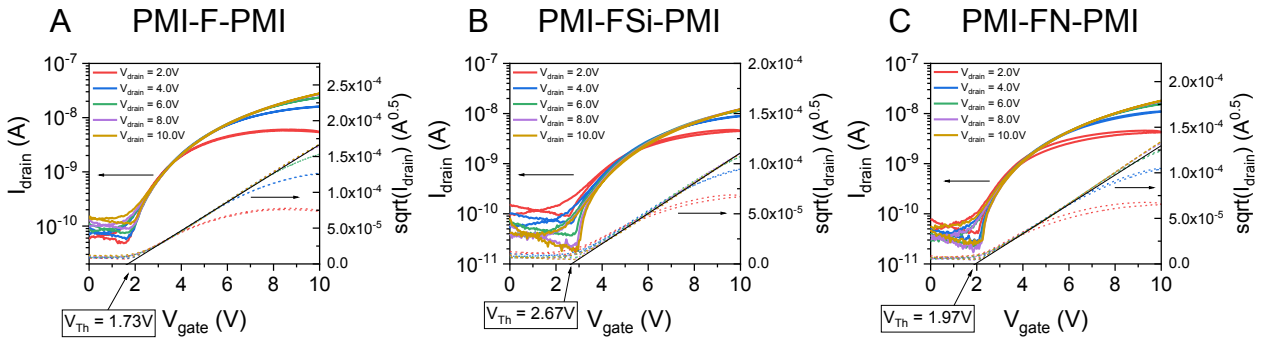

*Figure S15: OFET transfer characteristic of: A **PMI-F-PMI (3a)**, B **PMI-FSi-PMI (3b)** and C **PMI-FN-PMI (3c)**. V_{gate} is swept from 0 to 10 V with constant V_{drain}. After each sweep V_{drain} is increased by 2 V. The solid curves indicate the drain current on a logarithmic scale (left y-axis), while the dashed curves represent the square root of the drain current (right y-axis). The straight black line indicates the linear fit of $\sqrt{I_{drain}}$. The intersection of the black line with the x-axis allows to read out the values of the threshold voltage V_{Th}.*

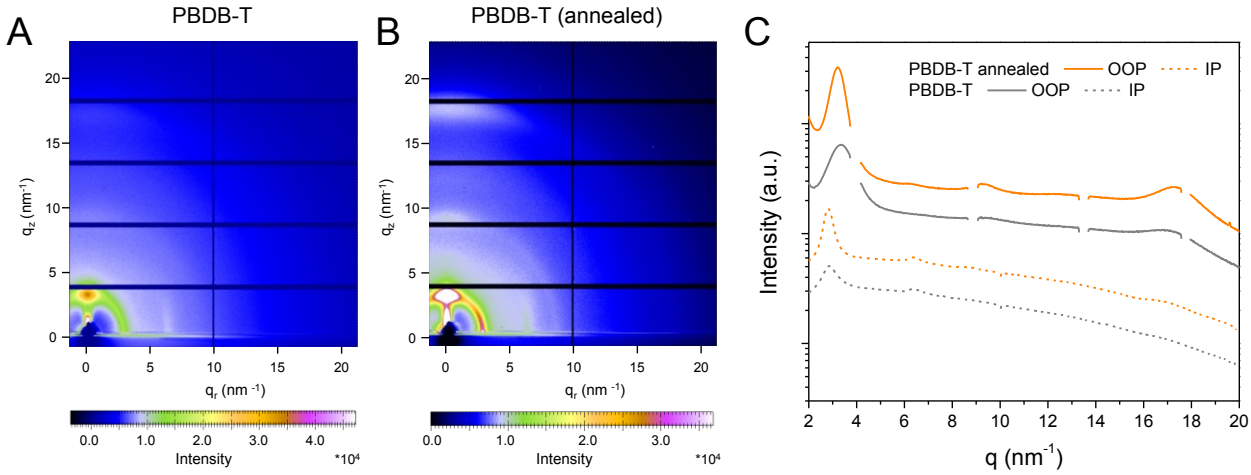

Figure S16: 2D GIWAXS patterns of (A) the donor PBDB-T w/o annealing and (B) w. annealing and (C) the corresponding 1D-line cuts in the out-of-plane (OOP) and in-plane (IP) direction. The scattering profiles are shifted vertically for better visibility.

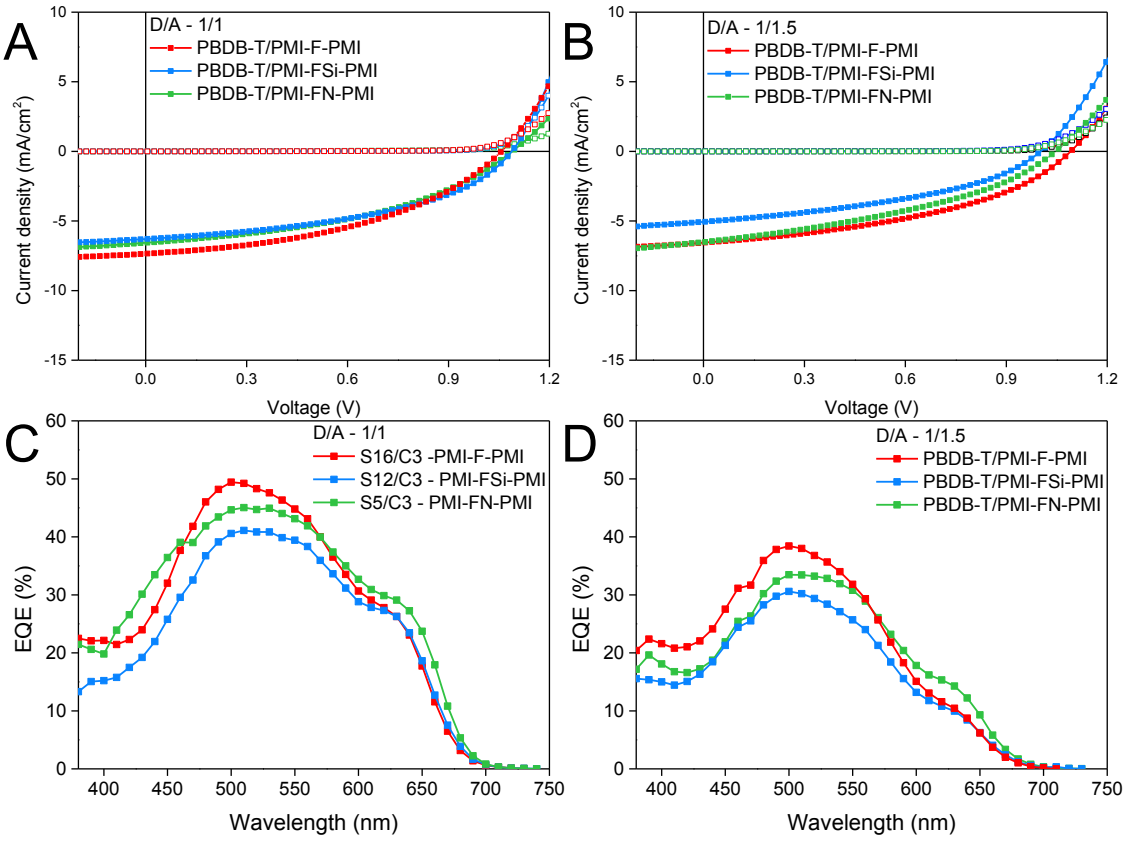

*Figure S17: J-V curves (under illumination - solid symbols and under dark conditions - hollow symbols; notice that the hollow curves overlay) and EQE spectra of the best solar cells with a D/A ratio of 1/1 (A, C) and 1/1.5 (B, D) for: red - **PMI-F-PMI (3a)**; blue - **PMI-FSi-PMI (3b)**; green - **PMI-FN-PMI (3c)**.*

*Table S2: Solar cell characteristics for the best solar cells based on **PMI-F-PMI (3a)**, **PMI-FSi-PMI (3b)** and **PMI-FN-PMI (3c)**, fabricated with a D/A ratio of 1/1 (top) and 1/1.5 (bottom) w/o annealing the absorber layer.*

D/A ratio – 1/1					
Acceptor	**Thickness (nm)**	**V_{OC} (V)**	**J_{SC} (mA/cm^2)**	**FF (%)**	**PCE (%)**
PMI-F-PMI	125	1.06	7.34	43.3	3.34
PMI-FSi-PMI	94	1.10	6.29	44.9	3.08
PMI-FN-PMI	124	1.10	6.56	42.2	3.02
D/A ratio – 1/1.5					
Acceptor	**Thickness (nm)**	**V_{OC} (V)**	**J_{SC} (mA/cm^2)**	**FF (%)**	**PCE (%)**
PMI-F-PMI	121	1.10	6.55	42.2	3.02
PMI-FSi-PMI	110	0.99	5.06	41.1	2.06
PMI-FN-PMI	120	1.06	6.50	37.8	2.58

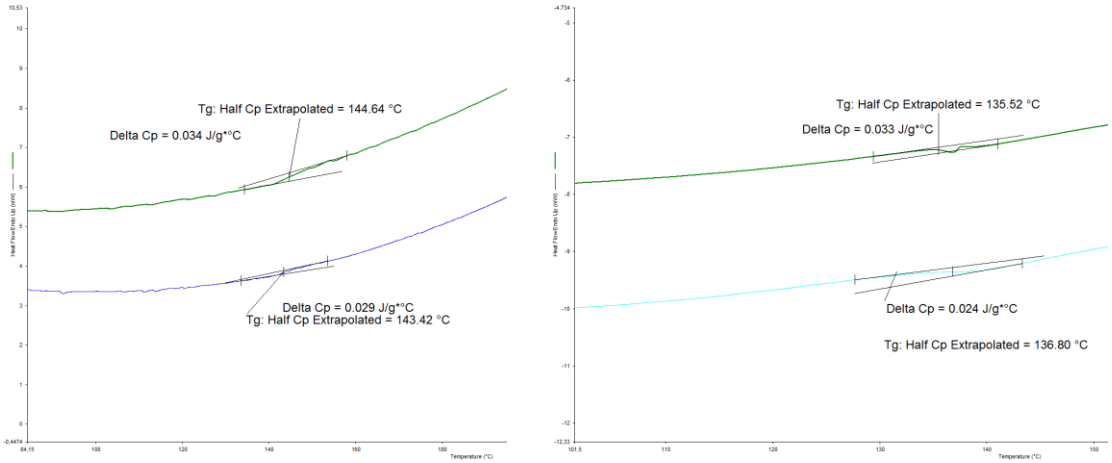

Figure S18: DSC measurements of PBDB-T: heating runs (left), cooling run (right) (measured with a heating (cooling) rate of 20 K/min (bottom curves) and with 40 K/min (top curves).

*Table S3: Characteristic solar cell parameters of the 15 best solar cells with PBDB-T – **PMI-F-PMI (3a)**, **PMI-FSi-PMI (3b)** and **PMI-FN-PMI (3c)** absorber layers (D/A – 1 /0.66) without and with annealing.*

D/A – 1/0.66					
Acceptor	**Annealing**	**V_{OC} (V)**	**J_{SC} (mA/cm^2)**	**FF (%)**	**PCE (%)**
PMI-F-PMI					
	-	1.10	7.04	45.4	3.48
	-	1.08	7.08	45.4	3.44
	-	1.04	6.81	46.0	3.23
	-	1.10	6.40	45.5	3.17
	-	1.08	6.57	44.6	3.14
	-	1.10	6.41	44.8	3.13
	-	1.04	6.43	46.6	3.09
	-	1.04	6.45	46.1	3.07
	-	1.08	6.79	42.0	3.06
	-	1.04	6.15	47.1	2.99
	-	1.04	6.60	43.3	2.95
	-	1.08	6.46	42.2	2.93
	-	1.04	6.17	45.8	2.92
	-	1.04	6.32	44.5	2.90
	-	1.06	6.50	41.9	2.88
PMI-F-PMI					
	135 °C	1.10	8.94	52.9	5.16
	135 °C	1.10	8.35	52.6	4.8
	135 °C	1.10	8.24	53.3	4.79
	135 °C	1.12	7.96	52.4	4.64
	135 °C	1.10	8.61	49.0	4.60
	135 °C	1.10	8.09	49.2	4.35
	135 °C	1.12	7.92	49.2	4.33
	135 °C	1.12	7.98	48.6	4.31
	135 °C	0.97	9.11	46.4	4.10
	135 °C	1.14	7.95	45.2	4.07
	135 °C	1.14	8.11	44.2	4.06
	135 °C	1.08	8.06	46.9	4.05
	135 °C	1.12	7.73	46.8	4.02
	135 °C	1.12	7.50	47.6	3.97
	135 °C	1.10	7.47	48.0	3.91

D/A – 1/0.66					
Acceptor	**Annealing**	**V_{OC} (V)**	**J_{SC} (mA/cm^2)**	**FF (%)**	**PCE (%)**
PMI-FSi-PMI					
	-	1.08	6.58	43.4	3.06
	-	1.04	6.28	44.8	2.90
	-	0.97	6.56	43.6	2.78
	-	1.10	6.02	41.9	2.75
	-	1.10	6.51	38.6	2.75
	-	1.02	6.22	43.0	2.72
	-	1.06	6.13	41.6	2.68
	-	1.12	5.95	40.6	2.67
	-	0.99	5.97	44.8	2.66
	-	1.10	5.74	42.4	2.64
	-	1.10	5.74	42.1	2.62
	-	0.97	6.27	42.5	2.59
	-	1.08	5.88	40.2	2.53
	-	0.99	5.88	43.5	2.54
	-	1.10	5.42	42.4	2.49
PMI-FSi-PMI					
	150 °C	1.14	8.55	53.4	5.16
	150 °C	1.10	8.41	54.9	5.05
	150 °C	1.10	8.21	54.8	4.92
	150 °C	1.10	8.05	54.7	4.82
	150 °C	1.14	8.09	51.9	4.75
	150 °C	1.14	7.87	53.3	4.74
	150 °C	1.12	8.01	52.9	4.72
	150 °C	1.10	7.90	54.1	4.67
	150 °C	1.14	8.21	50.0	4.65
	150 °C	1.12	7.88	53.0	4.62
	150 °C	1.14	7.76	52.7	4.61
	150 °C	1.10	7.46	55.4	4.52
	150 °C	1.12	7.52	53.3	4.43
	150 °C	1.14	7.33	50.7	4.19
	150 °C	1.14	7.02	52.3	4.15

D/A – 1/0.66					
Acceptor	**Annealing**	**V_{OC} (V)**	**J_{SC} (mA/cm^2)**	**FF (%)**	**PCE (%)**
PMI-FN-PMI					
	-	1.08	8.17	39.6	3.46
	-	1.08	7.86	39.4	3.32
	-	1.08	7.55	39.7	3.21
	-	1.08	7.42	39.2	3.11
	-	1.08	7.20	39.7	3.06
	-	1.08	7.21	38.9	3.00
	-	1.08	7.20	38.7	2.98
	-	1.04	7.17	39.5	2.92
	-	1.08	6.86	38.8	2.85
	-	1.08	6.74	39.1	2.82
	-	1.06	5.87	45.7	2.82
	-	1.04	5.79	45.7	2.72
	-	1.06	5.71	45.2	2.71
	-	1.06	6.70	38.4	2.71
	-	1.06	5.80	44.5	2.71
PMI-FN-PMI					
	150 °C	1.06	10.18	48.0	5.16
	150 °C	1.14	10.07	45.2	5.14
	150 °C	1.16	9.48	43.2	4.72
	150 °C	1.12	9.56	43.9	4.66
	150 °C	1.04	9.37	47.7	4.63
	150 °C	1.14	9.37	42.9	4.55
	150 °C	1.08	9.03	45.2	4.41
	150 °C	1.04	8.69	48.3	4.34
	150 °C	1.14	8.17	46.2	4.29
	150 °C	1.16	8.92	41.9	4.29
	150 °C	1.12	9.44	39.8	4.17
	150 °C	1.12	9.01	41.3	4.13
	150 °C	1.14	8.20	43.8	4.09
	150 °C	1.10	8.53	43.6	4.08
	150 °C	1.16	8.46	41.4	4.05

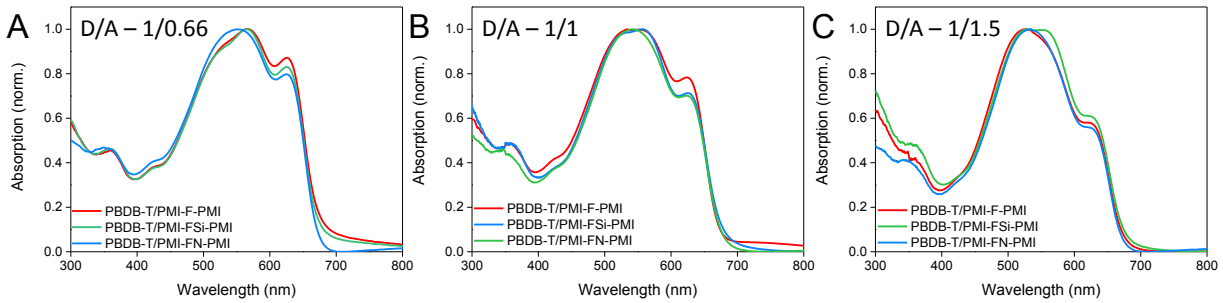

Figure S19: Optical absorption spectra of blend films (PBDB-T/acceptor) in different D/A ratios of 1/0.66 (A) 1/1 (B) and 1/1.5 (C).

*Table S4: Comparison between the current densities (mA/cm²) of solar cells based on **PMI-F-PMI (3a)**, **PMI-FSi-PMI (3b)** and **PMI-FN-PMI (3c)** in a D/A ratio of 1/0.66 (w/o and w. annealing), 1/1 and 1/1.5 (w/o annealing) from prior EQE- , from EQE- and post EQE measurements.*

D/A – 1/0.66			
	PMI-F-PMI (w/o annealing)	**PMI-FSi-PMI (w/o annealing)**	**PMI-FN-PMI (w/o annealing)**
J_{SC} (integrated)	6.37 mA/cm²	6.46 mA/cm²	6.88 mA/cm²
J_{SC} (before EQE)	7.27 mA/cm²	6.79 mA/cm²	7.97 mA/cm²
J_{SC} (after EQE)	6.66 mA/cm²	6.94 mA/cm²	7.44 mA/cm²
	PMI-F-PMI (annealed)	**PMI-FSi-PMI (annealed)**	**PMI-FN-PMI (annealed)**
J_{SC} (integrated)	6.98 mA/cm²	7.40 mA/cm²	10.02 mA/cm²
J_{SC} (before EQE)	8.83 mA/cm²	8.13 mA/cm²	10.18 mA/cm²
J_{SC} (after EQE)	5.81 mA/cm²	7.64 mA/cm²	9.33 mA/cm²
D/A – 1/1			
	PMI-F-PMI	**PMI-FSi-PMI**	**PMI-FN-PMI**
J_{SC} (integrated)	6.50 mA/cm²	5.19 mA/cm²	6.08 mA/cm²
J_{SC} (before EQE)	7.02 mA/cm²	6.05 mA/cm²	6.08 mA/cm²
J_{SC} (after EQE)	6.31 mA/cm²	5.85 mA/cm²	5.35 mA/cm²
D/A – 1/1.5			
	PMI-F-PMI	**PMI-FSi-PMI**	**PMI-FN-PMI**
J_{SC} (integrated)	4.03 mA/cm²	3.27 mA/cm²	3.85 mA/cm²
J_{SC} (before EQE)	6.45 mA/cm²	4.99 mA/cm²	6.51 mA/cm²
J_{SC} (after EQE)	3.01 mA/cm²	3.02 mA/cm²	4.40 mA/cm²

Chapter VI

PMI-FF-PMI as Alternative Perylene Monoimide-Based Non-Fullerene Acceptor in Organic Solar Cells

Another perylene-based acceptor, investigated within this thesis was comprised of two perylene monoimide units linked via an indenofluorene core – **PMI-FF-PMI** (**6**). It is one alternative to the NFAs **PMI-F-PMI** (**3a**), **PMI-FSi-PMI** (**3b**) and **PMI-FN-PMI** (**3c**), described in Chapter V. It was synthesized via Suzuki coupling using a perylene pinacol ester and the linker dihydroindeno[1,2-b]fluorene dibromide (**Scheme 1**; experimental see SI). The structure was verified by ^{1}H and ^{13}C APT NMR spectroscopy as well as MALDI-TOF mass spectrometry (SI – Figure S1 – S3). The linker exhibits a larger conjugated π-system in the donor subunit which might improve the optoelectronic properties of the NFA. Additionally four octyl-side chains should guarantee a good solubility in solvents like DCM, CB or $CHCl_3$. Furthermore, simultaneous thermal analysis displayed a melting point around 420 °C and decomposition temperature at 434 °C which indicates high stability and their potential as acceptor in photovoltaic applications.

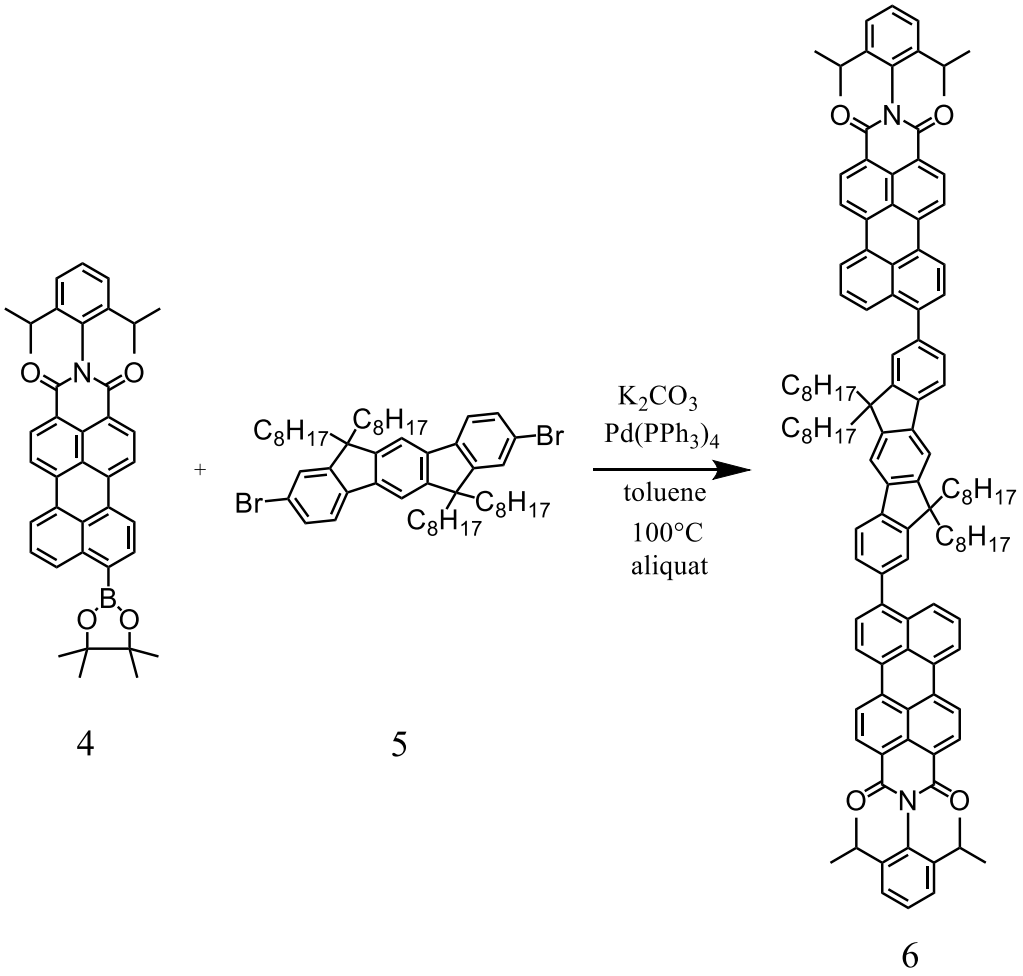

Scheme 1 *Synthesis procedure for* ***PMI-FF-PMI (6)****.*

Computations

Prior to experimental characterization, DFT computations with B3LYP/6-31G* / Gaussian 09 were conducted to compare the properties of **6** to the NFAs from Chapter V. The octyl-groups on the linker were therefore substituted with methyl groups to reduce the overall calculation time. Herein, slightly higher shifted HOMO and LUMO levels of -5.36 eV and -2.84 eV (compared to e.g. -5.42 eV and -2.88 eV for **PMI-F-PMI** (**3a**) were calculated, respectively, which translates to a band gap of 2.52 eV. The distribution of the energy density did not change by the introduction of the larger linker molecule. In its ground state (HOMO) the energy density is distributed alongside the perylene and the linker, whereas in the excited state it is shifted towards the perylene only (**Figure 1**). Also, similar to the fluorene derivatives from Chapter V, **PMI-FF-PMI** shows dihedral angles of around 55° and is isolobal.

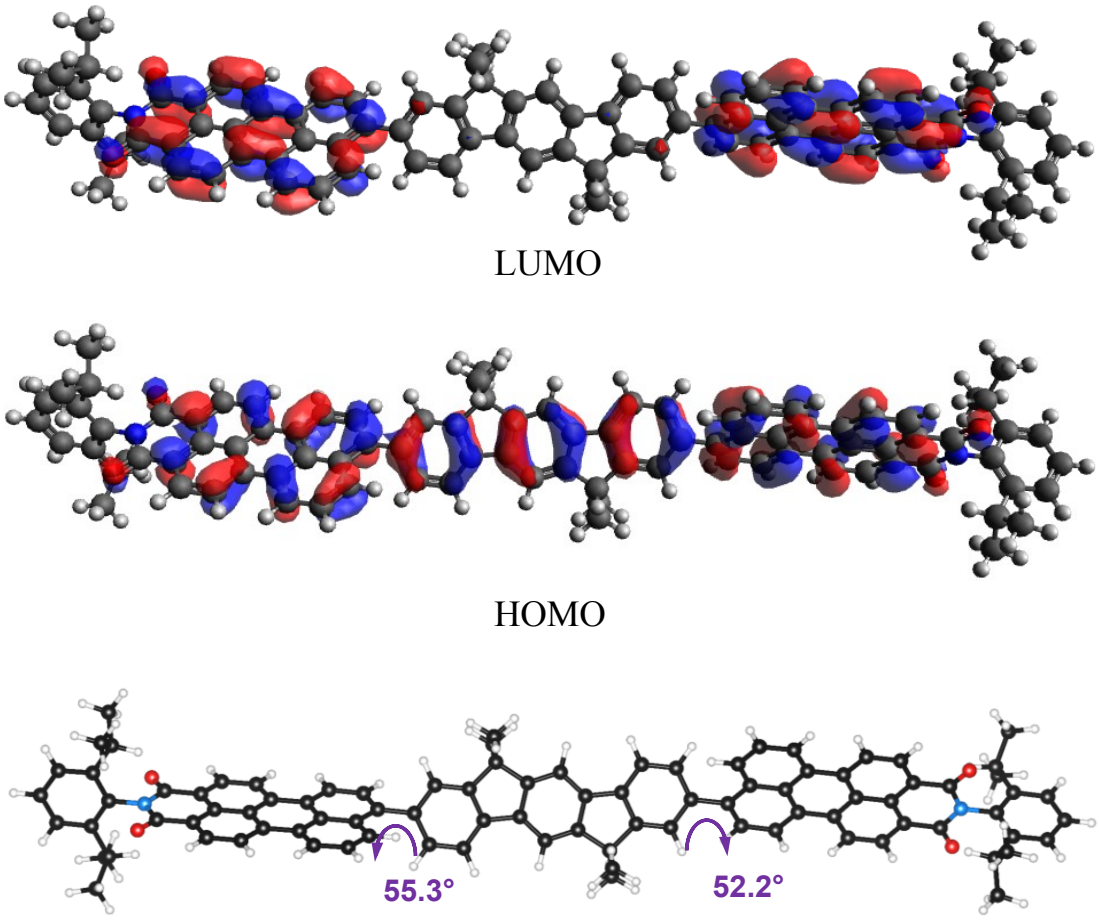

Fig. 1 *DFT (B3LYP/6-31G*) –Frontier molecular orbitals of* ***PMI-FF-PMI (6)*** *as well as optimal geometry and dihedral angles of* ***PMI-FF-PMI (6)****.*

Optical Spectroscopy

UV-Vis absorption spectra of **PMI-FF-PMI** (**6**) in $CHCl_3$ solution showed a similar absorption behavior compared to e.g. **PMI-F-PMI** (**3a**) with a maximum of 529 nm. A second absorption peak in the region from 300 to 400 nm was also observed indicating a second electron transfer (SI – Figure S4). The molar absorption coefficient was calculated to $9.1 \cdot 10^4$ M^{-1} cm^{-1} and is comparable with the NFAs described before, e.g. **PMI-F-PMI** ($9.0 \cdot 10^4$ M^{-1} cm^{-1}). Moreover, a Stokes shift of 78 nm was observed from excitation and emission spectra of **PMI-FF-PMI** (**6**) in $CHCl_3$ solution (**Figure 2A**). This is significantly higher than the Stokes shift of e.g. **PMI-F-PMI** of 57 nm.

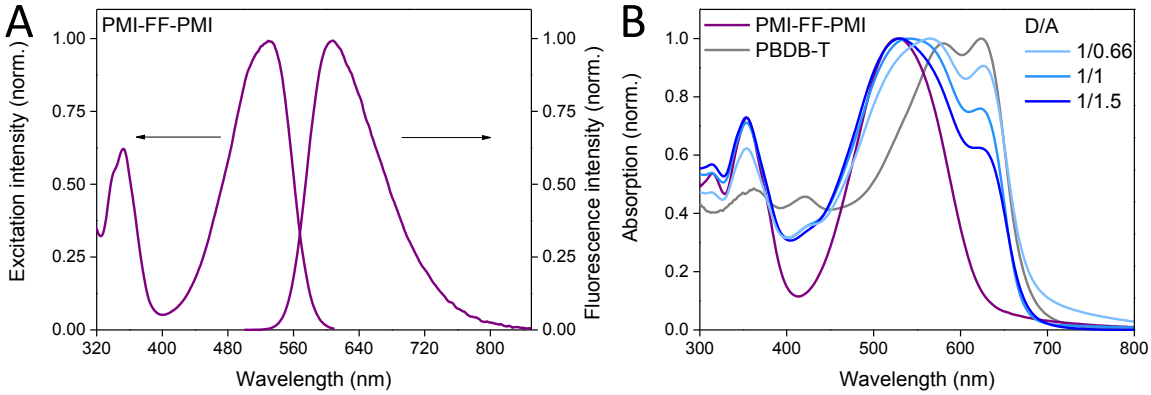

Fig. 2 *Optical spectroscopy of* ***PMI-FF-PMI (6)****; (A) excitation and emission spectra in $CHCl_3$ solution and (B) PBBD-T,* ***PMI-FF-PMI*** *thin films as well as their corresponding blends in D/A ratios of 1/0.66, 1/1 and 1/1.5.*

On thin films, the UV-Vis spectra of **PMI-FF-PMI** (**6**) is slightly broadened (compared to the one from solution) which can be ascribed to π-π-stacking. Additionally, the absorption coefficient was determined to $1.6 \cdot 10^7$ cm^{-1}. When blended with PBDB-T as donor (**Figure 2B**) a broad spectrum from 300 to 700 nm is covered and the influence of a varying D/A ratio is clearly visible.

Table 1 *Optical properties of* ***PMI-FF-PMI (6)****.*

Compound	$\lambda_{max, sol.}$ (nm)	$\lambda_{onset., sol.}$ (nm)	$\lambda_{max, (fluor., sol).}$ (nm)	E_g (eV)	ε (M^{-1} cm^{-1})	α (cm^{-1})	$\lambda_{max, film}$ (nm)
PMI-FF-PMI (6)	529	579	607	2.14[1]/2.00[2]	$9.1 \cdot 10^4$	$1.6 \cdot 10^7$	528

[1] solution, [2] thin film

Photovoltaic Performance

For a better comparison of the solar cells from Chapter V, the same device set-up and deposition parameters for the interlayers and electrodes were used. The blend solutions of PBDB-T/**PMI-FF-PMI** were prepared in CB (mixing temperature of 70 °C) in three different D/A ratios (D/A – 1/0.66, 1/1 and 1/1.5 w/w) and hot spin coated (70 °C) by a two-step spin coating process.

The finished solar cells were then tested by recording J-V measurements and the best cells are illustrated in **Figure 3A, C, E**. Herein, the same trend regarding the device performance with varying D/A ratio as for e.g. **PMI-F-PMI** was observed. Solar cells with a D/A ratio of 1/0.66 resulted in the highest device efficiencies of 4.03% w/o annealing of the absorber layer and remarkable 6.21% by annealing the absorber layer at 135 °C. Moreover, high open circuit voltages of 1.16 V and 1.18 V were recorded for non-annealed and annealed cells, respectively. This is also supported by slightly higher lying HOMO/LUMO levels of **PMI-FF-PMI** obtained from DFT compared to e.g. **PMI-F-PMI**. Also, there is no significant change in absorption. Upon annealing also the current density increased from mean 6.49 mA/cm^2 ± 0.32 to 7.71 mA/cm^2 ± 0.41 as well as the fill factor from mean 49.0% ± 4.3 to 62.2% ± 1.4 which might be ascribed to a better interface between the ZnO layer and absorber layer and an enhanced morphology of the absorber layer.

By increasing the acceptor content in the blend (D/A – 1/1 and 1/1.5 w/w) the overall device performance was reduced (see **Table 2**). While solar cells with a D/A ratio of 1/1 showed maximum device efficiencies of 3.75% and 5.24% for non-annealed and annealed cells, respectively, in solar cells with a D/A ratio of 1/1.5 the PCE was even further reduced to maximum efficiencies of 3.01% and 4.15%, respectively. The lower device performances are on the one side related to thicker absorber films which reduces the current density and fill factor. Especially, in solar cells with D/A – 1/1.5 the fill factor was significantly lower. On the other side, experiments showed that thinner films at around 110 nm with the same D/A ratio of 1/1.5 did not improve the power output (SI – Table S3). Nevertheless, annealing of the absorber layer at high temperatures seems to be a promising way to enhance the overall cell performance as observed with these materials in all three D/A variations.

Table 2 *Best and average device characteristics of PBDB-T/**PMI-FF-PMI** based solar cells with D/A ratios of 1/0.66, 1/1 and 1/1.5 with and without annealing of the absorber layer. The average values and standard deviations were calculated from the best 10 cells.*

D/A ratio	Annealing temperature	Thickness (nm)	V_{OC} (V)	J_{SC} (mA/cm^2)	FF (%)	PCE (%)
D/A – 1/0.66						
best cell	-	83 ± 3 nm	1.16	6.54	53.5	4.03
average			1.16 ± 0.01	6.49 ± 0.32	49.0 ± 4.3	3.68 ± 0.39
best cell	135 °C	80 ± 6 nm	1.18	8.49	62.4	**6.21**
average			1.15 ± 0.02	7.71 ± 0.41	62.2 ± 1.4	5.48 ± 0.39
D/A – 1/1						
best cell	-	98 ± 2 nm	1.12	6.32	53.6	3.75
average			1.14 ± 0.02	5.96 ± 0.33	49.8 ± 3.5	3.37 ± 0.36
best cell	135 °C	95 ± 2 nm	1.14	7.39	62.3	5.24
average			1.14 ± 0.01	6.83 ± 0.38	61.1 ± 1.0	4.73 ± 0.28
D/A – 1/1.5						
best cell	-	147 ± 2 nm	1.10	6.21	44.5	3.01
average			1.09 ± 0.01	5.98 ± 0.29	43.2 ± 2.5	2.81 ± 0.15
best cell	135 °C	132 ± 3 nm	1.10	7.36	51.6	4.15
average			1.11 ± 0.01	6.78 ± 0.32	50.8 ± 1.0	3.80 ± 0.20

Furthermore, EQE spectra of solar cells in all tested D/A ratios w. and w/o annealing were recorded (**Figure 3B, D, F**). The onset of photocurrent generation fits well to the recorded absorption spectra (**Figure 2B**). Photocurrent generation starts at the onset of around 700 nm and has its first shoulder at 630 nm which correspond to the absorption maximum of PBDB-T. The overall maximum of photocurrent is found at 510 nm, which can be attributed to **PMI-FF-PMI**. Moreover, the difference in D/A ratio is also visible as the maxima of shoulder 1 and shoulder 2 are shifted depending on the acceptor concentration (**Figure 2B**). The highest EQE values were

obtained from solar cells with annealed absorber layers with maximum values of 46%, 44% and 44% for PBDB-T/**PMI-FF-PMI** cells with D/A 1/0.66, 1/1 and 1/1.5, respectively. The current densities from EQE were calculated and compared to measured current densities from J-V measurements before and after the EQE measurement. Herein, the cells also started to degrade upon exposure to ambient atmosphere therefore reduced J_{SC} values were recorded and more likely fit to the obtained current densities from repeating J-V measurements after the EQE measurement.

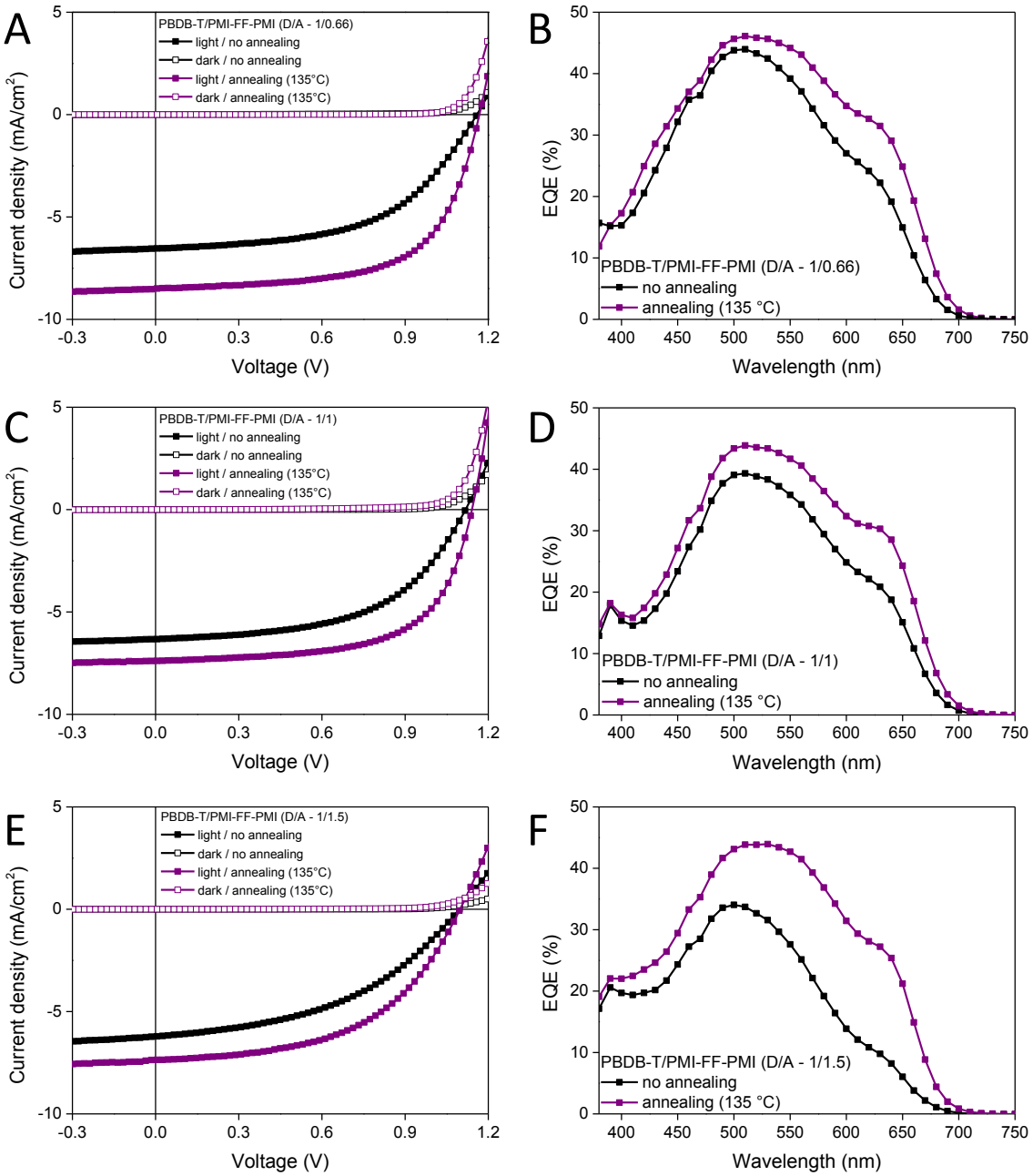

Fig. 3 *J-V curves (under illumination – solid symbols and under dark conditions – hollow symbols) and EQE spectra of the best cells of PBDB-T/**PMI-FF-PMI** in the D/A ratios of: A,B – 1/0.66, C,D: 1/1 and E,F – 1/1.5; w. and w/o annealing at 135 °C.*

Supporting Information

Synthesis of **PMI-FF-PMI** (**6**)

In a Schlenk tube, operated under nitrogen, 500 mg (0.823 mmol, 2.1 equiv.) of 8-(4,4,5,5-tetramethyl-1,3,2-dioxaborolan-2-yl)-*N*-(2,6-diisopropylphenyl)-perylene-3,4-dicarboximide (4) and 337 mg (0.392 mmol, 1 equiv.) of 2,8-dibromo-6,6,12,12-tetraoctyl-6,12-dihydroindeno[1,2-b]fluorene (5) (CAS Number 264281-45-0) were dissolved in 50 ml toluene followed by the addition of 1 M aqueous K_2CO_3 (5 ml) and 1 drop of Aliquat 336. Afterwards, $Pd(PPh_3)_4$ (0.039 mmol, 0.1 equiv.) was added and the reaction mixture was heated at 100 °C for 24 h. Upon completion, the reaction mixture was extracted with deion. H_2O and dried over Na_2SO_4 followed by evaporation of the solvent under reduced pressure. The residue was purified by column chromatography (eluent: CH_2Cl_2/pentane – 10/1) and further recrystallized using CH_2Cl_2/hexane to yield **6** as a violet solid. Yield: 228 mg (35%). R_f = 0.39 – 0.52 (CH_2Cl_2)

^{1}H NMR (500 MHz, $CDCl_3$): δ = 8.70 (dd, J = 11.83 Hz, 4H), 8.59 (d, J = 8.05 Hz, 2H), 8.56-8.52 (m, 6H), 8.11 (d, J = 8.50 Hz, 2H) 7.97 (d, J = 7.81 Hz, 2H) 7.79 (s, 2H), 7.73 (d, J = 7.76 Hz, 2H), 7.63 (t, J = 8.03 Hz 2H), 7.58 (d, J = 7.87 Hz, 2H), 7.56 (s, 2H), 7.49 (t, J = 7.90 Hz, 2H) 7.35 (d, J = 7.86 Hz, 4H), 2.84-2.75 (m, 4H), 2.14-2.10 (m, 8H), 1.12-1.10 (m, 64H), 0.88-0.83 (m, 8H), 0.82 (t, J = 7.04 Hz, 12H). ^{13}C NMR (75 MHz, $CDCl_3$): δ = 164.17, 151.72, 150.86, 145.89, 144.27, 141.52, 140.58, 138.45, 137.96, 137.84, 133.10, 132.32, 132.25, 131.26, 130.81, 129.67, 129.59, 128.98, 128.72, 128.57, 128.51, 127.17, 127.12, 124.90, 124.17, 124.12, 123.79, 121.20, 121.04, 120.52, 120.22, 119.82, 114.46, 55.20, 40.77, 32.00, 30.20, 29.48, 29.41, 29.31, 24.18, 22.79, 14.25.

MS (MALDI-TOF) calc. for $C_{120}H_{128}N_2O_4H$ 1662.9987, found 1662.9929.

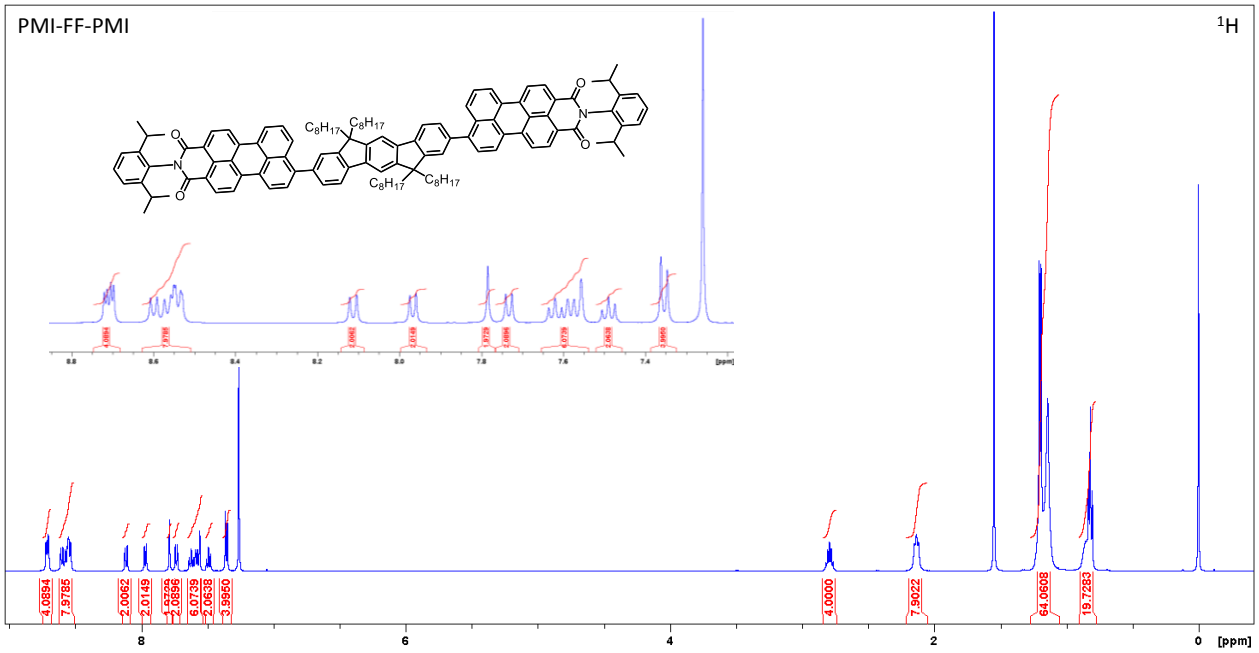

*Figure S1: ^{1}H NMR (500 MHz, $CDCl_3$) spectrum of **PMI-FF-PMI (6)** with an inset of the aromatic region, referenced to TMS.*

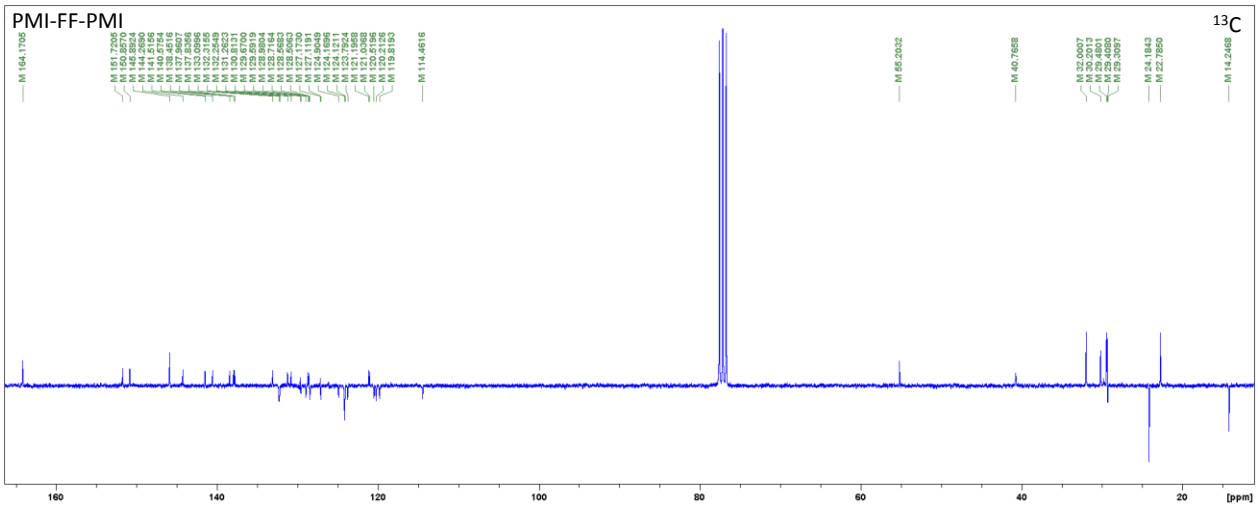

*Figure S2: ^{13}C APT NMR (75 MHz, $CDCl_3$) spectrum of **PMI-FF-PMI (6)**, referenced to $CDCl_3$.*

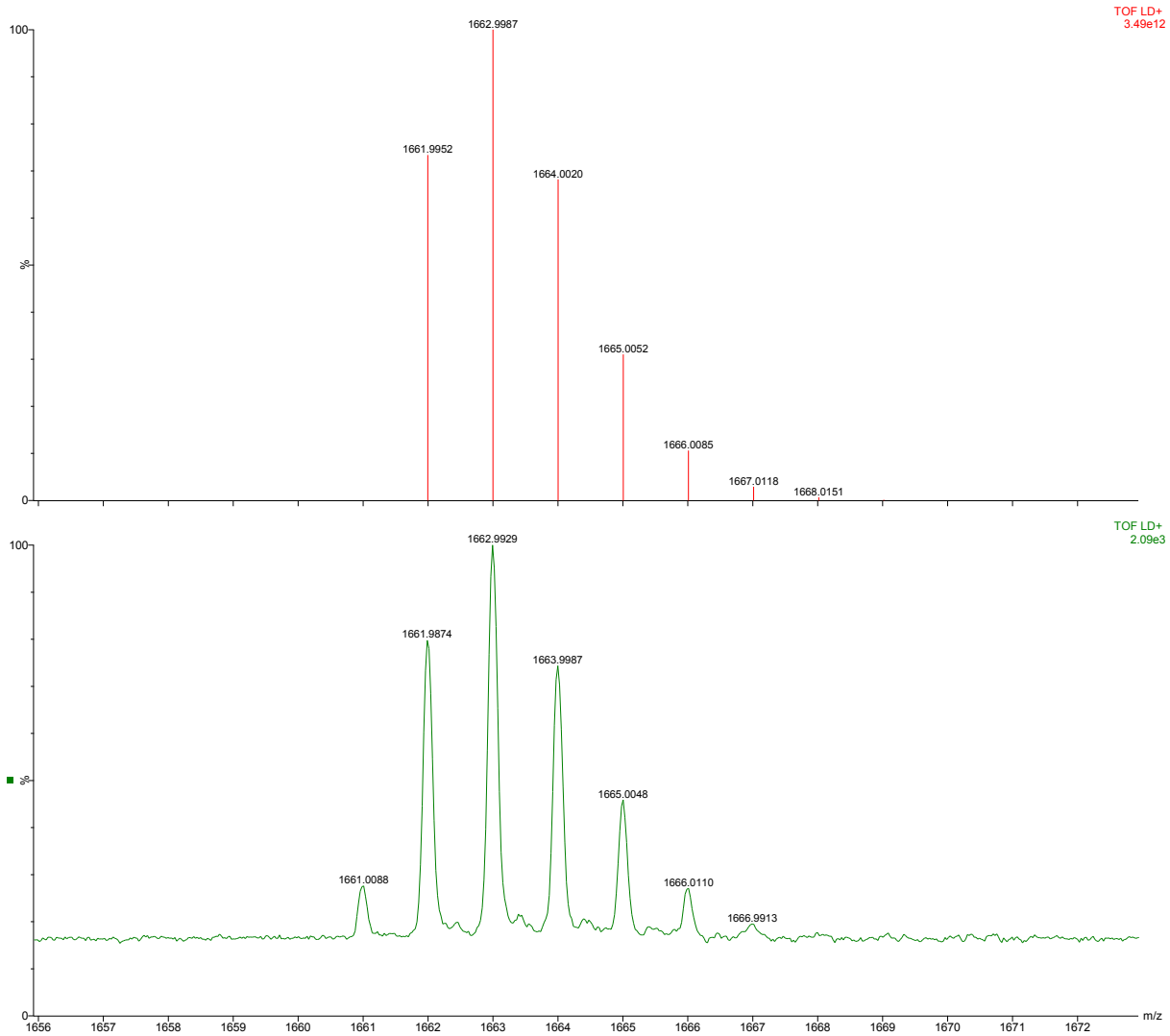

*Figure S3: HRMS (MALDI-TOF, Dithranol matrix) of **PMI-FF-PMI (6)**, upper – simulated, lower - found.*

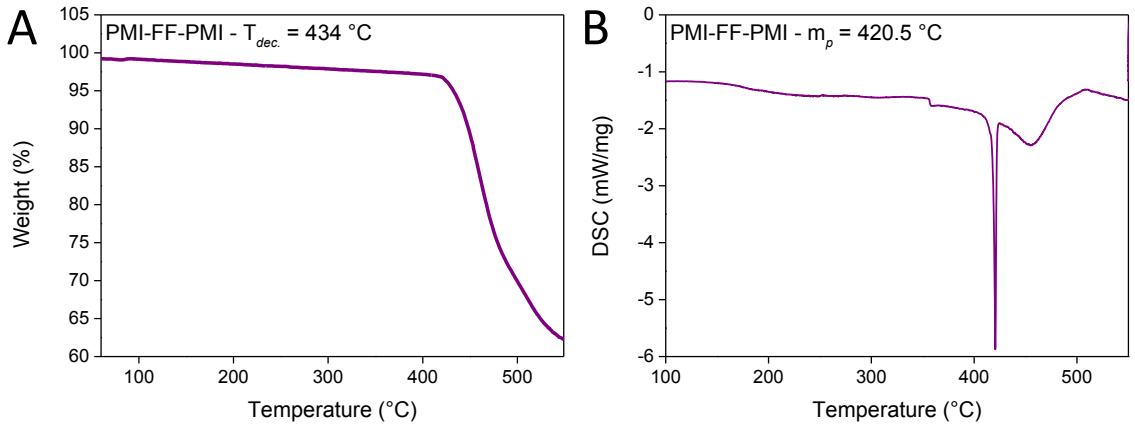

*Figure S4: Simultaneous thermal analysis of **PMI-FF-PMI (6)**; (A) thermogravimetric analysis and (B) differential scanning calorimetry.*

Table S1: Cartesian coordinates for the DFT (B3LYP/6-31G) optimized structure of* ***PMI-FF-PMI (6)****.*

PMI-FF-PMI (6)							
C	14.50213	-0.81582	-1.03839	H	14.66481	-2.05678	-2.76053
C	13.97870	-1.57256	-2.07347	H	12.23918	-2.31484	-3.05133
C	12.59635	-1.70860	-2.22756	H	11.28606	1.58550	2.41436
C	11.69062	-1.09411	-1.35866	H	13.72462	1.79622	2.63683
C	12.20928	-0.31228	-0.27845	H	10.31307	-2.42436	-3.30416
C	13.62575	-0.17828	-0.12693	H	7.88976	-2.60118	-3.58437
C	11.34105	0.33792	0.65485	H	6.35952	-1.53765	-1.97242
C	11.91462	1.08451	1.68780	H	6.94903	1.13123	1.95849
C	13.29919	1.21195	1.82756	H	9.35045	1.42913	2.18044
C	14.15859	0.59176	0.93556	H	20.44463	2.19993	-0.68634
C	10.23219	-1.22602	-1.51703	H	21.69884	0.59929	0.71764
C	9.35719	-0.59338	-0.57309	H	20.51269	-1.23716	1.86912
C	9.88585	0.19601	0.49856	H	16.71974	2.02445	-1.19872
C	9.67524	-1.94463	-2.57117	H	17.31011	4.41457	-1.25844
C	8.28677	-2.05427	-2.73393	H	17.53766	3.75934	0.37835
C	7.43111	-1.46535	-1.83005	H	18.93992	4.06679	-0.66137
C	7.93329	-0.74096	-0.71788	H	17.65738	2.89302	-3.30551
C	7.04984	-0.12299	0.23069	H	18.11782	1.19143	-3.07308
C	7.60419	0.65756	1.23322	H	19.29963	2.48169	-2.78741
C	8.98907	0.81563	1.36332	H	16.79912	-1.79041	1.60070
C	15.97053	-0.68967	-0.90406	H	17.81808	-4.01555	1.86493
C	15.62011	0.74501	1.11172	H	18.25707	-3.31413	0.29180
N	16.43973	0.08982	0.17160	H	19.43780	-3.34781	1.61329
O	16.75380	-1.22544	-1.67633	H	17.41704	-2.47263	3.88784
O	16.11195	1.40188	2.01943	H	17.57449	-0.71142	3.69792
C	17.87717	0.22906	0.32140	H	19.01917	-1.73913	3.71184
C	18.52834	1.28295	-0.34301	H	-9.35049	-1.42915	2.18047
C	19.91430	1.39546	-0.18405	H	-6.94906	-1.13129	1.95853
C	20.62260	0.49499	0.60593	H	-6.35948	1.53739	-1.97251
C	19.95265	-0.53893	1.25307	H	-7.88969	2.60088	-3.58451
C	18.56773	-0.69519	1.12459	H	-10.31301	2.42415	-3.30430
C	17.78217	2.28614	-1.21474	H	-13.72466	-1.79609	2.63688
C	17.90108	3.71597	-0.65373	H	-11.28610	-1.58547	2.41439
C	18.24338	2.20649	-2.68236	H	-12.23912	2.31469	-3.05145
C	17.86375	-1.83593	1.84984	H	-14.66476	2.05671	-2.76064

PMI-FF-PMI (6)							
C	18.37667	-3.20867	1.37523	H	-20.51261	1.23752	1.86912
C	17.97637	-1.67851	3.37836	H	-21.69886	-0.59892	0.71773
C	-7.04984	0.12285	0.23067	H	-20.44474	-2.19968	-0.68619
C	-7.93328	0.74079	-0.71793	H	-16.71985	-2.02438	-1.19862
C	-9.35718	0.59325	-0.57314	H	-17.31029	-4.41448	-1.25819
C	-9.88586	-0.19609	0.49853	H	-17.53781	-3.75914	0.37856
C	-8.98909	-0.81568	1.36333	H	-18.94009	-4.06661	-0.66113
C	-7.60420	-0.65765	1.23323	H	-17.65754	-2.89304	-3.30534
C	-7.43107	1.46512	-1.83014	H	-18.11792	-1.19141	-3.07302
C	-8.28672	2.05402	-2.73404	H	-19.29977	-2.48161	-2.78725
C	-9.67520	1.94442	-2.57128	H	-16.79904	1.79064	1.60059
C	-10.23216	1.22587	-1.51711	H	-17.81793	4.01583	1.86473
C	-11.69060	1.09401	-1.35874	H	-18.25697	3.31433	0.29164
C	-12.20927	0.31223	-0.27849	H	-19.43767	3.34811	1.61316
C	-11.34106	-0.33795	0.65484	H	-17.41689	2.47301	3.88771
C	-13.62575	0.17828	-0.12696	H	-17.57439	0.71180	3.69790
C	-14.15861	-0.59169	0.93556	H	-19.01904	1.73954	3.71178
C	-13.29923	-1.21187	1.82759	H	5.60597	-2.44137	0.20915
C	-11.91465	-1.08449	1.68781	H	3.15049	-2.70520	0.21474
C	-12.59630	1.70849	-2.22765	H	5.19956	1.84131	0.18356
C	-13.97866	1.57250	-2.07356	H	0.55141	-2.44996	0.20440
C	-14.50211	0.81581	-1.03844	H	-0.55141	2.44980	0.20430
C	-15.97052	0.68972	-0.90409	H	-5.19957	-1.84146	0.18364
C	-15.62014	-0.74488	1.11174	H	-5.60597	2.44122	0.20906
N	-16.43974	-0.08970	0.17159	H	-3.15048	2.70504	0.21465
O	-16.11199	-1.40170	2.01948	H	3.33026	3.23597	1.48201
O	-16.75377	1.22548	-1.67639	H	1.56802	3.41636	1.48508
C	-17.87718	-0.22887	0.32142	H	2.32221	2.07982	2.37575
C	-18.56769	0.69545	1.12458	H	3.32708	3.23036	-1.08831
C	-19.95262	0.53925	1.25310	H	2.31539	2.07192	-1.97397
C	-20.62261	-0.49468	0.60601	H	1.56469	3.41204	-1.08557
C	-19.91436	-1.39521	-0.18395	H	-3.32709	-3.23058	-1.08816
C	-18.52840	-1.28277	-0.34293	H	-2.31539	-2.07219	-1.97387
C	-17.78228	-2.28603	-1.21461	H	-1.56470	-3.41227	-1.08540
C	-17.90124	-3.71583	-0.65352	H	-1.56802	-3.41645	1.48524
C	-18.24351	-2.20646	-2.68223	H	-2.32221	-2.07987	2.37585
C	-17.86366	1.83620	1.84975	H	-3.33025	-3.23607	1.48216

PMI-FF-PMI (6)			
C	-18.37655	3.20893	1.37508
C	-17.97624	1.67887	3.37829
C	5.57201	-0.28462	0.18316
C	4.97250	-1.55930	0.18907
C	3.58666	-1.70969	0.20005
C	2.77772	-0.57081	0.20237
C	3.36263	0.71141	0.20200
C	4.74271	0.85471	0.19653
C	1.32017	-0.42230	0.20480
C	0.30756	-1.38991	0.20497
C	-1.01300	-0.95713	0.20445
C	-1.32017	0.42214	0.20479
C	-0.30756	1.38975	0.20492
C	1.01300	0.95697	0.20441
C	-2.77772	0.57065	0.20236
C	-3.36264	-0.71156	0.20204
C	-4.74271	-0.85487	0.19656
C	-5.57201	0.28447	0.18315
C	-4.97250	1.55914	0.18902
C	-3.58666	1.70954	0.19999
C	2.28912	1.79922	0.20142
C	-2.28912	-1.79938	0.20150
C	2.38332	2.68406	1.46503
C	2.37978	2.67947	-1.06570
C	-2.37979	-2.67969	-1.06558
C	-2.38332	-2.68416	1.46516

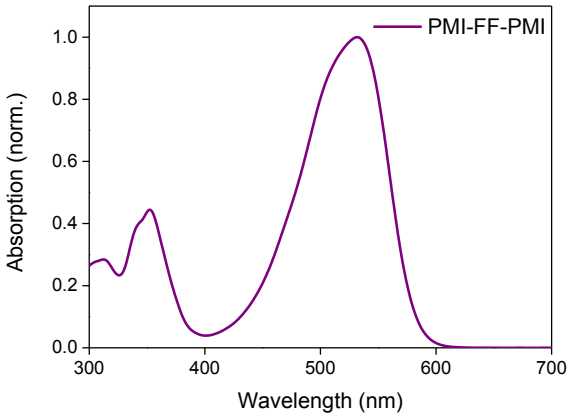

*Figure S5: UV-Vis absorption spectra of **PMI-FF-PMI (6)** in $CHCl_3$ solution.*

*Table S2: Comparison between the current densities (mA/cm^2) of solar cells based on **PMI-FF-PMI (6)** in a D/A ratio of 1/0.66 1/1 and 1/1.5 (w. and w/o annealing) from EQE, prior EQE and post EQE measurements.*

	D/A – 1/0.66	**D/A – 1/1**	**D/A – 1/1.5**
	PMI-FF-PMI (w/o annealing)	**PMI-FF-PMI (w/o annealing)**	**PMI-FF-PMI (w/o annealing)**
J_{SC} (integrated)	5.32 mA/cm^2	4.67 mA/cm^2	3.59 mA/cm^2
J_{SC} (before EQE)	6.54 mA/cm^2	6.25 mA/cm^2	6.21 mA/cm^2
J_{SC} (after EQE)	4.42 mA/cm^2	4.09 mA/cm^2	3.31 mA/cm^2
	PMI-FF-PMI (annealed at 135 °C)	**PMI-FF-PMI (annealed at 135 °C**	**PMI-FF-PMI (annealed at 135 °C)**
J_{SC} (integrated)	6.22 mA/cm^2	5.73 mA/cm^2	5.71 mA/cm^2
J_{SC} (before EQE)	7.85 mA/cm^2	7.38 mA/cm^2	7.36 mA/cm^2
J_{SC} (after EQE)	6.62 mA/cm^2	7.20 mA/cm^2	6.37 mA/cm^2

Table S3: Solar cell characteristics of PBDB-T/PMI-FF-PMI based solar cells with a D/A ratio of 1/1.5 and concentration of 7.5 mg/ml; best and mean values (best 8 cells).

D/A ratio	**Annealing temperature**	**Thickness (nm)**	**V_{OC} (V)**	**J_{SC} (mA/cm^2)**	**FF (%)**	**PCE (%)**
D/A – 1/1.5						
best cell	-	120 ± 8	1.14	5.90	44.7	2.98
average			1.13 ± 0.02	5.66 ± 0.27	41.8 ± 4.5	2.63 ± 0.28
best cell	135 °C	107 ± 2	1.10	7.36	51.6	4.15
average			1.11 ± 0.02	6.59 ± 0.21	57.8 ± 1.1	4.20 ± 0.10

The characterization of **PMI-FF-PMI** (**6**) as well as the fabrication of respective solar cells with their corresponding characterization methods was done according to the descriptions given in Chapter V – "Comparison of Fluorene, Silafluorene and Carbazol as Linkers in Perylene Monoimide Based Non-Fullerene Acceptors" if not otherwise stated.

Chapter VII

Summary and Outlook

Summary

Within the last decades, emerging photovoltaic technologies such as perovskite solar cells and organic solar cells were steadily improved. Power conversion efficiencies can nowadays rival already established solar cell technologies like crystalline silicon or CdTe. The high toxicity of lead for high performance PSCs motivated researchers to investigate lead-free alternatives such as tin or antimony. In OSCs, fused ring electron acceptors are at the moment the dominating acceptors species, however rylene derivatives are still an important acceptor group due to their easy tunability and synthesis procedures. Consequently they can be easily adjusted to available donor materials.

Antimony Perovskites

Antimony perovskites with the composition $Rb_3Sb_2Br_{9-x}I_x$ (x = 0 – 9) were selected for solar cell fabrication. $Rb_3Sb_2I_9$ was stepwise substituted by bromide to obtain the respective perovskite compositions. Single crystals were synthesized via vapor diffusion crystallization technique. The crystal structure of all perovskite compositions was determined to be monoclinic showing a $P2_1/n$ space group. Upon substitution towards higher bromine-based perovskites, the unit cell volume steadily decreased from 2403.01 $Å^3$ ($Rb_3Sb_2I_9$) to 1984.38 $Å^3$ ($Rb_3Sb_2Br_9$) according to Vegard's law. Moreover, all perovskite crystallized in a 2D-layered structure.

Thin films were prepared over a simple solution-based process and crystallized using an antisolvent dropping agent during spin coating. X-Ray diffraction spectra also displayed the introduction of bromide into the perovskite by a shift towards higher diffraction angles. While $Rb_3Sb_2I_9$ showed no preferential orientation, $Rb_3Sb_2Br_9$ crystallized in a preferred orientation alongside the (001) plane. Further, optical absorption spectra revealed a blueshift from ~600 nm ($Rb_3Sb_2I_9$) towards ~460 nm ($Rb_3Sb_2Br_9$). Nevertheless, the absorption coefficients remained in the range of $1 \cdot 10^5$ cm^{-1}. Fluorescence measurements of thin films and single crystals showed a similar optical shift. However, iodide rich compounds showed much higher intensities which may be related to the lower orientation from their X-Ray diffraction spectra.

Solar cells were fabricated with all perovskite compositions in an n-i-p device set-up using TiO_2 as ETL and spiro-OMeTAD as HTL. The highest device performance was measured with $Rb_3Sb_2I_9$ as absorber with an efficiency of 1.37%. $Rb_3Sb_2I_9$-based solar cells displayed only slight

hysteresis which was not influenced by the scan rate and bias conditions. Moreover, solar cells with $Rb_3Sb_2I_9$ displayed high stability of 84% from their initial efficiency for more than 150 days of storage under inert conditions. External quantum efficiency measurements revealed current generation over the whole spectral range of the perovskite absorption with a maximum value of 26.1% at 440 nm for $Rb_3Sb_2I_9$. With decreasing iodide content, the solar cell performance decreased to 0.01% for $Rb_3Sb_2Br_9$.

Tin Perovskites

For the fabrication of tin-based solar cells a triple cation tin perovskite with the composition $MA_{0.75}FA_{0.15}PEA_{0.1}Sn(Br_xI_{1-x})_3$ was selected. Partial substitution of iodide with bromide ($x = 0 – 0.33$) could improve the material properties which was reflected by higher solar cell efficiencies. The perovskites were synthesized over a solution-based process by mixing the respective metal salts in a DMSO/DMF mixture. Thin films were formed by spin coating and the perovskite crystallization was induced by an antisolvent dropping agent. Optical absorption spectra showed an increase in band gap from 1.29 eV ($x = 0$) to 1.50 eV ($x = 0.33$) as well as a shift towards higher diffraction angles in their corresponding X-Ray diffraction spectra which proved the successful incorporation of bromine into the perovskite. Furthermore, this is again in accordance with Vegard's law.

As pinhole-free perovskite layers are desired, the morphology of the perovskite thin films was investigated by SEM. Perovskites with a bromine content of $x = 0 – 0.25$ displayed fully covered films, however, with increasing bromine content ($x = 0.33$) pinholes were observed.

Solar cells in an p-i-n device set-up using PEDOT:PSS as HTL and $PC_{60}BM$ as ETL were fabricated for all perovskite compositions. Therein, with increasing bromine content, higher V_{OC} values were measured which can be related to the higher band gap. Moreover, the current density could also be increased for perovskite compositions $x = 0.08 – 0.25$. This led to average device efficiencies of ~3.9% for all three compositions, in comparison to an average of 2.7% for the pure iodide perovskite ($x = 0$). Moreover, the PSCs showed almost no hysteresis. The highest device efficiency was measured for $MA_{0.75}FA_{0.15}PEA_{0.1}Sn(Br_{0.25}I_{0.75})_3$ ($x = 0.25$) with a PCE value of 4.63%.

Upon increasing the bromine content to x = 0.33, the power conversion efficiency decreased to a maximum of 3.34% which can be ascribed to bad film formation (pinholes) and pronounced hysteresis. At last, external quantum efficiency spectra were recorded. Again, charge carrier generation over the whole spectral area of the perovskites was observed and is equal to the absorption from UV-Vis spectroscopy.

Non-Fullerene-Acceptors

Perylenes were selected as acceptor units in A-D-A type NFAs due to their high stability and easy synthesis routes. Over a two-step synthesis procedure, a reactive perylene monoimide bromide (PMI-Br) with good solubility was synthesized. Further on, two PMI-units were linked by Suzuki coupling with different fluorene derivatives, namely fluorene, silafluorene, carbazole and indenofluorene, to obtain the compounds PMI-F-PMI, PMI-FSi-PMI, PMI-FN-PMI and PMI-FF-PMI, respectively. The purity of the four compounds as well as intermediates was verified by ^{1}H- and ^{13}C-NMR spectroscopy and mass spectrometry.

In a first study the influence of the heteroatom in PMI-F-PMI, PMI-FSi-PMI and PMI-FN-PMI on the material properties, theoretical computations using DFT were performed. Thereby a first insight in their HOMO/LUMO levels, electron distribution in ground and excited state displayed similar behavior. Especially the twisting angle of 55° for all three compounds is important and noticeable as it may hinder π-π stacking of the molecules. The spectral coverage of the three NFAs showed a redshift compared to their PMI precursors due to the increased π-system. This is also visible by their three-times higher molar absorption coefficients of $9 \cdot 10^4\ M^{-1}\ cm^{-1}$ compared to their PMI-monomers ($3.3 \cdot 10^4\ M^{-1}\ cm^{-1}$). Moreover, in solution perylenes exhibited high quantum yields of 0.74, 0.74 and 0.72 for PMI-F-PMI, PMI-FSi-PMI and PMI-FN-PMI, respectively. Their optical band gaps were further determined to be 2.16 eV in solution and 2.06 eV in thin films. For comparison, also the electrical band gap was measured by cyclic voltammetry. Herein, band gaps of 2.19, 2.15 and 2.22 eV were obtained for PMI-F-PMI, PMI-FSi-PMI and PMI-FN-PMI, respectively, which are similar to the band gaps from optical spectroscopy.

The suitability of PBDB-T as donor material was given by a complementary absorption spectrum to the three NFAs and a HOMO offset of 0.25 eV and LUMO offset of 0.5 eV measured by cyclic voltammetry.

Before the fabrication of solar cells, GIWAXS measurements of the pristine acceptor films were recorded. The acceptor films displayed almost no features when measured at room temperature. However, at 150 °C small features concerning the crystallinity were visible, whereas PMI-FSi-PMI was identified to be the most crystalline upon those three. When blended with PBDB-T, the signals were dominated by the donor as strong features were already observed for the pristine donor films.

Finally, solar cells were fabricated with the device set-up: glass/ITO/ZnO/absorber/MoO_3/Ag. Different D/A ratios – 1/0.66, 1/1 and 1/1.5 – were tested for blend mixtures of PBDB-T/PMI-F-PMI, PBDB-T/PMI-FSi-PMI and PBDB-T/PMI-FN-PMI, respectively. With decreasing amount of acceptor, the power conversion efficiency increased to a maximum efficiency of 3.79%, 3.06% and 3.46% for PMI-F-PMI, PMI-FSi-PMI and PMI-FN-PMI, respectively. Higher amounts of the acceptor within the blend led to lower current densities and fill factors, reducing the overall device performance. However, independent on the D/A ratio, high open circuit voltages of >1 V could be reached.

Solar cells with the best performing D/A ratio were further optimized by annealing of the absorber layer. The efficiency could be boosted to a maximum of 5.16% with all three NFAs at 135 °C for PMI-F-PMI and 150 °C for PMI-FSi-PMI and PMI-FN-PMI. An annealing temperature in this range was selected due to the glass transition temperature of PBDB-T which is in the same range. In further measurements, the absorber surface was scanned by AFM. Herein, annealing of the absorber layer does not influence the miscibility of donor and acceptor and the roughness remained low. External quantum efficiency measurements revealed contribution of donor and acceptor to the charge carrier generation in their respective D/A ratios. The highest EQE values were obtained for the solar cells with annealed absorber layers with 53%, 53% and 57% at 510 nm for PMI-F-PMI, PMI-FSi-PMI and PMI-FN-PMI, respectively. Lastly, stability tests under constant illumination for 24 h displayed high stability of over 100% efficiency from their initial device performance.

One alternative material to PMI-F-PMI, PMI-FSi-PMI and PMI-FN-PMI examined was PMI-FF-PMI whose linker is composed of a larger conjugated π-system. The new NFA featured a higher Stokes shift of 77 nm compared to the other NFAs, otherwise similar optical properties were observed.

For comparison, also PBDB-T as donor was selected and D/A ratios of 1/0.66, 1/1 and 1/1.5 were tested. Thereby, reducing the acceptor concentration led to improved device efficiencies of 3.01%, 3.75% and 4.03% for a D/A of 1/1.5, 1/1 and 1/0.66, respectively. The solar cell performance could be further boosted by annealing of the absorber layer at 135 °C to a maximum efficiency of 6.21% with a V_{OC} of 1.18 V a J_{SC} of 8.49 mA/cm^2 and a FF of 62.4% with a D/A ratio of 1/0.66 and hereby shows its high potential in OSCs.

Outlook

Lead-free perovskite solar cells are still behind when it comes to power conversion efficiency compared to lead halide perovskite solar cells. Antimony perovskites with their $A_3B_2X_9$ composition may be enhanced via careful examination of its voltage losses. However, their efficiency is limited by their spectral absorption and it is highly unlikely that this class will be commercialized soon. On the other side, tin halide perovskites have the potential to replace lead-based perovskite in PSCs as they show the most promising efficiencies so far. However, a major concern is still their instability when exposed to air which has to be solved prior to the development of high performance cells.

The implementation of A-D-A based perylene monoimide species as NFAs in OSCs gave so far only moderate efficiencies. One possibility to improve the overall performance is optimization of the perylene by the addition of electron rich (e.g. chloride) or electron poor (e.g. silicon) side groups, substituted at the *bay*-position. This would result in a shift of their respective HOMO/LUMO levels hence give the opportunity to fit better to commercially available donors. Alternatively, mixing of different perylene species as acceptors with a suitable donor to form ternary blend systems is another approach worth testing. The highest chance for perylenes in OSCs is most likely the application in tandem solar cells as they display high open circuit voltages.

Chapter VIII

Appendix

List of Publications

Publications in peer reviewed journals

Results from this thesis

Stefan Weber, Jakob Hofinger, Thomas Rath, Matíss Reinfelds, David Pfeifer, Peter Fürk, Heinz Amenitsch, Markus Scharber, Gregor Trimmel, Comparison of Fluorene, Silafluorene and Carbazol as Linkers in Perylene Monoimide Based Non-Fullerene Acceptors, submitted to Materials Advances

Stefan Weber, Thomas Rath, Birgit Kunert, Roland Resel, Theodoros Dimopoulos, Gregor Trimmel, Dependence of material properties and photovoltaic performance of triple cation tin perovskites on the iodide to bromide ratio, *Monatshefte der Chemie*, **2019**, 150, 1921-2927

Stefan Weber, Thomas Rath, Roland Fischer, Birgit Kunert, Theodoros Dimopoulos, Andreas Steinegger, Gregor Trimmel, Effect of the iodide:bromide ratio on the structural and optoelectronic properties of rubidium antimony halide perovskites, *ACS Applied Energy Materials*, **2019**, 2, 539-547

Further papers

Stefan Weber, Thomas Rath, Jimmy Mangalam, Birgit Kunert, Anna Maria Coclite, Martin Bauch, Theodoros Dimopoulos, Gregor Trimmel, Investigation of NiO_x-hole transport layers in triple cation perovskite solar cells, *Journal of Materials Science: Materials in Electronics*, **2018**, 29, 1847-1855

Contributions to Publications in peer reviewed journals

Thomas Rath, Jasmin Handl, **Stefan Weber**, Bastian Friesenbichler, Peter Fürk, Lukas Troi, Theodoros Dimopoulos, Birgit Kunert, Roland Resel and Gregor Trimmel, Photovoltaic properties of a triple cation methylammonium/formamidinium/ phenylethylammonium tin iodide perovskite, *Journal of Materials Chemistry A*, **2019**, 7, 9523-9529

Jimmy Mangalam, Thomas Rath, **Stefan Weber**, Birgit Kunert, Theodoros Dimopoulos, Alexander Fian, Gregor Trimmel, Modification of NiOx hole transport layers with 4-bromobenzylphosphonic acid and its influence on the performance of lead halide perovskite solar cells, *Journal of Materials Science: Materials in Electronics*, **2019**, 30, 9602-9611

Oral Presentations

Stefan Weber, Matíss Reinfelds, Gregor Trimmel, New Non-Fullerene Acceptors for Organic Solar Cells, *18. Österreichische Chemietage Linz*, Linz, 26.09.**2019**

Stefan Weber, Substitution of iodine to bromine on rubidium-antimony-perovskites ($Rb_3Sb_2I_{9-x}Br_x$) and the change in crystal structure and photovoltaic performance, *Workshop Inorganic Chemistry in Austria (WACOE)*, 27.03.**2018**

Contributions to Oral Presentations

Thomas Rath, **Stefan Weber**, Jasmin Handl, Theodoros Dimopoulos, Birgit Kunert, Roland Resel, Gregor Trimmel, Exploring the Photovoltaic Properties and Stability of Triple Cation Tin Halide Perovskite Solar Cells, *18. Österreichische Chemietage Linz*, Linz, 26.09.**2019**

Matíss Reinfelds, **Stefan Weber**, Aileen Sauermoser, Sanela Alibegić, Rene Nauschnig, Bettina Schweda, Gregor Trimel, Rylene Dyes As Acceptors In Organic Solar Cells, *18. Österreichische Chemietage Linz*, Linz, 26.09.**2019**

Posters

Stefan Weber, Matíss Reinfelds, Rene Nauschnigg, Bettina Schweda, Sanela Alibegić, Aileen Sauermoser, Peter Fürk, Gregor Trimmel, Perylene Derivatives as Non Fullerene Acceptors for Organic Solar Cells, *17. Österreichische Photovoltaik Tagung und 10. Stromspeicher Tagung*, Wien, 05.11.**2019**

Stefan Weber, Thomas Rath, Rene Nauschnig, Gregor Trimmel, Functionalized Perylene Derivatives as Non Fullerene Acceptors for Organic Solar Cells, *International Conference on Hybrid and Organic Photovoltaics (HOPV19)*, Rom, 13.05.**2019**

Stefan Weber, Thomas Rath, Kathrin Fellner, Roland Fischer, Birgit Kunert, Theodoros Dimopoulos, Gregor Trimmel, Crystallographic and Optoelectronic Study of Rubidium Antimony Halide Perovskites, *16. Österreichische Photovoltaik Tagung*, IMC FH Krems, 22.11.**2018**

Stefan Weber, Bastian Friesenbichler, Thomas Rath, Birgit Kunert, Gregor Trimmel, Investigation of different tin perovskites as solar cell absorber materials, *15.* Österreichische Photovoltaik-Tagung, Wien, 13.11.**2017**

Stefan Weber, Jimmy Mangalam, Thomas Rath, Gregor Trimmel, Birgit Kunert, Anna Maria Coclite, Nickel (II) oxide nanoparticles as hole transport material in $Cs_x(MA_{0.17}FA_{0.83})_{(100-x)}Pb(I_{0.83}Br_{0.17})_3$ triple cation perovskite solar cells, *14. Österreichische Photovoltaik-Tagung*, Villach, 28.11.**2016**

Contributions to Posters

Peter Fürk, **Stefan Weber**, Matíss Reinfelds, Gregor Trimmel, Synthesis of Perylene-Linker-Perylene Triads and their Application in Organic Solar Cells, Central European Conference on Photochemistry (CECP 2020), Bad Hofgastein, 09.02.**2020**

Bettina Schweda, Matíss Reinfelds, **Stefan Weber**, Gregor Trimmel, Synthesis of Perylene-Monoimide-Phenylene-Perylene-Monoimide Acceptors and their Application in Non-Fullerene Solar Cells, 18. Österreichische Chemietage Linz, Linz, 24.09.**2019**

Gregor Trimmel, **Stefan Weber**, Thomas Rath, Jasmin Handl, Investigation of Triple Cation Tin Perovskite Solar Cells, International Conference on Hybrid and Organic Photovoltaics (HOPV19), 13.05.**2019**

Jimmy Mangalam, Thomas Rath, **Stefan Weber**, Birgit Kunert, Theodorous Dimoploulos, Alexander Fian, Gregor Trimmel, Investigating the effects of functionalized benzylphosphonic acid SAMs on triple cation perovskite based solar cells, MRS Boston, 27.11.**2018**

Jimmy Mangalam, Thomas Rath, **Stefan Weber**, Birgit Kunert, Theodorous Dimoploulos, Alexander Fian, Gregor Trimmel, R-functionalized benzylphosphonic acid SAMs for improved efficiency in inverted triple cation lead perovskite solar cells, International Conference on Hybrid and Organic Photovoltaics (HOPV18), Benidorm, Spain, 29.05.**2018**

Jimmy Mangalam, **Stefan Weber**, Thomas Rath, Birgit Kunert, Anna Maria Coclite, Martin Bauch, Theodorous Dimopoulos, Gregor Trimmel, Effect of hole transport layers on triple cation perovskite based conventional and inverted solar cell geometry, *15. Österreichische Photovoltaik-Tagung*, Wien, 13.11.**2017**

Abbreviation List

a:Si-H	Amorphous silicon
AFM	Atomic force microscopy
BWD	Backward
BDT-Th	4,8-di(thiophen-2-yl)benzo[1,2-b:4,5-b']dithiophene
CB	Chlorobenzene
CV	Cyclic voltammetry
CZTS	Copper Indium Tin sulfide
D/A	Donor/Acceptor
DCTB	trans-2-[3-(4-tert-butylphenyl)-2-methyl-2-propenylidene]malononitrile
DFT	Density functional theory
DMF	Dimethylformamid
DMSO	Dimethylsulfoxide
DSC	Differential Scanning Calorimetry
$EDAI_2$	Ethylenediammonium iodide
EQE	External quantum efficiency
ETL	Electron transport layer
F	Fluorene
FA	Formamidinium
$FAPbI_3$	Formamidinium Lead iodide
FK-209 Co (III) TFSI salt	tris(2-(1H-pyrazol-1-yl)-4-tert-butylpyridine)cobalt(III) tri[bis(trifluoromethane)sulfonimide]
FN	Carbazol
FREA	Fused ring electron acceptor
FSi	Silafluorene
FWD	Forward
GA^+	Guanidinium
GIWAXS	Grazing incidence wide angle X-Ray scattering
HI	Iodic acid
HTL	Hole transport layer

HOMO	Highest occupied molecular orbital
IBCA	Indene-C60 bis adduct
IDT	Indacenodithiophene
IDTT	Indacenodithieno[3,2-b]thiophene
IEIC	Indaceno[1,2-b:5,6-b0]dithiophene and 2-(3-oxo-2,3-dihydroinden-1-ylidene)malononitrile
INCN derivative	(5,6-difluoro-3-oxo-2,3-dihydro-1H-inden-1-ylidene)malononitrile
J-V	Current-Voltage
LiTFSI	Lithium bis(trifluoromethanesulfonyl)imide
LUMO	Lowest unoccupied molecular orbital
MA	Methylammonium
$MAPbI_3$	Methylammonium Lead iodide
m_{pp} tracking	Maximum power point tracking
N2200	NDI-bithiophene copolymer
NDI	Naphthalene diimide
NH_4SCN	Ammoniumthiocyanat
NFA	Non-fullerene acceptor
OSC	Organic solar cell
PBDB-T / PCE12	poly[(2,6-(4,8-bis(5-(2-ethylhexyl)thiophen-2-yl)-benzo[1,2-b:4,5-b']dithiophene))-alt-(5,5-(1',3'-di-2-thienyl-5',7'-bis(2-ethylhexyl)benzo[1',2'-c:4',5'-c']dithiophene-4,8-dione)]
$PC_{60}BM$	[6,6]-phenyl-C_{61}-butyric acid methyl ester
$PC_{70}BM$	[6,6]-phenyl-C_{71}-butyric acid methyl ester
PCE	Power conversion efficiency
PDI	Perylene diimide
PEA	Phenethylammonium
PEAI	Phenethylammonium iodide
PL	Photoluminescence
PMI	Perylene monoimide
PSC	Perovskite solar cell / Polymer solar cell

PTB7-Th / PCE10	poly[4,8-bis(5-(2-ethylhexyl)thiophen-2-yl)benzo[1,2-b;4,5-b']dithiophene-2,6-diyl-alt-(4-(2-ethylhexyl)-3-fluorothieno[3,4-b]thiophene-)-2-carboxylate-2-6-diyl)]
PTCDA	Perylene-3,4,9,10-tetracarboxylic anhydride
PTN-Br	poly[tetraphenylethene-3,3′-(((2,2-diphenylethene-1,1-diyl)bis(4,1-phenylene))bis(oxy))bis(*N*,*N*-dimethylpropan-1-amine)tetraphenylethene]
PVA	poly (vinyl alcohol)
SEM	Scanning electron microscopy
SI	Supporting Information
SMA	Small molecule acceptor
Spiro-OMeTAD	2,2′,7,7′-tetrakis[N,N-di(4-methoxyphenyl)amino]-9,9′-spirobifluorene
TCO	Transparent conductive oxide
T_g	Glass transition temperature
XRD	X-Ray diffraction

Author Contributions

Chapter III

The presented data in chapter III were published in ACS Applied Energy Materials. The synthesis of the perovskites, thin film analysis and fabrication of solar cells were done by S. Weber with the help of K. Fellner, A. Steinegger and B. Kunert. Analysis of the corresponding solar cells was done by S. Weber with help from T. Rath. Single crystal measurements and their evaluation were performed by R. Fischer. Scanning electron microscopy measurements were done by T. Dimopoulos. The main manuscript was written by S. Weber with the contribution of T. Rath, R. Fischer, R. Resel and G. Trimmel to the final version. All authors acknowledged the final version before submission.

Chapter IV

The presented data in chapter IV were published in Monatshefte der Chemie. The synthesis of the perovskites, thin film analysis and solar cell fabrication was performed by S. Weber with the help of B. Kunert for X-Ray diffraction measurements and R. Resel for X-Ray diffraction spectra interpretation. Solar cell characterization was done by S. Weber with the help of T. Rath. Scanning electron microscopy measurements of the perovskite surfaces were performed by T. Dimopoulos. The main manuscript was written by S. Weber with the help of T. Rath, R. Resel and G. Trimmel. All authors acknowledged the final version before submission.

Chapter V

The presented data in chapter V were submitted to Materials Advances. Synthesis and characterization of the acceptors, thin film analysis and solar cell fabrication was done by S. Weber with help from J. Hofinger who performed the mobility, cyclic voltammetry, atomic force microscopy and fluorescence measurements of the thin films including their analysis. M. Reinfelds contributed to the synthesis procedures and DFT calculations. D. Pfeifer and S. M. Borisov contributed to the synthesis and fluorescence measurements. T. Rath, P. Fürk and M. Reinfelds performed the GIWAXS measurements. T. Rath and H. Amenitsch contributed to the analysis of the GIWAXS measurements. The main manuscript was written by S. Weber with the help of J. Hofinger and T. Rath. S. Weber acknowledges G. Trimmel and M. C. Scharber for their discussions and comments to the manuscript. All authors acknowledged the final version before submission.